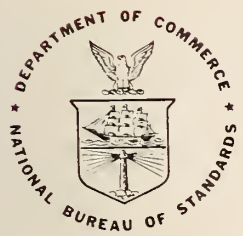


REFERENCE

NBS
Publica-
tions

NAT'L INST. OF STAND & TECH RIC

A11104 657265



NBS TECHNICAL NOTE **1190**

U.S. DEPARTMENT OF COMMERCE/National Bureau of Standards

NBS Reactor: Summary of Activities July 1982 Through June 1983



QC
100
.U5753
No. 1190
1934

NATIONAL BUREAU OF STANDARDS

The National Bureau of Standards¹ was established by an act of Congress on March 3, 1901. The Bureau's overall goal is to strengthen and advance the Nation's science and technology and facilitate their effective application for public benefit. To this end, the Bureau conducts research and provides: (1) a basis for the Nation's physical measurement system, (2) scientific and technological services for industry and government, (3) a technical basis for equity in trade, and (4) technical services to promote public safety. The Bureau's technical work is performed by the National Measurement Laboratory, the National Engineering Laboratory, and the Institute for Computer Sciences and Technology.

THE NATIONAL MEASUREMENT LABORATORY provides the national system of physical and chemical and materials measurement; coordinates the system with measurement systems of other nations and furnishes essential services leading to accurate and uniform physical and chemical measurement throughout the Nation's scientific community, industry, and commerce; conducts materials research leading to improved methods of measurement, standards, and data on the properties of materials needed by industry, commerce, educational institutions, and Government; provides advisory and research services to other Government agencies; develops, produces, and distributes Standard Reference Materials; and provides calibration services. The Laboratory consists of the following centers:

Absolute Physical Quantities² — Radiation Research — Chemical Physics — Analytical Chemistry — Materials Science

THE NATIONAL ENGINEERING LABORATORY provides technology and technical services to the public and private sectors to address national needs and to solve national problems; conducts research in engineering and applied science in support of these efforts; builds and maintains competence in the necessary disciplines required to carry out this research and technical service; develops engineering data and measurement capabilities; provides engineering measurement traceability services; develops test methods and proposes engineering standards and code changes; develops and proposes new engineering practices; and develops and improves mechanisms to transfer results of its research to the ultimate user. The Laboratory consists of the following centers:

Applied Mathematics — Electronics and Electrical Engineering² — Manufacturing Engineering — Building Technology — Fire Research — Chemical Engineering²

THE INSTITUTE FOR COMPUTER SCIENCES AND TECHNOLOGY conducts research and provides scientific and technical services to aid Federal agencies in the selection, acquisition, application, and use of computer technology to improve effectiveness and economy in Government operations in accordance with Public Law 89-306 (40 U.S.C. 759), relevant Executive Orders, and other directives; carries out this mission by managing the Federal Information Processing Standards Program, developing Federal ADP standards guidelines, and managing Federal participation in ADP voluntary standardization activities; provides scientific and technological advisory services and assistance to Federal agencies; and provides the technical foundation for computer-related policies of the Federal Government. The Institute consists of the following centers:

Programming Science and Technology — Computer Systems Engineering.

¹Headquarters and Laboratories at Gaithersburg, MD, unless otherwise noted;
mailing address Washington, DC 20234.

²Some divisions within the center are located at Boulder, CO 80303.

NBS Reactor: Summary of Activities July 1982 Through June 1983

Frederick J. Shorten, Editor

Reactor Radiation Division
National Measurement Laboratory
National Bureau of Standards
Washington, DC 20234

Ref
QC
100
115753
No. 1190
1984



U.S. DEPARTMENT OF COMMERCE, Malcolm Baldrige, Secretary
NATIONAL BUREAU OF STANDARDS, Ernest Ambler, Director

Issued April 1984

National Bureau of Standards Technical Note 1190
Natl. Bur. Stand. (U.S.), Tech. Note 1190, 202 pages (Apr. 1984)
CODEN: NBTNAE

U.S. Government Printing Office
Washington: 1984

For sale by the Superintendent of Documents, U.S. Government Printing Office, Washington, D C 20402

FOREWORD

The National Bureau of Standards Reactor was built not only to serve the needs of the NBS but also those of other government agencies as a National Center for the application of neutron methods to problems of national interest. The Reactor Radiation Division was established to operate the reactor and to foster its scientific and technological use. Toward this end, the Division has a small nucleus of scientists experienced in the use of reactors for a wide range of scientific and technical problems. In addition to pursuing their own research and developing sophisticated experimental facilities, they actively seek out and encourage collaboration with other scientists engaged in challenging programs whose work can benefit from use of the reactor, but who as yet do not have the reactor experience necessary to take full advantage of the facilities available. The Division also provides irradiation services to a wide variety of users as well as engineering and other technical services.

The reactor operates at 10 MW and is designed to provide more than 25 experimental facilities ranging from intense neutron beams to extensive irradiation facilities, making it one of the most versatile high flux research reactors in the country. Thus, it is able to serve a large number of scientists and engineers in a broad range of activities both within and outside the NBS.

This report attempts to summarize all the work done which is dependent on the reactor including a large number of programs outside the Division. The first section summarizes these programs carried out by scientists in the Reactor Radiation Division and their collaborators. The second section summarizes NBS work originating entirely outside the Division which requires no collaboration with Division scientists. The section entitled, "Service Programs," covers those programs originating outside NBS but for which the Division provides irradiation services. The remaining sections are self-explanatory.

Appreciation is extended to F. J. Shorten of the Reactor Radiation Division for his extensive contributions to the editing, organization, and preparation of this report, and T. Lindstrom, P. Andrew, S. Long, S. Tassey, and N. Rhyne for efforts in typing manuscripts.



R. S. Carter
Chief, Reactor Radiation Division
National Bureau of Standards

ABSTRACT

This report summarizes all those programs which depend on the NBS reactor. It covers the period from July 1982 through June 1983. The programs range from the use of neutron beams to study the structure and dynamics of materials through nuclear physics and neutron standards to sample irradiations for activation analysis, isotope production, radiation effects studies, neutron radiography, and nondestructive evaluation.

Key words: Activation analysis; crystal structure; diffraction; isotopes; molecular dynamics; neutron; neutron radiography; nondestructive evaluation; nuclear reactor; radiation.

DISCLAIMER

Certain trade names and company products are identified in order to adequately specify the experiment procedure. In no case does such identification imply recommendation or endorsement by the National Bureau of Standards, nor does it imply that the products are necessarily the best available for the purpose.

TABLE OF CONTENTS

FOREWORD	iii
ABSTRACT	iv
A. REACTOR RADIATION DIVISION AND COLLABORATIVE PROGRAMS	1
The Effect of Slit Height on Peak Positions, Widths, and Shapes in Powder Diffraction	1
The Structure of $\text{La}_3\text{WO}_6\text{Cl}_3$	3
Study of Hydrogen Bonds in $\text{Ca}_2\text{KH}_7(\text{PO}_4)_4 \cdot 2\text{H}_2\text{O}$	4
Structure Studies of the Superionic Conductor System $\text{Na}_{1+x}\text{Zr}_2\text{Si}_x\text{P}_{3-x}\text{O}_{12}$ (NASICON)	9
The Structures of Lithium Inserted Metal Oxides; $\text{Li}_2\text{FeV}_3\text{O}_8$	12
Neutron and X-Ray Diffraction Study on Polymorphism in Lithium Orthotantalate Li_3TaO_4	14
The Crystal Structure of Lithium Zirconate, $\text{Li}_6\text{Zr}_2\text{O}_7$	18
Studies of Zeolite Structure by Neutron Powder Diffraction	21
The Structure of Synthetic Zeolite Omega	25
Active Site of RNase: Neutron Diffraction Study of a Complex with Uridine Vanadate, A Transition State Analog	26
Microvoid Formation in Ammonium Nitrate	29
Nondestructive Characterization of Sub-Surface Residual Stress	31
Crystal Data (Produced by Automated Typesetting Procedures)	34
Progress Report on a Study of Specialized Lattices Using Matrix and Reduction Techniques	36
Space Group Frequencies for Organic Compounds	39
An Empirical Method for the Approximation of Densities	52
Thermal Properties of $(\text{KCN})_x(\text{KBr})_{1-x}$ in the Quadrupolar Glass State	56
Structure of Alkali Cyanide and Mixed Alkali Cyanide-Alkali Halide Crystals	57
Critical Behavior and Magnetic Ordering in Amorphous TbFe_2	59
Short Range Magnetic Ordering in $\text{Y}_6(\text{Fe}_{1-x}\text{Mn}_x)_{23}$	61
Deuterium Site Occupation and Magnetism in $\text{Ho}_6\text{Fe}_{23-x}\text{D}_x$ Compounds	63
Spin Dynamics of $\text{Fe}_{40}\text{Ni}_{40}\text{P}_{14}\text{B}_6$	65
Reentrant Spin Glass Behavior in Amorphous $(\text{Fe}_x\text{Ni}_{100-x})_{75}\text{G}_{125}$	68
Spin Dynamics of Dilute $\text{Pd}_{1-x}\text{Fe}_x$ Ferromagnets	71
Magnetic Phase Transition in the Superconductor HoMo_6Se_8	72

TABLE OF CONTENTS

Magnetic and Superconducting Properties of Ho Rich ($\text{Er}_{1-x}\text{Ho}_x\text{Rh}_4\text{B}_4$)	74
Critical Fluctuations in the Ferromagnetic Superconductor HoMo_6S_8	77
Advanced Neutron Methods	79
Small Angle Scattering from Ferrofluids	81
Characterizing Microporosity of Chemical Adsorbents by Small Angle Neutron Scattering	83
SANS Investigations of Porosity in YCrO_3 Ceramics	84
Small Angle Neutron Scattering (SANS) Study of Creep Damage in 304 Stainless Steel	86
Uniaxial Deformation of Rubber Network Chains by Small Angle Neutron Scattering	94
Small Angle Scattering from Amorphous DyCu	95
Generalized Theory of Neutron Scattering from Hydrogen in Metals	96
Theory of Excitation Bands of Hydrogen in Metals and of Their Observation by Neutron Scattering	99
Theory of Hydrogen Trapping by Interstitial Impurities in bcc Metals	103
Theory of SANS from Large Particles and Voids	105
Neutron Diffraction Structure Determination of the High-Temperature Form of Lithium Tritantalate, $\text{H-LiTa}_3\text{O}_8$	106
B. NON-RRD PROGRAMS	108
Activation Analysis Group FY 83	108
Atmospheric and Environmental Studies by Instrumental Neutron Activation Analysis	139
Validation of Stable Isotope Tracing for Study of Zinc Nutrition in Human Subjects	146
Neutron-Capture Prompt Gamma-Ray Activation Analysis	147
High Accuracy Determination of U-235 by Gamma-Ray Spectroscopy in Nondestructive Assay Standards	154
Summary of Activities Carried out by the Neutron Field Standards Group	156
Fission Cross Section Measurements in Reactor Physics and Dosimetry Benchmarks at NBS	160
Integral Cross Section Measurements in the ^{235}U Fission Neutron Spectrum	163
Neutron Personnel Dosimeter Calibrations and Testing	167
Range of Individual Fission Fragments in Matter	168

TABLE OF CONTENTS

C. REACTOR OPERATIONS AND SERVICES	169
D. SERVICES PROGRAMS	171
Neutron Activation Analysis at the Food and Drug Administration	171
Positron Annihilation in CuGe and CuZn Alloys	175
E. PERSONNEL ROSTER	180
F. PUBLICATIONS	186

A. REACTOR RADIATION DIVISION AND COLLABORATIVE PROGRAMS

THE EFFECT OF SLIT HEIGHT ON PEAK POSITIONS, WIDTHS, AND SHAPES IN POWDER DIFFRACTION

E. Prince

It is well known^{1, 2} that expressions giving peak positions, widths, and shapes in powder diffraction as functions of wavelength, cell constants, and instrumental resolution depend on approximations that are valid only if the axial extent of the instrumental resolution function is infinitesimally small. Because a real instrument must have a finite slit height, and because the actual scattered radiation for a particular Bragg reflection comes out in a cone with semiangle 2θ , the expressions are strictly correct only for $2\theta = 90^\circ$, and they must be corrected for diffraction at other angles. For $2\theta < 90^\circ$, the peak centroid is shifted toward lower angles, the peak is broadened, and an otherwise symmetric peak becomes skewed with a longer tail on the low angle side than on the high angle side. The mathematical analysis of these effects has much in common with another problem in crystallography, the probability distribution for an atomic position when thermal motion is curvilinear.

Figure 1 shows schematically a segment of a Debye-Scherrer ring as seen through a slit of finite height. A point on the ring at height z is displaced toward the center of the ring by an amount $\Delta = r(1 - \cos \alpha)$, where r is the radius of curvature of the ring, and is given by $r = R \tan 2\theta$, where R is the distance from the sample to the detector slit. If α is sufficiently small, $(1 - \cos \alpha) \approx \alpha^2/2 \approx z^2/2r^2$. The angular displacement of the point is

$$\delta = -(z^2/2R^2)\cot 2\theta. \quad (1)$$

The angular displacement of the peak is obtained by averaging δ over the vertical resolution function of the diffractometer.

$$\langle \delta \rangle = -\left(\langle z^2 \rangle / 2R^2\right) \cot 2\theta, \quad (2)$$

where $\langle z^2 \rangle = z^2 \rho(z)dz$, and $\rho(z)$ is the vertical resolution function. The peak is broadened so that its variance is given by

$$\sigma_b^2 = \sigma_0^2 + \langle \delta^2 \rangle - \langle \delta \rangle^2, \quad (3)$$

where σ_0^2 is the variance of the unbroadened peak and $\langle \delta^2 \rangle = (\langle z^4 \rangle / 4R^4) \cot^2 2\theta$. A Gaussian peak becomes skewed so that the shape function becomes

$$P(2\theta) = 1 + (3\kappa/6) H_3 \left[(2\theta - 2\theta_B - \langle \delta \rangle / \sigma_b) \right] G(2\theta, 2\theta_B + \langle \delta \rangle, \sigma_b), \quad (4)$$

where $H_3(x) = x^3 - 3x$, $G(x, \mu, \sigma) = (2\sigma^2)^{-1/2} \exp -(1/2)(x - \mu)^2/\sigma^2$, $2\theta_B$ is the Bragg angle for the unshifted peak, and 3κ is a third cumulant given by $3\kappa = \langle \delta^3 \rangle - 3\langle \delta^2 \rangle \langle \delta \rangle + 2\langle \delta \rangle^3$.

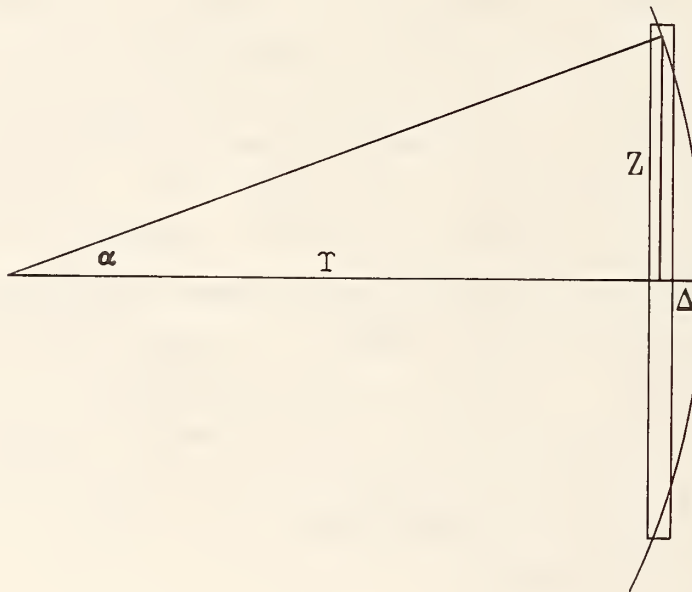


Figure 1. The effective Bragg position of points on a Debye-Scherrer ring above and below the horizontal plane of the diffractometer.

-
1. A. J. C. Wilson, "Mathematical Theory of X-ray Powder Diffractometry," p. 70-76, Eindhoven: Physics Technical Library (1963).
 2. M. J. Cooper and J. P. Sayer, J. Appl. Cryst. 8, 615-618 (1975).

THE STRUCTURE OF $\text{La}_3\text{WO}_6\text{Cl}_3$

J. B. Parise and L. H. Brixner
 (E. I. duPont de Nemours and Co., Wilmington, DE)
 and
 E. Prince

An x-ray determination of the structure of $\text{La}_3\text{WO}_6\text{Cl}_3$ ¹ found that the tungsten coordination polyhedron was a highly unusual trigonal prism instead of an octahedron. Cohesive energy calculations also indicated that this configuration should be energetically unfavorable. Because of this and also that the fact that the x-ray intensities tend to be dominated by the heavy metals, there was some doubt about the correctness of the crystal structure, so a neutron powder diffraction study was undertaken to verify it.

Neutron powder diffraction data were collected on the NBS high-resolution powder diffractometer, and the structure was refined by the Rietveld² method to $R_{wp} = 9.13$ percent, as compared with $R_e = 7.14$ percent. R_B , based on integrated intensities, was 6.00 percent. The trigonal prismatic coordination of the tungsten was confirmed. Table 1 gives the refined atomic parameters. Figure 1 shows the coordinations for W and La.

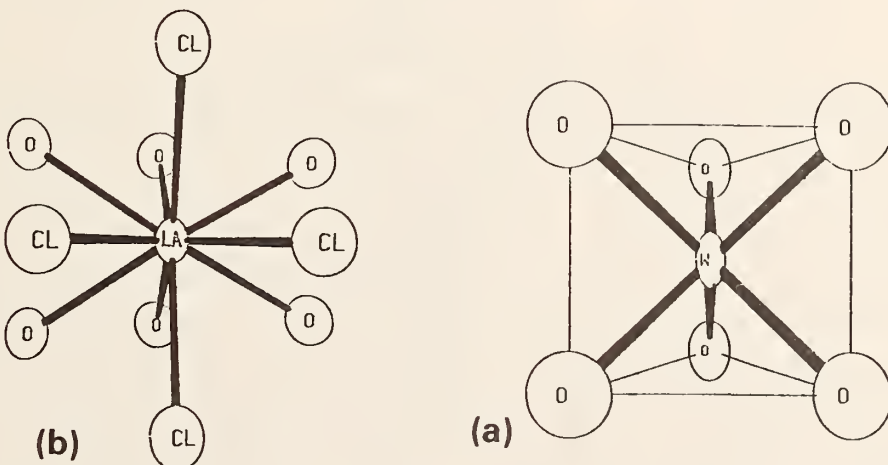


Figure 1. (a) The tungsten environment in $\text{La}_3\text{WO}_6\text{Cl}_3$. (b) The lanthanum environment in $\text{La}_3\text{WO}_6\text{Cl}_3$.

Table 1. Refined atomic parameters for $\text{La}_3\text{WO}_6\text{Cl}_3$. Standard deviations for the least significant figures are given in parenthesis. The space group is $P6_3/m$, $a = 9.4092(2)$, $c = 5.4276(2) \text{ \AA}$.

Atom	x	y	z	$B (\text{\AA}^2)$
La	0.0896(3)	0.6843(3)	3/4	0.50(5)
W	1/3	2/3	1/4	1.42(21)
Cl	0.2399(2)	0.0474(3)	3/4	0.42(4)
O	0.3627(3)	0.8370(3)	0.0231(5)	0.56(5)

-
1. L. H. Brixner, H. Y. Chen, and C. M. Foris, J. Solid State Chem. 44, 99 (1982).
 2. H. M. Rietveld, J. Appl. Cryst. 2, 65 (1969).

STUDY OF HYDROGEN BONDS IN $\text{Ca}_2\text{KH}_7(\text{PO}_4)_4 \cdot 2\text{H}_2\text{O}$

S. Takagi and M. Mathew
(American Dental Association)

and

E. Prince

A preliminary refinement of the structure of $\text{Ca}_2\text{KH}_7(\text{PO}_4)_4 \cdot 2\text{H}_2\text{O}$ in space group, P1, was reported previously.¹ In this centrosymmetric space group, three hydrogen bonds cross centers of symmetry, although they are unusually long (2.474 to 2.504 Å) for symmetric O...H...O hydrogen bonds. The potassium atom appears also to be randomly disordered across a center of symmetry. These facts suggested that the crystal might actually lack the center of symmetry, so the structure was further refined in space group P1. Two distinct non-centrosymmetric models were refined. In one the temperature factors of pairs of atoms that were related by the center of symmetry in the centrosymmetric model were constrained to be equal. In the other model these constraints were removed. Table 1 is a summary of the R indices for various models, together with the number of reflections and the number of parameters in each case. Each model is a significantly better fit, statistically, than the one with fewer parameters. However, the completely unconstrained model had one temperature factor tensor that was not definite, and the position parameters were not significantly different from the model with the constrained temperature factors. For

Table 1. Summary of the R indices, the number of reflections included in the refinement and the number of parameters for each of four models of $\text{Ca}_2\text{KH}_7(\text{PO}_4)_4 \cdot 2\text{H}_2\text{O}$

Model	Number of Reflections	Number of Parameters	R (%)	R_w (%)
P1-K on center	1381	170	5.9	7.0
P1-K split	1381	173	5.7	6.7
P1-TFs constrained	1383	227	5.1	6.0
P1-unconstrained	1379	323	4.5	5.2

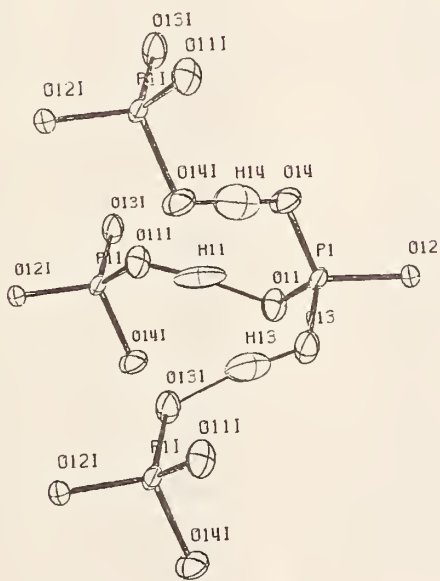


Figure 1. The three hydrogen bonds that cross pseudo centers of symmetry 014-H14-014I is still nearly symmetric in P1.

Table 2. Refined position parameters and equivalent isotropic thermal parameters for $\text{Ca}_2\text{KH}_7(\text{PO}_4)_4 \cdot 2\text{H}_2\text{O}$. Estimated standard deviations for the least significant digits are given in parenthesis. K was held fixed to define the origin.

Atom	x	y	z	$B_{\text{eq.}}$
Ca	-0.0032 (21)	0.0991 (12)	0.3005 (20)	0.87 (3)
CaI	-0.0019 (21)	-0.0980 (12)	-0.2961 (21)	0.87 (3)
K	0.4948	0.5377	-0.0154	4.34 (25)
P1	0.1372 (21)	0.6348 (12)	0.3768 (20)	1.12 (4)
P1I	-0.1664 (21)	0.3606 (12)	-0.3812 (21)	1.12 (4)
P2	0.4926 (20)	-0.0954 (12)	0.2103 (20)	0.75 (3)
P2I	-0.5014 (20)	0.0990 (12)	-0.2123 (20)	0.75 (3)
O11	0.0944 (22)	0.5954 (11)	0.1071 (20)	1.93 (4)
O11I	-0.1148 (22)	0.4055 (11)	-0.1127 (20)	1.93 (4)
O12	0.1460 (20)	0.7671 (11)	0.4505 (20)	1.03 (4)
O12I	-0.1335 (20)	0.2372 (11)	-0.4209 (20)	1.03 (4)
O13	0.4149 (21)	0.5951 (11)	0.5394 (22)	2.24 (4)
O13I	-0.4285 (21)	0.3986 (11)	0.4605 (22)	2.24 (4)
O14	-0.0652 (21)	0.5852 (12)	0.4108 (23)	2.15 (4)
O14I	0.0576 (21)	0.4146 (12)	-0.4159 (23)	2.15 (4)
O21	0.2406 (20)	-0.0388 (11)	0.1432 (20)	1.16 (3)
O21I	-0.2483 (20)	0.0317 (11)	-0.1418 (21)	1.16 (3)
O22	0.7443 (19)	-0.0314 (11)	0.3215 (20)	1.18 (3)
O22I	0.2516 (20)	0.0325 (11)	-0.3178 (20)	1.18 (3)
O23	0.5312 (20)	-0.1668 (12)	0.3912 (20)	1.27 (4)
O23I	0.4682 (20)	0.1705 (12)	-0.4055 (20)	1.27 (4)
O24	0.4623 (20)	-0.1836 (12)	-0.0305 (20)	1.74 (4)
O24I	-0.4666 (21)	0.1831 (12)	0.0342 (20)	1.74 (4)
O3	0.1428 (21)	0.2463 (11)	0.1761 (21)	1.48 (4)
O3I	-0.1437 (21)	-0.2507 (11)	-0.1728 (21)	1.48 (4)
H23	0.3664 (27)	-0.1881 (14)	0.4052 (28)	2.09 (6)
H23I	-0.3655 (27)	0.1913 (14)	-0.4177 (28)	2.09 (6)
H24	0.6253 (29)	-0.1973 (14)	-0.0642 (31)	2.58 (8)
H24I	0.3851 (29)	0.2058 (15)	0.0737 (30)	2.58 (8)
H31	0.0254 (29)	0.2966 (16)	0.0633 (30)	3.09 (7)
H31I	-0.0392 (29)	-0.2909 (16)	-0.0626 (30)	3.09 (7)
H32	0.2380 (39)	0.3048 (16)	0.3143 (30)	3.96 (11)
H32I	-0.2624 (38)	-0.2992 (16)	-0.3151 (30)	3.96 (11)
H11	-0.0335 (28)	0.4928 (21)	-0.0145 (36)	3.63 (19)
H13	0.4686 (29)	0.5106 (17)	0.5093 (33)	3.23 (22)
H14	0.0025 (40)	0.5037 (25)	0.5089 (40)	3.80 (14)

Table 3. Selected bond distances and angles in $\text{Ca}_2\text{KH}_7(\text{PO}_4)_4 \cdot 2\text{H}_2\text{O}$. Estimated standard deviations for the least significant digits are given in parenthesis.

Ca-012I	2.424 (10) Å	CaI-012	2.354 (10) Å
Ca-021	2.370 (11)	CaI-021	2.459 (10)
Ca-021I	2.485 (9)	CaI-021I	2.317 (11)
Ca-022	2.310 (9)	CaI-022	2.509 (9)
Ca-022I	2.507 (9)	CaI-022I	2.315 (9)
Ca-023I	2.611 (10)	CaI-023	2.608 (9)
Ca-024I	2.707 (10)	CaI-024	2.717 (10)
Ca-03	2.462 (10)	CaI-03I	2.502 (10)
K-011	2.676 (11) Å		
K-011I	2.801 (11)		
K-013	2.891 (12)		
K-014	2.757 (12)		
K-014I	2.891 (13)		
P1-011	1.564 (9) Å	011-P1-012	109.3 (5)°
P1-012	1.567 (9)	011-P1-013	108.6 (6)
P1-013	1.575 (9)	011-P1-014	109.2 (6)
P1-014	1.464 (9)	012-P1-013	105.5 (95)
		012-P1-014	113.6 (6)
		013-P1-014	110.4 (6)
P1I-011I	1.549 (9) Å	011I-P1I-012I	107.2 (5)°
P1I-012I	1.472 (9)	011I-P1I-013I	110.1 (6)
P1I-013I	1.499 (9)	011I-P1I-014I	105.8 (6)
P1I-014I	1.604 (9)	012I-P1I-013I	114.4 (6)
		012I-P1I-014I	109.0 (6)
		013I-P1I-014I	110.0 (6)
P2-021	1.461 (9) Å	021-P2-022	122.2 (6)°
P2-022	1.499 (8)	021-P2-023	111.2 (5)
P2-023	1.529 (9)	021-P2-024	103.1 (5)
P2-024	1.583 (10)	022-P2-023	102.7 (5)
		022-P2-024	111.6 (5)
		023-P2-024	105.2 (6)
P2I-021I	1.528 (9) Å	021I-P2I-022I	116.5 (6)°
P2I-022I	1.496 (9)	021I-P2I-023I	112.2 (5)
P2I-023I	1.606 (9)	021I-P2I-024I	102.5 (5)
P2I-024I	1.583 (10)	022I-P2I-023I	105.5 (5)
		022I-P2I-024I	110.9 (5)
		023I-P2I-024I	109.7 (6)
O3-H31	1.027 (15) Å	H31-O3-H32	98.6 (1.4)°
O3-H32	0.967 (18)		
O3I-H31I	0.912 (15) Å	H31I-O3I-H32I	111.1 (1.6)°
O3I-H32I	0.957 (18)		

REACTOR RADIATION DIVISION AND COLLABORATIVE PROGRAMS

H23-023	1.040 (12) Å	012-H23-023	171.2 (1.1) °
H23-012	1.569 (12)		
012-023	2.601 (8)		
H23I-023I	1.039 (12) Å	012I-H23I-023I	172.2 (1.3) °
H23I-012I	1.492 (12)		
012I-023I	2.525 (8)		
H24-024	1.023 (14) Å	024-H24-03I	165.3 (1.2) °
H24-03I	1.727 (14)		
024-03I	2.729 (10)		
H24I-024I	0.972 (14) Å	024I-H24I-03	173.9 (1.3) °
H24I-03	1.736 (14)		
024I-03	2.704 (10)		
H31-03	1.027 (15) Å	03-H31-011I	166.7 (1.2) °
H31-011I	1.839 (15)		
03-011I	2.848 (10)		
H31I-03I	0.912 (15) Å	03I-H31I-011	162.8 (1.4) °
H31I-011	1.861 (15)		
03I-011	2.746 (10)		
H32-03	0.967 (18) Å	03-H32-013I	140.6 (1.7) °
H32-013I	2.045 (19)		
03-013I	2.858 (10)		
H32I-03I	0.957 (18) Å	03I-H32I-013	145.5 (1.7) °
H32I-013	2.081 (19)		
03I-013	2.920 (10)		
H11-011	1.388 (20) Å	011-H11-011I	173.3 (1.6) °
H11-011I	1.126 (21)		
011-011I	2.509 (4)		
H13-013	1.041 (17) Å	013-H13-013I	171.9 (1.4) °
H13-013I	1.447 (17)		
013-013I	2.482 (4)		
H14-014	1.241 (30) Å	014-H14-014I	173.4 (1.9) °
H14-014I	1.250 (30)		
014-014I	2.487 (4)		

this reason, the constrained model was used for further analysis. Table 2 shows the refined position parameters and equivalent isotropic temperature factors for this model, and Table 3 is a summary of selected bond distances and angles for this model. Two of three hydrogen bonds that crossed centers of symmetry in the centrosymmetric model are asymmetric in this model. The third one, however, remains nearly symmetric. Figure 1 is a picture of part of the structure including these hydrogen bonds.

1. S. Takagi, M. Mathew, and E. Prince, NBS Tech. Note 1178, 31, F. J. Shorten, ed. (1983).

STRUCTURE STUDIES OF THE SUPERIONIC CONDUCTOR SYSTEM $\text{Na}_{1+x}\text{Zr}_2\text{Si}_x\text{P}_{3-x}\text{O}_{12}$ (NASICON)

L. J. Schioler and B. J. Wuensch
(Massachusetts Institute of Technology, Cambridge, MA)

and

E. Prince

Preliminary results of a structure study of four compositions of the superionic conductor system $\text{Na}_{1+x}\text{Zr}_2\text{Si}_x\text{P}_{3-x}\text{O}_{12}$, called NASICON, were reported previously.¹ During the year covered by this report, two further things were done: a refinement of the structure of the $x = 3.0$ end member of the series, and a detailed analysis of the structures of the intermediate compositions in order to elucidate the structural basis for the high-ionic conductivity.

A sample with the nominal composition $\text{Na}_4\text{Zr}_2(\text{SiO}_4)_3$ was prepared, but an x-ray powder pattern showed that it contained a substantial amount of ZrO_2 . After further heat treatment at 1200 ZC for 46 hours (We are indebted to Dr. R. S. Roth for this processing.), there were still traces of ZrO_2 in the x-ray powder pattern, but the lines were not visible in a neutron powder pattern collected on the NBS high-resolution powder diffractometer. Starting from the parameters given in a single crystal x-ray refinement by Tran Qui, Capponi, Joubert, and Shannon,² the structure was refined by the Rietveld method³ to $R_{wp} = 7.05$ percent, compared with $R_E = 6.19$ percent. R_B , based on integrated intensities, was 3.39 percent. Table 1 shows the refined parameters compared with the parameters given by Tran Qui, et al. It is apparent that the agreement of position parameters is extremely good. The agreement of temperature factors is less good, but in several important ways the two

Table 1. Refined parameters for $\text{Na}_4\text{Zr}_2(\text{SiO}_4)_3$, compared with those from the single crystal refinement of Tran Qui et al.

Atom	Parameter	This work	Tran Qui et al.
	<u>a</u>	9.1874(2) Å	9.1863(5) Å
	<u>c</u>	22.1850(5) Å	22.181(2) Å
Na(1)	B_{11}	2.45(25)	2.05(9)
	B_{33}	1.71(37)	0.63(11)
Na(2)	<u>x</u>	-0.36259(51)	-0.36253(26)
	B_{11}	1.52(17)	0.13(7)
	B_{22}	0.98(20)	1.05(7)
	B_{33}	4.00(28)	4.60(10)
	B_{13}	0.30(9)	0.38(4)
Zr	<u>z</u>	0.14682(10)	0.14679(1)
	B_{11}	0.59(6)	0.410(8)
	B_{33}	0.36(10)	0.426(8)
Si	<u>x</u>	0.29677(35)	0.29683(12)
	B_{11}	0.59(13)	0.410(16)
	B_{22}	0.47(13)	0.36(2)
	B_{33}	0.47(13)	0.70(3)
	B_{13}	0.21(5)	0.05(1)
O(1)	<u>x</u>	0.18562(20)	0.18532(23)
	<u>y</u>	0.16640(21)	0.16658(26)
	<u>z</u>	0.08490(8)	0.08488(9)
	B_{11}	0.44(8)	0.60(6)
	B_{22}	0.61(8)	0.86(7)
	B_{33}	1.07(7)	0.82(7)
	B_{12}	-0.03(7)	1.02(5)
	B_{13}	0.23(8)	0.64(5)
	B_{23}	0.21(7)	0.13(6)
O(2)	<u>x</u>	0.18501(24)	0.18458(28)
	<u>y</u>	-0.01707(25)	-0.01714(30)
	<u>z</u>	0.19118(7)	0.19119(12)
	B_{11}	1.18(10)	2.20(7)
	B_{22}	1.26(10)	1.42(8)

Table 1. (Continued).

Atom	Parameter	This work	Tran Qui et al.
	B_{33}	1.71(9)	1.70(9)
	B_{12}	0.64(9)	0.72(6)
	B_{13}	-0.61(7)	-0.73(6)
	B_{23}	0.08(8)	0.06(6)

Table 2. Critical radii for the window between Na(1) and Na(2) sites.

	$R_c - P_{1-1}$	$R_c - P_{1-2}$	$R_c - P_{1-3}$
$x = 0.0$	1.003	--	--
$x = 1.0$	1.023	--	--
$x = 1.6$	0.970	1.025	1.125
$x = 2.0$	0.933	1.057	1.139
$x = 2.5$	1.010	--	--
$x = 3.0$	0.941	--	--

refinements are remarkably consistent. In particular, the equivalent isotropic temperature factors have similar magnitudes for all atoms and the component of thermal motion of Na(2) parallel to the hexagonal c axis is much larger than any other.

The conductivity of NASICON is strongly temperature dependent, but at all temperatures the conductivity is highest for an intermediate composition in the vicinity of $x = 2.0$. There are various reasons for believing that this has a structural basis. In their study of the $x = 3.0$ end member, Tran Qui et al. proposed several possible "windows" through which the sodium ions could pass in jumping from one site to another. Each path has one or more critical points at which the space between surrounding oxygen ions is least. With the refined structures of all the intermediate compositions, it is possible to determine the radii of these critical

openings as a function of composition. Table 2 shows the critical radius for jumps from Na(1) to Na(2). Two things are particularly notable. First, the critical radius is smaller for the end member compositions than for intermediate ones even in the region where the structure is rhombohedral. Second, in the compositions in the range from $x = 1.6$ to $x = 2.0$, where the conductivity is highest and the structure is monoclinic, there are three independent pathways, one of which has a conspicuously large opening.

1. L. J. Schioler, B. J. Wuensch, and E. Prince, NBS Tech. Note 1178, F. J. Shorten, ed., 42 (1983).
2. D. Tran Qui, J. J. Capponi, J. C. Joubert, and R. D. Shannon, J. Sol. State Chem. 39, 219 (1981).
3. H. M. Rietveld, J. Appl. Cryst. 2, 65 (1969).

THE STRUCTURES OF LITHIUM INSERTED METAL OXIDES; $\text{Li}_2\text{FeV}_3\text{O}_8$

R. J. Cava, D. W. Murphy, and S. Zahurak
(Bell Laboratories, Murray Hill, NJ)

and

A. Santoro and R. S. Roth

As part of our studies on lithium inserted metal oxides, the structure of $\text{Li}_2\text{FeV}_3\text{O}_8$ has been determined by neutron diffraction powder profile analysis.

The title compound crystallizes in space group $C2/m$ with lattice parameters $a = 11.963(3)$, $b = 3.899(2)$, $c = 6.464(2)\text{\AA}$, and $\beta = 107.5(3)^\circ$. The location of the Li^+ ions in the structure was found by means of Fourier difference analysis. The results of the neutron refinement are given in Table 1.

The FeV_3O_8 host structure contains perovskite-like cavities in which the Li^+ ions can be accommodated. The insertion of lithium cannot cause extensive distortions of the host as the oxygen octahedra share both corners and edges. This is in sharp contrast with the behavior of ReO_3 where the insertion of lithium causes extensive distortions because the ReO_6 octahedra share only corners. The insertion of Li^+ in ReO_3 converts the original perovskite-like cavity into two distorted octahedra sharing faces. In FeV_3O_8 , on the other hand, the cavities do not deform into octahedral sites and the Li^+ ions must be accommodated in coordination geometries already defined by the preexistent atomic arrangement. In $\text{Li}_2\text{FeV}_3\text{O}_8$, in fact, the Li^+ ions are located in two five-coordinated square pyramidal sites.

Table 1. Structure of $\text{Li}_2\text{FeV}_3\text{O}_8$.

<u>Atom</u>	Space group: C 2/m			
	X	Y	Z	B(Å ²)
Li	0.951(2)	0.0	0.659(3)	3.4(3)
M1	0.278(2)	0.0	0.585(4)	0.0(1)
M2	0.3968(7)	0.0	0.314(1)	0.0(1)
O1	0.3494(4)	0.0	0.9954(8)	0.59(3)
O2	0.2287(4)	0.0	0.3416(8)	0.59(3)
O3	0.4424(5)	0.0	0.6413(7)	0.59(3)
O4	0.1207(4)	0.0	0.6840(7)	0.59(3)
N_1^{Fe}	0.0625		$N_2^{\text{Fe}} = 0.1875$	
N_1^{V}	0.4375		$N_2^{\text{V}} = 0.3125$	

$$R_N = 9.15\% \quad R_p = 5.84\% \quad R_w = 7.77\% \quad R_E = 3.45\%$$

$$R_N = \frac{\sum |I(\text{obs}) - I(\text{calc})|}{\sum I(\text{obs})}$$

$$R_p = \frac{\sum |y(\text{obs}) - y(\text{calc})|}{\sum y(\text{obs})}$$

$$R_w = \left\{ \frac{\sum w [(y(\text{obs}) - y(\text{calc}))^2]}{\sum w [y(\text{obs})]^2} \right\}^{1/2}$$

$$R_E = \left\{ \frac{N - P + C}{\sum w [y(\text{obs})]^2} \right\}^{1/2}$$

where N = number of independent observations, P = number of parameters, C = number of constraints, y = counts at angle 2θ , I = integrated Bragg intensities, and w = weights.

NEUTRON AND X-RAY DIFFRACTION STUDY ON POLYMORPHISM IN LITHIUM ORTHOTANTALATE,
 Li_3TaO_4

M. Zocchi and M. Gatti
 (Politecnico of Milano, Italy)

and

A. Santoro

and

R.S. Roth
 (National Measurement Laboratory)

The structure of lithium orthotantalate, Li_3TaO_4 , has been investigated by Blasse¹ who found that the crystal is pseudo-tetragonal with a unit cell of parameters $a_t = 6.01$ and $c_t = 16.67 \text{ \AA}$. The Ta^{5+} ions were located by using x-ray powder diffraction intensities, and their arrangement suggested a 3:1 ordering of the Li^+ and Ta^{5+} ions in a rock salt-type structure having subcell of parameter a_c related to the parameters a_t and c_t by the expressions $a_t = b_t \approx a_c \sqrt{2}$ and $c_t = 4a_c$.

Martel and Roth² have found that Li_3TaO_4 is, in fact, trimorphic, with the first-phase transition occurring at about 900°C and the second between 1400°C and 1450°C . The low-temperature phase was found to have the same lattice parameters as the modification described by Blasse¹.

Our purpose in beginning this work was to verify, complete, and refine Blasse's model for the low-temperature phase (referred to in what follows as the β -phase), and to solve the structure of the high-temperature form (called α -phase in what follows). No attempts have been made to obtain and analyze the intermediate temperature modification. Both neutron powder and x-ray single-crystal diffraction methods have been used in the present study.

Neutron powder diffraction measurements were made at room temperature with the high-resolution five-detector diffractometer at the National Bureau of Standards Reactor³. The data were analyzed with the Rietveld method⁴, modified by Prince⁵ to simultaneously process the intensities collected by the five counters of the diffractometer.

X-ray intensity data on a single crystal of $\alpha\text{-Li}_3\text{TaO}_4$ were collected with a Nonius CAD-4 four-circle diffractometer using $\text{MoK}\alpha$ radiation ($\lambda = 0.71069 \text{ \AA}$) and the $0-2\theta$ scan method. The crystal used in the experiment had a regular shape with an average diameter smaller than 0.1 mm. A total of 4025 reflections were measured.

In the case of the β -form (space group $C2/c$) a trial model was derived using the results obtained by Blasse¹ and simple crystal-chemical considerations. In the

case of the α -phase (space group P2/n) a plausible trial model was obtained from the results of a preliminary single-crystal x-ray diffraction study. In both cases, the trial models were refined with the Rietveld method using neutron powder data. The results of the two refinements are given in Table 1 (β -form) and Table 2 (α -form).

In the β -phase the ordering of the Li^+ and Ta^{5+} ions along the c_t axis of the pseudo-tetragonal cell forms a sequence . . . Ta-Li(1)-Li(2)-Li(3)-Ta. . . , and each set of crystallographically equivalent cations forms a chain of conformation $t\ g^+\ g^-$. The cation-cation distances along the chains are similar for $\text{Li}(1)^+$ and $\text{Li}(3)^+$ [2.95(6) and 2.94(4) Å for $\text{Li}(1)^+$ and 3.12(8) and 2.91(5) Å for $\text{Li}(3)^+$], while they are significantly different for $\text{Li}(2)$ and Ta [3.35(9) and 2.98(7) for $\text{Li}(2)^+$ and 3.15(3) and 2.95(2) for Ta^{5+}].

The distances between oxygen ions constituting common edges of the coordination octahedra of Ta^{5+} ions are significantly shorter than the average of all the O-O distances. Since these short distances occur only in the case of the edge-sharing coordination octahedra of Ta^{5+} ions, one may infer that this atomic arrangement in the structure has the function of decreasing the electrostatic repulsion between closely located and highly charged Ta^{5+} ions.

The structure of the α -form can be best described in relation to that of the β -phase. The shifts of the Ta^{5+} ions necessary to go from one structure to the other occur within layers perpendicular to the c_t axis, and their sequence has a repeat period $d = 3c_t$. In this sense, d may be considered as a parameter representing the pattern of the transformation in the direction parallel to c_t . The resulting arrangement of the Ta^{5+} ions gives chains of conformation $t\ g^+\ g^+\ t\ g^- g^-$ (it is worthwhile to mention that the Li^+ ions also could be connected in a similar way).

In the α -modification there are no significant differences among the Ta-Ta interatomic distances along the chains (differences in the Li-Li interatomic distances cannot be discussed meaningfully because of the large standard deviations). This finding is in contrast to the case of the β -phase discussed above. The sequences of cations along the direction c_t of the pseudo-tetragonal cell are of type . . . Ta-Li-Li-Li-Li-Ta. . . for Ta(1) and Ta(4), and . . . Ta-Li-Ta-Li-Li-Ta. . . for Ta(2) and Ta(3).

As in the previous case, in the α -phase the distances between the oxygen ions forming the common edges of the coordination octahedra of the Ta^{5+} ions are shorter than the average of all the O-O distances.

It is well known that the presence in a structure of anionic octahedra sharing edges introduces unfavorable electrostatic repulsion between the central metal ions

TABLE 1
Results of the Rietveld Refinement of the Structure
of $\beta\text{-Li}_3\text{TaO}_4$

Atom	x	y	z	$B(\text{\AA}^2)$
Ta	0.075(2)	-0.126(1)	0.123(2)	1.07(7)
Li(1)	0.329(4)	-0.116(5)	0.607(3)	0.8(2)
Li(2)	0.567(6)	-0.132(4)	0.107(4)	3.0(3)
Li(3)	0.817(5)	-0.120(6)	0.622(3)	0.8(2)
O(1)	0.158(1)	-0.125(1)	0.358(1)	0.28(3) ^(*)
O(2)	0.438(1)	-0.128(1)	0.887(1)	0.28(3)
O(3)	0.693(1)	-0.118(1)	0.371(1)	0.28(3)
O(4)	0.941(1)	-0.106(1)	0.886(1)	0.28(3)

$$R_N = 100[\sum |I(\text{obs}) - I(\text{cal})| / \sum I(\text{obs})] = 8.3$$

$$R_P = 100[\sum |y(\text{obs}) - y(\text{cal})| / \sum y(\text{obs})] = 9.7$$

$$R_W = 100\{\sum w[y(\text{obs}) - y(\text{cal})]^2 / \sum w y^2(\text{obs})\}^{1/2} = 12.3$$

$$R_E = 100[N-P+C] / \sum w y^2(\text{obs})]^{1/2} = 7.5$$

In the above formulas, N is the number of statistically independent observations, P the number of parameters refined, C the number of constraints, I the integrated intensities, y(obs) and y(cal) the observed and calculated intensities, and w the weights associated with the data points y(obs).

(*) The oxygen atoms were constrained to have a common temperature factor.

NOTE:

Numbers in parenthesis are standard deviations in the last decimal figure.

Space Group: C2/c, Z = 8, calculated density $d_1 = 5.87 \text{ gr. cm}^{-3}$

Lattice Parameters: $a_1 = 8.500(3)$, $b_1 = 8.500(3)$, $c_1 = 9.344(3)\text{\AA}$, $\beta_1 = 117.05(2)^\circ$

Table 2. Results of the Rietveld refinement of the structure of $\alpha\text{-Li}_3\text{TaO}_4$.

Atom	x	y	z
Ta(1)	1/4	0.580(2)	3/4
Ta(2)	0.403(1)	0.134(1)	0.0821(5)
O(1)	-0.016(1)	0.142(1)	0.2579(6)
O(2)	0.487(1)	0.386(1)	0.7432(7)
O(3)	0.162(2)	0.360(1)	0.0779(5)
O(4)	0.652(2)	0.357(2)	0.0906(5)
O(5)	0.681(2)	0.116(2)	0.5876(6)
O(6)	0.145(3)	0.113(1)	0.5729(5)
Li(1)	3/4	0.124(4)	3/4
Li(2)	0.396(3)	0.416(3)	0.594(2)
Li(3)	-0.084(4)	0.130(6)	0.096(2)
Li(4)	1/4	0.416(6)	1/4
Li(5)	1/4	0.132(7)	3/4
Li(6)	0.608(4)	0.369(4)	-0.081(2)

$$R_N = 6.70, R_P = 7.48, R_W = 9.67, R_E = 5.09$$

Space group P2/n, Z = 6, calculated density $d_h = 5.87 \text{ gr.cm}^{-3}$

Lattice Parameters: (i) x-ray measurements, $a_h = 6.027(2)$, $b_h = 6.004(2)$,

$c_h = 12.882(4) \text{ \AA}$, $\beta_h = 103.53(1)^\circ$ (**)

(*) For the definition of the R-factors, see Table 1.

(**) The difference between the lattice parameters determined by x-ray and neutron diffraction are almost certainly due to errors in the calibration of the instruments used for the measurements.

and that the resulting stress depends on the charge on the cations. The stress can be relieved by increasing the distance between the cations. In the structure of β - Li_3TaO_4 , one of the two Ta-Ta distances along the $\text{t g}^+ \text{t g}^-$ chains has a value of 2.95(2) Å, i.e., is significantly less than the other Ta-Ta distance along the same chain (3.15 Å). On the contrary, in the α -phase the Ta^{5+} ions are arranged so that no Ta-Ta distance is shorter than 3.10 Å, and their average distance is 3.16 Å. The stress introduced by the edge-sharing octahedra, therefore, is smaller in the α -phase than in the β . This reduction of stress may well be one of the driving forces leading to the transformation observed in the title compound.

1. G. Blasse, Z. Anorg. Allg. Chem. Band 331, 44 (1964).
2. L. C. Martel and R. S. Roth, Bull. Amer. Ceram. Soc. 60, 376 (1981).
3. E. Prince and A. Santoro, National Bureau of Standards US Technical Note 1117, edited by F. Shorten (1980).
4. H. M. Rietveld, J. Appl. Cryst. 2, 65 (1969).
5. E. Prince, National Bureau of Standards US Technical Note 1117, edited by F. Shorten (1980).

THE CRYSTAL STRUCTURE OF LITHIUM ZIRCONATE, $\text{Li}_6\text{Zr}_2\text{O}_7$

M. Zocchi and M. Gatti
(University of Milano, Italy)

and

A. Santoro

and

R. S. Roth
(National Measurement Laboratory)

The single-crystal x-ray diffraction study of the title compound was carried out as part of our structural investigations of mixed oxides of lithium and transition metals.

$\text{Li}_6\text{Zr}_2\text{O}_7$ crystallizes in space group C2/c with $a = 10.440(4)$, $b = 5.991(1)$, $c = 10.204(2)$ Å, $\beta = 100.25(3)^\circ$. The intensities of 4229 Bragg reflections were measured with a Nonius CAD-4 diffractometer using monochromated MoK α radiation and empirically corrected for absorption. The structure was solved by Patterson and Fourier methods and refined by least squares to conventional and weighted R factors

REACTOR RADIATION DIVISION AND COLLABORATIVE PROGRAMS

Table 1Table of Atomic Parameters

No.	Name	X	Y	Z	B11	B22	B33
1	Zr	0.18351	-0.12162	0.36469	0.00012	0.00165	0.00066
2	Li(1)	0.207	0.369	0.395	0.89		
3	Li(2)	0.433	0.142	0.418	1.50		
4	Li(3)	0.065	0.096	0.102	0.79		
5	O(1)	0.2499	0.1112	0.2452	0.0022	0.0033	0.0018
6	O(2)	0.1333	-0.3662	0.5018	0.0004	0.0031	0.0014
7	O(3)	0.1230	0.1230	0.4774	0.0007	0.0032	0.0015
8	O(4)	0.0000	0.1491	0.2500	0.0006	0.0086	0.0022
		B12	B13	B23			
1	Zr	0.00013	0.00011	0.00012			
2	Li(1)						
3	Li(2)						
4	Li(3)						
5	O(1)	-0.0017	0.0016	0.0009			
6	O(2)	-0.0006	0.0002	0.0000			
7	O(3)	0.0003	0.0008	-0.0002			
8	O(4)	0.0000	-0.0013	0.0000			

Table 2Isotropic Parameters of Thermal Motion (in Å²)

Zr	.166 (2)
Li(1)	.89 (8)
Li(2)	1.50 (9)
Li(3)	.79 (8)
O(1)	.65 (2)
O(2)	.38 (2)
O(3)	.43 (2)
O(4)	.84 (3)

of 0.048 and 0.061 respectively for the 2966 reflections with $I \geq 3\sigma$ (I). The structural parameters are given in Table 1.

The rock salt-type structure is characterized by an ordering of the cations with sequences $(O-Zr)_2-(O-li)_6$ along with a direction parallel to one of the edges of the face centered pseudocubic cell ($a_c \approx 4.28 \text{ \AA}$) which can be obtained from the monoclinic cell with the transformation

$(-\frac{1}{8} \frac{1}{2} \frac{1}{4} / -\frac{1}{8} \frac{1}{2} \frac{1}{4} / \frac{3}{8} 0 \frac{1}{4})$. One of the oxygen ions in the asymmetric unit

$(Li_3ZrO_3)_{3.5}$ is in special position (on a twofold axis) and therefore the structure is characterized by an ordered anionic deficiency, with 32 cations and 28 oxygen ions in the unit cell. Indeed on the twofold axes of the monoclinic cell every other anionic site, expected for the idealized NaCl structure, is empty and, as a consequence, the coordination number of the lithium ions is five with two kinds of coordination polyhedra, i.e., distorted square pyramids and trigonal bipyramids. The Zr coordination number is six and the oxygen octahedron is significantly distorted.

It may be interesting to compare the structure of Li_6ZrO_3 with that of Li_2ZrO_3 , looking for possible correlations with their ionic conduction properties.

Both structures are of the NaCl type. However, the distribution of the cations is different in the two phases, and for this reason they cannot be considered isostructural.

In Li_2ZrO_3 all cations have octahedral coordination and the structure has to be considered as close packed, and only the relatively large Li-O average distance of 2.212 Å may explain the small conductivity shown by this phase.

In $Li_6Zr_2O_7$ the coordination number of the Li^+ ions is five, as a consequence of the fact that on the two-fold axes present in this structure every other anionic site, expected for the idealized NaCl structure, is empty. Thus the structure of $Li_6Zr_2O_7$ is more "open" than the one of Li_2ZrO_3 , and for this reason both the Li^+ and O^{2-} ions may have higher mobility in $Li_6Zr_2O_7$ than in Li_2ZrO_3 . These results are in agreement with conductivity measurements.

Whether the conductivity in $Li_6Zr_2O_7$ is cationic or anionic or both is not clear. Hellstrom and Van Gool² do not take into consideration the possibility of a significant mobility of the oxygen ions. However, in view of the high values of the thermal parameters for O(1) and O(4) (See Table 2) and in view of the well-known fact that conduction in zirconia-based electrolytes is due to the mobility of the oxygen ions, one cannot exclude that a similar mechanism is, at least partially, active also in $Li_6Zr_2O_7$. More specific conductivity experiments, with a variable partial pressure of oxygen at the anode, may give an answer to this question.

A variable-temperature powder neutron diffraction study is planned with the aim of better defining the correlations between the structure and the ionic conduction properties of this material.

-
1. J.L. Hodeau, M. Marezio, A. Santoro, and R.S. Roth, *J. Solid State Chem.* 45, 170- (1982).
 2. E.E. Hellstrom and W. Van Gool, *Solid State Ionics* 2, 59- (1981).

STUDIES OF ZEOLITE STRUCTURE BY NEUTRON POWDER DIFFRACTION

J. B. Parise
(E. I. DuPont de Nemours & Co. Wilmington, DE)
and
E. Prince

Zeolites are a class of compounds whose structures are based on frameworks made up of AlO_4 and SiO_4 tetrahedra that share corners. This relatively rigid framework contains pores of various sizes that are occupied by a sufficient number of cations to balance the deficiency of positive charge due to the aluminum in the framework, and also may be occupied by very loosely bound molecules of various types. The specific sizes of the pores may be utilized to produce highly selective absorbants and catalysts for chemical processes. A detailed knowledge of the sizes and shapes of the pores is needed to gain an understanding of these processes.

We have studied several compositions of two types of zeolite, each of which is based on a body centered cubic arrangement of cubo-octahedral units. In zeolite Rho these units share hexagonal faces along [111] directions, and they are connected along [100] directions (in an idealized structure) by octagonal prisms - so called double eight rings. In zeolite ZK5 a hexagonal prism - a double six ring - is interposed between the units in [111] directions, and the extra space between the units along [100] directions becomes a second, somewhat smaller, type of pore that has planar eight rings on two opposite faces and puckered eight rings on the sides. Figure 1 shows stereo pair representations of these structures.

We have studied two compositions of each of these types at several temperatures. Using Rietveld refinement and Fourier methods we have determined

Table 1. Summary of structural data for zeolite ZK-5. The space group Im3m. T indicates Al or Si, disordered.

	$\text{Cs}_{9.7}\text{K}_{13}\text{Al}_{22.7}\text{Si}_{73.3}\text{O}_{192}$ 298K	$\text{Cs}_{3.9}\text{K}_{8}\text{D}_{17.5}\text{Al}_{22.2}\text{Si}_{73.8}\text{O}_{192}$ 298K
a	18.671(1)A	18.660(2)A
T(961)		18.673(1)A
x	0.0825(3)	0.0828(4)
y	0.2023(3)	0.2029(5)
z	0.3211(3)	0.3219(5)
01(48k) x=y		
y	0.1280(2)	0.1277(3)
z	0.3145(3)	0.3140(3)
02(48k)x=y		
y	0.2522(2)	0.2522(3)
z	0.4081(3)	0.4082(4)
03(48j) x=0		
y	0.1783(3)	0.1785(4)
z	0.3369(3)	0.3390(4)
04(48i) x=1/4, y=1/2-z		
z	0.3915(2)	0.3909(3)
Cs(12e) x=y=0		
z	0.314(1)	0.314(1)
K1(12d) x=0, y=1/4, z=1/2		
K2(16f) x=y=z		
z	0.150(3)	0.152(9)
		-

Table 2. Summary of structural data for zeolite Rko. The space group is I₄₃m. T indicates Al or Si, disordered.

	$\text{Cs}_6\text{Al}_6\text{Si}_{42}\text{O}_{96}$	$\text{Cs}_{1.2}\text{D}_{9.1}\text{Al}_{10.3}\text{Si}_{37.7}\text{O}_{96}$
	298K	493K
a	14.6652(5) Å ^o	14.7014(8) Å ^o
T(48h)		
x	0.2670(4)	0.2694(5)
y	0.1191(5)	0.1152(7)
z	0.4186(3)	0.4164(5)
01(24g) x=y		
y	0.2095(2)	0.2075(4)
z	0.3956(4)	0.3912(7)
02(24g) x=y		
y	0.1339(3)	0.1359(4)
z	0.6216(3)	0.6236(6)
03(48h)		
x	0.0275(2)	0.0237(4)
y	0.2092(2)	0.2081(4)
z	0.3867(3)	0.3864(4)
Cs(6b) x=1/2, y=0, z=0		

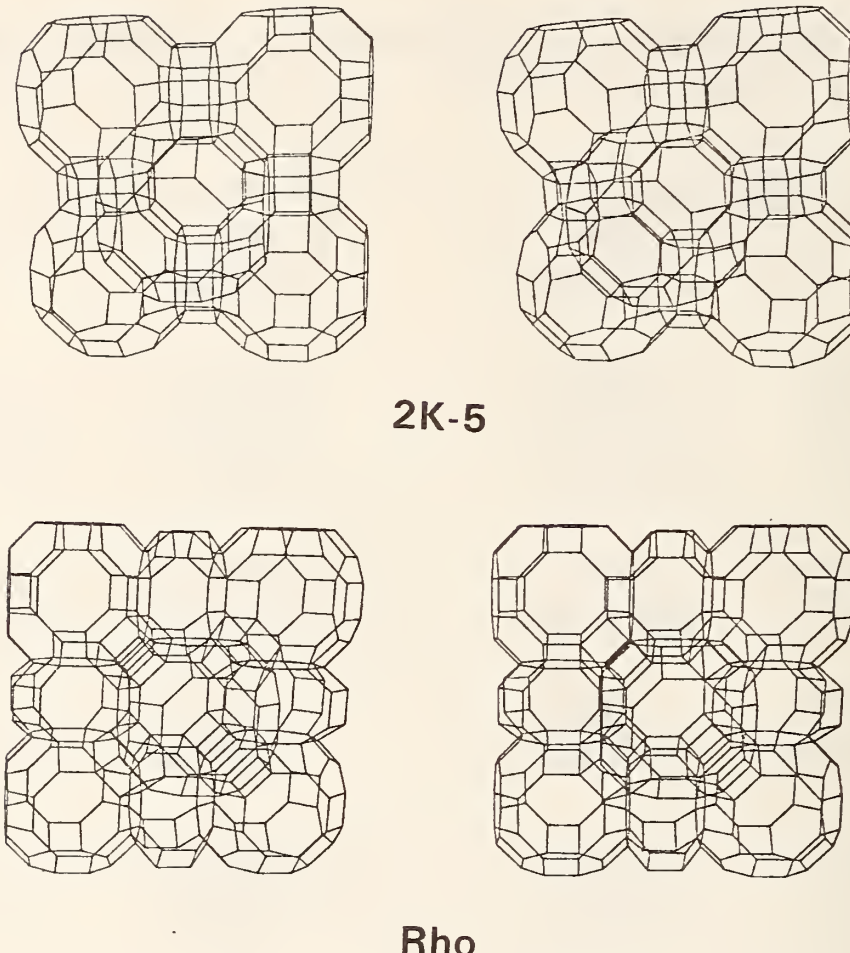


Figure 1: Stereo = pairs showing the idealized structures of zeolites ZK5 and Rho. the nodes of the framework are aluminum or silicon positions. Oxygen positem's are approximately at the centers of the line segments. Adapted from Atlas of Zeolite Structure Types by W. M. Meier and D. H. Olson, published by the Structure Commission of the International Zeolite Association (1975).

cation binding sites in both structures types, and in Rho it was determined that the double eight ring units were distorted in such a way as to make the space group of the structure $I\bar{4}3m$ rather than $Im\bar{3}m$. Table 1 is a summary of structure data for ZK5, and Table 2 gives structure information for Rho.

THE STRUCTURE OF SYNTHETIC ZEOLITE OMEGA

P. A. Wright

(University of Cambridge, Cambridge, England)

and

J. B. Parise

(E. I. duPont de Nemours and Co., Wilmington, DE)

and

E. Prince

A structure belonging to space group $P6_3/mmm$ was proposed for the synthetic zeolite designated omega by Barrer and Villiger¹ on the basis of x-ray powder diffraction data. However, when the structure of the natural zeolite mazzite was determined by Rinaldi, Pluth, and Smith, they observed that the powder pattern for its structure, which belongs to space group $P6_3/mmc$, was very similar to that of omega and suggested that the structure of omega might be incorrect. In order to resolve this question, a study was undertaken of a synthetic omega zeolite using high resolution neutron powder diffraction and Rietveld refinement.

The best fit that could be obtained between observed and calculated patterns using the Barrer and Villiger model was $R_B = 40.3$ percent; $R_{wp} = 16.71$ percent ($R_e = 5.52$ percent). The mazzite structure, however, refined satisfactorily to $R_B = 13.51$ percent, $R_{wp} = 9.25$ percent, and after the positions of certain extra-framework atoms were determined from Fourier maps, R_{wp} was further reduced to 7.23 percent. It is thus confirmed that synthetic zeolite omega has the same structure as mazzite. Table 1 is a summary of the refined position parameters of the framework atoms.

Table 1. Position parameters of the framework atoms in synthetic zeolite omega. The space group is $P6_3/mmc$. T indicates Al and Si, disordered.

Atom	x	y	z
T1	0.1636(14)	0.4875(18)	-1/4
T2	0.0850(11)	0.3574(11)	0.0307(21)
O1	0.2535(10)	0.5069(18)	-1/4
O2	-0.4226(7)	-0.8451(14)	1/4
O3	0.0927(11)	0.3786(10)	1/4
O4	0.1092(7)	0.4386(8)	-0.0765(11)
O5	0.1635(6)	0.3270(12)	0.0060(20)
O6	0	0.2670(10)	0

-
1. R. M. Barrer and H. Villiger, Chem. Comm. 659-660 (1969).
 2. R. Rinaldi, J. J. Pluth, and J. V. Smith, Acta Cryst. B31, 1603 (1975).

**ACTIVE SITE OF RNASE: NEUTRON DIFFRACTION STUDY OF A COMPLEX
WITH URIDINE VANADATE, A TRANSITION STATE ANALOG**

A. Wlodawer

(National Bureau of Standards)

and

(National Institute of Arthritis, Diabetes, Digestive and
Kidney Diseases, Bethesda, MD)

and

Maria Miller

(Laboratory of Molecular Biology, National Institutes
of Health, Bethesda, MD)

and

L. Sjolin

(National Bureau of Standards, Washington, DC)

and

(Chalmers Institute of Technology, Gothenburg, Sweden)

and

(National Institute of Arthritis, Diabetes, Digestive and
Kidney Diseases, Bethesda, MD)

A complex of RNase A with a transition state analog, uridine vanadate, has been studied by a combination of neutron and x-ray diffraction. A crystal was prepared by soaking it in a solution of inhibitor for three months, with simultaneous exchange of a maximum number of hydrogen atoms for deuterium. Upon completion of the exchange, a number of small pieces were cut from the crystal using a scalpel blade, and a large piece ($4.5 \times 3.5 \times 1.2$ mm) was mounted in a quartz tube as previously described. Reflections which could not be recorded with the flat-cone method and levels with h between 0 and 3 were measured using equatorial geometry. These data were later used for scaling. After final scaling, the number of unique observed data ($I > 1.5\sigma(I)$) was 6315, which corresponded to 73% of all possible data to 2 \AA resolution, with an extra 8% of possible reflections in the shell of $2 - 1.75 \text{ \AA}$.

X-ray data were measured from a single fragment of the original crystal, thus assuring identical deuteration and substitution of the inhibitor. The number of significant reflections in the 2 - to $10\text{-}\text{\AA}$ resolution range was 6617, 85% of those theoretically accessible.

The refinement of the structure on the complex was accomplished using an algorithm of Wlodawer and Hendrickson, in which the model is refined with both neutron and x-ray data. The final model resulting from the joint refinement was characterized by standard crystallographic R factors of 0.191 (x-ray) and 0.207 (neutron), with r.m.s. deviations of bond length from ideality of 0.024 Å (bonds not involving

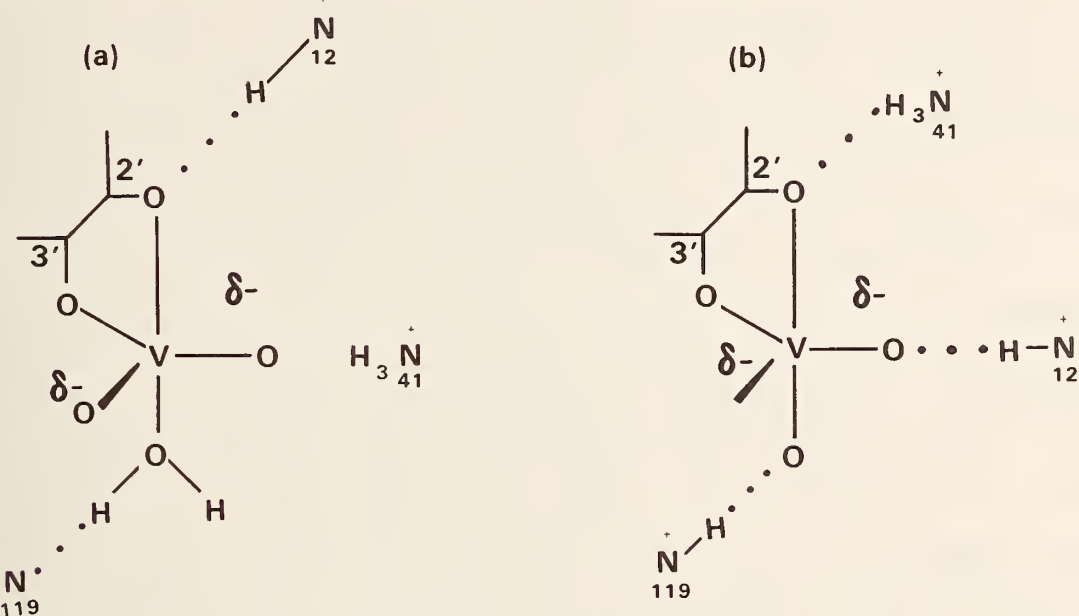


Figure 1. a) Hypothetical partial structure for the complex of RNase with uridine vanadate, postulated by Lindquist et al.
b) Diagram of the structure observed in the current investigation.

hydrogen) and 0.021 Å (bonds involving hydrogen). The r.m.s. shift of the non-hydrogen protein coordinates from the initial model was 0.38 Å.

Although both the x-ray and neutron difference Fourier maps were reasonably clear even before the commencement of the refinement procedures, they were improved further following the refinement. The x-ray and neutron densities were also very clear for all the amino acid side chains involved in the catalytic activity. Both histidines appeared to be protonated, in agreement with the increase of the pK of these groups in the presence of inhibitors observed by NMR. The movement of these side chains did not exceed 0.2 Å from the positions observed in the native structure of RNase. The end group of Lys 41 moved 0.6 Å from the position found in the native enzyme, and the average temperature factor for this side chain was lowered from 20 \AA^2 to 8 \AA^2 . No major movement of other groups was detected in the area of the active site.

A diagram of the arrangement of the inhibitor and of the surrounding side chains of the protein is shown in Figure 1. As expected on the basis of theoretical considerations, the vanadium atom lies in the center of a distorted trigonal bipyramidal, with the oxygens O2' and O7 found in the apical positions, while the oxygens O3', O6, and O8 lie in the basal plane. The distance of the vanadium atom from the best least-squares plane formed by V, O3', O6, and O8 is 0.085 Å. The angle formed by O2'-V-O7 is 156°, indicating the distortion in the bipyramid. This angle refined to within 5° independently of the type of restraints placed on the standard group.

Unexpectedly, the hydrogen bonds formed between the side chains of RNase and the oxygens surrounding the vanadium atom did not appear to conform to the predictions based on the theoretical considerations. In particular, it is Lys 41 rather than His 12 which appears to be hydrogen bonded to the apical O2'-oxygen. The distance between the NZ of Lys 41 and O2' is 2.79 Å and the angle NZ-DZ1-O2' is 165°. There is a clear indication of a continuous density in the neutron difference Fourier map, as expected at this resolution for hydrogen-bonded atoms. The distance between NZ of Lys 41 and the closest equitorial oxygen of the bipyramid (O6) is 3.38 Å, with no indication of a hydrogen bond. Conversely, NE2 of His 12 is 2.62 Å from the equatorial oxygen O8, with the angle NE2-DE2-O8 of 160°. Again, these atoms are connected by a continuous density in the Fourier map. The distance between NE2 of His 12 and O2' is 3.22 Å, with no indication of a hydrogen bond.

The interpretation of these results and their reconciliation with the mechanistic model is not straightforward. The in-line model of the catalytic action is well established, and the observed atomic arrangement of the bipyramid is in good agreement with the requirement that the leaving groups in both the first or the second step of the reaction should always be apical. It is improbable that a group other than histidine could act as both a general acid and a general base during the catalysis, and thus the observed hydrogen bonding pattern may indicate that the proton transfers do not follow the simplest route. It is unlikely that the amino group of Lys 41 could assume the role of general acid-general base, even though it forms a clear hydrogen bond with the apical oxygen of the complex. It is also unclear why the temperature factor of Lys 41 is lowered by a factor of 2.5 compared to that in the native structure, where a hydrogen bond to the phosphate is also made. Nevertheless, these results should enhance our knowledge of the three-dimensional structure of the active site of RNase and should attest to the usefulness of neutron diffraction and least squares refinement in such studies.

MICROVOID FORMATION IN AMMONIUM NITRATE

C. S. Choi and H. J. Prask
 (EMD, LCWSL, AMCCOM, Dover, NJ)
 and
 (National Bureau of Standards, Washington, DC)
 and
 C. J. Glinka

Ammonium nitrate (AN) is a material of considerable interest to the military for a variety of "energetic material" applications. However, because of the several phase transitions which occur at ambient pressure, and the resulting irreversible growth, use of NH_4NO_3 has been severely limited.

We have continued our studies of NH_4NO_3 with the overall aim of providing information by which irreversible growth could ultimately be reduced. Our most recent studies consider two aspects not examined previously: three-dimensional characterization of lattice parameter changes accompanying a phase transition and characterization of microvoids accompanying a phase transition. Initially, both aspects have been studied for the $\text{IV} \leftrightarrow \text{V}$ transition in NH_4NO_3 .

1. Dimensional Expansion at the IV to V Transition

The unit cell of the phase V is a supercell of phase IV with the transformation matrix; 110/110/002/ (or 110/110/002/ for the twin pair). Since the phase IV lattice is not cubic, the orientation of the phase V lattice planes are expected to be generally different from the equivalent planes of phase IV, except for two lattice planes which we designate as invariant planes (or directions). These invariant planes were investigated by single-crystal neutron diffraction studies at room temperature (for phase IV) and at 240 K (for phase V). It was found that the direction of (110) [or its twin pair (110)] and (001) of phase V coincide with those of (100) [or (010)] and (001) of phase IV, respectively, within 0.2° . The unit cell dimensions of both phases at the transition temperature were obtained from the thermal expansion formula as given in a previous study. From these the linear expansions along the invariant directions in the IV to V phase transition were found to be the following:

(100) _{IV}	direction	-1.8%
(010) _{IV}	direction	+5.3%
(001) _{IV}	direction	-0.4%.

The large and anisotropic expansion of the crystallites, as shown above, is expected to create considerable mismatch at crystallite boundaries and production of

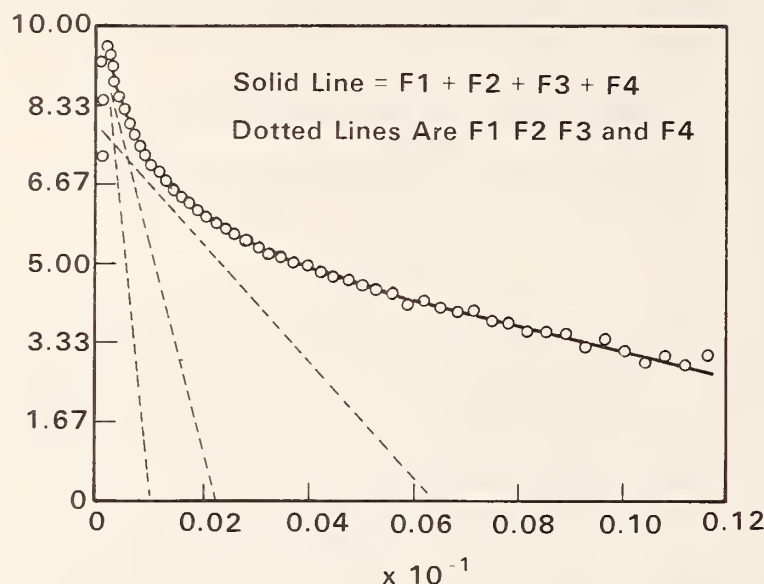


Figure 1. The small angle scattering from the microvoids in the sample, expressed as $\ln I$ vs. Q^2 . Observed data are shown as circles, best-fit curve as a solid line.

Table 1. The results of non-linear least-squares refinement for the multiple Guinier functions model in the form, $I(Q) = \sum Y_i \exp(-R_{gi}^2 Q^2 / 3_i)$. R.S.D. is a residual standard deviation for each function as defined by $\{\sum (F_{obs} - F_{cal})^2 / N\}^{1/2}$, where N is number of degree of freedom. The refinements were conducted for each function separately, within the Q -ranges as specified. The R-factor, $R = \sum (I_{di} - I_{cal}) / \sum I_{di}$ was calculated for the entire observed Q -range.

	F_1	F_2	F_3	F_4
Y_i	314(28)	2566(80)	13844(925)	57641(4896)
$R_{gi}^2 (\text{\AA}^2)$	775(39)	3664(49)	12503(265)	33438(876)
R.S.D.	3.	4.	9.	32.
$Q (\text{\AA}^{-1})$.073/.106	.040/.071	.026/.038	.017/.024
QR_{gi}	2.0/2.9	2.4/4.3	2.9/4.2	3.0/4.5
R-factor (overall) =	0.007			

microvoids. This could be as much as 5 percent in volume fraction if the negative expansion coefficients make a negligible contribution to the contraction because of the geometrical hindrance of the grain arrangement.

2. Microvoid Measurement by SANS

A thin plate-like sample, approximately 2 mm in thickness, was prepared from molten AN (90% deuterated). The sample was wrapped with Al foil and mounted on the sample holder of a cryostat. Using neutrons of 4.85 \AA with $\Delta\lambda/\lambda = 0.25$ and a minimum Q of 0.016 \AA^{-1} , the scattering curves were measured at two different temperatures: room temperature and 230 K. The scattering intensity of the latter was about 20 percent more intense than the former, which was attributed mainly to microvoid formation in the sample since the experimental conditions were exactly identical except for the sample temperature. The scattering curve for the microvoids was obtained by simple subtraction of room temperature data from the 230 K data. Assuming that the microvoids can be approximated as a collection of globular-particles with a few different average sizes, the scattering curve can be expressed by a sum of Guinier functions:

$$\frac{d\Sigma_s}{d\Omega} = \rho^2 \sum_i n_i v_i^2 \exp(-Q^2 R_{gi}^2/3).$$

Here, ρ is the scattering length density, n_i , v_i , and R_{gi} are the particle density, average volume of the particle, and radius of gyration of the i -th function, respectively. The results are shown in Figure 1 and Table 1. In Table 1, the QR_g values are less than 3.0 in most of the fitting ranges and the residual factors (R) are less than 1 percent, which indicates that the model function describes the microvoid distribution quite satisfactorily.

NONDESTRUCTIVE CHARACTERIZATION OF SUB-SURFACE RESIDUAL STRESS

H. J. Prask and C. S. Choi
(EMD, LCWSL, AMCCOM, Dover, NJ)

and

(National Bureau of Standards, Washington, DC)

In earlier work it was demonstrated that the precision and reproducibility of the neutron diffraction method were sufficient for residual stress measurements.¹ It was also found, however, that for the differential volumes of interest in technological applications ($< 20 \text{ mm}^3$ as shown in Figure 1) and employing conventional

θ - 2θ scans, texture could produce shifts in apparent peak positions greater than any expected from residual stress.

To minimize the role of texture in residual stress measurements we have adopted an "energy dispersive" approach² utilizing a three-axis spectrometer and in which sample orientation remains fixed with respect to incident and diffracted neutron beam directions, and monochromator and analyzer wavelengths are matched and scanned.

Initial measurements have centered on an aluminum (2024-T353) ring-plug sample fabricated for use as a standard reference sample for ultrasonic measurements.³ In this shrink-fit type of cylindrical sample the theoretical stress distribution is given by:

$$\sigma_r = \frac{PR_1^2}{R_2^2 - R_1^2} \left(1 - \frac{R_2^2}{r^2} \right) \quad r > R_1 \quad (1)$$

$$\sigma_\theta = \frac{PR_1^2}{R_2^2 - R_1^2} \left(1 + \frac{R_2^2}{r^2} \right) \quad r > R_1 \quad (2)$$

$$\sigma_\theta = \sigma_r = -P \quad r \leq R_1 \quad (3)$$

and

$$P = \frac{E(R_2^2 - R_1^2)\delta}{2R_2^2} \quad (4)$$

where R_1 is the plug radius, R_2 is the ring outer radius, E is Young's modulus, and δ is the differential radial interference. In the ultrasonic reference sample $E = 73100$ MPa, Poisson's ratio is 0.33, $R_1 = 1.27$ cm, $R_2 = 3.81$ cm, with a thickness of 2.5 cm.

The measurements were made using the (200) reflection and a differential volume of $1.5 \times 1.5 \times 20$ mm at a scattering angle of 90° . If the unstressed d-spacing (d_o) is known, residual stresses for the three principal directions could be obtained directly by three strain measurements at each point of interest in the sample. Alternatively, $(\sigma_r - \sigma_\theta)$ can be obtained at each point of interest without a knowledge of d_o .⁴ Values for σ_r and σ_θ can then be extracted by application of the overall equations of equilibrium and the use of an analytical model.

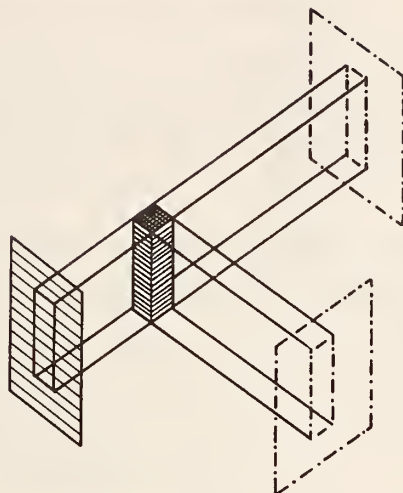


Figure 1. The intersection of ingoing and 90°-scattered collimated neutron beams showing the examined differential volume.

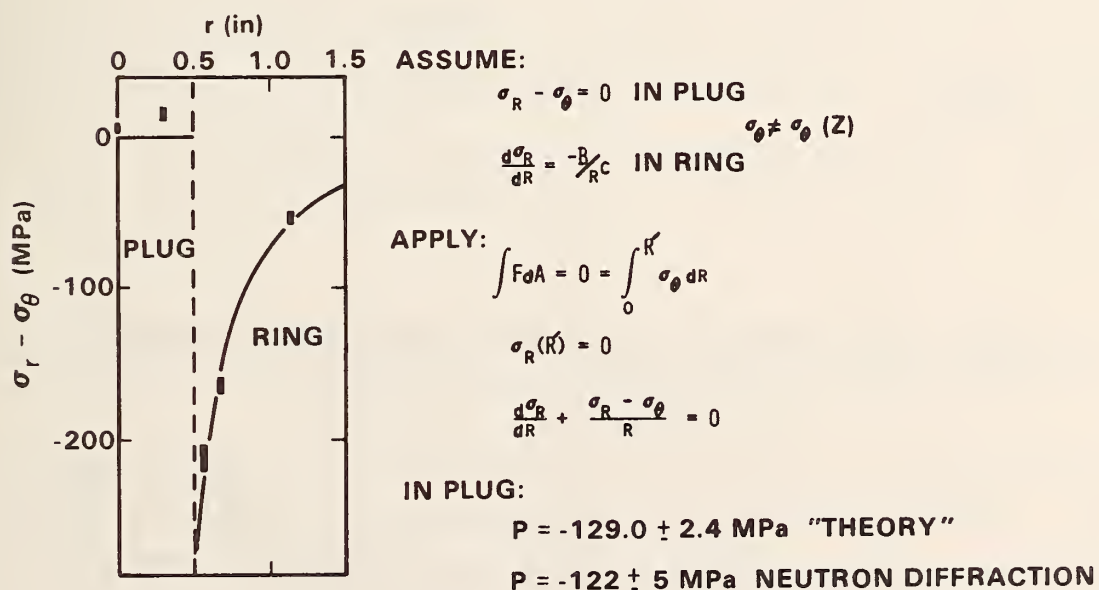


Figure 2. Measured and calculated $(\sigma_r - \sigma_\theta)$; and equilibrium conditions and assumptions employed to obtain P in plug region.

In Figure 2a, measured $\sigma_r - \sigma_\theta$ values for selected points in the sample are shown. Also shown are the $\sigma_r - \sigma_\theta$ distribution calculated from equations (1)-(4), using the measured, pre-assembly, differential radial interference. Under the assumptions shown in Figure 2, and applying the equilibrium conditions, an experimental $P = -122 \pm 5$ MPa is obtained in excellent agreement with the calculated $P = -129.0 \pm 2.4$ MPa.

In view of the success with the aluminum ring/plug sample, the energy-dispersive neutron diffraction method is being applied to a material which has posed serious difficulties for conventional residual stress measurement techniques: depleted uranium. Initial results on two 2.5 cm diameter extruded cylinders with quite different thermo-mechanical histories show markedly different strain distributions. It is anticipated that three-dimensional stress profiles will be obtained at selected points in the samples in the very near future with existing instrumentation.

1. C. S. Choi et al., NBS Tech. Note 995, p. 34 (1979).
2. L. Pintschovius et al., in "Residual Stress and Stress Relaxation" (ed. E. Kula and V. Weiss), Plenum Press, New York, 1982, 467.
3. N. N. Hsu, T. M. Proctor, Jr., and G. V. Blessing, J. Test. Eval. 10, 230 (1982).
4. See, for example, J. B. Cohen, H. Dolle, and M. R. James, NBS Special Publication 567, 453 (1980).
5. In reference 3 an incorrect value of $P = 65$ MPa was quoted.

CRYSTAL DATA (PRODUCED BY AUTOMATED TYPESETTING PROCEDURES)

A. D. Mighell and J. K. Stalick

Work on Volume 5 in the Third Edition Series of Crystal Data has been completed. The book contains about 10,000 entries on crystalline compounds. The data are ordered by crystal system and within each system the entries are arranged as a function of the lattice parameters. The volumes in the Third Edition Series are used by the industrial and academic communities for identification, for phase characterization, and for many other applications. Volume 5 will be published in the fall of 1983 jointly by the U. S. Department of Commerce, National Bureau of

Standards, and the JCPDS--International Centre for Diffraction Data. Production of Volume 5 of Crystal Data has been done in collaboration with the Cambridge Crystallographic Data Centre.

The book was produced by computer-oriented procedures in a two stage process. First, the Crystal Data Master Data Base was produced for Volume 5 by using the computer program NBS*AIDS80.¹ This program was used to evaluate the data, to calculate new data parameters, to transform cell data, and to build the Master Data Base. Thus, every item in each entry in the Master Data Base was defined, evaluated, and represented in standard form. Second, computer-typesetting procedures were applied to the Master Data Base to extract the relevant data and to produce the book and indexes. The typesetting routines were written by the Data Systems Development Group of the Office of Standard Reference Data.

Future volumes in the Crystal Data Series will be produced by the same strategy (i.e., directly from the Master Data Base by automated computer procedures). Likewise other products can be generated. For example, the Crystal Data Center prepares the NBS Crystal Data Identification File from the Master Data Base in parallel with the books. The Identification File can be used independently or in conjunction with the Crystal Data books in the Third Edition Series. This file is designed for the rapid identification of unknown materials and is distributed on computer tape by the JCPDS. The Identification File can also be accessed by on-line computer search systems in the U. S. and in Canada. Similar methods could conveniently be used by other data centers for file preparation and product production. In fact, the JCPDS-International Centre for Diffraction Data plans to generate printed and magnetic tape products directly from their AIDS80 formatted Master Data Base which contains powder data.

1. NBS*AIDS80: A FORTRAN program for Crystallographic Data Evaluation (1981), A. D. Mighell, C. R. Hubbard, and J. K. Stalick, NBS Technical Note 1141.

PROGRESS REPORT ON A STUDY OF SPECIALIZED LATTICES USING MATRIX AND
REDUCTION TECHNIQUES

V. L. Himes* and A. D. Mighell

An area of research in progress concerns the classification of lattices in the NBS Crystal Data Identification File (NBS*ID File, 1982) according to types of specialization in the reduced cell or reduced form. Thus, methods to seek and define specialization are being investigated. One way is to analyze the relationships between the symmetrical and unsymmetrical scalars in the reduced form. A second, and perhaps more general way, is to analyze the matrices that relate the cell to those metrically identical to it. These matrices fall into two types: matrices whose elements are only integers, and matrices whose elements are integers and simple rational numbers. Classifications of specialized reduced forms may be used as frameworks to establish lattice relationships. With a given classification, patterns in the data may be recognized and correlated with potential indexing problems, with errors made in experimental procedures, or with physical properties of the compounds. A general plan for this project has been devised and many of the computer programs required for this research have been written.

In order to systematically classify and analyze specialized reduced forms, it was necessary to design data file structures and to develop computer code and strategies to efficiently manipulate large sets of data. For example, two different 1-line (132 characters per entry) data bases have been derived from the 4-line (four 80 character records per entry) NBS*ID File. These 1-line data bases will be used to create 1-line sub-files of lattices having specialized reduced forms.

Preliminary analyses with the 1-line files using software specific to this research project show that although many specialized reduced forms exist, two general categories may be defined. The first class includes those specialized reduced forms in which the metric symmetry exceeds the reported crystal symmetry. The second class of specialized reduced forms results when the crystal and metric symmetry agree, but there is at least one relationship within the reduced form that is not required by the crystal symmetry.

*National Bureau of Standards - National Research Council Postdoctoral Research Associate.

Once suitable sub-files have been created, it is planned to use a combination of reduction and matrix techniques to identify the first class of specialized reduced forms [i.e., those reduced forms with higher metric symmetry or pseudosymmetry; (Himes and Mighell, 1982)]. Using these strategies, preliminary analyses have been carried out. For example, triclinic and monoclinic 1-line organic files have been used to create sub-files with $a = b$, $b = c$, and $a = b = c$. Analyses of these sub-files using the matrix method have revealed that many triclinic and monoclinic lattices have orthorhombic metric symmetry. These specialized reduced forms may be due to structural reasons, or the true crystal symmetry could have been missed. Regardless of the reasons, experience has shown that the presence of higher metric symmetry or pseudosymmetry in a lattice leads to the existence of metrically similar unit cells that index differently the same set of diffraction data. Once the higher symmetry or pseudosymmetry is recognized, the resulting indexing problems can be avoided. Several hundred references from these categories of specialized reduced forms have been collected for more detailed analyses.

The specialization in the second class of reduced forms may be due to certain properties of compounds such as packing, twinning, and conductivity, or it may result from errors made in experimental procedures. For example, a specialized reduced form may suggest that the unit cell obtained by indexing powder data is not a primitive cell of the lattice but rather a derivative cell. Likewise, a derivative subcell could have been determined using a single-crystal diffractometer if rows of diffraction spots were missed. Lower symmetry derivative subcells of higher symmetry lattices will show specialization in the reduced form.

Both practical examples and a brief survey of lattices from the NBS*ID File suggest that the 1-line sub-files of specialized reduced forms should be analyzed to see whether a derivative sub- or super-cell has been determined. Subcells and supercells for selected specialized reduced forms will be calculated and attempts will be made to relate these derivative lattices to other lattices in the data base. A match of a derivative lattice with one already in the data base could help one to understand the specialization in the reduced form. For example, an experimental error could have been made or the literature may cite structural reasons such as temperature- or pressure-dependent phase transitions. For each lattice that is characterized by a primitive cell, there are 55 subcells with $1/2$, $1/3$, and $1/4$ times the volume and 55 supercells with 2, 3, and 4 times the volume of the primitive cell (Santoro and Mighell, 1973). Thus, an efficient computer strategy and program are required to match a series of primitive cells and derivative cells against the entire

NBS*ID File. Accordingly, several search strategies for an identification/registration program based on lattice-matching have been developed. The computer programs, written using standard FORTRAN code, are currently being modified and tested. The identification/registration programs utilizing "sequential access" and "grouped-entry direct access" searches have proved to be efficient strategies. In particular, the grouped-entry direct access program will allow about 1,000 cells to be checked against approximately 30,000 entries from the NBS*ID File in only two minutes (Univac 1100/82 computer), making the derivative-lattice analysis of specialized reduced forms feasible.

Additional preliminary computer analyses will be made and practical examples of lattices having specialized reduced forms will be studied. These efforts will help to define and select appropriate sub-files of specialized reduced forms to study in detail. The results of these analyses should lead to a better understanding of lattice relationships and should have a direct impact in many areas of experimental and theoretical crystallography.

-
1. V. L. Himes and A. D. Mighell, Acta Cryst. A38, 748-749 (1982).
 2. NBS Crystal Data Identification File (1982). A magnetic tape of crystal data distributed by the JCPDS - International Centre for Diffraction Data, 1601 Park Lane, Swarthmore, PA 19081, USA.
 3. A. Santoro and A. D. Mighell, Acta Cryst. A29, 169-175 (1973).

SPACE GROUP FREQUENCIES FOR ORGANIC COMPOUNDS

A. D. Mighell and V. L. Himes*

and

J. R. Rodgers

(National Research Council of Canada, Ottawa, Canada)

1. Introduction

Using the NBS Crystal Data Identification File (1982), the frequency of occurrence has been calculated for each of the 230 space groups. The space group frequencies presented in Table 1 were calculated for organic materials (i.e., carbon-containing compounds). Most of these compounds (~ 89.9%) correspond to entries that result from full structure determinations. The types of structures reported in the literature have been influenced by a variety of factors such as the techniques available to solve structures and special interest in selected categories of compounds. Nevertheless, since it was possible to tabulate space group frequencies for 29,059 organic compounds that have been reported up to 1981, the results should be fairly representative of their distribution in nature.

The space group frequency table may be used in routine structure work. We have found it helpful to check a list of space group frequencies as soon as a space group has been assigned or limited to a few possibilities. The frequencies may indicate that a space group determination should be rechecked if the substance has been characterized by a rare or previously unoccupied space group. If the compound has, indeed, crystallized in a rare space group, the NBS Crystal Data Identification File may be used to find references for a structure comparison. For reasons discussed below, however, it is important not to have a false sense of security when a commonly reported space group has been determined.

Inspection of the data in Table 1 reveals that most organic compounds have been assigned to a relatively small number of space groups. In fact, 75 percent of the compounds have been described in only five space groups and 90 percent in 16 space groups. A comparison of the percent occupancy of the five most common space groups with corresponding data calculated earlier using a smaller sample of 21,051 compounds (Mighell and Rodgers, 1980) reveals that the percentages for the five most frequently occurring space groups are fairly constant. The percentages are as follows, with the earlier data given in parentheses: $P2_1/c$, 36.0% (35.5%); $\bar{P}1$, 13.7% (13.3%); $P2_12_12_1$,

*National Bureau of Standards - National Research Council Postdoctoral Research Associate.

11.6% (12.4%); $P2_1$, 6.7% (7.6%); $C2/c$, 6.6% (6.9%). In contrast, there are 117 space groups with very low frequencies (five or fewer compounds assigned to them). Of these 117 space groups, 29 space groups have one entry and 35 have no entry at all. Thus, it may be possible to develop theories which would explain why certain space groups are rare or uninhabited, or one may be able to correlate the molecular shape, physical properties, etc. with the probability that the compound crystallizes in a given space group.

As a further aid to experimental and theoretical work, space group frequencies for the 86 chemical classes (steroids, silicon compounds, metal complexes, etc.) listed in Molecular Structures and Dimensions (1970-1982) are being prepared and will be submitted for publication.

2. Discussion

It is important to remember that the frequencies of occurrence are approximate since certain space group frequencies may be under- or overestimated. Detailed analyses of several cases in which crystal structures have been described in space groups of unnecessarily low symmetry have been carried out; examples are given in the following references: Davies, Kopf, and Weiss, 1982; Herbstein and Marsh, 1982; Marsh and Schomaker, 1980; Schomaker and Marsh, 1979; Marsh and Schomaker, 1979. These references demonstrate that what appears to be a satisfactory structural refinement does not necessarily imply a correct space group determination. The errors in space group assignments that are discussed in the above references can be divided into two categories: 1) incorrect space group but correct crystal system; 2) incorrect space group and incorrect crystal system. Errors of the second type can be prevented or detected by determining the metric symmetry of the lattice. Using a matrix technique (Himes and Mighell, 1982) to analyze the metric symmetry of ~ 30,000 organic entries in the NBS Crystal Data Identification File, it has been found that many crystals reported in triclinic and monoclinic space groups have higher metric symmetry. Depending on the values used for "reasonable" errors on the cell parameters, it was found that for 3 to 12 percent of the compounds the metric symmetry exceeds the crystal symmetry reported by the authors in the original reference. Inspection of samples from selected categories of these papers further revealed that, in many instances, the compounds have probably been described in space groups of too low symmetry.

Many of the errors in space group determination can be attributed to blind acceptance of the results of automated diffractometers, failure to inspect carefully the final structural parameters for possible higher symmetry, failure to ascribe

unusual molecular or packing symmetry to a refinement in an incorrect space group, assuming that the e.s.d.'s on the cell parameters indicate accuracy rather than precision, and errors in space group determination strategy.

It is a serious error in strategy for the experimentalist not to check explicitly for the highest metric symmetry. This can lead to an assignment of a space group in the wrong crystal system. Traditionally, one of the first steps in assigning a space group for a compound is to select unit cell parameters to be consistent with the observed intensity symmetry. The defect in this method is that the full intensity symmetry is not always easy to see. Thus, one could select a centered monoclinic cell consistent with the apparent Laue symmetry, check for systematic extinctions, and conclude that everything is correct for the assignment of a centered monoclinic space group. However, the space group may be rhombohedral because the metric symmetry was not checked and the true Laue symmetry is higher. Our analysis of metric symmetry for organic compounds suggests that the rhombohedral system with approximately 300 reported compounds should have 10 to 20 percent more compounds assigned to it. Two examples of missed rhombohedral symmetry are discussed below.

The first example of missed crystal symmetry is S(-)-cyclophosphamide. S(-)-cyclophosphamide has been reported in a triclinic space group, P1, with cell parameters $a = 10.500(4)$, $b = 10.490(4)$, $c = 10.761(4) \text{ \AA}$, $\alpha = 110.0(2)^\circ$, $\beta = 110.0(2)^\circ$, and $\gamma = 108.9(2)^\circ$ (Adamiak, Saenger, Kinas, and Stec, 1977). In contrast, R(+)-cyclophosphamide has been reported in a rhombohedral space group, R3, with $a = 10.520(5) \text{ \AA}$ and $\alpha = 108.9(1)^\circ$ (Karle, Karle, Egan, Zon, and Brandt, 1977). Both compounds were characterized by full structure determinations and, in each case, the cyclophosphamide molecules form hydrogen-bonded trimers. Both reduction and matrix techniques show that the metric symmetry for each compound is rhombohedral suggesting that S(-)-cyclophosphamide was refined in a space group of too low symmetry. The matrix procedure yielded six matrices which are characteristic of rhombohedral lattice symmetry while the reduced cell matrices ($\underline{\underline{a}} \cdot \underline{\underline{a}} \ \underline{\underline{b}} \cdot \underline{\underline{b}} \ \underline{\underline{c}} \cdot \underline{\underline{c}}$ / $\underline{\underline{b}} \cdot \underline{\underline{c}} \ \underline{\underline{a}} \cdot \underline{\underline{c}} \ \underline{\underline{a}} \cdot \underline{\underline{b}}$) calculated for both S(-)- and R(+)-cyclophosphamide correspond to the rhombohedral reduced form #4 (Mighell and Rodgers, 1980; International Tables for X-ray Crystallography, 1969):

$$\begin{bmatrix} 110.04 & 110.23 & 110.25 \\ -35.93 & -35.68 & -35.75 \end{bmatrix}$$

S(-)-cyclophosphamide

$$\begin{bmatrix} 110.67 & 110.67 & 110.67 \\ -35.85 & -35.85 & -35.85 \end{bmatrix}$$

R(+)-cyclophosphamide

Tables 2 and 3 give a summary of these results. Within experimental error, the atomic coordinates for S(-)-cyclophosphamide can be transformed to those reported for R(+)-cyclophosphamide.

A detailed analysis of a typical example of missed rhombohedral symmetry has been reported by Davies, Kopf, and Weiss (1982). In this case, it was shown that the structure of sodium tert-butoxide, which was originally reported in the monoclinic space group, Cc, with $a = 30.995(23)$, $b = 19.378(14)$, $c = 18.269(13)$ Å and $\beta = 121.01(2)^\circ$ can be described in the rhombohedral space group, R₃c, with $a = 18.274$ Å and $\alpha = 64.07^\circ$. A transformation matrix relating the C-centered monoclinic cell to the primitive rhombohedral cell (= reduced cell) is (0 0 -1 / 1/2 1/2 0 / 1/2 -1/2 0). By using metric methods, one can immediately establish from the originally reported monoclinic cell parameters that the lattice is metrically rhombohedral. For example, the reduction method gives rhombohedral reduced form #2 (Mighell and Rodgers, 1980; International Tables for X-ray Crystallography, 1969) while the matrix technique, when applied to a primitive cell of the lattice, yields six matrices indicating the rhombohedral lattice symmetry (see Table 4).

In Table 5, we outline a procedure to help prevent errors in space group determination. The procedure is similar to one presented earlier (Mighell and Rodgers, 1980) except that we have added a check using a matrix technique, a check of the NBS Crystal Data Identification File, and a check of the space group frequency table. As the table shows, the metric symmetry is determined as soon as a primitive unit cell of the lattice has been found. The metric symmetry may be determined using both matrix and reduction techniques. When using reduction techniques, the metric symmetry can be determined directly from the Niggli reduced form, or by alternative procedures recommended by Clegg (1981) and Le Page (1982). When assigning a space group, one should start by considering space groups consistent with the highest possible metric symmetry.

Table 1. Space group frequencies for 29059 organic crystalline compounds

Space Group Symbol	Space Group Number	Frequency	Space Group Symbol	Space Group Number	Frequency
P1	1	305	Pmn2 ₁	31	37
P1̄	2	3986	Pba2	32	9
P2	3	11	Pna2 ₁	33	513
P2 ₁	4	1957	Pnn2	34	14
C2	5	273	Cmm2	35	2
Pm	6	1	Cmc2 ₁	36	56
Pc	7	102	Ccc2	37	6
Cm	8	22	Amm2	38	0
Cc	9	277	Abm2	39	5
P2/m	10	5	Ama2	40	14
P2 ₁ /m	11	239	Aba2	41	47
C2/m	12	189	Fmm2	42	8
P2/c	13	141	Fdd2	43	115
P2 ₁ /c	14	10450	Imm2	44	3
C2/c	15	1930	Iba2	45	31
P222	16	7	Ima2	46	5
P222 ₁	17	9	Pmmm	47	4
P2 ₁ 2 ₁ 2 ₂	18	187	Pnnn	48	3
P2 ₁ 2 ₁ 2 ₁	19	3359	Pccm	49	1
C222 ₁	20	86	Pban	50	2
C222	21	5	Pmma	51	9
F222	22	0	Pnna	52	23
I222	23	7	Pmna	53	15
I2 ₁ 2 ₁ 2 ₁	24	5	Pccca	54	13
Pmm2	25	2	Pbam	55	12
Pmc2 ₁	26	12	Pccn	56	101
Pcc2	27	0	Pbcm	57	64
Pma2	28	1	Pnnm	58	30
Pca2 ₁	29	242	Pmmn	59	23
Pnc2	30	3	Pbcn	60	341

Table 1. Cont.

Space Group Symbol	Space Group Number	Frequency	Space Group Symbol	Space Group Number	Frequency
Pbca	61	1261	P ₁ 422	91	3
Pnma	62	548	P ₁ 42 ₁ 2	92	101
Cmcm	63	61	P4 ₂ 22	93	2
Cmca	64	96	P4 ₂ 2 ₁ 2	94	7
Cmmm	65	4	P4 ₃ 22	95	1
Cccm	66	12	P4 ₃ 2 ₁ 2	96	44
Cmma	67	2	I422	97	2
Ccca	68	14	I4 ₁ 22	98	1
Fmmm	69	3	P4mm	99	0
Fddd	70	30	P4bm	100	0
Immm	71	4	P4 ₂ cm	101	0
Ibam	72	27	P4 ₂ nm	102	4
Ibca	73	8	P4cc	103	0
Imma	74	5	P4nc	104	3
P4	75	1	P4 ₂ mc	105	0
P4 ₁	76	47	P4 ₂ bc	106	1
P4 ₂	77	3	I4mm	107	2
P4 ₃	78	7	I4cm	108	1
I4	79	12	I4 ₁ md	109	6
I4 ₁	80	9	I4 ₁ cd	110	9
P4	81	7	P42m	111	1
I4	82	59	P42c	112	0
P4/m	83	6	P42 ₁ m	113	17
P4 ₂ /m	84	3	P42 ₁ c	114	68
P4/n	85	37	P4m2	115	1
P4 ₂ /n	86	48	P4c2	116	0
I4/m	87	28	P4b2	117	2
I4 ₁ /a	88	98	P4n2	118	4
P422	89	1	I4m2	119	1
P42 ₁ 2	90	4	I4c2	120	2

REACTOR RADIATION DIVISION AND COLLABORATIVE PROGRAMS

Table 1. Cont.

Space Group Symbol	Space Group Number	Frequency	Space Group Symbol	Space Group Number	Frequency
I ⁻ 42m	121	12	P3 ₁ 12	151	0
I ⁻ 42d	122	22	P3 ₁ 21	152	27
P4/mmm	123	0	P3 ₂ 12	153	0
P4/mcc	124	8	P3 ₂ 21	154	8
P4/nbm	125	4	R32	155	23
P4/nnc	126	1	P3m1	156	1
P4/mbm	127	2	P31m	157	4
P4/mnc	128	14	P3c1	158	3
P4/nmm	129	19	P31c	159	5
P4/ncc	130	16	R3m	160	21
P4 ₂ /mmc	131	3	R3c	161	39
P4 ₂ /mcm	132	1	P31m	162	0
P4 ₂ /nbc	133	2	P31c	163	13
P4 ₂ /nnm	134	2	P3m1	164	15
P4 ₂ /mbc	135	1	P3c1	165	17
P4 ₂ /mmm	136	17	R3m	166	20
P4 ₂ /nmc	137	8	R3c	167	36
P4 ₂ /ncm	138	3	P6	168	0
I4/mmm	139	17	P6 ₁	169	14
I4/mcm	140	4	P6 ₅	170	16
I4 ₁ /amd	141	11	P6 ₂	171	5
I4 ₁ /acd	142	19	P6 ₄	172	0
P3	143	10	P6 ₃	173	33
P3 ₁	144	21	P6	174	1
P3 ₂	145	10	P6/m	175	1
R3	146	40	P6 ₃ /m	176	75
P3	147	26	P622	177	2
R3	148	122	P6 ₁ 22	178	6
P312	149	0	P6 ₅ 22	179	1
P321	150	5	P6 ₂ 22	180	4

Table 1. Cont.

Space Group Symbol	Space Group Number	Frequency	Space Group Symbol	Space Group Number	Frequency
P ₆ 422	181	1	Ia3	206	5
P ₆ 322	182	6	P432	207	0
P6mm	183	0	P ₄ 32	208	0
P6cc	184	0	F432	209	1
P ₆ 3cm	185	1	F ₄ 32	210	3
P ₆ 3mc	186	15	I432	211	0
P ₆ m2	187	0	P ₄ 32	212	1
P ₆ c2	188	0	P ₄ 32	213	1
P ₆ 2m	189	0	I ₄ 32	214	0
P ₆ 2c	190	9	P ₄ 3m	215	7
P6/mmm	191	1	F ₄ 3m	216	1
P6/mcc	192	7	I ₄ 3m	217	18
P ₆ 3/mcm	193	0	P ₄ 3n	218	6
P ₆ 3/mmc	194	9	F ₄ 3c	219	2
P23	195	0	I ₄ 3d	220	4
F23	196	0	Pm3m	221	3
I23	197	3	Pn3n	222	0
P ₂ 13	198	15	Pm3n	223	5
I ₂ 13	199	0	Pn3m	224	1
Pm3	200	2	Fm3m	225	22
Pn3	201	0	Fm3c	226	0
Fm3	202	0	Fd3m	227	1
Fd3	203	1	Fd3c	228	4
Im3	204	3	Im3m	229	8
Pa3	205	36	Ia3d	230	0

Table 2. Metric lattice symmetry determination for S(-)-cyclophosphamide.

	Unit Cell Parameters			\underline{B} -Matrices		
	a	b	c (Å)			
	α	β	γ (°)			
Initial triclinic cell	10.500(4)	10.490(4)	10.761(4)	$\begin{bmatrix} -1 & -1 & -1 \\ 1 & 0 & 0 \\ 0 & 0 & 1 \end{bmatrix}$	$\begin{bmatrix} -1 & 0 & 0 \\ 1 & 1 & 1 \\ 0 & 0 & -1 \end{bmatrix}$	$\begin{bmatrix} 0 & -1 & 0 \\ -1 & 0 & 0 \\ 0 & 0 & -1 \end{bmatrix}$
	110.0(2)	110.0(2)	108.9(2)	$\begin{bmatrix} 0 & 1 & 0 \\ -1 & -1 & -1 \\ 0 & 0 & 1 \end{bmatrix}$	$\begin{bmatrix} 1 & 0 & 0 \\ 0 & 1 & 0 \\ 0 & 0 & 1 \end{bmatrix}$	$\begin{bmatrix} 1 & 1 & 1 \\ 0 & -1 & 0 \\ 0 & 0 & -1 \end{bmatrix}$
(0 -1 0 / 1 1 1 / -1 0 0)						
Reduced cell	10.490	10.499	10.500	$\begin{bmatrix} -1 & 0 & 0 \\ 0 & 0 & -1 \\ 0 & -1 & 0 \end{bmatrix}$	$\begin{bmatrix} 0 & -1 & 0 \\ -1 & 0 & 0 \\ 0 & 0 & -1 \end{bmatrix}$	$\begin{bmatrix} 0 & 0 & -1 \\ 0 & -1 & 0 \\ -1 & 0 & 0 \end{bmatrix}$
	109.02	108.90	108.94	$\begin{bmatrix} 0 & 0 & 1 \\ 1 & 0 & 0 \\ 0 & 1 & 0 \end{bmatrix}$	$\begin{bmatrix} 0 & 1 & 0 \\ 0 & 0 & 1 \\ 1 & 0 & 0 \end{bmatrix}$	$\begin{bmatrix} 1 & 0 & 0 \\ 0 & 1 & 0 \\ 0 & 0 & 1 \end{bmatrix}$

Table 3. Matrices found for R(+)-cyclophosphamide.

Initial cell $a = 10.520$ $b = 10.520$ $c = 10.520 \text{ \AA}^0$
 (= reduced cell) $\alpha = 108.9$ $\beta = 108.9$ $\gamma = 108.9^\circ$

B-Matrices

$$\begin{bmatrix} -1 & 0 & 0 \\ 0 & 0 & -1 \\ 0 & -1 & 0 \end{bmatrix}$$

$$\begin{bmatrix} 0 & -1 & 0 \\ -1 & 0 & 0 \\ 0 & 0 & -1 \end{bmatrix}$$

$$\begin{bmatrix} 0 & 0 & -1 \\ 0 & -1 & 0 \\ -1 & 0 & 0 \end{bmatrix}$$

$$\begin{bmatrix} 0 & 0 & 1 \\ 1 & 0 & 0 \\ 0 & 1 & 0 \end{bmatrix}$$

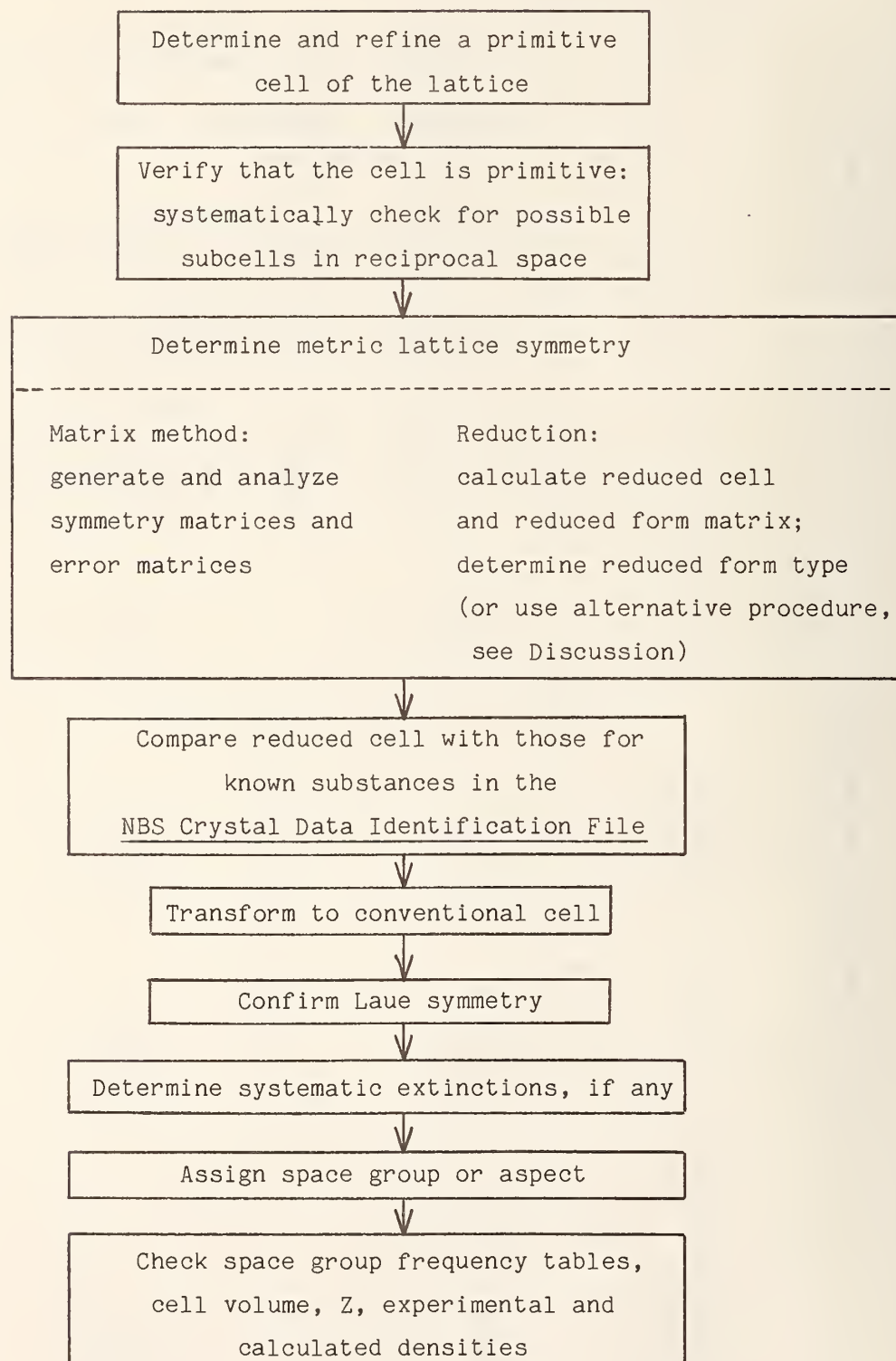
$$\begin{bmatrix} 0 & 1 & 0 \\ 0 & 0 & 1 \\ 1 & 0 & 0 \end{bmatrix}$$

$$\begin{bmatrix} 1 & 0 & 0 \\ 0 & 1 & 0 \\ 0 & 0 & 1 \end{bmatrix}$$

Table 4. Metric lattice symmetry determination for sodium tert-butoxide.

	Unit Cell Parameters			B-Matrices
	a α	b β	c γ (°)	
Initial monoclinic cell (Cc)	30.995(23) 90	19.378(14) 121.01(2)	18.269(13) 90	
	(0 -1 0 / -.5 .5 0 / 0 0 -1)			
Primitive cell	19.378 115.90	18.277 90.00	18.269 122.01	$\begin{bmatrix} -1 & -1 & -1 \\ 1 & 1 & 0 \\ 0 & -1 & 0 \end{bmatrix}$
	(0 0 -1 / 0 1 0 / 1 1 0)			$\begin{bmatrix} 0 & 1 & 1 \\ 0 & 0 & -1 \\ -1 & -1 & 0 \end{bmatrix}$
Reduced primitive cell	18.269 64.03	18.277 64.10	18.277 64.10	$\begin{bmatrix} 0 & -1 & 0 \\ -1 & 0 & 0 \\ 0 & 0 & -1 \end{bmatrix}$
	(0 0 -1 / 0 1 0 / 1 1 0)			$\begin{bmatrix} 1 & 0 & 0 \\ -1 & -1 & 0 \\ 0 & 0 & -1 \end{bmatrix}$
	(0 0 -1 / 0 1 0 / 1 1 0)			$\begin{bmatrix} 1 & 0 & 0 \\ 0 & 1 & 0 \\ 0 & 0 & -1 \end{bmatrix}$
	(0 0 -1 / 0 1 0 / 1 1 0)			$\begin{bmatrix} 1 & 0 & 0 \\ 0 & 1 & 0 \\ 0 & 0 & -1 \end{bmatrix}$

Table 5. Space group determination.



1. D. A. Adamiak, W. Saenger, R. Kinas, and W. J. Stec, *Z. Naturforsch.*, 32c, 672-677 (1977).
2. W. Clegg, *Acta Cryst.*, A37, 913-915 (1981).
3. J. E. Davies, J. Kopf, and E. Weiss, *Acta Cryst.*, B38, 2251-2253 (1982).
4. F. H. Herbstein and R. E. Marsh, *Acta Cryst.*, B38, 1051-1055 (1982).
5. V. L. Himes and A. D. Mighell, *Acta Cryst.*, A38, 748-749 (1982).
6. International Tables for X-ray Crystallography, Vol. I, 530-535. Birmingham: Kynoch Press (1969).
7. I. L. Karle, J. M. Karle, W. Egan, G. Zon, and J. A. Brandt, *J. Am. Chem. Soc.*, 99, 4803-4807 (1977).
8. Y. Le Page, *J. Appl. Cryst.*, 15, 255-259 (1982).
9. R. E. Marsh and V. Schomaker, *Inorg. Chem.*, 18, 2331-2336 (1979).
10. R. E. Marsh and V. Schomaker, *Acta Cryst.*, B36, 219-220 (1980).
11. A. D. Mighell and J. R. Rodgers, *Acta Cryst.*, A36, 321-326 (1980).
12. Molecular Structures and Dimensions (1970-1982). Published for the Crystallographic Data Centre, Cambridge and the International Union of Crystallography.
13. NBS Crystal Data Identification File (1982). A magnetic tape of crystal data distributed by the JCPDS-International Centre for Diffraction Data, 1601 Park Lane, Swarthmore, PA 19081.
14. V. Schomaker and R. E. Marsh, *Acta Cryst.*, B35, 1094-1099 (1979).

AN EMPIRICAL METHOD FOR THE APPROXIMATION OF DENSITIES

J. K. Stalick

It is frequently useful to know what the density of a substance should be, particularly in evaluating the correctness of a chemical composition and/or experimental unit cell parameters. Techniques exist for the approximation of densities for some types of organic compounds¹ and for simple ionic substances² provided that the structure is known. However, difficulties arise when the substance is complex or the structure is unknown. In particular, a method was needed to detect errors in the Crystal Data data base. The most easily found errors are those where the formula and Z (number of molecules per unit cell) are not compatible, resulting in x-ray calculated densities, D_x , wrong by a factor of two or more. It was also hoped to be able to detect certain errors in chemical composition or unit-cell data.

In order to calculate an approximate density, D_g , it was assumed that the molecular volume as determined by x-ray studies, V_x , is equal to the sum of the individual atomic volumes, V_i . A least-squares refinement was carried out with up to 2000 equations (compounds) and 106 unknowns (atomic volumes) using data from the Crystal Data data base. The function minimized was $V_x - \sum N_i V_i$, where N_i is the number of atoms of each type. The data sets were adjusted so that each atom i was represented in at least 10 equations. The three basic divisions of the data base (organics and organometallics, metals and intermetallics, and inorganics) were treated separately. Subsets of data of a more homogeneous nature, for example all compounds containing only C, H, and O, were also examined.

Tests using the three basic divisions of substances indicated that a correction for electronegativity difference is valuable for all except the primarily covalent organics and organometallics. The correction is especially important when a data set containing entries for diverse compound types is used. Since no bonding information is available in the data base, the average electronegativity difference, Δ , was defined as follows:

$$\Delta = \frac{\sum N_i \chi_i}{i} - \frac{\sum N_j \chi_j}{j}$$

where χ is the electronegativity on the Allred-Rochow scale³ and N is the number of atoms of each type. The atoms in each substance were divided into two equal groups, where the subscript i refers to the most electronegative atoms and the subscript j

Table 1. Summary of results of approximate density calculation. % discrepancy = $\frac{AD_x - D_g^A}{D_x} \times 100$, where D_x is the x-ray density and D_g is the approximate density.

Data Set	Number of Compounds	Compounds within Discrepancy, %					Average Discrepancy, %
		5	10	15	20	25	
All compound types	1580	78	96	99	100	--	3.4
Cu and non-metals	705	79	97	100	--	--	3.2
Organics and Co organometallics	390	73	96	99	100	--	3.8
Zn organometallics	106	77	98	100	--	--	3.4
C, H, O only	891	75	97	100	--	--	3.5
*All compound types, set 1	1992	64	88	95	98	99	5.6(5.4)†
*All compound types, set 2	1997	57	82	94	98	99	6.0 (5.7)
Non-metals excluded	430	81	98	100	--	--	2.9
Inorganics	1920	47	76	88	94	96	8.0 (8.0)
Metal oxides	874	54	80	91	95	97	6.6 (6.3)
	198	59	82	91	95	96	6.4

*Data set not corrected for possible errors.

†Numbers in parentheses refer to refinements corrected for electronegativity difference.

Table 2. Change in effective atomic volume with compound type for selected elements.

Atom	Elements	Atomic Volume, \AA^3		
		Metals and Intermetallics (600 compounds)	Inorganics (2800 compounds)	Organics and Organometallics (1580 compounds)
C	9*	6 (10)†	20	14
H	--	6 (8)	7	5
O	--	--	10	10
Cl	29+	--	29	25
Br	33‡	--	34	31
S	26	29 (26)	25	26
P	20	17 (19)	19	29
Co	11	10 (11)	9	32
Cu	12	11 (12)	10	30
Pt	15	17 (14)	13	36
Ag	17	19 (21)	20	26
La	37	34 (42)	23	--
Ba	63	50 (62)	29	43
Na	40‡	32 (37)	17	17
K	76‡	45 (62)	27	29

*Graphite.

†Numbers in parentheses refer to refinements corrected for electronegativity difference.

‡Low-temperature studies.

refers to the least electronegative atoms. The approximate molecular volume, V_g , was then calculated assuming

$$V_g = (1 - K\Delta^x) \sum N_i V_i$$

where V_i are the individual atomic volumes, and k and x are empirical correction factors. The best agreement between V_g and the molecular volume as determined by x-ray studies was obtained for $k \approx 0.2$ and $x \approx 0.6$. Although the improvement in average discrepancy was not large, the agreement for metallic elements was significantly better.

The results for all data sets examined are given in Table 1. The average agreement of the approximate density with the x-ray calculated density is within 4 percent for organics and organometallics, 6 percent for metals and intermetallics, and 8 percent for inorganics; nearly all substances agree within 25 percent. The effective atomic volumes vary significantly with compound type (Table 2); thus the separation of the data base into the three basic divisions helps in evaluating the data. The use of limited data sets (Table 1) also improves the reliability of the derived approximate densities.

The effective atomic volumes obtained from this study have been used in the evaluation of approximately 20,000 organic and organometallic entries for the Crystal Data data base. Errors in Z were readily detected. In addition, errors in chemical composition (e.g. omission of solvent molecules) and unit-cell data were also found and corrected.

-
1. A. Immirzi and B. Perini, *Acta Cryst. or Sect. A*, 33, 216 (1977).
 2. W. H. Baur, *American Crystallographic Association Winter Meeting Abstracts*, 41 (1983).
 3. A. L. Allred and E. G. Rochow, *J. Inorg. Nucl. Chem.* 5, 264 (1958).

THERMAL PROPERTIES OF $(KCN)_x(KBr)_{1-x}$ IN THE QUADRUPOLAR GLASS STATE

J. DeYoreo and R. Pohl
(Cornell University, Ithica, NY)

and

J. M. Rowe and J. J. Rush

and

S. Susman
(Argonne National Laboratory, Argonne, IL)

Samples of $(KCN)_x(KBr)_{1-x}$ can be prepared as solid solutions over the entire range of x from 0.0 to 1.0, and have been extensively studied by a number of techniques. For x greater than approximately 0.6, phase transitions to structures in which the electric quadrupole moments are ordered are observed as the temperature is lowered, with the transition for $x = 0.6$ occurring at approximately 85 K. For x less than 0.6, no transitions to structures in which the quadrupole moments have long range order has been observed. Michel and Rowe¹ proposed a model for the behavior of samples with x less than 0.6 in which the quadrupole moments would order collectively in a phase analogous to the magnetic spin glass state. This model has been criticized^{2, 3} on the basis of recent dielectric relaxation measurements which showed that the CN ions remained orientationally mobile at temperatures well below the postulated "freezing" temperature T_f , and that the relaxation simply slowed down continuously with temperature. However, the dielectric data are not necessarily inconsistent with the model, since the quantity measured is the electric dipole susceptibility, not the quadrupolar susceptibility. Further, to the extent that the dielectric data reflect Debye relaxation (as they clearly do in pure KCN⁴), they are a measure of the single particle behavior rather than the collective behavior; i.e., they are a result of the reorientation of individual CN ions in the applied field, which is observed in pure KCN below both the quadrupolar and the dipolar transitions. In order to clarify this situation, as well as to establish the low temperature thermal properties of the mixed crystals, we have measured the thermal conductivity and specific heat of samples with x less than or equal to 0.5 as a function of temperature between 0.8 and 100 K. The results are quite similar to the behavior observed for amorphous solids and show that these systems may be quite useful as models for the low energy excitations in amorphous solids. In addition, we observe an anomaly in the thermal conductivity for $x = 0.25$ at temperatures close to those proposed for T_f on the basis of neutron scattering measurements of the dynamics of the same samples. However, the temperature at which this anomaly occurs is not

reproducible when the sample is remounted in the cryostat although it always occurs at temperatures of the same order as T_f . This effect is not simply an experimental artifact of the particular arrangement used - no such effect was observed for a sample of silica measured under the same conditions. Thus the nature of the formation of the glassy state remains somewhat ambiguous until further measurements can be performed. However, the present work shows that the $(\text{KCN})_x(\text{KBr})_{1-x}$ system is a good model system for the study of the low energy excitations found in amorphous solids, especially since the nature of the low energy excitations is well-known for very small x , where the CN ions are isolated rotators tunneling in the crystal field. Further work is currently in progress to clarify the nature of the high temperature anomaly.

1. K. H. Michel and J. M. Rowe, Phys. Rev. B22, 1417 (1980)
2. A. Loidl, R. Feile and K. Knorr, Phys. Rev. Lett. 48, 1263 (1982)
3. S. Bhattacharya, S. R. Nagel, L. Fleishman and S. Susman, Phys. Rev. Lett. 48, 1267 (1982)
4. F. Luty and J. Ortiz-Lopez, Phys. Rev. Lett. 50, 1289 (1983)

STRUCTURE OF ALKALI CYANIDE AND MIXED ALKALI CYANIDE-ALKALI HALIDE CRYSTALS

J. M. Rowe and J. J. Rush

and

S. Susman

(Argonne National Laboratory, Argonne, IL)

and

F. Luty

(University of Utah, Salt Lake City, UT)

During the past year, we have completed an extensive series of measurements on $(\text{KCN})_x(\text{KBr})_{1-x}$ with $x = 0.95, 0.90$ and 0.80 as functions of temperature using neutron powder diffraction. The data have been analysed by the method of total profile refinement. In each case, there is a phase transition as the temperature is reduced from the high temperature cubic phase to a monoclinic structure with space group Cc. This structure is related to the cubic one by a combination of E_g and T_{2g} strains with the T_{2g} strain ($e_4 + e_5$) being the largest. (The other strains are all less

than 1%).) No evidence of electric dipole ordering is observed in the monoclinic phase, even though both ferro and antiferro ordering are consistent with the symmetry of the Cc space group. For $x = 0.95$ and 0.90 , a further transition to the orthorhombic structure observed for pure KCN below 168 K is observed, but this transition does not go to completion, so that the low temperature diffraction pattern contains both monoclinic and orthorhombic peaks. The amount of orthorhombic phase present is greater for $x = 0.95$ than for $x = 0.90$, and no evidence for any orthorhombic component is observed for $x = 0.80$. That portion of the samples which did transform to an orthorhombic phase also transformed at lower temperatures to the antiferroelectric structure observed for pure KCN below 83 K. The lack of complete transformation to the orthorhombic structure probably arises from internal strains in the grains of the powdered samples which build up as the grains transform. This suggests that a large single crystal might not show any measurable amount of orthorhombic phase at all, thus explaining the total absence of any electric dipole ordering in such samples (note that as stated above, electric dipole order has never been observed in the monoclinic structure, even in pure RbCN as discussed below).

We have also measured the neutron diffraction patterns of pure RbCN as a function of temperature, and have analysed the results by the method of total profile refinement. The low temperature structure is analogous to that found for the mixed crystals, with space group Cc. However, the strains required to derive this structure from the high temperature cubic structure are somewhat larger, being of the order of 1% for the E_g strain and 6% for the T_{2g} strain. These strains are still considerably smaller than those required to derive an orthorhombic cell, and this may be the explanation for the fact that this structure is preferred both in the presence of the larger Rb ions and when there are defects present such as Br⁻ ions. Once again, no evidence for electric dipole ordering is found for temperatures as low as 4 K - the structure remains monoclinic with electric dipole disorder. These results present two problems requiring theoretical explanation - first, the effect of strain on the relative stability of the monoclinic and orthorhombic structures and second, the lack of electric dipole ordering in the monoclinic structure. With respect to the latter problem, it is likely that the transition temperature to an ordered state is so low that the dipole relaxation rate is too slow to allow the transition to take place. A calculation of this transition temperature using the measured structure would be very helpful in resolving this question.

Finally, in both the mixed crystals and pure RbCN, the orientation of the CN ion is along a direction close to a [301] axis in the original cubic cell, a result inconsistent with earlier assumptions that it would be close to a [111] axis of the original cubic cell.

CRITICAL BEHAVIOR AND MAGNETIC ORDERING IN AMORPHOUS TbFe₂

J. J. Rhyne and C. J. Glinka

The development of magnetic order in rapidly sputtered amorphous TbFe₂ and the response of the "ordered" magnetic state to an applied field has been studied using neutron small angle scattering techniques (SANS). The NBS area detector SANS facility was used for measurements over the scattering wave vector range ($0.014 < q < 0.14 \text{ \AA}^{-1}$) in zero field and in fields applied in an horizontal direction.

TbFe₂ is part of a class of rare earth amorphous magnetic alloys which exhibit large random crystal field anisotropy of comparable magnitude to the rare earth-iron exchange coupling. In such anisotropic random systems it has been shown¹ that the lower critical dimensionality is 4, and thus no phase transition to ferromagnetism exists except in the limit of vanishingly small anisotropy. Instead the transition to a spin frozen state is predicted to occur with a finite correlation length proportional to $(I/D)^2$, where I and D are the mean values of exchange and anisotropy interactions on the rare earth spins. This lack of critical divergence in the correlation length and the absence of a true long-range ferromagnetic state is confirmed in these results.

The zero field scattering above the magnetization-determined $T_c = 409 \text{ K}$ shows a conventional Lorentzian line shape with a spin correlation length which increases to about 135 \AA at and just below the bulk T_c . There is only a weak indication of a cusp in the scattering at fixed q in the vicinity of T_c ; rather below T_c the scattering continues to increase with decreasing temperature, finally saturating below about 40 K. The Lorentzian behavior observed above T_c gradually evolves into a power law dependence $I \sim q^{-n}$ with $n \sim 3.3$ for temperatures below about 300 K. This subcritical scattering can also be approximately represented by the sum of Lorentzian (L) and Lorentzian-squared (L²) terms as suggested for random field systems with large fluctuations [2]. Such behavior may be expected in TbFe₂ based on the analogy between random anisotropy systems and the random field problem of a 2d antiferromagnet in an applied field [3].

On application of a field in the range 2-12 kOe at 295 K, the overall scattering at finite q is sharply suppressed indicating an increase in the nearly ferromagnetic component with field. The residual magnetic scattering exhibits a prolate distortion of the intensity with respect to the direction of H which demonstrates that the remaining spin clusters do not exhibit a ferromagnetic response. The (L + L²) model well represents the q -dependence of the residual

scattering with the L₂ term becoming more dominant at higher H. This random fluctuation model yields an effective spin correlation length which drops from the 135 Å at H = 0 to less than 50 Å at 4 kOe and above. The correlation length also exhibits some low field hysteresis as shown in the figure.

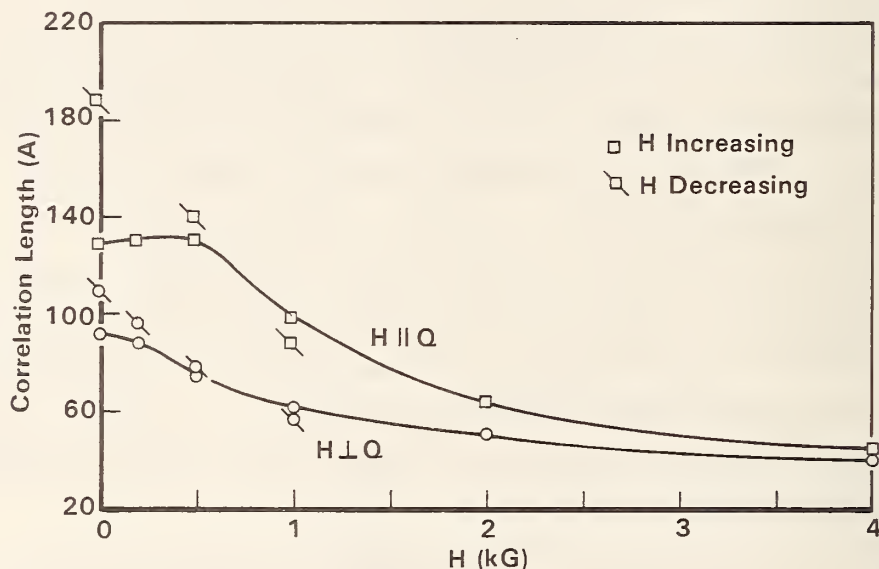


Figure 1. Field dependence of the effective spin correlation length below T_c as derived from a Lorentzian plus Lorentzian representation of the SANS data for TbFe₂ at 295K. Curves are shown for scattering in narrow sectors parallel and perpendicular to the applied magnetic field direction. Some hysteresis is indicated at the lower fields.

-
1. E. Pytte, Ordering in Strongly Fluctuating Condensed Matter Systems, Edited by T. Riste, Plenum Press, New York (1979), pp 445-452.
 2. H. S. Kogon, and D. J. Wallace, J. Phys A 14, L527 (1981).
 3. A. Aharony and E. Pytte, Phys Rev. B 27, 5872 (1983).

SHORT RANGE MAGNETIC ORDERING IN $Y_6(Fe_{1-x}Mn_x)_{23}$

J. J. Rhyne

and

K. Hardman-Rhyne
(Inorganic Materials Division)

$Y_6(Fe_{1-x}Mn_x)_{23}$ shows anomalous magnetic properties in the range approximately $0.4 < x < 0.75$. In particular the Curie temperature, as defined from magnetization data, vanishes in this region and the bulk magnetization tends toward 0 over the same range. Neutron diffraction and Mossbauer results¹ demonstrate conclusively that there is no long range magnetic order present in samples of these compositions.

To investigate the possibility of cluster or spin glass ordering occurring in this intermediate range, SANS experiments were carried out on $Y_6(Fe_{0.4}Mn_{0.6})_{23}$ from room temperature down to 10 K over a range of scattering vectors Q from $0.01 < Q < 0.2$ using the NBS area detector SANS facility. The scattering observed was isotropic in Q and very weak for all Q's and temperatures studied. The scattering integrated over the entire Q range showed less than a 10% increase from 250 K down to 10 K which clearly suggests that there is no tendency to form ferromagnetic spin clusters in $Y_6(Mn_{0.6}Fe_{0.4})_{23}$.

In contrast, antiferromagnetically ordered clusters will not contribute to the small angle scattering, but rather would be expected to produce broadened or diffuse peaks at angles corresponding to Bragg reflections (e.g. (100)) in a unit cell doubled in one or more directions. High resolution diffraction scans using a neutron wavelength of 2.4 Å on $Y_6(Fe_{0.4}Mn_{0.6})_{23}$ as well as $Y_6(Fe_{0.25}Mn_{0.75})_{23}$ showed strong evidence of antiferromagnetic short range cluster ordering in the form of short range order peaks appearing at the (100) superlattice reflection as shown in Figure 1. The occurrence of this reflection implies a doubling of the cell along one of the cubic edges with antiferromagnetic ordering along this direction.

The diffuse scattering is seen to be most intense for the $x = 0.6$ composition and to sharply die out in the $x = 0.4$ and $x = 0.8$ composition near the critical compositions for establishment of ferrimagnetic long-range order. The short range order peaks were found to be strongly temperature dependent essentially becoming unobservable in $Y_6(Fe_{0.4}Mn_{0.6})_{23}$ above about 150 K.

The average spin cluster size was determined by assuming the magnetic cluster scattering to be the magnetic analog of particle size broadening of nuclear peaks which yielded an average cluster size of 29 Å for the $x = 0.6$ and 0.75 compounds.

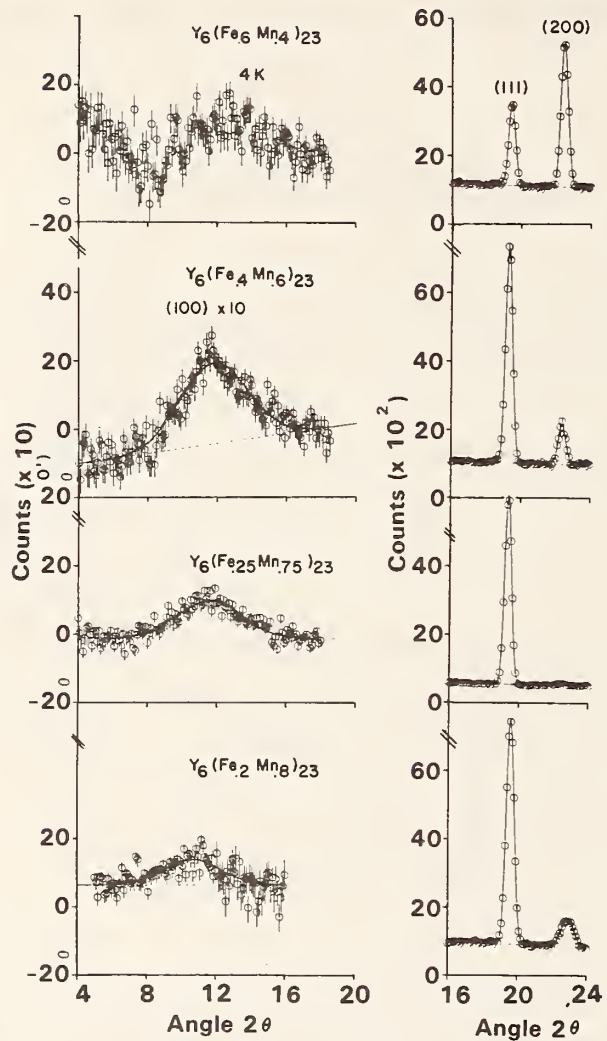


Figure 1. Diffuse (100) short range order peaks (left) observed for Mn compositions which exhibit no long-range magnetic order. The intensity is multiplied by a factor of 10 compared to the nuclear (111) and (200) peaks shown on the right. The diffuse scattering data are difference patterns between scans at 4 K and room temperature (above the temperature at which the short range order disappears). This subtraction eliminates background contributions and other extraneous scattering processes. The solid lines through the peaks are fitted Gaussian curves.

1. Gary J. Long, private communication (1983).

The widths for the other compositions were not considered sufficiently reliable for analysis due to their much weaker diffuse scattering.

The average Mn moment contributing to the cluster ordering was obtained by calculating the magnetic structure factor for the (100) reflection assuming that only Mn atoms contribute to the magnetic scattering and using the nonstoichiometric Mn occupancy factors of the 4 Mn sites. The Fe was assumed to be nonmagnetic as confirmed by the absence of an Fe hyperfine field from the Mossbauer spectra.¹ Assuming equal Mn moments on each site, the average Mn moment was found to be 1.4 Bohr magnetons in $\text{Y}_6(\text{Fe}_{.4}\text{Mn}_{.6})_{23}$.

These results suggest that the introduction of Mn moments into the iron rich ternary compounds leads to a breakdown of ferromagnetic order near $x = 0.3$ through exchange "frustration" produced by the Mn spins. This antiferromagnetic-ferromagnetic exchange competition leads to the formation of a spin-glass like state, and for still higher Mn concentrations, finally results in the establishment of Mn-Mn long-range ferrimagnetic order for $x \geq 0.8$ and greater.

DEUTERIUM SITE OCCUPATION AND MAGNETISM IN $\text{Ho}_6\text{Fe}_{23}\text{D}_x$ COMPOUNDS

J. J. Rhyne

and

K. Hardman-Rhyne
(Inorganic Materials Division)

and

H. Kevin Smith and W. E. Wallace
(University of Pittsburgh, PA)

High resolution neutron diffraction techniques have been used to establish the hydrogen (deuterium) site occupation and sublattice magnetization of a series of $\text{Ho}_6\text{Fe}_{23}\text{D}_x$ compounds. Four compounds were studied with nominal deuterium compositions of $x = 1.5, 8.2, 12.1$, and 15.7 .

The $\text{D}_{1.5}$ compound showed almost no lattice distortion from the pure $\text{Ho}_6\text{Fe}_{23}$ compound while higher compositions showed volume increases varying up to 10.4% for the $\text{D}_{15.7}$ compound. The fcc structure of the parent compound was maintained except for the $\text{D}_{12.1}$ sample which exhibited a tetragonal distortion with $c\sqrt{2} a = 1.030$. The fcc lattice was re-established for the higher $\text{D}_{15.7}$ composition. The diffraction data demonstrate conclusively that the D atoms in the $\text{D}_{1.5}$ material fully occupy the octahedral site with the residual in the tetrahedral f site.

This composition showed virtually no lattice expansion. At the $D_{8.2}$ level, the a site has become empty and the D atoms occupy the f_3 and j_1 tetrahedral sites only. At the $D_{15.7}$ composition, the D atoms occupy both a j_1 and j_2 site in addition to the f site, again with no occupancy of the a site. The tetragonal $D_{12.1}$ structure shows a full occupancy of tetrahedral n_3 sites and partial filling of m_1 , m_2 , l_1 , and l_2 tetrahedral sites.

The unusual depopulation of the a site in the higher concentration deuterides was also confirmed by inelastic scattering measurements of the deuterium vibrational frequencies using the Be filter analyzer of the BT-4 instrument at the NBSR. These data shown in Figure 1 showed a peak at the characteristic frequency for octahedral D in the $Ho_6Fe_{23}D_{1.5}$ and its absence in $Ho_6Fe_{23}D_{15.7}$. The latter compound showed strong peaks at frequencies characteristic of D in tetrahedral sites.

Magnetization measurements¹ show that the Curie temperatures increase from 510 K for Ho_6Fe_{23} up to 702 K for $Ho_6Fe_{23}D_{15.7}$. The neutron results for the individual sublattice magnetic moments showed that the 4 K Ho moment was near the free ion value of $10 \mu_B$ for all compounds, and oriented antiparallel to all four iron site moments (b, d, f_1 , and f_2). For the cubic materials the magnetization on the Fe sites varied

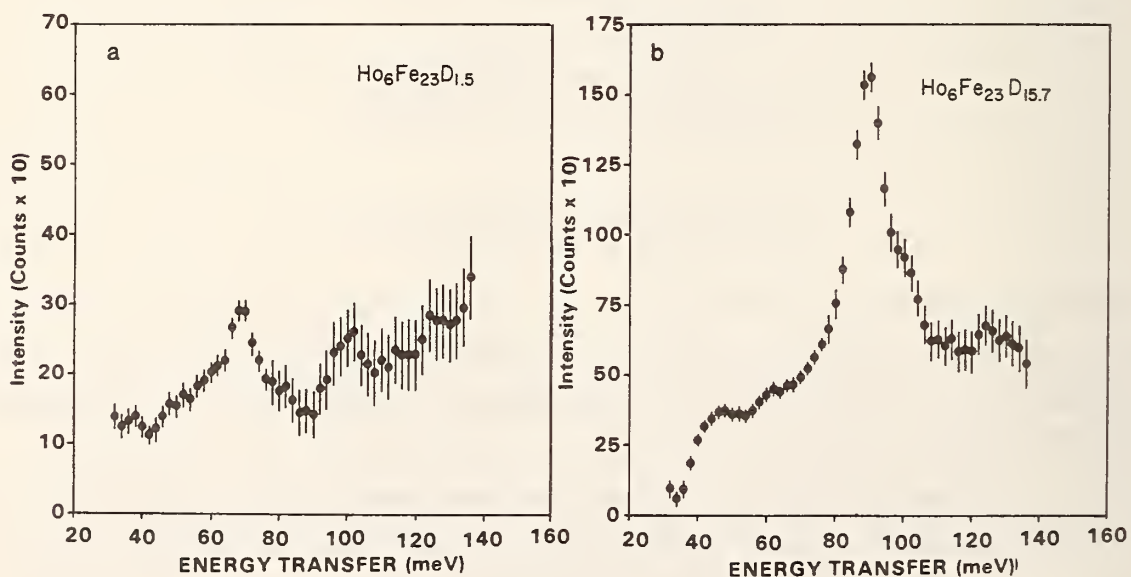


Figure 1: Inelastic scattering spectra of $Ho_6Fe_{23}D_{1.5}$ (left) and $Ho_6Fe_{23}D_{15.7}$ (right). The peak at 70 meV is indicative of D atoms in the octahedral a site, and is absent in the $D_{15.7}$ compound. The higher energy peak(s) (90-100 meV) reflect D atoms in tetrahedral sites.

with deuteration in the range 0.8 to 2.4 μ_B , with the $D_{15.7}$ compound showing the highest Fe moment for all sites.

In the tetragonal material a spin re-orientation was found to occur between room temperature and 4 K, with the Ho moment rotating from the basal plane up 45° out of the plane. The b and n_1 Fe site moments re-oriented antiparallel to the Ho atoms while the c, f, and n_2 site moments remained fixed in the base plane. A similar re-orientation may be expected to occur in the other compositions, but is undetectable by neutron scattering in a cubic structure.

- (1) A. T. Pedziwiatr, H. K. Smith, and W. E. Wallace, J. Solid State Chem. (to be published 1982)

SPIN DYNAMICS OF $Fe_{40}Ni_{40}P_{14}B_6$

J. W. Lynn
 (University of Maryland, College Park, MD)
 and
 (National Bureau of Standards, Washington, DC)
 and
 J.J. Rhyne

Small-angle inelastic neutron scattering techniques have been used to investigate the long wavelength spin dynamics in $Fe_{40}Ni_{40}P_{14}B_6$ (metglas^R). This is a structurally amorphous transition metal system which is produced by rapid quenching from the melt. Magnetically the system is locally (as well as globally) nearly perfectly isotropic, which has led to a number of commercial applications. From a fundamental point of view, the system represents the best-known isotropic ferromagnet, and thus it should prove to be an ideal candidate for a comprehensive study of the spin dynamics. As a first step in the process we have studied the nature of the long wavelength collective excitations below the Curie temperature ($T_c = 513K$).

Conventional spin wave theory predicts that the spin wave dispersion relation should be given by

$$E_{SW} = D(T)q^2 \quad (1)$$

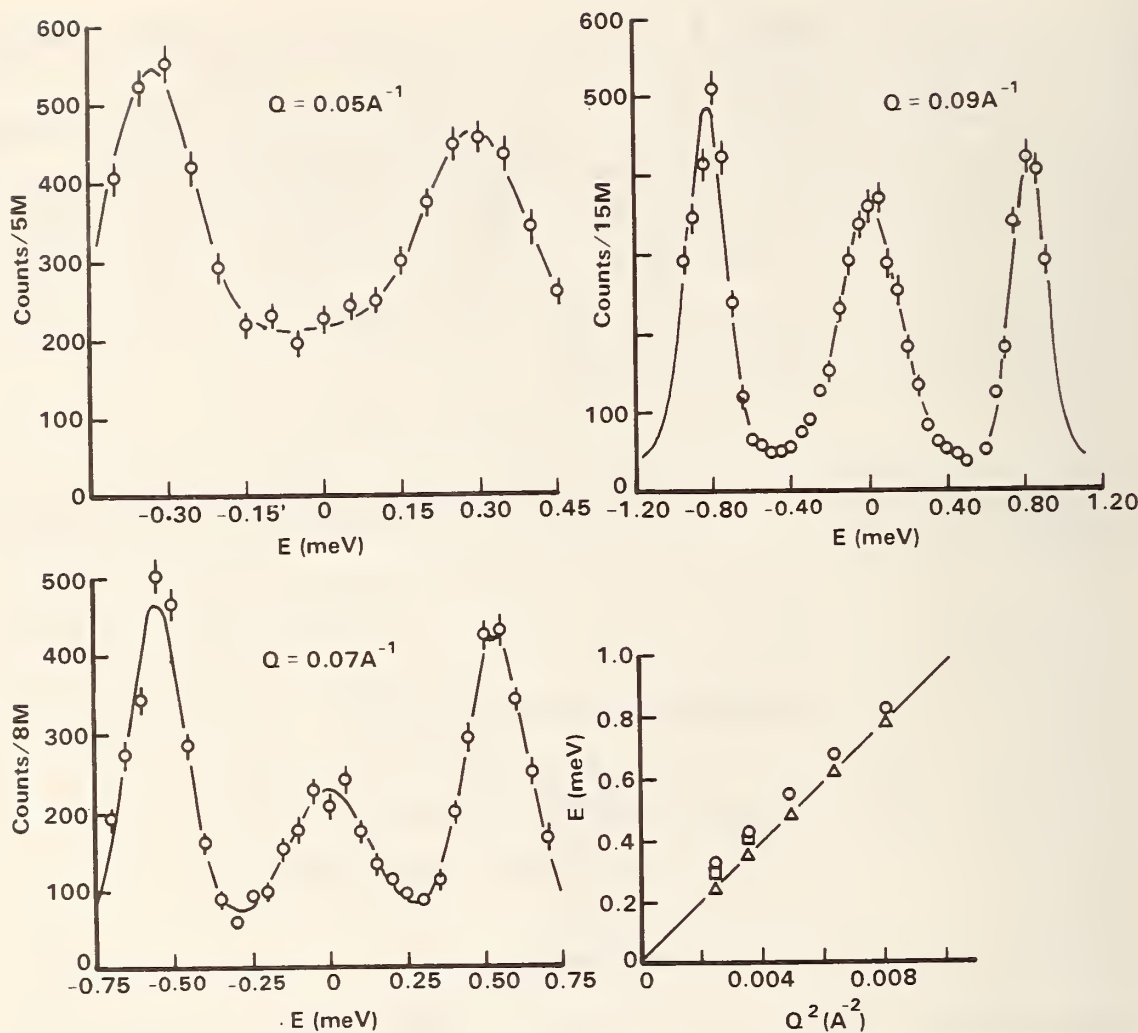


Figure 1. Small wave vector inelastic scattering for $\text{Fe}_{40}\text{Ni}_{40}\text{P}_{14}\text{B}_6$ observed at room temperature. The magnons are observed in neutron energy gain ($E < 0$) and energy loss ($E > 0$). The elastic peak is nonmagnetic scattering which originates from the sample and furnace. The dispersion relation for energy gain (circles) and energy loss (squares) is seen to be quadratic to a very good approximation after correction (triangles) for the instrumental resolution.

at sufficiently small wave vectors q . Any gap in the spectrum should be completely negligible in such an isotropic system. Indeed well defined spin waves are observed below T_c as shown in Figure 1. These data were taken at room temperature with a fixed incident energy of 13.7 meV, pyrolytic graphite monochromator, analyzer and filter, and 12' FWHM collimators before and after the monochromator and analyzer. The observed peaks for neutron energy gain ($E < 0$) and energy loss ($E > 0$) are due to the destruction and creation of magnons, respectively. The elastic peak originates from nuclear scattering from the sample and furnace. The solid curves are a least-squares

fit to a sum of three Gaussians, with the position of the central Gaussian fixed at $E = 0$ and the width fixed to the measured energy resolution of 0.33 meV. The observed widths of the spin waves are solely instrumental in origin at these low temperatures. Note that at small values of Q the data cannot be extended to larger energy transfers due to the restrictions imposed by conservation of neutron energy and momentum.

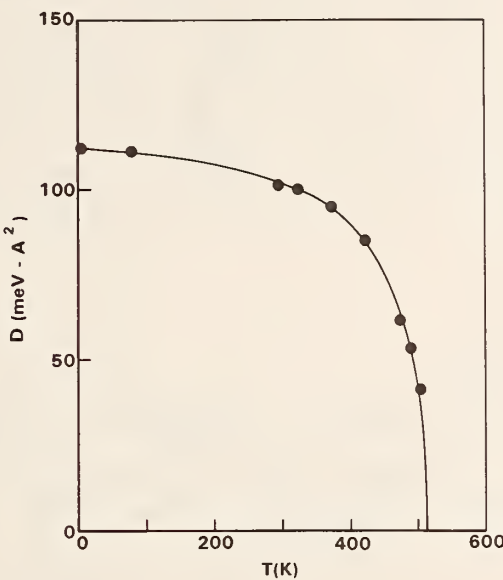


Figure 2. Temperature dependence of the spin wave stiffness constant.

The spin wave energies are also shown in Figure 1 as a function of the square of the wave vector. The open circles give the peak positions for energy gain and the squares give the peak positions for energy loss. The statistical accuracy for these data are smaller than the size of the points. There are significant corrections due to the effects of finite instrumental resolution, and the corrected data are shown by the triangles. These data are seen to obey equation 1 very well. The solid curve is a least-squares fit to a straight line, which yields a slope of $(97 \pm 3) \text{ meV} \cdot \text{\AA}^2$ at room temperature.

The stiffness coefficient D obtained from such data is shown in Figure 2 as a function of temperature. The renormalization of the spin wave dispersion relation is typical of isotropic ferromagnetic systems. Note that at room temperature D has attained 83 percent of the saturated low temperature value. Thus, we do not expect much change in the dynamic susceptibility in going from room temperature to low temperatures; the primary effect for the observed scattering will be due to the change in the thermal population of the magnetic excitations of the system. A

detailed study of the low temperature spin dynamics at large wave vectors is presently under way.

1. A number of experiments have shown that long-wavelength spin waves can be measured by neutron scattering in metallic glasses. The first measurements were made by J. D. Axe, L. Passell, and C. C. Tsuei, AIP Conf. Proc. 24, 119 (1975), and H. A. Mook, D. Pan, J. D. Axe, and L. Passell, AIP Conf. Proc. 24, 112 (1975). See also J. W. Lynn, G. Shirane, and R. J. Birgeneau, AIP Conf. Proc. 34, 313 (1976); J. D. Axe, G. Shirane, T. Mizoguchi, and K. Yamauchi, Phys. Rev. B15, 2763 (1977); R. J. Birgeneau, J. A. Tarvin, G. Shirane, E. N. Gyorgy, R. C. Sherwood, H. S. Chen, and C. L. Chien, Phys. Rev. B18, 2192 (1978); J. J. Rhyne, J. W. Lynn, F. E. Luborsky, and J. L. Walter, J. Appl. Phys. 50, 1583 (1979); and references therein.

REENTRANT SPIN GLASS BEHAVIOR IN AMORPHOUS $(\text{Fe}_{x}\text{Ni}_{100-x})_{75}\text{G1}_{25}$

J. W. Lynn and R. W. Erwin
 (University of Maryland, College Park, MD)
 and
 (National Bureau of Standards, Washington, DC)
 and
 J. J. Rhyne
 and
 H. S. Chen
 (Bell Laboratories, Murray Hill, NJ)

Within the concentration range $17 \leq x \leq 40$, members of this amorphous alloy system exhibit a ferromagnetic (FM) phase transition followed at lower temperatures by spin glass (SG) phenomena. These phenomena include: field sensitive reductions in d.c. magnetization,¹ increased a.c. susceptibility and hysteresis,² enhanced spin resonance line widths,³ and the collapse and damping of the spin wave excitations. The last of these we have pursued with neutron scattering studies to investigate the dynamics of the system as the SG state is approached.

Results for $x = 40$ and 30 were previously reported,⁴ with the lower concentration showing the more dramatic change in the spin wave spectra. Concomitant with the spin wave collapse for $x = 30$ is the growth of a resolution-limited elastic component to the scattering which was identified with the formation of a spin frozen state. The spins are frozen on a time scale of at least 10^{-18} sec. as determined by an upper limit to any intrinsic linewidth of the elastic scattering.⁵ It was

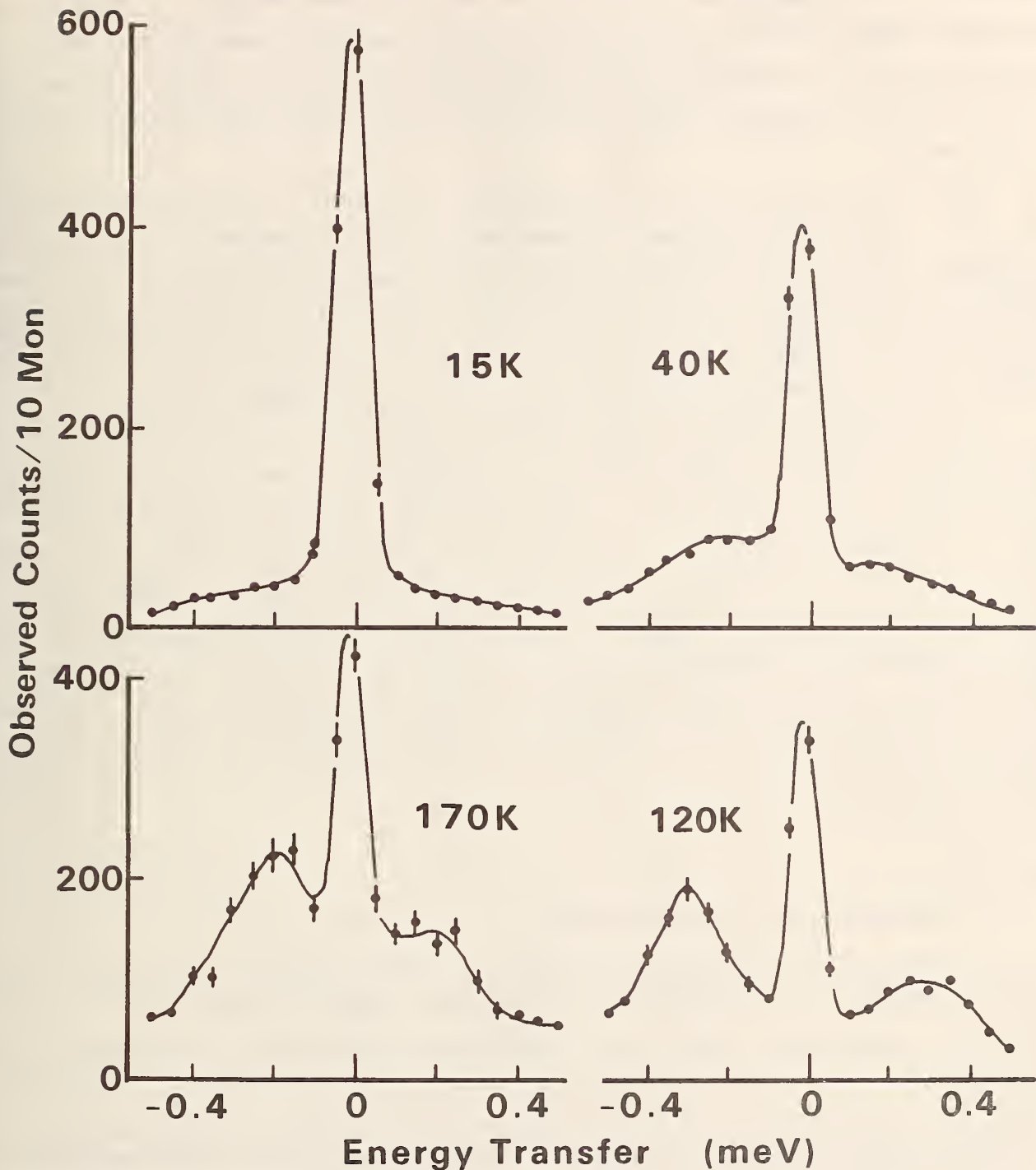


Figure 1. Observed spectra for $(\text{Fe}_{25}\text{Ni}_{75})_{75}\text{G1}_{25}$ at $Q = 0.10 \text{ \AA}^{-1}$, showing that the spin wave energies increase and then decrease as the temperature is lowered. No distinct excitations are observable at 15K. The asymmetries are due to instrumental resolution and thermal population effects. The solid lines are guides to the eye.

possible to identify distinct peaks in the inelastic spectrum down to about 10K, with the energy widths indicating that the excitations are overdamped for $T < 10K$. Since in addition the d.c. magnetization was not observed to vanish down to 4K, while the SG order parameter appeared above 20K, the conclusion was drawn that the FM and SG states coexist.

Our recent results for $x = 25$ are shown in Figure 1. Below T_c ($= 197K$) the spin wave energies renormalize to higher energy down to 80K and then decrease again below 80K. Below $\epsilon \sim 40K$, the spectrum has become completely diffusive. This suggests that the FM state has been destroyed and d.c. magnetization measurements¹ support this conclusion. Again, a purely elastic component to the scattering is observed, which is identified as the freezing of spins into a spin glass state.

An irreversible component of the magnetization has also been observed¹. Both components of the bulk magnetization are extremely field sensitive. For example, in fields of only a few gauss, the d.c. magnetization is maintained and the irreversible part is no longer evident. This sensitivity appears to be absent in the neutron results which are, of course, observations on a much shorter length scale. In particular, it requires kilogauss fields to alter the spin wave spectra and to destroy the elastic component of the scattering. It may be that the field sensitivity in the SG state is provided by only the largest clusters. This length scale may be accessible to small angle neutron scattering and such studies are presently under way.

1. S. M. Bhagat et al., to be published.
2. S. M. Bhagat, J. A. Geuhegan, and H. S. Chen, Sol. St. Commun. 36, 1 (1980); J. A. Geohegan and S. M. Bhagat, J. Magn. Mater. 25, 17 (1981).
3. S. M. Bhagat, M. L. Spano, K. V. Rao, and H. S. Chen, Solid State Comm. 33, 303 (1980).
4. J. W. Lynn, R. W. Erwin, J. J. Rhyne, and H. S. Chen, J. Appl. Phys. 52, 1738 (1981); J. W. Lynn, R. W. Erwin, J. J. Rhyne, and H. S. Chen, NBS Technical Note 1178, 93 (1983).
5. A. Magerl, private communication.

SPIN DYNAMICS OF DILUTE $Pd_{1-x}Fe_x$ FERROMAGNETS

J. A. Gotaas and J. W. Lynn
 (University of Maryland, College Park, MD)
 and
 (National Bureau of Standards, Washington, DC)

and

N. C. Koon
 (Naval Research Laboratory, Washington, DC)

A great deal of attention has been focussed on the addition of magnetic impurities (such as Fe, Co, or Ni) to "exchange-enhanced" paramagnetic metals such as Pd and Pt, due to the resulting formation of giant-moment clusters.¹ In the case of dilute $Pd_{1-x}Fe_x$ alloys, the magnetic Fe atom possesses a moment of $\sim 3\text{-}4 \mu_B$, but the polarization of the Pd d-band leads to a total moment of $\sim 10 \mu_B$ per Fe atom, with the polarization cloud extending $\sim 10 \text{\AA}$. For very dilute concentrations ($x \ll 0.001$), where the giant-moment clusters are effectively isolated from each other, the system seems to become a spin-glass at low temperatures. At higher concentrations ($x > 0.001$) a ferromagnetic state occurs.

The critical concentration for the existence of a ferromagnetic state is $x_p = 0.0012$, but a relatively uniform ferromagnetic state is not achieved until $x > 0.03$. In the intermediate dilute ferromagnetic regime, it is expected that the magnetic excitations (at least for small wave vectors) are more or less conventional spin waves. Such spin wave excitations have been observed using inelastic neutron scattering in both chemically ordered and disordered Pd_3Fe , but in the dilute ferromagnetic regime only indirect evidence had existed, based upon the neutron diffraction technique, bulk magnetization, and specific heat measurements.

Earlier measurements of spin waves in polycrystalline $Pd_{.985}Fe_{.015}$ ² using inelastic neutron scattering about the forward (000) scattering direction have been extended to the additional concentrations $x = 0.01$ and 0.02 and to lower temperatures. For both $x = 0.015$ and 0.020 , reasonably well-defined spin waves have been observed below the respective Curie temperatures of 57 K and 78 K. The observed spin wave dispersion is consistent with the quadratic relation $E = DQ^2$ expected for an isotropic ferromagnet, with $D = 60 \text{ meV\AA}^2$ ($x = 0.015$) and 80 meV\AA^2 ($x = 0.020$) at low temperatures. For $x = 0.010$, inelastic scattering was observed below the Curie temperature of 38 K, but the "spin wave" linewidths in the accessible wave vector range were too large to obtain meaningful information about spin wave energies or dispersion. There are indications that inhomogeneities in the polycrystalline sample may have contributed to the linewidth broadening, and further work is under way to investigate this.

-
1. G. J. Nieuwenhuys, Adv. Phys. 24, 515 (1975).
 2. J. W. Lynn, J. J. Rhyne, and J. I. Budnick, J. Appl. Phys. 53, 1982 (1982).

MAGNETIC PHASE TRANSITION IN THE SUPERCONDUCTOR HoMo_6Se_8

J. W. Lynn, J. A. Gotaas and R. W. Erwin
 (University of Maryland, College Park, MD)
 and
 (National Bureau of Standards, Washington, DC)
 and
 R. N. Shelton and P. Klavins
 (Ames Laboratory, Ames, IA)
 and
 (Iowa State University, Ames, IA)

Neutron scattering experiments have been carried out to investigate the magnetic properties of the superconductor ($T_c = 5.6\text{K}$) HoMo_6Se_8 . Bragg scattering as a function of magnetic field shows that the saturated magnetic moment is reduced to $6 \mu_B$ by crystal field effects. Thus in comparison to the related ferromagnetic-superconductor¹ HoMo_6S_8 ($T_c = 1.8\text{K}$, $\mu = 9.1\mu_B$) the superconducting state is stronger and the magnetic properties are weaker, which could lead to a more equitable competition between these two cooperative phenomena if the system prefers parallel alignment. Figure 1 shows that this is indeed the case; a long range ordered sinusoidal magnetic state forms at low temperatures. The characteristic wavelength of this state is $\sim 100\text{\AA}$ with the superconducting state surviving (in zero field) the magnetic ordering.

Figure 2 shows the temperature dependence of the integrated intensity (related to the square of the order parameter) as well as the characteristic wave vector q_0 as a function of temperature. The wave vector is seen to be strongly temperature dependent in contrast to the behavior of HoMo_6S_8 ¹ or ErRh_4B_4 ². The intensity analysis of the scattering indicates that the full holmium moment available in the crystal-field ground state has ordered at low temperatures.

The origin of the temperature dependence of q_0 is not yet known conclusively. Theoretically³ a linearly polarized state yields a periodicity whose temperature dependence is qualitatively the same as that observed, but such a state requires a very large anisotropy to make it energetically favorable over other possible states. The expected periodicity for the spontaneous vortex state is in the opposite direction to that observed. A spiral state, which is the type of magnetic state

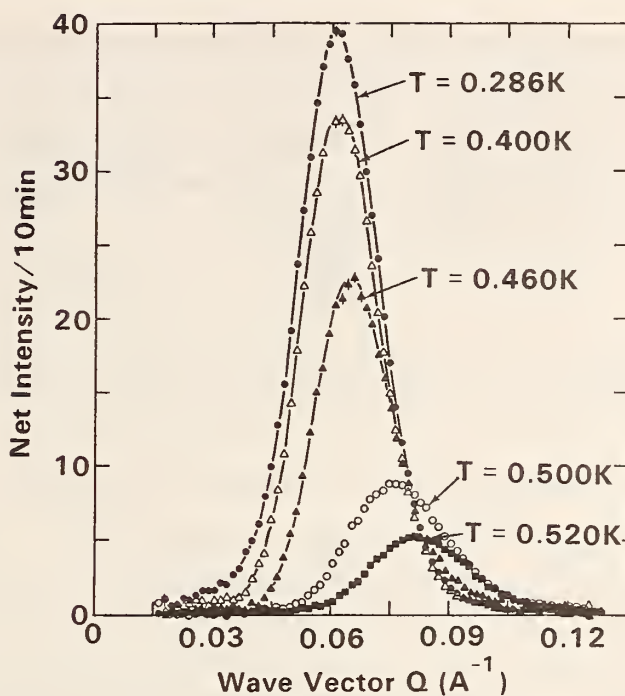


Figure 1. Intensity as a function of wave vector at several temperatures, showing the intensity and wave-vector dependence of the Bragg peak in the oscillatory magnetic state. These data were taken on the small-angle neutron spectrometer (SANS).

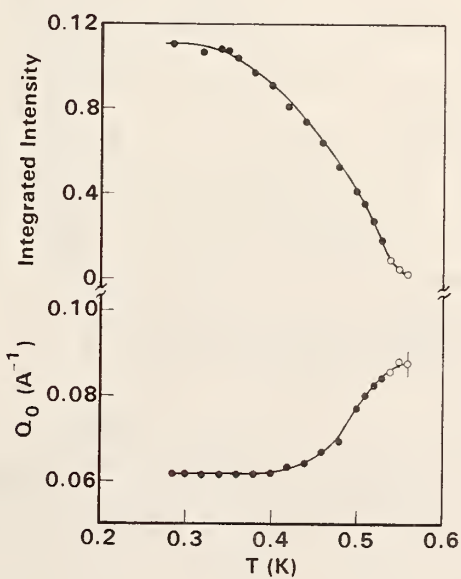


Figure 2. Temperature dependence of the integrated intensity and wave vector q_0 . The full Ho moment has ordered at low temperatures.

expected for an isotropic system, has a predicted periodicity with little temperature dependence. However it is possible that the superconducting parameters themselves renormalize during the development of magnetic order and this renormalization could produce the temperature dependence of q_0 . Further theoretical work will be needed in order to determine if this is indeed the case.

1. J. W. Lynn, G. Shirane, W. Thomlinson, R. N. Shelton and D. E. Moncton, Phys Rev B24, 3817 (1981).
2. S. K. Sinha, G. W. Crabtree, D. G. Hinks and H. Mook, Phys Rev Lett 48, 950 (1982)
3. H. S. Greenside, E. I. Blount and C. M. Varma, Phys Rev Lett 46, 49 (1981)

MAGNETIC AND SUPERCONDUCTING PROPERTIES OF HO RICH $(Er_{1-x}Ho_x)Rh_4B_4$

J. W. Lynn and J. A. Gotaas
 (University of Maryland, College Park, MD)
 and
 (National Bureau of Standards, Washington, DC)
 and
 R. N. Shelton
 (Ames Laboratory, Ames, IA)
 and
 (Iowa State University, Ames, IA)

Neutron scattering, susceptibility, and resistivity measurements have been carried out on $(Er_{1-x}Ho_x)Rh_4B_4$ for $x = 1.0, 0.89, 0.84$, and 0.75 , which span the "multicritical" point ($x_c \sim 0.9$) where the magnetic and superconducting phase boundaries meet.¹ For all concentrations studied, a transition to long range ferromagnetic order is observed, with the Ho moments ordering along the tetragonal axis. The holmium spins are in fact locked along the c-axis by large crystal-field anisotropies, yielding Ising-like magnetic behavior in this concentration region. The temperature dependence of the order parameter is in fact mean-field like to a good approximation, suggesting that the range of the magnetic interactions is large.

For $x > x_c$, no superconducting state is observed, whereas for $x < x_c$ superconductivity is present over a temperature interval $T_{c2} < T < T_{c1}$ as shown in Figure 1. The superconducting transitions have been determined by both a.c. susceptibility and resistivity on the identical samples used for the neutron

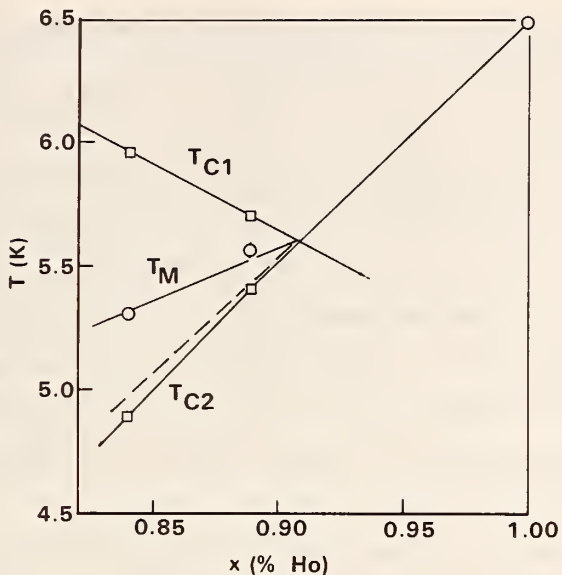


Figure 1. Measured transition temperatures as a function of holmium concentration x . T_{c1} is the upper superconducting transition, T_{c2} is the lower (reentrant) superconducting transition, and T_M is the ferromagnetic transition.

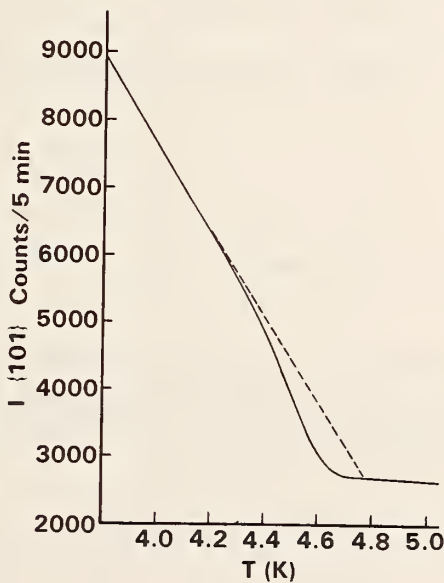


Figure 2. Ferromagnetic intensity (which is proportional to the square of the magnetization) for $x = 0.75$. The dashed line is the expected intensity in the absence of superconductivity.

measurements. The ferromagnetic transitions, as measured by neutron magnetic Bragg scattering, appear to be continuous and reversible and occur within the region of superconductivity for $x \leq x_c$. Thus, there is some kind of "coexistence" of ferromagnetism and superconductivity in these samples. The nature of this coexistence, however, cannot be determined unambiguously. In particular the experimental evidence in this system is not sufficient to decide if there is true microscopic coexistence, or whether some portions of the sample are ferromagnetic and normal while other regions are superconducting and paramagnetic (macroscopic coexistence). No evidence for an oscillatory component of the magnetization was observed for any concentration or temperature, in contrast to the behavior² of ErRh_4B_4 .

At the lowest concentration studied ($x = 0.75$), the magnetization was found to be reduced in magnitude from the value expected in the temperature region where superconductivity appears as shown in Figure 2. The intensity (which is proportional to the square of the magnetization) was found to be continuous and reversible, as was the case at the higher holmium concentrations. The noteworthy point here is that an analogous suppression was not found at higher x . A similar suppression has been observed³ at $x = 0.6$, accompanied by hysteresis in the ferromagnetic state at low temperatures (and not in the "mixed" ferromagnetic-superconducting region). No hysteresis was observed in the present measurements at any temperature or concentration.

-
1. H. B. MacKay, L. D. Woolf, M. B. Maple, and D. C. Johnston, Phys. Rev. Lett. 42, 918 (1979).
 2. D. E. Moncton, D. B. McWhan, P. H. Schmidt, G. Shirane, W. Thominson, M. B. Maple, H. B. MacKay, L. D. Woolf, Z. Fisk, and D. C. Johnston, Phys. Rev. Lett. 45, 2060 (1981); S. K. Sinha, G. W. Crabtree, D. G. Hinks, and H. Mook, Phys. Rev. Lett. 48, 950 (1982).
 3. H. A. Mook, W. C. Koehler, M. B. Maple, Z. Fisk, D. C. Johnston, and L. D. Woolf, Phys. Rev. B25, 372 (1982).

CRITICAL FLUCTUATIONS IN THE FERROMAGNETIC SUPERCONDUCTOR HoMo_6S_8

J. W. Lynn, J. A. Gotaas, and R. W. Erwin
 (University of Maryland, College Park, MD)

and
 (National Bureau of Standards, Washington, DC)

HoMo_6S_8 becomes superconducting at $T_{c1} = 1.82$ K, and reenters the normal conducting state at $T_{c2} \sim 0.64$ K due to the establishment of ferromagnetic order.^{1, 2} Above this first order reentrant transition, the competition between ferromagnetism and superconductivity gives rise to an oscillatory magnetic state ($T_{os} = 0.728$ K) with a wavelength of 200 Å. We have recently constructed a He^3 refrigerator with high temperature-stability ($\pm 10 \mu\text{K}$) which we have used to study the critical dynamics and order parameter of this oscillatory magnetic phase. The data were taken on the small angle scattering facility (SANS).

In the absence of an applied magnetic field, the (powder) scattering is symmetric about the forward beam direction, and the data were therefore averaged radially. Figure 1 shows the wave vector dependence of the scattering at a series of temperatures (on cooling). These data were taken with a neutron wavelength of 8.0 Å in the "coarse" resolution mode. Data were collected at temperature intervals of 2.5 mK. For $T \geq 0.740$ K there was no structure evident in the scattering, with the intensity distribution being consistent with a correlation function of the Ornstein-Zernike form. With decreasing temperature, a peak develops at $Q_o \sim 0.03 \text{ \AA}^{-1}$ whose intensity and width are strongly temperature dependent. We have analyzed these data assuming that there are two magnetic components to the scattering, the peak at Q_o , and a broad distribution of scattering. The solid curves are least squares fit to a Gaussian peak plus a linear (sloping) background, which gave a satisfactory fit to the data over the temperature region of interest. From this analysis, we found that the broad component to the scattering did not vary significantly with temperature, while the width of the peak became resolution limited for $T \leq 0.7275$ K. The position Q_o was essentially temperature independent while the amplitude was strongly temperature dependent as shown in Figure 2. For temperatures below 0.700 K, a first-order transition from the oscillatory - superconducting state to the ferromagnetic - normal state takes place. The ferromagnetic state introduces an intense small-q component to the scattering which quickly dominates the scattering near Q_o . At sufficiently low temperatures, $T < 0.61$ K, the entire sample reverts to the normal conducting state, with a conventional ferromagnetic state present.

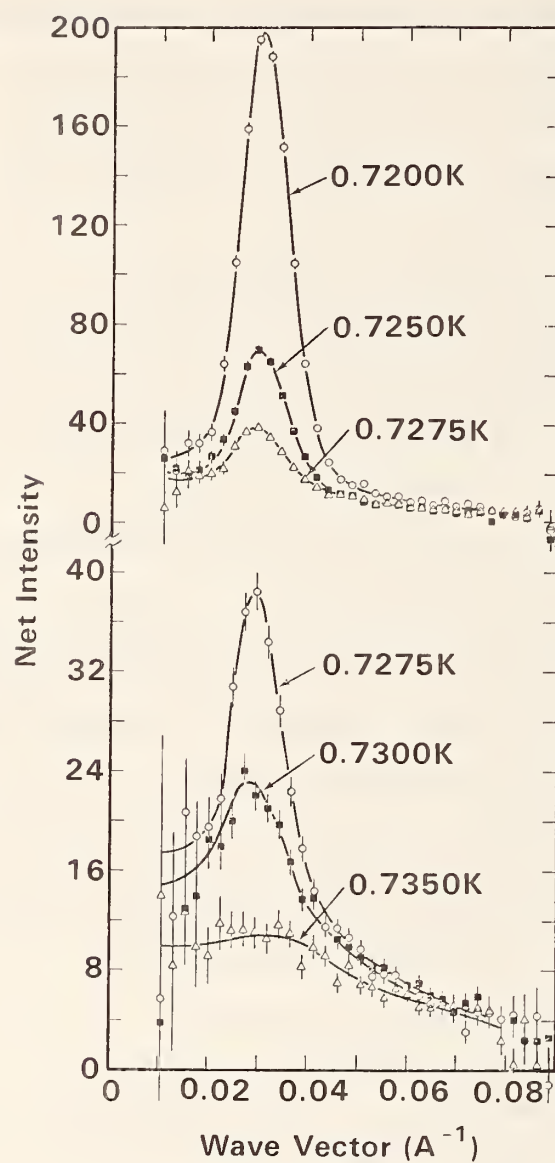


Figure 1. Intensity distribution as a function of wave vector for several temperatures.

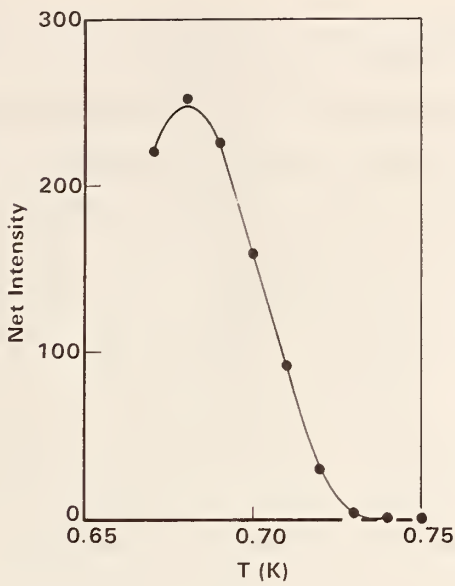


Figure 2. Intensity vs. temperature at Q_0 .

1. J. W. Lynn, G. Shirane, W. Thomlinson, R. N. Shelton, and D. E. Moncton, Phys. Rev. B24, 3817 (1981) and references therein.
2. J. W. Lynn, R. Pynn, J. Joffrin, J. L. Ragazzoni, and R. N. Shelton, Phys. Rev. B27, 581 (1983).

ADVANCED NEUTRON METHODS

N. Berk, D. Fravel, C. J. Glinka, J. LaRock, and J. M. Rowe

1. Small Angle Neutron Scattering (SANS)

The SANS facility operated nearly trouble free over the past year with less than 5 percent of the available beam time lost due to instrument down time. During this period efforts have continued to improve the capabilities of the facility and to make it easier to use. For example, a modified version of the converging beam collimation system used for high-resolution measurements is now being built which is designed to be free of any trace of parasitic scattering from the edges of the beam collimating masks. In addition, the new collimating masks will be equipped with quick coupling flanges to enable users to change from pinhole collimation to converging beam collimation in a few minutes. A temperature controlled tube furnace has been designed for the SANS instrument (by E. Case, U. of California and the Inorganic Materials Division) for the study of ceramic specimens at temperatures up

to 1200 °C either under vacuum or in a controlled gas environment. For studies of magnetic phenomena at low temperatures, a cryostat has been adapted to mount between the pole faces of a large electromagnet to enable scattering measurements to be made at temperatures down to 4K in fields up to 10 kilogauss. The addition of a floating point accelerator and a higher density disk drive have substantially increased the computing speed and storage capacity of the instrument's data acquisition computer. These improvements are essential for future real-time studies and will enable some elementary data reduction and analysis to be done directly at the instrument.

Computer software for the reduction and analysis of SANS data has also been expanded and made more user friendly. Detailed calculations of the instrumental resolution have been carried out by N. Berk and incorporated into a program which enables users to readily assess the effects of instrumental smearing on the shape of an arbitrary scattering function. These calculations will be included in a generalized least-squares fitting routine for fitting model functions to SANS data. An extensive and extremely versatile data fitting and plotting package, developed by the Center for Applied Mathematics, called DATAPLOT is now running on the VAX data reduction computer and is being widely used for curve fitting and plotting. Documentation for much of the SANS software is now stored on the computer and can be readily accessed by a user at a video terminal as needed.

In the past year more than ninety individual experiments were performed comprising roughly forty distinct research problems. These experiments involved the active participation of scientists from six NBS divisions, more than fifteen universities, and approximately six industrial and government laboratories. The bulk of this work can be broadly classified as either microstructural studies of metallic or ceramic materials, measurements of molecular conformation of polymers and biomaterials, or studies of magnetic correlations in novel magnetic materials.

Studies in the area of metallurgy have included, for example, the extension of initial measurements of creep cavitation in stainless steel (by S. Singhal and R. Fields) to a wider range of aging times and stress states in an effort to quantify the effects of these two parameters on the production of cavities. In a related study, M. Fatemi (Naval Research Laboratory) has measured the sizes of small voids in hydrogen charged steels and J. Weertman (Northwestern Univ.) has measured the scattering from carbides in ferritic steels in order to determine the volume fraction and carbide size distribution produced by various heat treatments.

A new program has developed in collaboration with the Inorganic Materials Division (involving N. Berk, K. Rhyne of IMD, and E. Case, U. of California) to study the evolution of the porous microstructure in selected ceramic materials from the

prefired, so-called green, state through various stages of sintering to the final densified product. One aim of this effort is to determine whether SANS can be useful for detecting defects (agglomerated particles, cavities, etc.) in the green state which can affect the mechanical properties of the sintered materials. SANS measurements are also being carried out (by L. Sander, Center for Analytical Chemistry) to obtain quantitative information on the pore structure of chemical adsorbents used, for example, in chromatography. Here absolute intensity measurements are being made to determine the specific pore surface area and pore volume fraction of several types of porous silica.

SANS studies on magnetic materials have ranged from detailed measurements (by J. Lynn and J. Gotaas, U. of Maryland) of the development of long-range oscillatory magnetic ordering in the magnetic superconductors HoMo_6S_8 and HoMo_6Se_8 , to the study of single domain magnetic particles in ferrofluids (C. Glinka and D. Chung, Howard Univ.). Other experiments have focused on the finite ranged magnetic correlations which develop in spin glasses.

Some of the work mentioned above is discussed in greater detail in other articles in this report.

2. Time-of-Flight Spectrometer (TOF)

A complete redesign and rebuilding of this facility was begun during the past year. The existing instrument has been used in studies of H in metals, of molecules on catalytic surfaces, and of molecular reorientation in solids. However, a number of problems with the current configuration have been noticed in these experiments, which will be addressed in the new design. We have completed the detailed design of a new horizontal flight path which will be evacuated, and a contract has been let for construction of this component. In addition, the electronics used for both neutron detection and chopper control have been replaced. A new monochromator mechanism and shield which will allow more flexibility in resolution and achieve higher intensity on the sample has been designed, and is presently under construction. This entire project is scheduled for completion within the next year, and will be installed during the shutdown for the reactor upgrade for 20 MW operation. In the meantime, the present facility is still being used for some experiments.

SMALL ANGLE SCATTERING FROM FERROFLUIDS

C. J. Glinka

and

D. Y. Chung
(Howard University, Washington, DC)

Ferrofluids consist of small ($\sim 100 \text{ \AA}$), single-domain particles of ferromagnetic material suspended in a carrier liquid. These magnetic fluids are used in a wide range of technological applications which depend to a large degree on the magnetic particles remaining in suspension in the presence of strong magnetic fields and field gradients. Important to the stability, and hence the performance, of ferrofluids are the sizes and shapes of the particles and the interactions between them. Because neutrons can be scattered both by interactions with the atomic nuclei in the particles and by interactions between the neutron's magnetic moment and the particles' magnetic moments, small angle neutron scattering (SANS) is a particularly powerful technique for examining both the physical structure and magnetic correlations in ferrofluids.

SANS measurements have been initiated on a commercial water-based ferrofluid (Georgia Pacific Lignosite FML) which consists of particles of magnetite, Fe_3O_4 , coated with a polymer (lignosulfonate) which acts as the dispersing agent. This fluid has a nominal bulk saturation magnetization of 140 gauss which, compared to bulk magnetite, would imply a volume fraction of magnetic particles of about 2.3 percent. The low-Q portion of a SANS pattern for this fluid measured in zero magnetic field is shown in Figure 1. Although a detailed analysis of this scattering is complicated by the presence of three phases in the system (magnetite, polymer and water), the overall shape of the curve is indicative of a broad range of particle sizes ranging up to 300 \AA in diameter.

Data were also taken in a magnetic field of 1 kilogauss which is more than sufficient to saturate the magnetization of the sample. In an applied field the observed intensity is the sum of nuclear and magnetic contributions

$$I(Q, H) = I_N(Q, H) + (1 - \cos^2 \phi) I_M(Q, H) \quad (1)$$

where ϕ is the angle between the scattering vector Q and the direction of the applied field H . The nuclear, $I_N(Q, H)$, and magnetic, $I_M(Q, H)$, contributions to the anisotropic scattering observed for $H = 1$ kilogauss are also shown in Figure 1 and are seen to be quite different at the smaller Q values.

In the absence of an applied field, the scattering is isotropic and given by

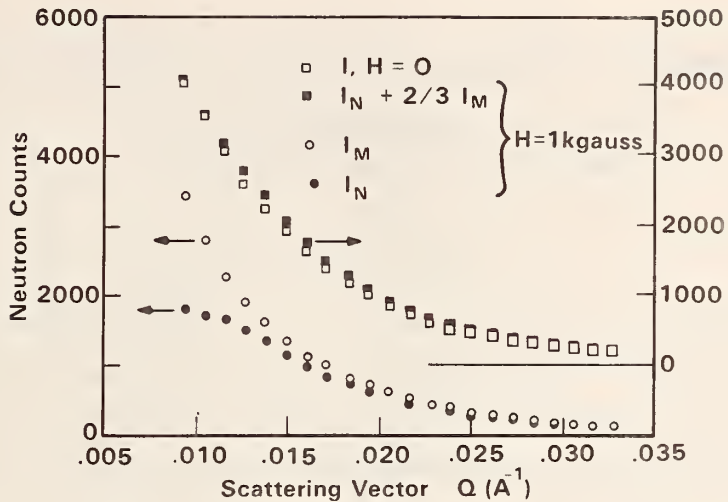


Figure 1. Comparison of the small angle scattering from a commercial ferrofluid observed in zero magnetic field and in a field on 1 kilogauss. The open squares are the zero field data and the open and filled circles are the magnetic and nuclear contribution, respectively, to the scattering in the applied field. The filled squares are the "reconstructed" zero field data obtained from the weighted sum, $I_N + 2/3 I_M$, of the nuclear and magnetic contributions to the applied field data.

$$I(Q, 0) = I_N(Q, 0) + 2/3 I_M(Q, 0) \quad (2)$$

where the $(1 - \cos^2 \phi)$ term in equation (1) takes on the value $2/3$ owing to the random orientations of the magnetic moments of the particles. To compare the 1 kilogauss data with the zero field data the components I_N and I_M derived from the anisotropic scattering were added in the ratio 1:2/3, respectively. Figure 1 shows that, treated in this way, the applied field data (filled squares) closely follow the observed zero field scattering (open squares). This implies that the primary effect of the field is simply to align the particle moments and not to produce any significant degree of particle aggregation, which would change the shape of the scattering curve.

These preliminary SANS results are consistent with ultrasonic measurements which indicate that Lignosite FML is a particularly stable type of water-based ferrofluid. In future SANS measurements, different types of ferrofluids will be compared and higher concentrations will be studied in an effort to observe interparticle interaction effects.

CHARACTERIZING MICROPOROSITY OF CHEMICAL ADSORBENTS BY SMALL ANGLE NEUTRON SCATTERING

Lane Sander
(Analytical Chemistry Division)

and

C. J. Glinka

The performance of microporous adsorbents used, for example, for chemical separation in liquid chromatography depends critically on parameters such as the specific surface area, specific pore volume, and mean pore diameter which characterize the pore structure of the material. For pore sizes ranging from roughly 20 Å to 1000 Å, small angle neutron scattering (SANS) can in principle provide values, on an absolute scale, for all of these important parameters. Moreover, in contrast to techniques such as mercury porosimetry or gas adsorption measurements, in which either the physical structure or chemical purity of the specimen may be altered, SANS is a completely nonintrusive technique and thus cannot affect the properties or performance of the adsorbent.

Our initial SANS measurements have focused on determining the specific surface area of pores in a number of commercial fine powders of porous silica. The 5-10 micron sized particle in these powders consist of submicron, nonporous silica beads which have been partially sintered to produce mechanically stable structures. The size, shape and packing arrangement of the nonporous beads determine the pore structure of the aggregate particles. The scattered intensity from such a sharply defined, two-phase system (silica and voids) is proportional to the total pore surface area in the large Q limit of the scattering pattern where Porod law behavior, $I \propto Q^{-4}$, is expected. Thus by making absolute measurements of the scattering in the Porod region, the pore surface area can be obtained directly.

For most of the porous silica samples studied to date, a well defined Porod region is observed in the scattering. An example is shown in Figure 1 where the measured intensity, multiplied by Q^4 , from a specimen with a nominal pore diameter of 300 Å is plotted versus Q^4 (Porod plot). On this type of plot, data in the Porod region lie on a straight line. The data in Figure 1 were put on an absolute scale by reference to the isotropic incoherent scattering from vanadium measured under identical conditions. The resulting specific surface area for this specimen was $50 \text{ m}^2/\text{gm}$ with an estimated uncertainty of about 10 percent.

Further measurements and analysis are planned in an effort to completely characterize the pore structure of various types of porous silica. In some cases,

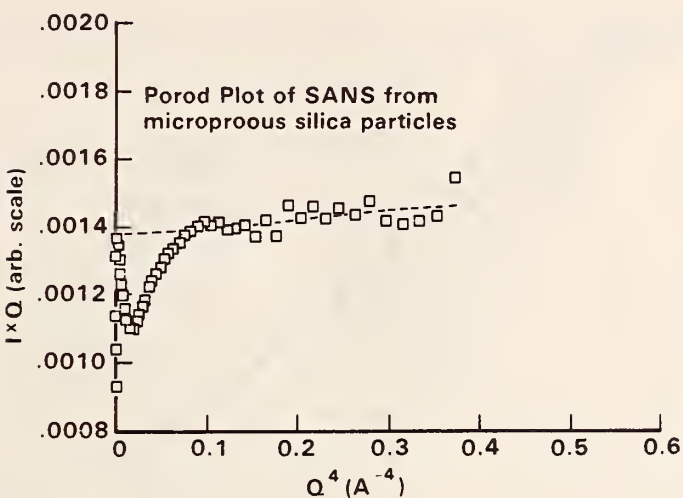


Figure 1. Porod plot (IQ^4 versus Q^4) of the small angle scattering from a powder sample of microporous silica particles. The vertical intercept of the dashed line fit to the linear region of the plot is proportional to the total surface area of the porous particles.

materials with the same nominal pore size are known to perform quite differently in chromatographic applications. Thus, it is hoped that SANS will reveal differences in pore structure that can be related to variations in performance.

SANS INVESTIGATIONS OF POROSITY IN YCrO_3 CERAMICS

N. F. Berk

and

K. Hardman-Rhyne and E. Case
(Inorganic Materials Division)

A quantitative SANS study of porosity in YCrO_3 ceramics is in progress having the goal of providing reliable measurements of average pore size in bulk materials at different stages of densification with the aid of appropriate theoretical analysis. At present, data have been acquired from two samples which were similarly prepared pure powders isobarically pressed at 30,000 kbar. One, a greenstate compact has 58 percent theoretical density. Measurements were made at several neutron wavelengths and are shown for the greenstate compact as a function of scattering wavevector in Figure 1. The full widths at half maximum of these curves were determined by approximate Gaussian fits and increase linearly with wavelength in the range shown, a behavior characteristic of multiple range shown, a behavior characteristic of

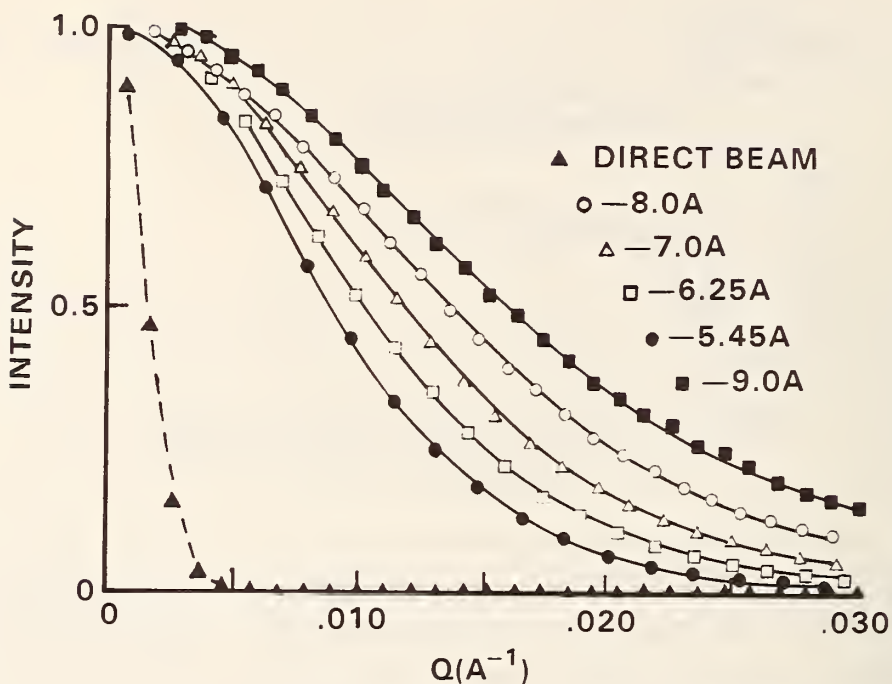


Figure 1. SANS intensities from YCRO_3 greenstate compact at several neutron wavelengths; the normalization is arbitrary.

multiple scattering from large particles and thus consistent with the evident porosity of the greenstate. In contrast, the scattering from the sintered sample (not shown) exhibits no wavelength dependence on this scale, indicating the absence of comparably large pores. Clearly, even a qualitative analysis of such data reveals a strong effect of processing on the population of neutron scatterers in these materials, but quantitative measures of void sizes are less straightforward. If the scattering in Figure 1 is assumed to be describable only as multiple refraction by voids, then a preliminary estimate of average void radius gives a value of approximately $2\mu\text{m}$, which appears to be physically reasonable for the greenstate compact. For the wavelengths of these measurements, however, this corresponds to scattering phase shifts well within an intermediate range of values in which the scattering is not expected to be simply analyzable in terms of refractive (i.e., ray optical) behavior alone. For this reason, in parallel with these experimental investigations, we are developing¹ an appropriate generalization of available theoretical technique in order to provide a sound basis for the quantitative analysis of the SANS data from these and similar materials.

1. N. F. Berk, this report.

SMALL ANGLE NEUTRON SCATTERING (SANS) STUDY OF CREEP DAMAGE IN 304 STAINLESS STEEL

S. P. Singhal and B. Mozer

and

R. J. Fields
(Fracture and Deformation Division)

304 stainless steel used in high-temperature applications consists of $M_{23}C_6$ (M stands for Cr and other metallic elements in the carbide) type of carbides at the grain boundaries. The carbide-austenite interface is a preferential site for the nucleation of cavities during high-temperature degradation--a phenomenon called cavitation. The structure after cavitation consists of three phases; namely, austenite, carbide, and cavities. The attempt to use SANS as a reference method to nondestructively evaluate the evolution of creep cavities from very early stages of cavity growth (inaccessible to conventional methods) requires that the creep induced changes in volume fraction, size distribution, and spacial distribution of carbides do not contribute significantly to the scattered intensity. At this point there is no theoretical or experimental study to indicate that this limitation is not important, yet by adapting special experimental procedures, the effects due to such changes could be minimized. The following two procedures were employed:

- a. All samples were given a stabilizing heat treatment of 100 hours at 600 °C prior to the initiation of creep thereby precipitating out the entire volume fraction of carbides.
- b. A control sample (undeformed) was heat treated along with the crept samples over the period of creep deformation. SANS spectra from the undeformed sample were used as a baseline to delineate the cavity contribution from the deformed samples. The creep parameters of two samples (x-6, x-8), which fulfilled these requirements in this and a previous study, are described in Table 1. This report describes recent results on these samples and compares them with the previous study.¹

The SANS studies were carried out on the NBS reactor facility using a converging collimation and a neutron wavelength of 6.25 Å. With the choice of collimation and wavelength parameters, a scattering vector (Q) range of 0.005 \AA^{-1} to 0.15 \AA^{-1} could be measured in these experiments. This Q range measures the scattering contribution of the inhomogeneities in the size range of approximately 40 Å to 1200 Å. By using converging collimation we have been able to measure the

scattering intensity at Q values about a factor of three lower than a previous preliminary study.¹

Detailed theory and procedures for analyzing the SANS data have been described by Kostorz.² A few salient features will be discussed here. If scattered intensity is denoted by Z, then the macroscopic differential scattering cross section of the scattering entities is given by

$$\frac{d\epsilon}{d\Omega} = CZ/tMT \quad (1)$$

In this equation, t is the sample thickness, M is the total monitor count, T is the sample transmission, and C is a combination of experimental constants for the instrument. Creep damage as related to the evolution of cavities and changes in carbide size, shape, and spacial distribution is measured by the difference in the $d\epsilon/d\Omega$ for the deformed (D) and undeformed sample (U), i.e.,

$$\left(\frac{d\epsilon}{d\Omega}\right)_{\text{damage}} = \left(\frac{d\epsilon}{d\Omega}\right)_D - \left(\frac{d\epsilon}{d\Omega}\right)_U = C[Z_D/t_D M_D T_D - Z_U/t_U M_U T_U] \quad (2)$$

In further discussion, we have assumed that contribution to $\left(\frac{d\epsilon}{d\Omega}\right)_{\text{damage}}$ comes predominantly from creep cavities. Figures 1 and 2 show scattering patterns for the deformed and undeformed samples of x-6 and x-8, respectively. We can see that in these (also, in all other samples measured) the deformed sample always showed higher scattered intensity than the undeformed, thereby emphasizing cavity contribution to the scattering. Figures 3 and 4 show only cavity contribution, i.e., after subtracting the spectra for the undeformed sample from the deformed one. The steep fall of scattering intensity in Figure 3 is indicative of very narrow size distribution of cavities.

One parameter of major interest is the growth of average cavity size as a function of creep deformation at constant stress. A Guinier analysis was performed on these spectra (Figures 3 and 4) to obtain an average cavity size. Guinier² showed that for a randomly distributed, monosized, spherical heterogeneity, the intensity (Z) and scattering vector (Q) relationship can be described by the equation

$$Z = Z_0 \exp\left(\frac{-Q^2 R^2 g}{3}\right) \quad (3)$$

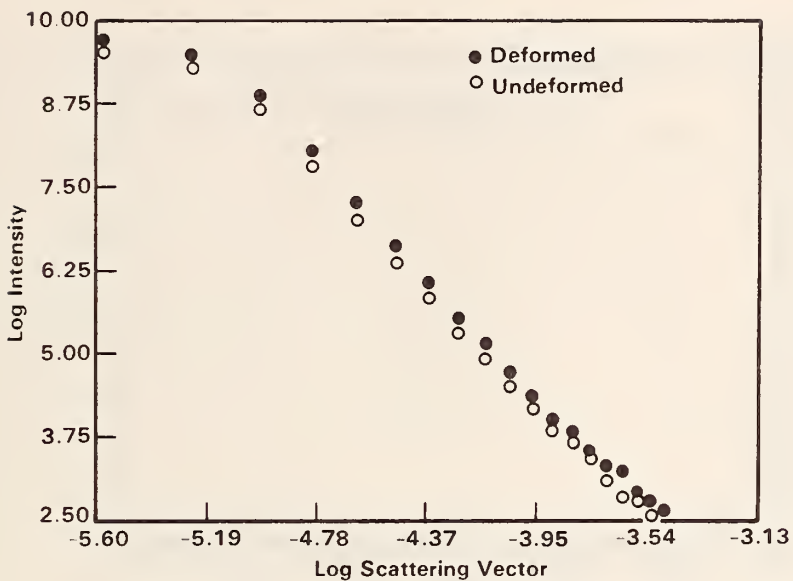


Figure 1. SANS spectra on deformed and undeformed x-6 specimens. Deformation under 21 ksi stress was carried out at 600 °C for 1493 hours. The undeformed sample was heat treated at 600 °C for 1493 hours.

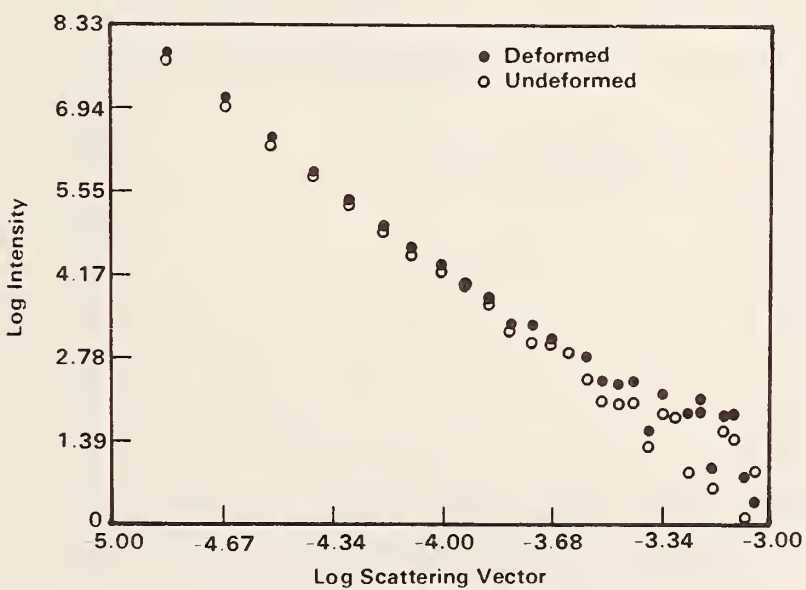


Figure 2. SANS spectra on deformed and undeformed x-8 specimens. Deformation under 18 ksi stress was carried out at 600 °C for 1537 hours. The undeformed sample was heat treated at 600 °C for 1537 hours.

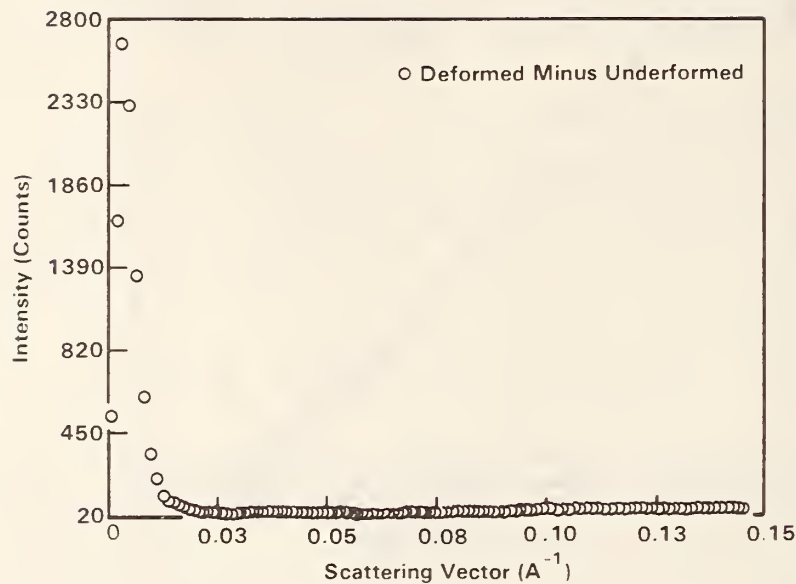


Figure 3. SANS spectra showing the scattering due to creep-induced cavities for x-6 specimen.

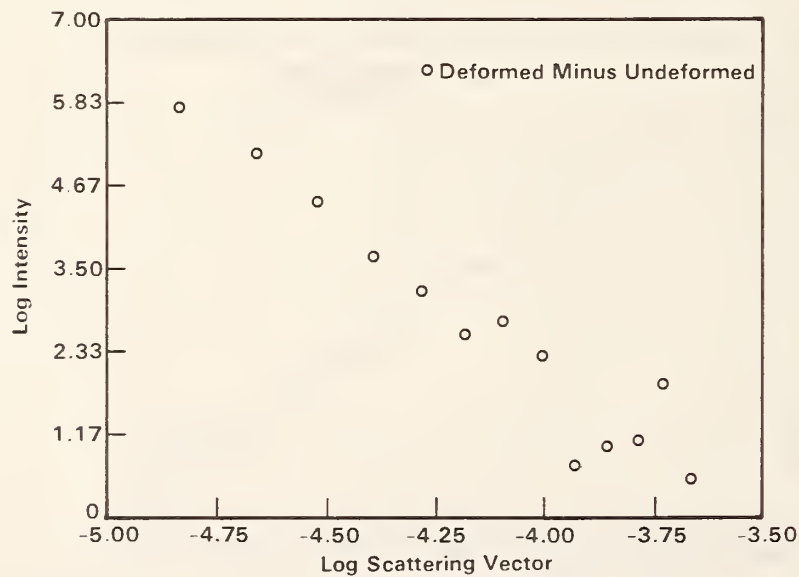


Figure 4. SANS spectra showing the scattering due to creep-induced cavities for x-8 specimen.

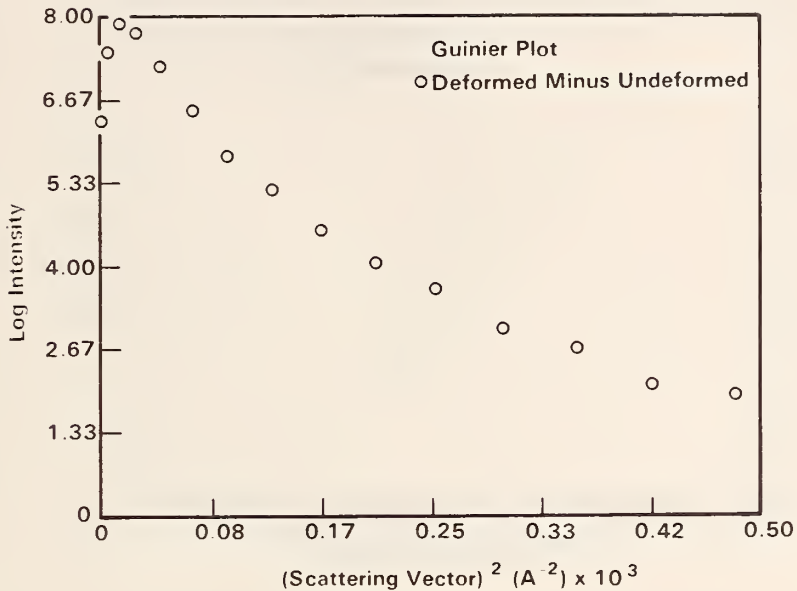


Figure 5. Guinier plot showing the scattering contribution of creep cavities in x-6 specimen.

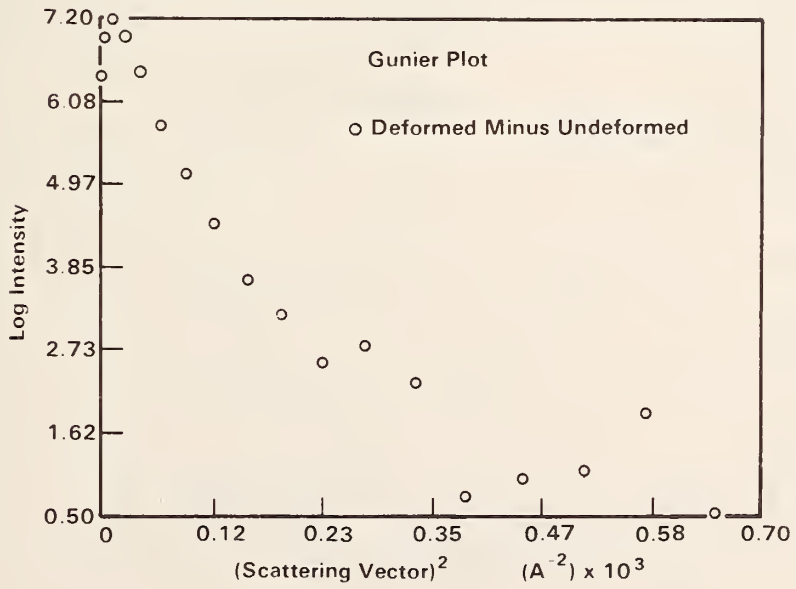


Figure 6. Guinier plot showing the scattering contribution of creep cavities in x-8.

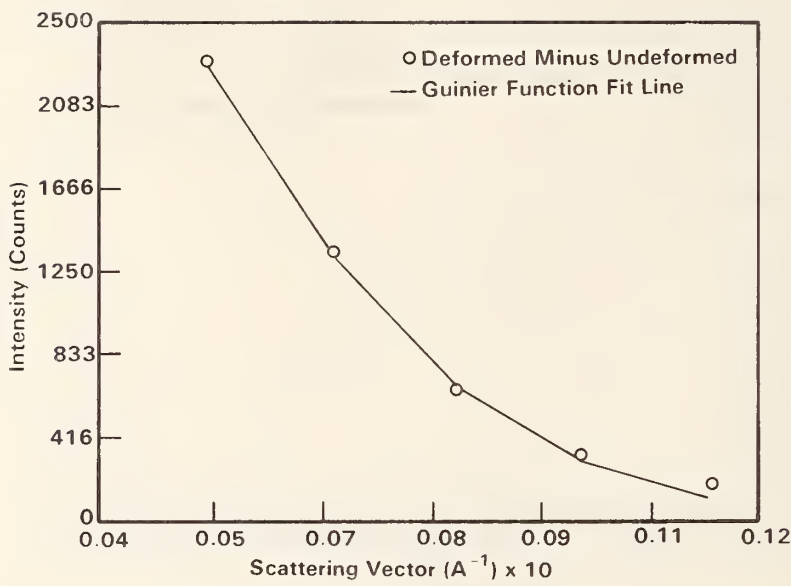


Figure 7. Least square fit of the Guinier function of the data in the selected range of figure 3 for x-6 specimen.

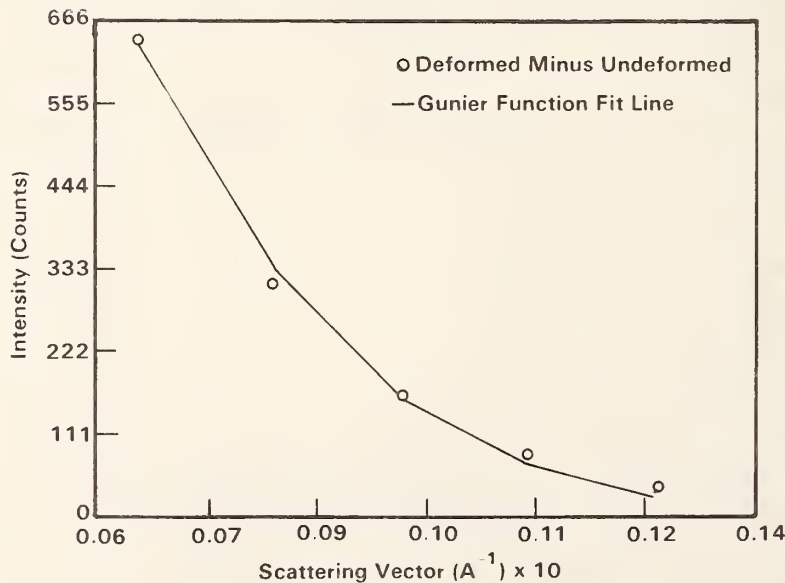


Figure 8. Least square fit of the Guinier function to the cavity scattering data in the selected Q range for the x-8 specimen.

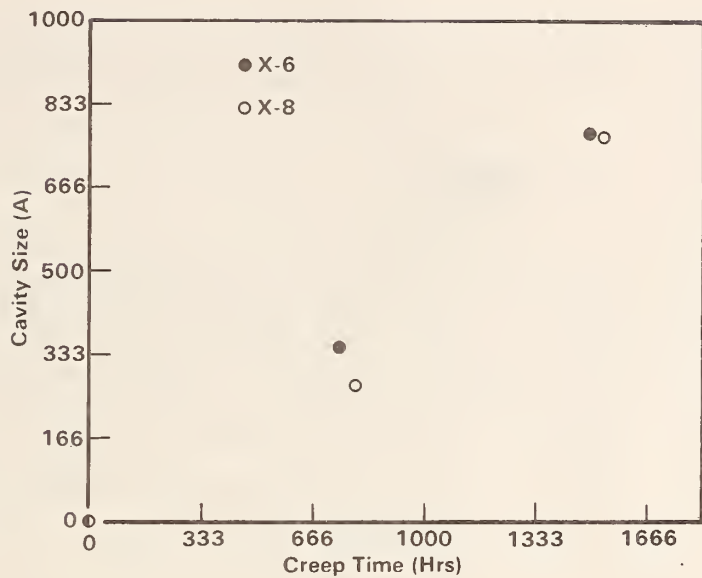


Figure 9. Size growth of creep cavities as a function of creep time at 600 °C for x-6 and x-8 specimens.

Table 1. Growth of creep cavities as a function of time at constant stress in 304 stainless steel.

Sample #	Creep Parameters	Average Cavity Diameter from Guinier Approximations	
		(Å)	(nm)
x-6	745 at 21 ksi (144.8 MPa)	346	34.6
	1493 at 21 ksi (144.8 MPa)	770	77.0
x-8	789 at 18 ksi (124.1 MPa)	266	26.6
	1537 at 18 ksi (124.1 MPa)	763	76.3

Here R_g is the radius of gyration of the particles and is related to their diameter (D) by the equation

$$D = \sqrt{10/3} R_g \quad (4)$$

Z_0 is the constant related to the volume and number density of the cavities. If heterogeneities are not monosized, then the utility of Guinier approximation is limited to only a very small Q range near the 0. Figures 5 and 6 represent Guinier plot [Log Z vs. Q^2] for cavities in samples x-6 and x-8. It is clear from these plots that cavities must have a size distribution as a straight line in these plots can be fitted only in the narrow Q region near the peak. The cavity diameter obtained by this procedure normally over-estimates the contribution of large cavities, yet it is a very useful parameter to study cavity growth as a function of creep time while degradation is in progress. Using a least square fit subroutine, equation (3) was fitted to the data points in the relevant Q range of Figures 5 and 6. The experimental data points and the fit line are shown in Figures 7 and 8. A reasonably accurate fit was obtained in the selected Q range for both cases. The average cavity sizes derived from these fits for the two samples are

$$\langle D_{\text{cavity}} \rangle \approx 770 \text{ \AA} \text{ for x-6}$$

and

$$\langle D_{\text{cavity}} \rangle \approx 763 \text{ \AA} \text{ for x-8.}$$

Table 1 shows that doubling the creep time at the same stress has the effect of doubling the average cavity size for sample x-6. Figure 9 shows the growth of cavity size as a function of creep time in the two samples assuming that at the initiation of creep, the cavity size is negligible. If we include the point at the origin, there appears to be a linear time dependent size growth of the cavities in x-6; but in the absence of more data points, only a limited significance can be attached to the trend in Figure 9. In the previous report,¹ we concluded that x-6 has higher average cavity size despite the longer creep time because x-6 was stressed at 21 ksi as opposed to 18 ksi for x-8, therefore resulting in the enhanced stress induced coarsening of cavities. In this study we find that average cavity size in the two samples is not very different. This indicates that for longer creep times the size growth of cavities is perhaps less sensitive to the small changes in applied stress. This is because the stress difference between these two samples is only about 3 ksi. The other possibility as debated by Weertman³ is that when a large fraction of

cavities grow large enough to scatter at the Q values below minimum Q in the experiments, the average size and volume fraction parameter from the standard SANS analysis are highly underestimated and also the Guinier region is inaccessible. The confirmation that this has taken place at a certain stage of the creep requires the void size and volume fraction determinations by TEM and density measurements, respectively. Such measurements are currently in progress. To refine the general application of SANS as a reference method to quantify creep cavity growth in alloys, further work must be performed on simpler metals or model alloys to absolutely identify the contribution of interacting microstructures and defects in structural alloys.

-
1. E. R. Fuller, Jr., R. J. Fields, E. D. Case, S. Singhal, and C. J. Glinka, "Nondestructive Evaluation of Distributed Damage," Annual Report, Reactor Radiation Division, NBS (1983).
 2. G. Kostorz, "Neutron Scattering in Materials Science," Chapter 5 in Treatise in Materials Science and Technology 15, ed. G. Kostorz, (Academic Press, New York, 1979).
 3. J. R. Weertman, M. Yang, and M. Roth, "Grain Boundary Cavitation in Copper Subjected to High Temperature Creep," Annex to Annual Report, Institut Laue-Langevin, Grenoble, France, p. 263 (1982).

UNIAXIAL DEFORMATION OF RUBBER NETWORK CHAINS BY SMALL ANGLE NEUTRON SCATTERING

H. Yu, T. Kitano, C. Y. Kim, E. Amis, M. Landry, J. A. Wesson, and T. Chang
(University of Wisconsin, Madison, WI)

and

C. Han and T. P. Lodge
(Polymer Science and Standards Division)

and

C. J. Glinka

Small angle neutron scattering (SANS) measurements were performed on poly(isoprene) networks at different uniaxial strains, i.e., $1.0 \leq \lambda$ (extension ratio) ≤ 2.1 . The network strands were prepared from anionically polymerized α , ω -dihydroxy-poly(isoprene) precursors (H-chains) and the corresponding poly(isoprene-d₈) isotopic counterparts (D-chains), crosslinked in concentrated tetrahydrofuran solutions by a tri-functional crosslinker, tris-isoajanate. The isotopic contents of

the networks at 8 percent and 15 percent were used in determining the two components, of the radius of gyration of elastic strands, parallel and perpendicular to the strain axis from the SANS data. Three molecular weights of D-chains, 26,000, 64,000, and 82,000, crosslinked with approximately similar molecular weights of H-chains (29,000, 68,000, and 72,000, respectively) were examined for a possible molecular weight effect on the deformation behavior. From the observed changes in the parallel and perpendicular components of the radius of gyration relative to the macroscopic extention ratio, appropriately corrected for the contributions from nonelastic (dangling) chains, we conclude that the chain deformation is given by an intermediate behavior between the junction affine model and the "phantom network" model having unrestricted fluctuations of network junctions. The deformation behavior is also found to be the same for all three molecular weights.

SMALL ANGLE SCATTERING FROM AMORPHOUS DyCu

S. J. Pickart

(University of Rhode Island, Kingston, RI)

and

(National Bureau of Standards, Washington, DC)

and

H. A. Alperin

(Naval Surface Weapons Center, Silver Spring, MD)

and

(National Bureau of Standards, Washington, DC)

and

R. J. Gambino and T. R. McGuire

(IBM, Yorktown Heights, NY)

The unusual magnetic transition¹ for the random anisotropy amorphous alloy DyCu was investigated by small angle neutron scattering (SANS) methods. The measurements were made on two 150-micron sputtered films with incident 6.0 Å wavelength, at temperatures between 5 and 77K, and for wavevectors $0.016 \leq q \leq 0.165 \text{ \AA}^{-1}$. The small angle magnetic intensity shows a pronounced break at $T \approx 17\text{K}$, corresponding very closely to the weak-field susceptibility cusp as measured on the same sample. The line shape at all temperatures were observed to be Lorentzian, with a correlation length slowly increasing as T decreases to a maximum of $\sim 13\text{\AA}$ at 17K and remaining sensibly constant there after.

The results for the correlation length as a function of temperature that were extracted from the data are shown in Figure 1. These results were compared with susceptibility² and specific heat measurements³.

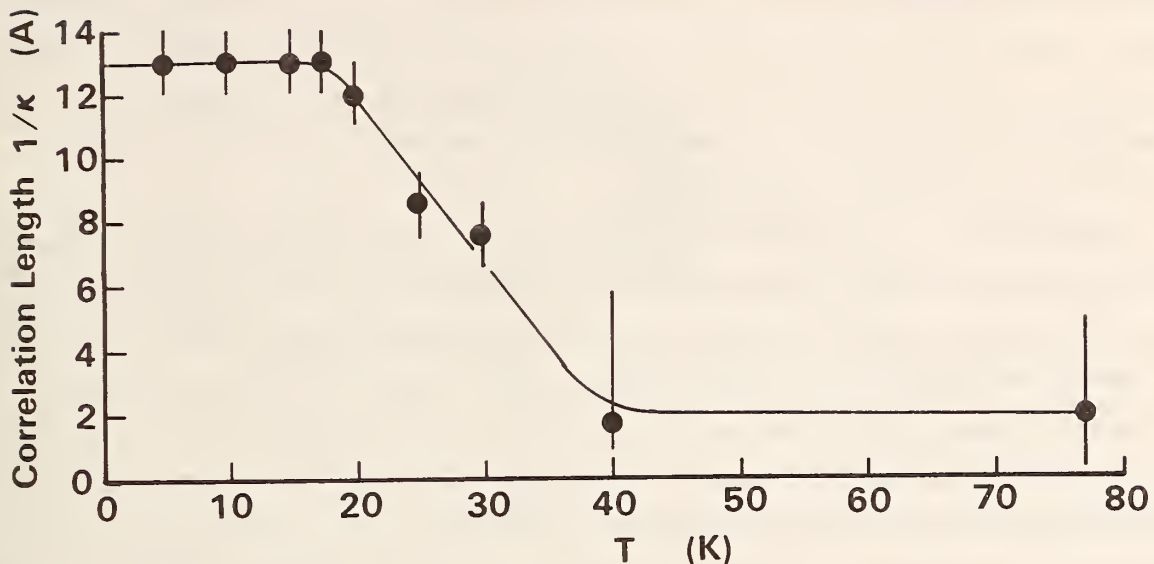


Figure 1. The magnetic correlation length of amorphous DyCu as determined from small angle neutron scattering measurements.

-
1. S. von Molnar, T. R. McGuire, R. J. Gambino and B. Barbara, *J. Appl. Phys.* 53, 73 (1982).
 2. S. von Molnar, B. Barbara, T. R. McGuire and R. J. Gambino, *J. Appl. Phys.* 53, 1350 (1982).
 3. S. von Molnar, G. N. Guy, R. J. Gambino and T. R. McGuire, *J. Magn. Matl.* 15-18, 1391 (1980).

GENERALIZED THEORY OF NEUTRON SCATTERING FROM HYDROGEN IN METALS

R. C. Casella

Neutron scattering from hydrogen in various materials is usually thought of as incoherent in the sense that the random relative spin orientations of an array of protons therein destroys the phase coherence in the Huygens construction associated with a potential diffracted neutron wave. There is, however, another sense in which one must distinguish between coherence and incoherence in the scattering of neutrons from dilute hydrogen in, say, metals. That is, when a neutron scatters from a single interstitial hydrogen atom (electronically shielded proton) which moves about in the metal, it matters whether or not the protonic motion exhibits quantum coherence in the sense that the relative phase of the proton wave function is retained over dis-

tances of the order of a few lattice parameters. The existence of coherent effects of the second type in the scattering of neutrons from hydrogen in metals at low temperature has been demonstrated experimentally via the observation of tunneling transitions among the split ground-state components of a two-well trap for hydrogen in niobium near added O impurities.¹

Experimental observation of sizable band widths $O(10 \text{ meV})$ for the inelastic scattering of neutrons from hydrogen in metals, inducing transitions to excited states $O(100 \text{ meV})$ above the ground state in pure and defected metals by Rush, Rowe, and their collaborators² at the NBS Reactor facility, has led me to an intensive theoretical investigation of the processes involved. These include the possibilities of transitions to excited states in the two-well trap^{3, 4} as well as transitions to excited-state protonic energy bands as discussed in the accompanying report.⁵ The coherent band motion can lead to finite widths for the neutron excitation bands, even in the absence of other width-producing factors such as lifetime effects due to the spontaneous decay of the excited proton to its local-oscillator ground state and incoherent hopping between excited oscillator states centered at nearby interstitial sites. In contrast, most quasielastic neutron scattering processes, which typically involve energy transfers less than $O(1 \text{ meV})$, have widths dominated by the incoherent hopping process as first discussed in this context by Chudley and Elliott (CE).

I have generalized my band theory of inelastic neutron scattering from hydrogen in metals⁵ to include the presence of spontaneous decay to the ground state and incoherent hopping of the proton as well as the coherent protonic band transport I had considered earlier. Similarly, I have generalized the CE analysis of quasielastic scattering and its structural extension by Rowe, Skold, Flotow, and Rush to include the effects of coherent band transport, as well as the incoherent hopping mechanism they had considered.

To do so, I have developed a general formalism which encompasses quasielastic as well as inelastic scattering of neutrons from hydrogen in metals and allows for the coexistence of coherent and incoherent protonic transport processes. At each level of complexity, the expressions I obtain for the neutron cross section $d^2\sigma/d\Omega d\epsilon$ can be shown to reduce to earlier results in the limits when either the coherent or incoherent contributions to the ground or excited-state band widths can be ignored. For example, for the special case of only one hydrogen occupancy site per unit cell (and ignoring the degeneracy of the excited local-oscillator states), I obtain the following expression for the inelastic neutron scattering cross section:

$$d^2\sigma/d\Omega d\epsilon = (k_F/k_I) |\bar{a}|^2 |\tilde{F}(\vec{q})|^2 G'(\vec{q}, \omega)/2\pi \quad (1)$$

The generalized proton self-correlation function $G'(\vec{q}, \omega)$ which appears in Eq.(1) is given by the relation

$$G'(\vec{q}, \omega) = (1/N) \sum_{\vec{k}} \frac{\Gamma'(\vec{q}, \omega)}{[\omega + E_{ex}(\vec{k} - \vec{q}) - E_o(\vec{k})]^2 + [\Gamma'(\vec{q})]^2} \quad (2)$$

In the above ω and \vec{q} denote the energy and momentum transfer to the neutron; $E_o(\vec{k})$ and $E_{ex}(\vec{k})$ are the ground and excited-state band energies, respectively; $\Gamma'(\vec{q})$ is the incoherent width due to hopping with loss of phase memory by the proton and to its decay from the excited to the ground state of the local oscillator; remaining symbols are defined in the accompanying report.⁵ In the limit when $\Gamma'(\vec{q})$ can be treated as infinitesimal, it can be shown that Eq.(2) reduces to a form given by Eq.(1) in the accompanying report. That is, the band-theoretic result, expressing $d^2\sigma/d\Omega d\epsilon$ in terms of the excited-state band density of states $g(\omega)$ is recovered. In the opposite limit, when the coherent band width (i.e., the width of $g(\omega)$) is small compared with $\Gamma'(\vec{q})$, Eq.(2) simplifies such that together with Eq.(1) above, I obtain

$$d^2\sigma/d\Omega d\epsilon = (k_F/k_I) |\bar{a}|^2 |\tilde{F}(\vec{q})|^2 \frac{\Gamma'(\vec{q})}{[\omega + \Delta]^2 + \Gamma'(\vec{q})^2}. \quad (3)$$

Here Δ is the band gap, which reduces to the local-oscillator excitation energy in this limit. $\Gamma'(\vec{q})$ is a known function of the momentum transfer \vec{q} , expressible in terms of two parameters, the lifetime against spontaneous decay of the proton to the local-oscillator ground state and that due to incoherent hopping of the proton to a nearby interstitial site.

High statistics experiments will be required to distinguish between the various possibilities. Further details of the theoretical development may be found in reference 6.

-
1. H. Wipf et al., Phys. Rev. Lett. 46, 947 (1981).
 2. A. Magerl et al., Phys. Rev. B27, 927 (1983). J. J. Rush et al., Bul. Am. Phys. Soc. 26, 337 (1981).
 3. R. C. Casella, Phys. Rev. B24, 2913 (1981).
 4. R. C. Casella, J. Phys. (Paris) Colloq. 42, C6-923 (1981).
 5. R. C. Casella, subsequent report; also R. C. Casella, Phys. Rev. B27, 5943 (1983).
 6. R. C. Casella, preprint, to appear in Phys. Rev. B.

THEORY OF EXCITATION BANDS OF HYDROGEN IN METALS AND OF THEIR OBSERVATION
BY NEUTRON SCATTERING

R. C. Casella

My earlier work¹ on the energy-band structure of dilute hydrogen in excited oscillator states in bcc metals (produced by overlap of the protonic wave functions) has been extended in three ways:

1. The prior analysis¹ was limited to nearest-neighbor overlap terms in the tight-binding expansion of the band wave functions in terms of local oscillator states centered at interstitial sites. Second-nearest-neighbor terms have since been included. For the case of the ω_I bands (first oscillator excitation), these terms were found to introduce only minor corrections as may be seen by comparing the dashed and solid curves in Figure 1. For the higher ω_{II} bands, the second-neighbor corrections introduce qualitative modifications in the band structure: (a) The earlier presence¹ of eigenvalues at $\hbar\omega_{II} \pm E$ has been shown to be an artifact of the nearest-neighbor approximation. (b) The presence of a pseudo Brillouin zone boundary in the plane normal to the wave vector $\vec{k} = (2\pi/a)(1/2, 0, 0)$ is removed by the second-neighbor corrections, although some vestiges remain in the form of zero slopes near the former band-crossing points. The modified ω_{II} bands are shown in Figure 2.

2. The expression for the differential cross section $d^2\sigma/d\Omega d\epsilon$ for inelastic neutron scattering from dilute hydrogen in metals, inducing transitions to the excited oscillator bands was previously limited to the special case of only one hydrogen occupancy site in the primitive cell. For the case of hydrogen in real bcc metals such as V, Nb, and Ta, there are six tetrahedral occupancy sites in each cell. I have since demonstrated that the effect of the added structure leads to a neutron cross section, which in first approximation, takes on a form similar to that for a Bravais occupancy-site lattice:

$$\frac{d^2\sigma}{d\Omega d\epsilon} = \frac{k_F}{k_I} |\bar{a}|^2 |\hat{F}(\vec{q})|^2 g(\omega). \quad (1)$$

An exact, but more complex, expression has also been derived. In Eq.(1) k_I and k_F are the initial and final neutron momenta, \bar{a} is the Fermi scattering length (renormalized by the lattice Debye-Waller factor), $\hat{F}(\vec{q})$ is an average of the local oscillator form factors within the unit cell, \vec{q} and ω are the momentum and energy

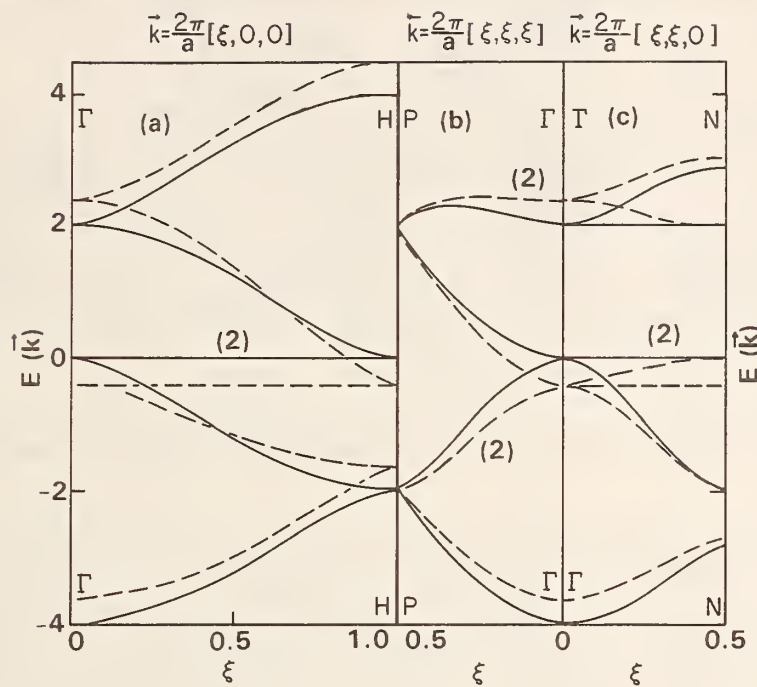


Figure 1. Effects of second-neighbor overlap on the band structure $E(\vec{k})$ for the ω bands. $E(\vec{k})$ is given for $\vec{k} = (2\pi/a)(\xi, \eta, \zeta)$ along (a) [100], (b) [111]_I, and (c) [110]_I. Solid curves: nearest-neighbor approximation ($Y = 0$). Dashed curves: next-nearest neighbors included ($Y = -0.2$). Y is the ratio of the overlap integrals graph (d)/graph (a) as shown in figure 3. The energy scale is equal to the overlap integral H_I , where H_I is symbolized by graph (a) of figure 3. The zero energy is equal to that of the isolated local oscillator, excited by an amount $\hbar\omega_I$.

transfer to the neutron, and $g(\omega)$ is a normalized density-of-state factor associated with the \vec{k} dependence of the excited band, which, in the absence of other width-producing factors, yeilds the width and shape of the inelastic neutron absorption band:

$$g(\omega) = (1/hd) \sum_{\alpha=1}^{hd} (1/N) \sum_{\vec{k}} \delta[\omega + E_{\alpha}(\vec{k})]. \quad (2)$$

h designates the number of occupancy sites in the unit cell; d , the degeneracy of the excited local-oscillator states; N , the number of unit cells; and $E_{\alpha}(\vec{k})$, the sub-band eigenvalues produced by the overlap of the local-oscillator wave functions. $g(\omega)$ is normalized such that $\int d\omega g(\omega) = 1$. Various irreducible overlap integrals are symbolized in Figure 3.

3. Although, as yet, definitive experimental proof of the existence of excited-state hydrogen (i.e., protonic) energy bands is lacking, the band structure I

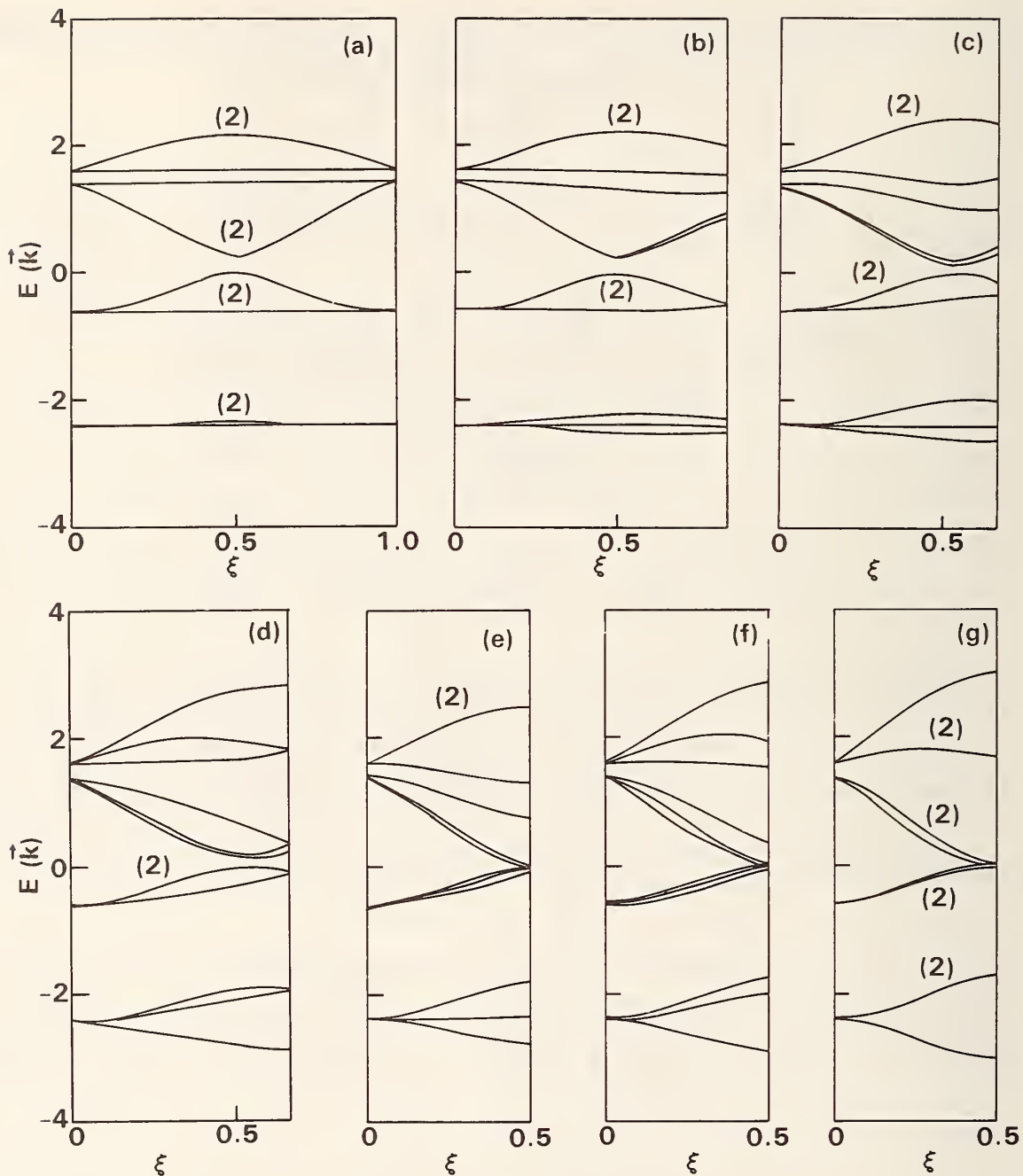


Figure 2. Effect of second-nearest neighbor corrections on the band structure $E(\vec{k})$ for the ω_{II} bands. $E(\vec{k})$ is given for \vec{k} along (a) [100], (b) [1 1/5 0], (c) [1 1/2 0], (d) [1 1/2 1/2], (e) [110], (f) [11 1/2], (g) [111]. $S = 0.5$, $T = 0.2$, $U = 0.2$. S , T , and U are the ratios of overlap integrals diagrammed in figure 3. $S = \text{graph (c)}/\text{graph (b)}$, $T = \text{graph (e)}/\text{graph (b)}$, $U = \text{graph (f)}/\text{graph (b)}$ of figure 3. The energy scale is equal to the overlap integral H_{II} (graph (b) of figure 3). The zero energy is equal to that of the isolated local oscillator, excited by an amount $\hbar\omega_{II}$. $\vec{k} = (2\pi/a)(\xi, \eta, \zeta)$.

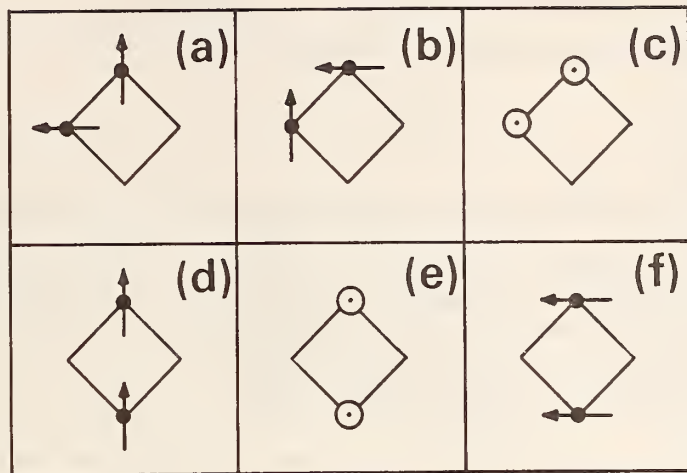


Figure 3. Diagrams for the various irreducible overlap integrals. Arrows signify the symmetry of the p-orbital cubic harmonics which characterize the excited oscillator states from which the Bloch states are constructed. Graphs (a)-(c) designate nearest-neighbor overlap integrals, (d)-(f) second-nearest-neighbor terms. Graphs (a) and (d) refer to the first (ω_I) excitation band; (b), (c), (e), and (f) belong to the second (ω_{II}) band.

have obtained has been shown to be consistent with the experimental results of Rush, Rowe, and collaborators² in two respects. (a) I predict that the band widths Γ of the inelastic neutron scattering peaks ought to satisfy the inequalities

$$\Gamma(V) > \Gamma(Nb) > \Gamma(Ta), \quad (3)$$

when comparison is made among these three metals. They do.² (b) I find that the ratio of the widths $\Delta E_{II}/\Delta E_I$ of the ω_{II} to ω_I bands within a given metal ought to satisfy the approximate relation

$$\Delta E_{II}/\Delta E_I = (\omega_{II}/\omega_I)^2 T, \quad (4)$$

where T is a nearly a universal constant ($\sim 3/4$) for the bcc metals. Experimentally (and consistent with either a local-oscillator or a tight-binding band model) the peak frequencies satisfy $(\omega_{II}/\omega_I)^2 \sim 2$, whence, identifying ΔE with Γ , I predict $\Gamma_{II}/\Gamma_I \sim 1.5$. Direct comparison with experiment for dilute hydrogen in these metals at low temperatures is complicated by the hydride (ϵ) phase transition, requiring the introduction of trapping impurities such as O or N, which, while inhibiting the phase transition, perturbs the bands as derived in this model. Nevertheless, the predicted ratio compares favorably with the value 1.7 obtained by averaging the low-temperature

experimental neutron widths for hydrogen in association with O and N impurities in Nb.² Further details may be found in reference 3.

1. R. C. Casella, NBS Tech. Note No. 1178, p. 79 (F. Shorten, Ed., 1983).
2. A. Magerl, J. J. Rush, J. M. Rowe, D. Richter, and H. Wipf, Phys. Rev. B27, 927 (1983); J. J. Rush, A. Magerl, and J. M. Rowe, Bul. Am. Phys. Soc. 26, 337 (1981). The latter deals with pure systems.
3. R. C. Casella, Phys. Rev. B27, 5943 (1983).

THEORY OF HYDROGEN TRAPPING BY INTERSTITIAL IMPURITIES IN BCC METALS

N. F. Berk

We are calculating the elastic interaction energy between an octahedral (O) site interstitial impurity and a self-trapped proton occupying a tetrahedral (T) interstitial in its neighborhood. The aim of the study is to help elucidate the nature of experimentally observed trapping of hydrogen by interstitial impurities in BCC metals and to seek, in particular, the most likely candidates for the specific trap site,¹ which we assume to correspond to a local minimum of the mutual strain field interaction energy.

In our approach the proton self-trapping is taken explicitly into account using the adiabatic approximation and a model proton-metal interaction potential.² Thus, in these calculations the proton Kanzaki forces are not rigid but are a function of position relative to the O-site. The O-site impurity is modeled by a rigid set of forces. The total interaction energy is then represented by

$$E = -F_O \cdot G \cdot F_T - \Delta E_S + \Delta E_0$$

where site indices and summations are implicit. F_O is the Kanzaki force centered at the O-site, E_T is the T-site Kanzaki force, G is the pure metal harmonic lattice greens function, ΔE_S is the change in the proton self-trapping energy due to changes in the self-consistently determined metal atom displacements, and ΔE_0 is the change in the proton zero-point energy due to the alteration of the interaction potential near the impurity. The system of equations to be solved is symbolized by

$$F_T\{u\} = \int [-\nabla V(r|u)] \psi_0^2 (r|u) d^3r$$

$$u = G \cdot F_O + G \cdot F_T\{u\}$$

$$\left[\frac{-k^2}{2m} \nabla^2 + V(r|u) \right] \psi_0 = E_0 \psi_0$$

where $V(r|u)$ is the proton metal interaction potential for a given set of metal atom displacements $\{u\}$, and $\psi_0(r|u)$ is the ground state wave function of the proton self-trapped in this potential. The actual displacements $\{u\}$ and thus all the u -dependent quantities, are determined by iterating this set of equations to solution. The same technique will be used to study the low-lying excited states of the perturbed self-trapped sites in order to make contact with neutron spectroscopy of impurity-trapped hydrogen.¹

Neutron studies have led to the prediction¹ that the proton is trapped at fourth neighbor T-site, $(1/2, 3/4, 0)$ if the impurity is at $(0, 0, 1/2)$. The current calculations,³ however, find a weak local interaction energy minimum (of approximately 30 MeV for models of both O and N impurities in V metal) only at a fourth neighbor $(1, 1/4, 1/2)$ T-site, which is not equivalent to the one mentioned above. No other distinct local minima are found here; the general trend is a monotonic increase in the attraction with decreasing separation, the interaction energy relative to infinite separation being lowered by about 100 MeV for all fourth neighbor T-sites and more for closer in-sites. It is possible, of course, that direct repulsion by the O-site prevents the proton from falling to third neighbor sites from any fourth neighbor site. However, strain interaction alone appears to favor only the $(1, 1/4, 1/4)$ T-site vs. a specific trap site.

1. A. Magerl, J. J. Rush, J. M. Rowe, D. Richter, and H. Wipf, Phys. Rev. B27, 927 (1983).
2. H. Sugimoto and Y. Fukai, J. Phys. Soc. Japan 50, 3709 (1981).
3. N. F. Berk, Bulletin of the Amer. Phys. Soc., 28, 451 (1983).

THEORY OF SANS FROM LARGE PARTICLES AND VOIDS

N. F. Berk

A new program¹ to investigate densification in ceramics using small angle neutron scattering (SANS) has stimulated a theoretical interest in the general problem of small angle scattering from a population of large particles, a topic that apparently has not received close attention for many years. The nature of small angle scattering from particles or voids is determined by a phase shift parameter, ρ , that for a given material composition is proportional to the product of the incident neutron wavelength and the radius of the scattering particle, assumed here to be spherical. In the limit of small phase shift, $\rho \ll 1$, the scattering is described by the Born approximation which in SANS is identified with small angle diffraction. The scattering cross section is very much smaller than the limit determined by the geometric cross section and except for very thick samples or dense populations of scatterers, the measured scattered intensity is characteristic of the scattering from individual particles. Typically this limit accounts for scattering from particles of radius less than 0.1 μm and applies to the vast majority of quantitative SANS experiments. At the opposite extreme, $\rho \gg 1$, the scattering becomes describable in terms of ray optics with each particle refracting neutrons as a lens. The scattering cross section approaches its geometric limit and the observed intensity is dominated by multiple scattering effects which depend not only on particle size but on macroscopic sample properties such as particle (void) volume fraction and sample thickness. At typical neutron wavelengths the refractive limit is reached by particles of radius greater than 10 μm . In these two limits the scattered intensity has very different predicted dependences on neutron wavelength--as a function of the scattering wavevector diffraction is independent of wavelength while refraction produces a linearly dependent "beam broadening."

For intermediate values of the phase shift, $\rho \approx 1$, the scattering is not simply described in terms of either limiting case and no general theoretical predictions appear to exist for data analysis in this regime, including the exact nature of the wavelength dependence. Since for typical measuring wavelengths this corresponds to radii in the neighborhood of 1 μm --which encompasses an important regime of void size in the early stages of ceramics densification, for example--the need for appropriate theoretical development is evident. Thus we are engaged in working out a practical synthesis of a general description of the single particle scattering cross section for small angle scattering and a general approach to multiple scattering in the small

angle limit. Specifically, we are incorporating the formal integral expression for the cross section as derived by Weiss,¹ and which is valid for all values of the phase shift, into the multiple scattering formalism developed by Snyder and Scott.² In the latter the scattering path is projected onto a plane, which entails no loss of information for isotropic scattering but corresponds observationally to infinite thin slit geometry. We adapt this projection method to the desired case of pin-hole SANS geometry by formally applying a "slit correction" to the final integral transform of the theory. At present we have analytically reduced the required projection and Fourier analysis to manageable computational forms and are developing the final numerical analysis.

1. N. F. Berk, K. Hardman-Rhyne, and E. Case, this report.
2. R. J. Weiss, Phys. Rev. 83, 379(1951).
3. H. S. Snyder and W. T. Scott, Phys. Rev. 76, 220(1949).

NEUTRON DIFFRACTION STRUCTURE DETERMINATION OF THE HIGH-TEMPERATURE FORM OF LITHIUM TRITANTALATE, H-LiT₃Ta₈O₁₂

J. L. Hodeau and M. Marezio
(C.N.R.S., Grenoble Cedex, France)

and

A. Santoro

and

R. S. Roth
(National Measurement Laboratory)

The crystal structure of H-LiT₃Ta₈O₁₂ has been re-examined by electron and neutron diffraction techniques. Neutron Weissenberg^{*} and electron diffraction^{**} photographs show that the space group of the compound is Pmmn and not Pmma as determined previously by x-ray diffraction techniques. There are eight molecules in the unit cell of lattice parameters $a = 16.718(2)$, $b = 7.696(1)$, $c = 8.931(1)\text{Å}$. These values show that the b-axis of the new cell is doubled with respect to the parameter measured by x-rays. The structural refinement was based on 1074 independent reflections measured on a single-crystal with a four-circle neutron diffractometer. The positions of all atoms, including the lithium atoms have been determined. The

final R and wR factors were 0.036 and 0.035, respectively. The eight lithium cations occupy two sets of 4f positions ($x, 1/4, z$) of the Pmmn space group. The ordering of four lithium ions over two sets of possible positions (4j) of space group Pmma is responsible for the doubling of b axis. The other four Li⁺ occupy two sets of positions (2d) of space group Pmma. All lithium ions are surrounded by 12 oxygen atoms arranged as cuboctahedra. The large thermal vibrations found for the lithium atoms and the ionic conductivity of H-LiT₃O₈ at high temperatures are consistent with weak Li-O bonding.

The structure has been refined also by neutron diffraction powder profile analysis. The powder refinement, however, yielded wrong positions for one-fourth of the lithium ions. This result may be due to the presence of impurities and/or inhomogeneities in the sample, or to the fact that the large anisotropic temperature factors of the lithium atoms were not refined because of the limited number of intensity data in the powder pattern. This is one case in which the size of the unit cell (~ 1150 Å³) is too large to be analyzed from patterns measured with the resolution now available at the NBS reactor. A problem of this complexity would require a resolution of the order of that obtainable with diffractometers giving a full width at half maximum of 0.1° at the focussing position, and using a take-off angle of the monochromator of 120°.

*The neutron diffraction Weissenberg photographs were obtained with the Weissenberg camera of the Laue-Langevin Institute in Grenoble.

**The electron diffraction studies were carried out at CSIC in Madrid on a Siemen's Elmiskop-102 microscope.

B. NON-RRD PROGRAMS

ACTIVATION ANALYSIS GROUP FY 83

R. Zeisler

The Activation Analysis Group is part of the Inorganic Analytical Research Division, Center for Analytical Chemistry. The group is located in the reactor building and utilizes the facilities provided here: stable climate counting rooms, clean and radiochemistry laboratories, a class 100 clean room, and the neutron irradiation facilities.

The principle objectives of the Activation Analysis Group are the development of nuclear analytical techniques for better sensitivity, higher selectivity, and increased accuracy. A high level of competence has been developed for various reactor-based activation analysis techniques which include instrumental and radiochemical neutron activation analysis (INAA and RNAA), prompt gamma activation analysis (PGAA), and the nuclear track technique (NTT). The utilization of the thermal neutron beam depth profiling (NDP) facility has added a new and strong research component to the group. Non-reactor-based techniques include photon activation analysis (PAA), fast neutron activation analysis, and charged particle activation analysis, which have been used on a more limited scale. With this wide variety of techniques, support is provided for the diversified NBS and other agency programs requiring analytical measurement services. For example, simultaneous multielement determinations over a broad dynamic range in complex matrices as well as highly selective determinations of constituents in the sub-nanogram range have been provided for programs such as Standard Reference Materials, Environmental Measurements, Recycled Oil, Resource Recovery, Nuclear Safeguards, and other interdisciplinary research programs at NBS.

A considerable part of the groups research and measurement efforts is directed to communities outside NBS, which include other government agencies as well as industries. The NBS/EPA sponsored Pilot National Environmental Specimen Bank Program (NESB) is an on-going effort to measure trace element baseline data and to preserve valid specimens. Samples of the second year collection of human livers are now being evaluated. A pollutant monitor for the marine environment has been added to the program and first evaluations for the human food intake are under way. New interest in high accuracy trace element data has been created by this program in the medical and nutrition communities. The NDP program is of similar importance to the outreach to communities which need unique measurements and reference data. With the NDP facility, the group will be participating in materials research related to high

technology industries.

One of the fruits of these expanding efforts is the increasing direct participation of scientists from these communities in our work. The Activation Analysis Group hosts several research associates, guest workers, and assignments under the IPA act, who all bring in new expertise in key research areas such as materials science and bioanalytical research. Other industrial contacts have significantly accelerated the development of a new generation of multichannel pulsheight analyzer systems, a development which will enhance our capabilities for high precision and high accuracy analysis of certain nuclear species.

The recent research accomplishments and applications of the nuclear analytical techniques are highlighted in the sections below. For the future, we foresee increasing demand in the "classical" activation analysis area because of its multielement capabilities and the ability to analyse critical elements at extremely low levels. Research efforts during the coming year will focus on the extension of procedures to fulfill these requirements. In the area of "non-conventional" activation analysis epithermal activation, the use of short-lived nucleides, and possibly the activation with fast neutrons and/or charged particles will be explored.

1. Chemical Analysis with Nuclear Techniques

a. Ultratrace Determinations of Critical Elements in Biological Materials Using Improved Radiochemical Separations

R. R. Greenberg

Accurate analyses of Ag, As, Cd, Cr, Cu, Mo, Sb, and Se are frequently required in studies of environmental pollutions, human nutrition, and a variety of other areas of biomedical research. The need to determine these elements at lower and lower concentrations frequently necessitates improvements in the analytical methodology used.

A radiochemical procedure was previously developed¹ to determine As, Cr, Sb, and Se via neutron activation analysis with the use of hydrated manganese dioxide (HMD) inorganic ion exchanger. Copper and Cd were subsequently extracted from the eluent using Bi and Zn diethyldithiocarbamates (DDC) in chloroform, and their concentrations were determined.¹ Silver and Mo were later found to be quantitatively retained by HMD and could also be determined with the same procedure.

Unfortunately, most or all of the P contained in a sample is also retained by HMD when the above procedure is used. Phosphorous can interfere with the determination of the elements of interest by producing an elevated background level of bremsstrahlung radiation from the β - decay of P-32. This can be particularly serious when analyzing biological materials such as animal tissues and body fluids, milk, leafy vegetables, etc. where the P concentration can be as high as 1% (on a dry weight basis).

A procedure has been developed which, with carefully controlled experimental parameters, reduces the levels of P-32 retained on an HMD column by 80-90%, and has only minimal effects on the other elements. Basically, the procedure involves a pretreatment of the column with 1 M H_3PO_4 and 1 M HNO_3 , followed by elution of P-32 with dilute (0.0025 M) H_3PO_4 in 1 M HNO_3 . Other modifications involving the amount of resin and carries used, and changes in the dissolution procedure are also required. With these additional steps, Ag, As, Mo, and Sb are quantitatively retained (> 99.5%), Cr and Se are nearly quantitatively retained (98.5-99.5%), and Cu and Cd are quantitatively eluted (> 99.5%).

This procedure has been used to analyze Bovine Liver (SRM 1577) and the new Milk Powder (proposed SRM 1549) which is currently being certified. The observed concentrations in the Bovine Liver are in agreement with the certified values, as shown in table 1. The amount of P-32 retained by the HMD was between 10-20% of the amount originally present, and this resulted in a corresponding reduction in the

Table 1. Elemental concentrations observed in Bovine Liver, SRM 1577.

Element	Unit	Mean \pm 2S	Certified
Ag	(ng/g)	58 \pm 4	(60) ^a
As	(ng/g)	50 \pm 4	55 \pm 5
Cd	(ng/g)	293 \pm 15	270 \pm 40
Cr	(ng/g)	85 \pm 10	88 \pm 12
Cu	(μ g/g)	192 \pm 7	193 \pm 10
Mo	(μ g/g)	3.18 \pm 0.05	(3.4)
Sb	(ng/g)	5.6 \pm 1.4	(5)
Se	(μ g/g)	1.08 \pm 0.07	1.1 \pm 0.1

^aConcentrations in parenthesis are "information only" values.

Table 2. Elemental concentrations (ng/g) observed in Milk Powder, SRM 1549.

	<u>Mean \pm 2S</u>
Ag	<0.5
As	1.8 \pm 0.2
Cd	0.47 \pm 0.14
Cr	3 \pm 2
Cu	606 \pm 9
Mo	310 \pm 30
Sb	0.24 \pm 0.08
Se	110 \pm 3

background levels for most elements by a factor of 5-10. This lower level of background radiation not only improved the counting statistics (typically by a factor of 2-3), but also allowed samples to be counted closer to the detector for an additional improvement in sensitivity. This added sensitivity was particularly important for the analysis of the Milk Powder where the concentration of Ag, As, Cr, Mo, Sb, and Se are considerably lower than in the Bovine Liver, as shown in table 2, while the P concentration is comparable.

Although Cd could be determined in the Bovine Liver (and in most biological materials) as part of the multielement procedure, its concentration was too low to be determined in the Milk Powder. Cadmium could be determined in the Milk Powder with several procedural changes including: less post-irradiation decay time prior to sample processing, elimination of the HMD procedure to save time and minimize radiation dose to personnel, and several modifications to the $Zn(DDC)_2$ procedure used to extract Cd. These modifications involve washing the Cd containing $Zn(DDC)_2$ /chloroform solution twice with aqueous solution containing 100 mg of unirradiated Zn to reduce the level of radioactive Zn from the sample and back-extracting the Cd into 2 M HCl. Although this separation procedure is not quantitative, the observed recovery is highly reproducible, $95.2 \pm 0.4(1s)\%$. Cadmium is essentially free of all other radionuclides from the sample and its detection limit is determined primarily by the amount of natural background radiation reaching the detector through the shield. Five 500 mg samples of the Milk Powder were analyzed and the observed Cd concentration was $0.47 \pm 0.07(1s)ng/g$.

When coupled to an appropriate radiochemical separation, neutron activation analysis has the capability of determining many elements at biologically important levels. Improved radiochemical procedures have been developed to separate and determine eight biologically active elements at the trace and ultratrace levels frequently required in current biomedical research. Two of these elements, Cd and Sb, have been determined at the sub-ppb level in Milk Powder.

1. M. Gallorini, R. R. Greenberg, and T. E. Gills, Anal. Chem. 50, 1479 (1978).

b. The Determination of Natural Iodine by Epithermal Neutron Activation Analysis
G. Lutz

During the past year, an epithermal neutron activation analysis (ENAA) experiment was developed and tested in the NBSR. The impetus behind this effort was the necessity to develop a rapid, efficient nondestructive method for the determination of natural iodine at sub-ppm levels. This was required both for the reliable determination of iodine in SRMs as well as the natural iodine content of environmental and biological samples.

There are two elements suitable for screening out thermal neutrons thus allowing more selective epithermal activation-boron and cadmium. The activation analysis group had previous experience with a boron nitride container for the sample at the reactor at the University of Michigan. The containers used in the current work are identical with those used at the University of Michigan. Figure 1 is a photograph of the container. It will accomodate a 2/5 dram (1.3 ml) vial. Thus, sample masses in the range of 0.5-1 gram are possible.

It has become necessary to do extensive hazards evaluation. The mass of the container assembly is 25 grams. Testing with temperature sensors indicated that a twelve second irradiation in RT-3 would bring the boron nitride container to a temperature in excess of 100 °C. To allow for a sufficient safety margin, it was decided that eight seconds would be the maximum irradiation time allowed.

Preliminary experiments have been completed on some SRMs which have been analyzed for iodine by other methods. ENAA is a very satisfactory method and it is expected with experience that we will be able to get down to 0.1 ppm.

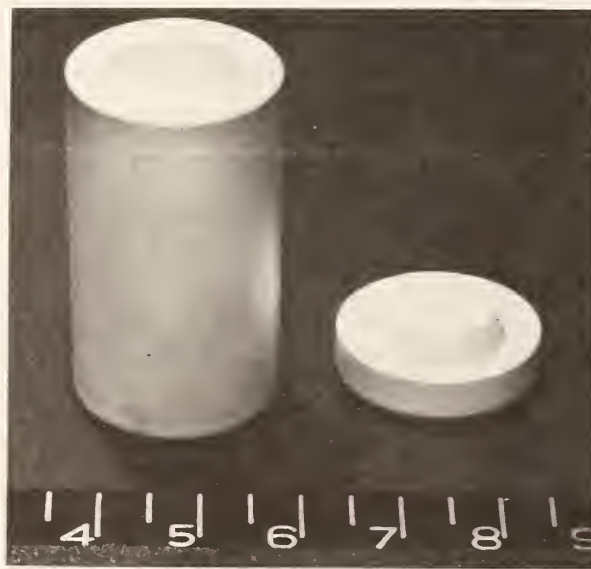


Figure 1. Boron Nitride Container

c. The Determination of I-129 by Neutron Activation Analysis

G. Lutz and R. Lindstrom

The procedure which has been under development for almost three years has been modified slightly and is now in routine use in the determination of I-129 in a variety of vegetation and other samples.

The analysis consists of a pre-irradiation separation, an irradiation in the reactor, and a post-irradiation separation.

The apparatus for the pre-irradiation separation is shown in figure 1-129A. The sample, usually after freeze drying, is placed in a boat in the combustion tube. Sample masses are usually 1-10 grams. A known amount (typically 10 Bq) of I-125 is added to the sample prior to combustion to measure the chemical yield.

The dimensions of the apparatus are--the silica furnace tube is 60 cm long and has an inside diameter of 2.4 cm. The high purity quartz trap sealed to the furnace tube has an inside diameter of 0.6 cm. In the small tube are a column (3 cm) of hydrated manganese dioxide followed by two columns (2 cm and 1 cm) of activated charcoal.

The combustion apparatus has two oxygen inlets which can be controlled independently. The inlet which terminates at the downstream end of the furnace tube assures complete combustion of volatile decomposition products of the sample. After sample destruction is complete, the large combustion tube is heated to 800 °C with a resistance furnace and a hand torch downstream to the HMD trap. The HMD trap is then heated with the torch to red heat for 5 minutes. The HMD accomplishes a partial decontamination from bromine and also removes a volatile white material, believed to be ammonium chloride.

The iodine is collected on the first charcoal trap. Oxygen flow rate is reduced, the first trap is ignited, and the iodine is collected on the smaller trap. The size of the charcoal trap to be irradiated is kept small to minimize the amount of fission product iodine which will be produced from uranium impurity in the charcoal. Finally, the tube containing the charcoal trap is sealed under vacuum. I-125 is assayed for yield determination and the sample is irradiated.

All irradiations are conducted in the pneumatic transfer facility RT-4 of the NBS research reactor. The thermal neutron flux is $1.3 \times 10^{13} \text{ n/cm}^2 \text{ sec}^{-1}$. Irradiations are typically conducted overnight.

After irradiation, the quartz tube containing the activated charcoal trap is rinsed with hot dilute acid. The tube is cooled in liquid nitrogen, wrapped in tissue paper along with a small piece of filter paper on which a solution containing

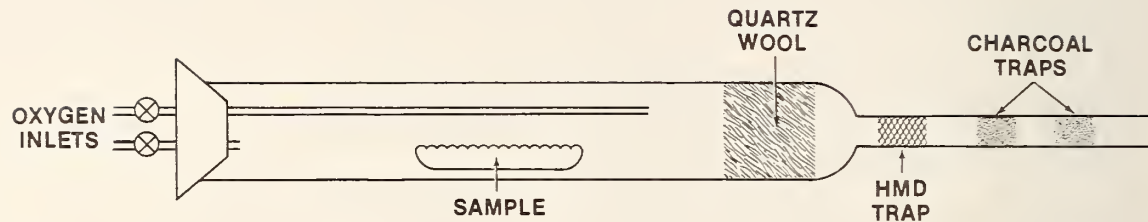


Figure 1. Apparatus for pre-irradiation separation of I-129.

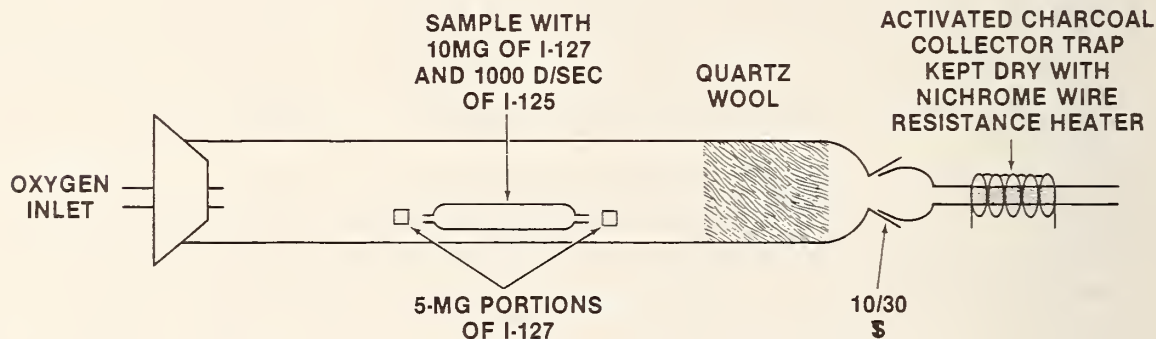


Figure 2. Apparatus for separating iodine from the bulk of the irradiated sample

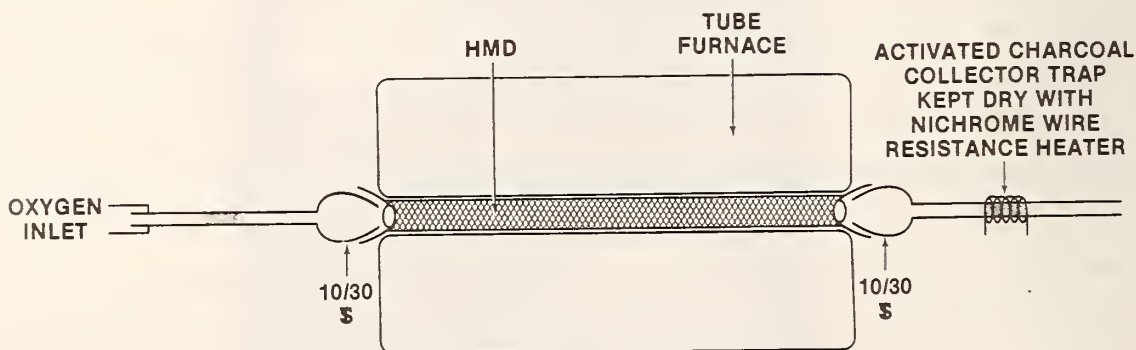


Figure 3. HMD trap.

10 mg of I-127 and approximately 1000 Bq of I-125 has been evaporated, and the tube is then broken. This is placed in a furnace tube with two 5 mg portions of I-127, as shown in figure 1. The oxygen flow is adjusted and the apparatus is heated from the downstream I-127 to the activated charcoal trap. The downstream I-127 is then heated strongly. The liberated iodine rinses the system finally being collected in the charcoal trap. Then the sample with carrier and I-125 spike is burned to liberate the iodine. Finally, the upstream iodine is liberated as a final purge of the system. During the procedure, the apparatus is heated sufficiently to assure that no iodine can condense anywhere in the system except on the charcoal trap.

Finally, the charcoal trap containing the iodine is connected to an HMD column as shown in figure 3. The oxygen flow is adjusted and the HMD is heated in a small tube furnace to 200 °C. The charcoal containing the iodine and other volatiles is ignited. After the trap is burned, the ash is heated strongly to assure complete combustion. The HMD trap is rapidly brought to 600 °C and held there for 10 minutes. The assembly is allowed to cool and the collection trap is assayed for iodine yield and bromine decontamination. The procedure can be repeated, if necessary, with fresh HMD columns. When adequate bromine decontamination is achieved, the collection trap is assayed for yield and finally cooled overnight for I-130 content. A lower limit of determination of approximately 2×10^8 atoms/gram of sample is usually achievable.

d. Elemental Characterization of the New Milk Powder SRM Via Instrumental and Radiochemical Neutron Activation Analysis

R. R. Greenberg

Well characterized reference materials have proven to be valuable aids in verifying the accuracy of analytical procedures. The need for suitable reference materials is particularly acute for quality assurance of trace element analyses in the biological and medical fields. It is generally recognized that a number of trace elements produce toxic effects at very low levels and so accurate measurements of their concentrations in foods, animal tissues, and other biologically important materials are often necessary. Other elements are essential, in trace quantities, for human nutrition and therefore accurate determinations of their concentrations in various foods may be required. Unfortunately, accurate trace and ultra-trace level analyses of foods and animal tissues are often extremely difficult due to a wide variety of problems including chemical blank, sample contamination, matrix effects, interferences, losses during sample dissolution, etc. This was recently illustrated by a round-robin intercomparison of milk powder¹ conducted by the International

Atomic Energy Agency (IAEA). Some of the results of this study are summarized in table 1. The reported concentrations of a number of biologically important elements varied over a range of three orders of magnitude and the reported Cr concentrations varied by almost five orders of magnitude; clearly indicating the need for suitable reference materials in ultra-trace level analysis.

The National Bureau of Standards is currently preparing a Milk Powder Standard Reference Material to provide assistance in overcoming the difficulties in accurate, ultra-trace analysis of foods and other biologically important materials. As part of the certification process, this Milk Powder has been analyzed by neutron activation analysis (NAA), as well as by a number of other analytical techniques. For a number of important elements in milk, neutron activation analysis possesses the required sensitivities and is free from interferences and other matrix effects. It also can be performed in a blank-free manner and thus not be limited by reagent blank.

The concentrations of 21 elements, including all those listed in table 1, have been determined in the NBS Milk Powder SRM by NAA and are listed in table 2. Both instrumental and radiochemical procedures have been employed. All sample preparation (pre-irradiation) steps were performed in a class-100 clean room to prevent sample contamination. Standard instrumental procedures were used; however, extremely long counts were required for some elements, and additional care was required to integrate some peaks on the high phosphorus bremsstrahlung background. A number of different

Table 1. Ranges of concentrations reported in IAEA Milk Powder^a concentration - $\mu\text{g/g}$ unless indicated.

Element	Lowest Value	Highest Value
As (ng/g)	4.45 \pm 0.14	544 \pm ? ^b
Cd (ng/g)	1.1 \pm 0.1	1660 \pm 200
Co	0.004 \pm ?	51.5 \pm 2.1
Cr	0.016 \pm ?	1160 \pm ?
Cu	0.082 \pm ?	72.2 \pm 2.4
Fe	0.70 \pm 0.11	281.8 \pm 6.1
Hg (ng/g)	1.33 \pm 0.57	667 \pm 52
Sb (ng/g)	1.16 \pm 0.13	1010 \pm ?

^aFrom reference 1.

^bNo uncertainty reported.

Table 2. Elemental concentrations determined in Milk Powder (SRM 1549) by neutron activation analysis.

Element	Units	Mean \pm 2s
As ^a	(ng/g)	1.8 \pm 0.2
Br	(μ g/g)	11.6 \pm 0.8
Ca	(%)	1.33 \pm 0.04
Cd ^a	(ng/g)	0.47 \pm 0.14
Cl	(%)	1.085 \pm 0.009
Co	(ng/g)	4.1 \pm 0.5
Cr ^a	(ng/g)	3 \pm 2
Cs	(ng/g)	17.6 \pm 1.2
Cu ^a	(ng/g)	606 \pm 9
Fe	(μ g/g)	1.8 \pm 0.3
Hg ^a	(ng/g)	0.16 \pm 0.03
I	(μ g/g)	3.2 \pm 0.8
K	(%)	1.69 \pm 0.04
Mg	(μ g/g)	1190 \pm 60
Mn	(ng/g)	230 \pm 30
Mo ^a	(ng/g)	310 \pm 30
Na	(μ g/g)	4890 \pm 40
Rb	(μ g/g)	12.4 \pm 0.3
Sb ^a	(ng/g)	0.24 \pm 0.08
Se ^{a,b}	(ng/g)	110 \pm 3
Zn	(μ g/g)	46.6 \pm 0.9

^aConcentrations determined after radiochemical separation.

^bSe concentration also determined instrumentally (110 \pm 9).

radiochemical separation procedures were used to analyze the Milk Powder and some of these had to be modified to further isolate the elements of interest from the background-elevating matrix elements. An improved group separation, based on the inorganic-ion exchanger HMD (hydrated manganese dioxide), made it possible to analyze As, Cr, Mo, Sb, and Se. Individual separations using solvent extraction procedures with appropriate metal diethyldithiocarbamate compounds allowed Hg, Cu, and Cd to be determined.

When certification is completed, the Milk Powder SRM will be an extremely useful reference material for trace and ultra-trace analyses in biological matrices. The determination of trace elements at these low levels illustrates the advantage of NAA being essentially blank-free.

1. R. Dybczynski, A. Veglia, and O. Suschny, "Report of the Intercomparison Run A-11 for the Determination of Inorganic Constituents of Milk Powder," IAEA Report RL/68, July 1980.

2. Neutron Depth Profiling at the National Bureau of Standards

R. G. Downing, R. F. Fleming, J. K. Langland, and D. H. Vincent

The National Bureau of Standards recently has established a dedicated thermal neutron depth profiling (NDP) facility. The NDP technique, originally developed in 1972 by Ziegler et al.,¹ has proven valuable in the measurement of concentration versus depth distributions. Table 1 lists principal elements, sensitivities, and the nuclear reactions that are utilized by NDP. The physics of the technique is discussed in references (1) and (2). Analyses are virtually nondestructive and nearly independent of either matrix effects or the chemical state of the material.

a. Description of Facility

1. Beam quality and collimation

The NBS 10 MW, enriched-uranium fueled, heavy-water (D_2O) moderated reactor provides a high intensity source of neutrons. A series of steel, lead, and cadmium collimators 1.22 m long defines the neutron beam as it passes through the reactor's biological shield to the NDP target chamber. The emerging neutron beam is 9.5 mm in diameter with an intensity of $3 \times 10^8 n/s$. Figure 1 shows the vertical profile of the neutron beam at the sample position measured with a thermal neutron radiograph. The beam intensity remains uniform over the 9.5 mm central region and decreases smoothly with a full width at half maximum of 13 mm. Gamma radiography shows that the gamma

ray component of the beam has much the same shape. Table 2 compares the characteristics of other NDP facilities for which published information exists.

A high quality NDP beam should have good thermal neutron intensity and minimum contamination with fast neutrons and gamma rays. Figure 2 shows the neutron source, filters, and optics used to accomplish this. The split-core design of the NBS reactor means that the beam tube views the heavy-water region between the fuel but does not see the intense gamma and fast neutron source of the U-235 itself. The filtering of the beam through 200 mm of single crystal sapphire³ and 80 mm of single crystal silicon further reduces the epithermal neutron and gamma ray components entering the collimator. The result is an intense thermal neutron beam with a cadmium ratio for gold of greater than 10^4 and a gamma intensity of about 200 mr/h.

2. Target chamber

The NDP target chamber (figure 3) is constructed of aluminum to reduce mass and background and is designed in three major pieces. The base plate contains the electrical feed-throughs and vacuum port and is mounted on two machine ways to provide precise adjustment in the horizontal and vertical directions perpendicular to the beam. The chamber wall is machined from a 305 mm I.D. tube and contains the

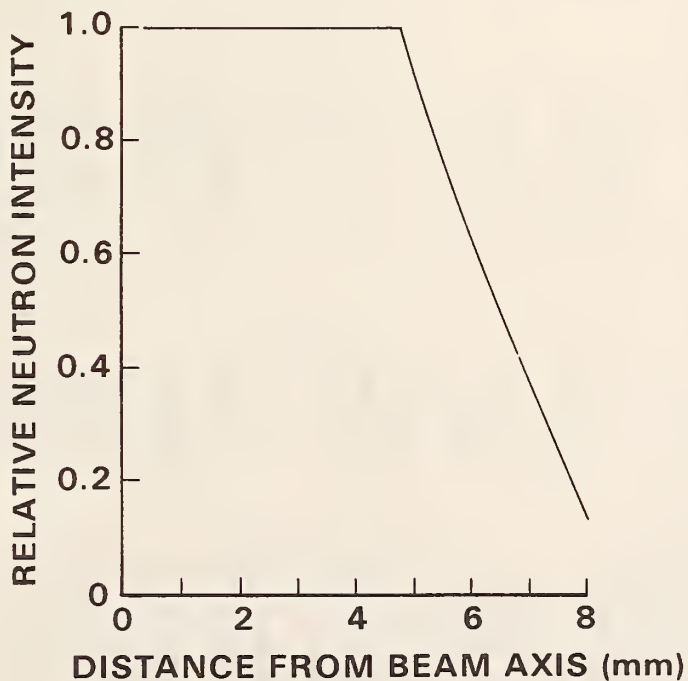


Figure 1. Vertical neutron intensity profile taken by Au-198 autoradiography at the sample position in the target chamber.

Table 1. Summary of reaction characteristics for neutron depth profiling. The sensitivity for the target nucleus was calculated assuming 0.1 counts per second, 0.1% detector solid angle and a neutron intensity of 3×10^8 s⁻¹.

Elem.	Reaction	Target Half-life	atoms/mci or (% abun.)	Energy of Emitted Particles in (keV)	Cross Section (barns)	Sensitivity (atoms/cm ²)
He	$^3_{\text{He}}(\text{n},\text{p})\text{T}$	Stable	(0.00014)	573	191	5327
Li	$^6_{\text{Li}}(\text{n},\alpha)\text{T}$	Stable	(7.5)	2056	2728	940
B	$^{10}_{\text{B}}(\text{n},\alpha)^7_{\text{Li}}$	Stable	(20.0)	1472	840	3836
Be	$^{7}_{\text{Be}}(\text{n},\text{p})^7_{\text{Li}}$	53 day	2.5×10^{14}	1439	206	48000
Na	$^{22}_{\text{Na}}(\text{n},\text{p})^{22}_{\text{Ne}}$	2.6 year	4.4×10^{15}	2248	102	36000
Ni	$^{59}_{\text{Ni}}(\text{n},\alpha)^{56}_{\text{Fe}}$	8×10^4 yr	1.3×10^{20}	4753	340	12
N	$^{14}_{\text{N}}(\text{n},\text{p})^{14}_{\text{C}}$	Stable	(99.63)	584	42	1.8
O	$^{17}_{\text{O}}(\text{n},\omega)^{14}_{\text{C}}$	Stable	(0.038)	1415	404	0.235
S	$^{33}_{\text{S}}(\text{n},\alpha)^{30}_{\text{Si}}$	Stable	(0.75)	3081	411	0.14
C1	$^{35}_{\text{Cl}}(\text{n},\text{p})^{35}_{\text{S}}$	Stable	(75.77)	598	17	0.49
K	$^{40}_{\text{K}}(\text{n},\text{p})^{40}_{\text{Ar}}$	Stable	(0.012)	2231	56	4.4
						7.6×10^{16}

Table 2. Reported parameters for neutron depth profiling facilities.

Institution/Reactor	Reactor Power MW	Neutron Flux - cm ⁻² s	Beam Diameter mm	Cadmium Ratio	Gamma Dose Rate mr/h	Beam Filtering
Institut Max von Laue-Paul Langevin/High-Flux Reactor [4,5]	57	1 x 10 ⁹	10	~	30	Neutron Guide Tube
Brookhaven National Laboratory/High-flux Beam Reactor [1]	60	2.3 x 10 ⁸	20	?	?	?
Hahn-Meitner-Institut f. Kernforschung Berlin/ BER II [5]	5	3 x 10 ⁷	>20 (variable)	>3 x 10 ⁴	3 x 10 ³	20 cm Single Crystal Bi
Czechoslovak Academy of Sciences/VVR/S CsKAЕ Research Reactor [6]	6	1.6 x 10 ⁸	65	?	?	30 cm Single Crystal Si
University of Michigan/Ford Nuclear Reactor [7]	2	1.4 x 10 ⁷	13 x 12	2.8	?	None
National Bureau of Standards/NBS Research Reactor	10	4 x 10 ⁸	9.5	>10 ⁴	200	20 cm Single Crystal Sapphire

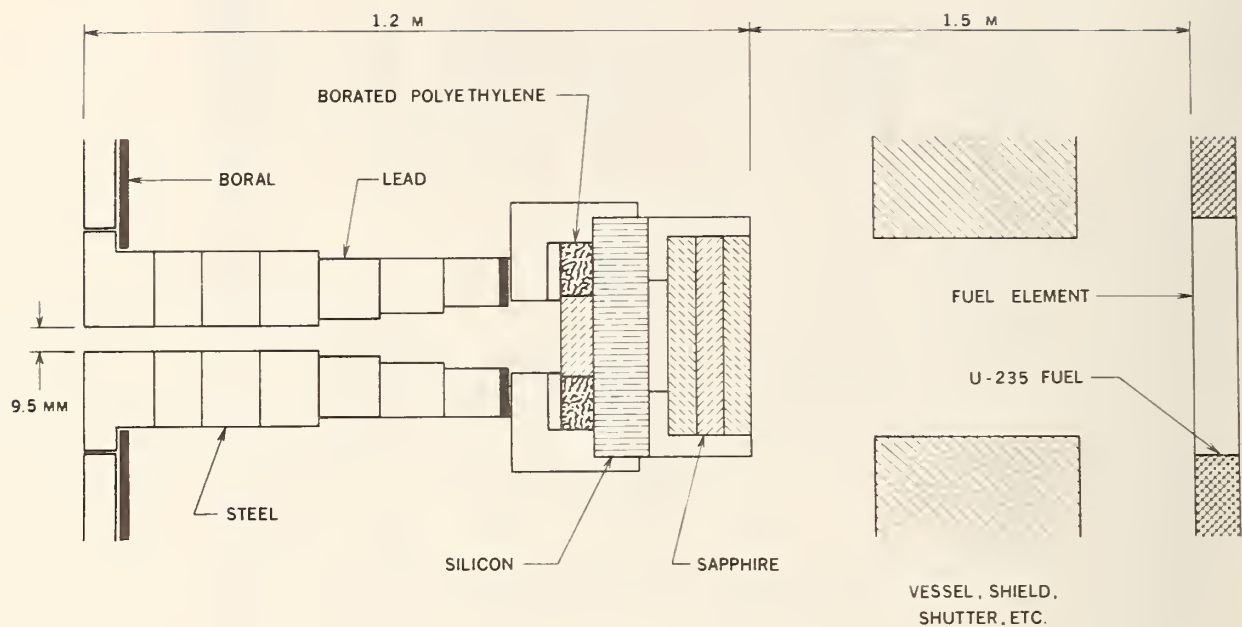


Figure 2. Side view of the reactor neutron source and the neutron collimator and filter.

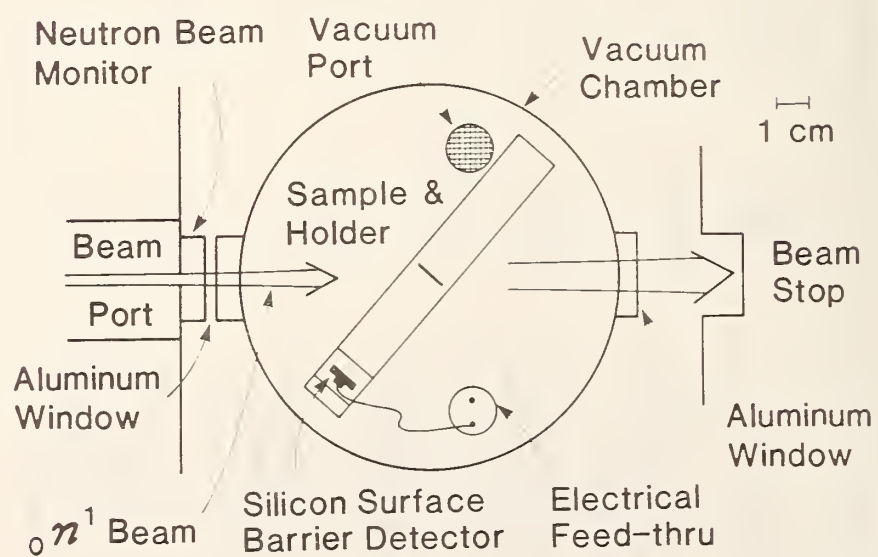


Figure 3. Neutron depth profiling target chamber.

NBS Neutron Depth Profiling Electronic Diagram

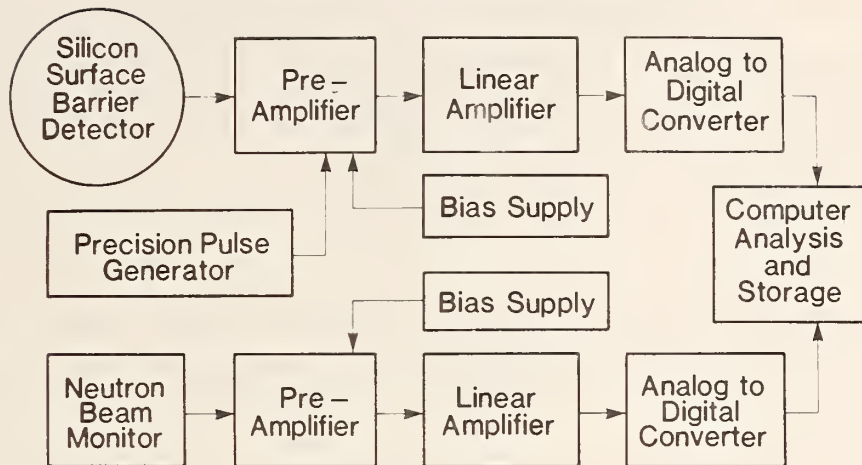


Figure 4. Diagram of the data acquisition and analysis electronics.

50 mm diameter by 0.13 mm thick aluminum entrance and exit windows for the neutron beam. The top plate contains an 85 mm diameter quartz viewing window, kept covered during operation. The three sections are joined by two rubber O-rings to provide the vacuum seal. Initial pump-down is accomplished with a compressed-air driven Venturi pump followed by a liquid-nitrogen cooled sorption pump. During operation the vacuum is maintained at 10^{-4} Pa by a 30 L/s ion pump.

3. Electronic components

Figure 4 shows a diagram of the data acquisition electronics. A silicon surface-barrier detector with an 11 mm active diameter is used to measure the charged particle spectrum from the sample. A high precision reference pulse is fed into the preamplifier parallel to the signal allowing the monitoring and correction of any gain shift in the electronics. The neutron beam intensity is monitored at the target chamber entrance window. All signals are processed and the spectra stored in a dedicated computer-based multi-channel analyzer to provide real-time display of depth profiles.

4. Conclusions

Steps to improve the beam quality, beam intensity, detection sensitivity, and resolution are planned. In addition to the applications described elsewhere in this report, the facility is intended to contribute to the certification of depth profiling Standard Reference Materials. The profiling of bismuth⁸ using the delayed alpha emission of Po-210 is being carried out in parallel to the neutron beam profiling described here.

We would like to acknowledge the following people for helpful discussions and for supplying samples: J. R. Ehrstein, Center for Electronic and Electrical Engineering, NBS; J. R. Riley, Jr., Bell Telephone Laboratories, Murray Hill, NJ; and J. N. Cox, Intel Corporation, Santa Clara, CA.

-
1. J. F. Ziegler, G. W. Cole, and J. E. E. Baglin, *J. Appl. Phys.* 43, 3809 (1972).
 2. J. P. Biersack, D. Fink, R. Henkelmann, and K. Muller, *Nucl. Instr. and Meth.* 149, 93 (1978).
 3. H. F. Nieman, D. C. Tennant, and G. Dolling, *Rev. Sci. Instrum.* 51, 1299 (1980).
 4. K. Muller, R. Henkelmann, and H. Boroffka, *Nucl. Instr. and Meth.* 129, 557 (1975).
 5. D. Fink, J. P. Biersack, and H. Liebl, Proc. of the Fourth International Conf. on Ion Implantation: Equipment and Techniques, Berchtesgaden, Sept. 1982 (to be published).
 6. J. Cervena, V. Hnatowicz, J. Hoffmann, Z. Kosina, J. Kvitek, and P. Onheiser, *Nucl. Instr. and Meth.* 188, 185 (1981).
 7. W. G. Halsey, Ph.D. Thesis, University of Michigan, 1980 and D. Wehe, priv. comm. (1983).
 8. R. G. Downing, R. F. Fleming, D. S. Simons, and D. E. Newbury, *Microbeam Analysis-1982*, ed. K. F. J. Heinrich (San Francisco Press, 1982). p. 219.

b. Thermal Release of Ion-Implanted He-3 from Single Crystal Nickel Samples

D. H. Vincent, J. T. Maki, R. G. Downing, and R. F. Fleming

A new approach to the problem of identifying trapping sites and trap binding energies for helium in metals at low helium concentrations has been developed. This is based on using ion implantations of He-3 and subsequent depth profiling of the implanted helium using a thermal neutron beam. The thermal release of the helium is studied by measuring the depth distribution of the helium remaining in the sample after each anneal. While this method has been used before to observe helium release from molybdenum, niobium, and copper, this work will represent the first unambiguous determinations of detrapping energies.

The diffusion and trapping of helium, as well as of other inert gases in metals, became of great practical interest during recent years because of materials problems related to nuclear energy production, e.g., the void formation in structural materials under neutron bombardment in fission reactors and the ablation of first wall materials in future fusion reactors.

Since the solubility of helium in metals is quite low, studies often require the introduction of helium atoms into a metal by implantation as helium ions in an accelerator. It has been found that, if such implantations are performed at ion energies above a few keV, with the sample held at room temperature, the implanted helium is quantitatively trapped. Each helium atom is trapped very close to the end of its range in the metal, so that concentration profiles of the implanted helium can be used to determine range distributions of the implanted ions. An example of such a range distribution is shown in Figure 1. If a metal sample containing implanted helium is brought to a sufficiently high temperature, some or all of the helium atoms will be released from their trapping sites. Once the helium is detrapped, it is released from the metal surface almost instantaneously, indicating a very large diffusivity for helium in metals.

Most of the measurements dealing with helium in nickel have been done as desorption experiments in which helium-implanted samples were subjected to a temperature ramp, and the helium release was observed by mass spectroscopy. Implantation energies were usually low (of the order of 1 to 10 keV), and implantation surface doses were comparatively high, so that the formation of helium atom aggregates was likely before release.

The present work differs from previous investigations in two respects. First, a relatively high implantation energy is used (150 keV), and the implantation dose is kept low enough, so that the formation of larger helium aggregates (bubbles) is

avoided as much as possible. Secondly, helium release is being observed not by measuring the amount of gas released through the surface of the sample, but by observing changes in the helium concentration inside the sample as a function of depth. Using this method, it will be possible not only to measure activation energies for helium detrapping, but also to relate the activation energies to specific trapping sites along the range distribution of the implanted ions.

The activation energy for helium detrapping is likely to depend on the particular kind of lattice defect at which the helium is trapped. In order to reduce the variety of trapping sites as much as possible, single crystal nickel samples are used for helium implantation. This confines the helium traps mainly to isolated vacancies and excludes trapping at extended defects such as dislocations and grain boundaries.

Samples for helium implantation were prepared by cutting slices of approximately 1 mm thickness from a single crystal nickel rod. One surface of each slice was carefully polished and its crystallinity tested by obtaining a Laue x-ray pattern. These patterns indicate that the normal of the samples is well away from any ion channeling direction, so that helium ion channeling should not occur during implantation if the sample surface is perpendicular to the ion beam axis.

A first set of samples has been implanted with He-3 ions at an ion implantation accelerator at the Naval Research Laboratory. Precautions were taken to prevent ion beam heating of the samples during implantation. Ion beam currents of approximately 300 nA were used, and implantation surface doses were 2×10^{16} , 1×10^{16} , 6×10^{15} , and 1×10^{15} He-3 ions/cm². The largest dose (2×10^{16} He-3 ions/cm²) produced a maximum concentration of about 0.9 atom% He-3 at the peak of the range distribution for 150 keV He-3 ions. This may be compared with the solubility of helium in nickel at room temperature which is = 1×10^{-7} atom%.

The depth distribution of the helium after implantation was measured at the Neutron Depth Profiling facility at the NBS research reactor. The distance from the surface of specific implanted He-3 atoms was determined by measuring the energy loss of protons from the nuclear reaction $^3\text{He}(n,p)^3\text{H}$. This reaction has a large cross section at thermal neutron energies (5327 barns) and produces protons with an energy of 572.5 keV. The energy spectrum of protons emerging from the surface of the sample as it is irradiated with thermal neutrons is measured with a silicon surface barrier detector. This energy spectrum was converted to a depth distribution for the implanted He-3 atoms with the aid of the known proton stopping power (dE/dx) in

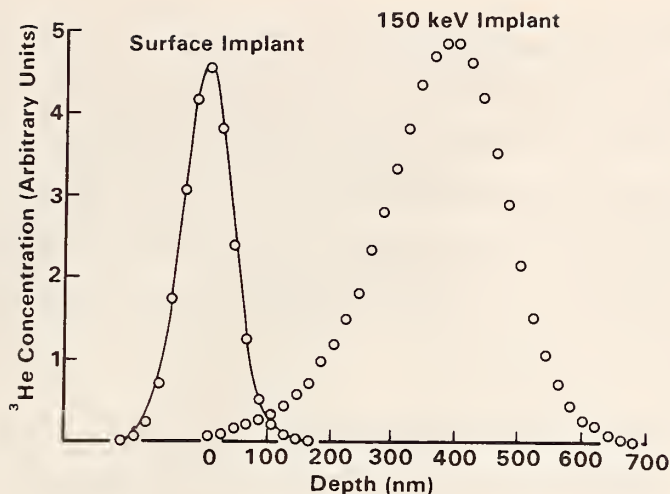


Figure 1. Helium depth profiles in nickel for a 150 keV implant, and for a 250 eV surface implant which represents the system resolution function.

nickel. Figure 1 shows the depth distribution of helium atoms in a sample implanted with 150 keV He-3 ions to a surface does of 2×10^{16} He-3 ions/cm². This depth distribution is broadened by the energy resolution of the detector and the associated electronic equipment. To indicate the width of the resolution function, a spectrum from a surface implantation of helium ions (250 eV implantation energy) is also shown in figure 1. The mean projected range of the 150 keV implant is 372 nm. This compares well with the value of 367 nm obtained by interpolation from a set of theoretical mean ranges at various energies given by Biersack et al.¹

Annealing experiments on the implanted samples are in progress. Activation energies for detrapping of the implanted helium will be determined by a combination of isochronal and isothermal anneals. It is planned to extend the present work to include He-3 profiling and thermal release studies of nickel-based metallic glasses. Both the trapping efficiencies and the detrapping behavior will be investigated. A further application of He-3 depth profiling will be the decoration of radiation-induced defects in pure metals, in metallic glasses, and in silicate glasses. Of these, the silicate glasses may be the most promising materials for an application of this method, since helium is known to permeate these materials easily at room temperature. Preliminary experiments on this new application of He-3 depth profiling are planned.

1. J. P. Biersack, D. Fink, R. Henkelmann, and K. Muller, *J. Nucl. Mater.* 85/86, 1165 (1979).

c. Neutron Depth Profiling of Boron

R. F. Fleming, R. G. Downing, J. E. Riley Jr., and D. H. Vincent

The first year of neutron depth profiling (NDP) at the NBS Reactor¹ has focused on the determination of the concentration profiles of B-10 in the near-surface region of several materials. The samples chosen demonstrated the technique in semiconductors, glasses, and glassy metals. Work on boron distributions in metals is in progress.

1. B-10 Ion-Implanted Silicon

Neutron depth profiling was first used to determine the distribution of ion-implanted boron in silicon.² Since then, a considerable amount of data on boron profiling in silicon has accumulated. It seemed, therefore, appropriate to use the measurement of boron profiles in silicon as a test for the performance of the neutron depth profiling facility. We have measured depth profiles of B-10 implanted into <111> oriented silicon wafer with energies of 70 keV and 200 keV and B-10 surface doses of $4 \times 10^{14} \text{ cm}^{-2}$, $1 \times 10^{15} \text{ cm}^{-2}$, $4 \times 10^{15} \text{ cm}^{-2}$, and $1 \times 10^{16} \text{ cm}^{-2}$. The wafers had been tilted 7Z with respect to the beam axis during implantation to avoid channeling effects.

We find that our results for the projected range and the range straggling agree within a few percent with values obtained by interpolating between - or extrapolating from - experimental results obtained by Ryssel et al.³ who used implantation energies different from ours. Like these authors we observe a considerably larger straggling than predicted by theoretical calculations which is thought to be due to residual channeling. Our values for range and range straggling were obtained directly from the first and second moments of the raw data after background subtraction but without fitting a Pearson-IV distribution to the data. Shown in Figure 1 is a typical profile compared to a secondary ion mass spectrometry (SIMS) measurement of a $10^{16} \text{ atom/cm}^2$, 70 keV implant. The narrow peak at 200 nm on the broad distribution is a boron precipitate formed at those depths where the concentration exceeds the solubility of boron in silicon.

2. Boron Depletion of Glass Surfaces

Recently the distribution of boron near the surface of borosilicate glasses has been of concern.⁴ We have measured the relative boron concentration in a number of borosilicate glasses whose surfaces had undergone various surface treatments. Figure 2 gives an indication of the depth resolution of the method. It shows the gradient of the boron concentration across the surface of two borosilicate glass samples (12.6 wt% B_2O_3), broadened by the finite resolution of our detection system.

The data in the figure were obtained by subjecting the observed energy distribution of the 1472.3 keV alpha particles from the $^{10}\text{B}(\text{n},\alpha)^7\text{Li}$ reaction to a 7-point quadratic smoothing followed by a 3-point first order differentiation.⁵ The left-hand peak is the result for an untreated surface obtained by fracturing one of our samples. The derivative of the boron distribution is centered about depth zero and has a width (FWHM) of 50 nm, corresponding closely to the resolution of the detection system. The other peak was obtained for an aqueously polished sample [sample E of ref (4)]. The shift of the peak indicates a depletion of boron in the first 15 nm of the sample. In addition we observe a broadening of the peak to 60 nm which shows that the boron concentration of the polished surface rises to the bulk value less steeply than that of the fractured glass surface.

3. Boron Distribution in Borophosphosilicate Glass

Borophosphosilicate glass (BPSG) is used as an insulating layer and for forming tapered contours over steep steps of oxide and silicon on high density integrated circuits.⁶ Boron, added to lower the glass's flow-point temperature, needs to be evenly distributed in the film to insure continuity and uniformity of the flow during circuit fabrication. Knowledge of film thickness is also required for production of state-of-the-art multilayer circuits. Figure 3 is an overlay of two NDP measurements made on a BPSG film. The boron distribution is shown both for the film as it was deposited on a silicon wafer and for the same film after processing. NDP is able to determine in a single nondestructive measurement the sample thickness, the homogeneity of the boron distribution, and its absolute concentration at discrete depths. Together the plots show the leveling of boron distribution after processing and the apparent removal of some of the matrix. Nonetheless, the integrals of the two peaks are equal, indicating no boron loss has occurred.

4. Boron Distribution in Iron-Boron Metallic Glasses

Thin films of sputter deposited $\text{Fe}_{0.8}\text{B}_{0.2}$ metglass were provided by Professor Lawrence Pilione of Pennsylvania State University. Figure 4 shows a spectrum obtained with a sample of 1 μm thickness consistent with a uniform boron distribution.

5. Future Work

Work is in progress for extending the NDP technique to the profiling of lithium, sodium, and beryllium. These samples include Na-22 in semiconductor silicon, Be-7 in GaAs, and Li-6 diffused into high-purity copper.

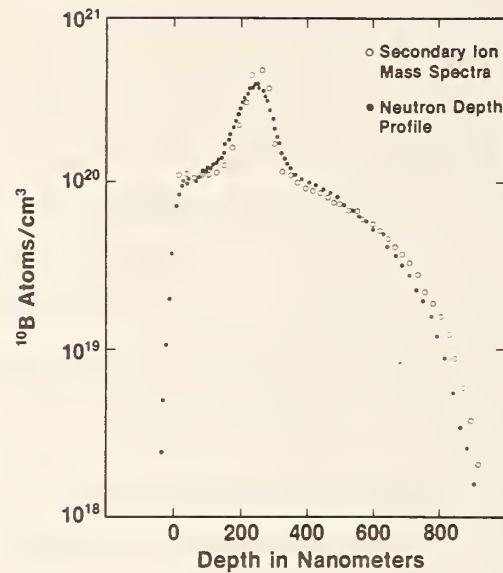


Figure 1. Comparison of SIMS and NDP results for a 70 KeV Boron-10 implant in Silicon at 10^{16} $^{10}\text{B}/\text{cm}^2$ annealed for 30 minutes at 1000°C.

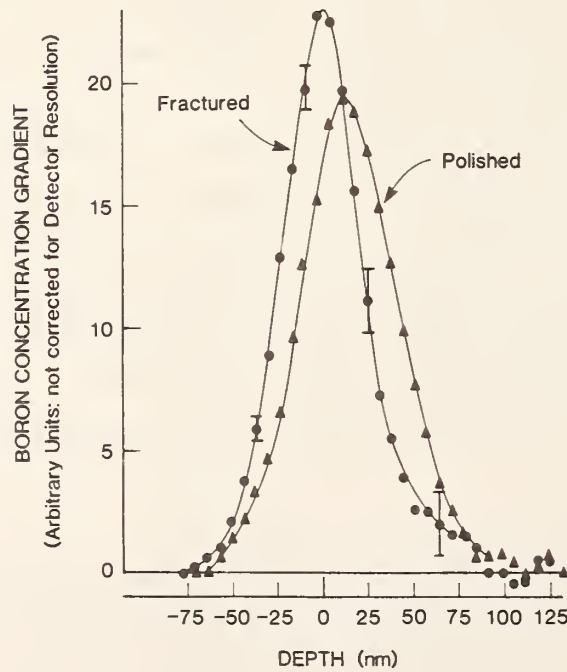


Figure 2. Boron concentration gradient-broadened by the system resolution - across two surfaces of the same glass: fractured surface and aqueously polished surface.

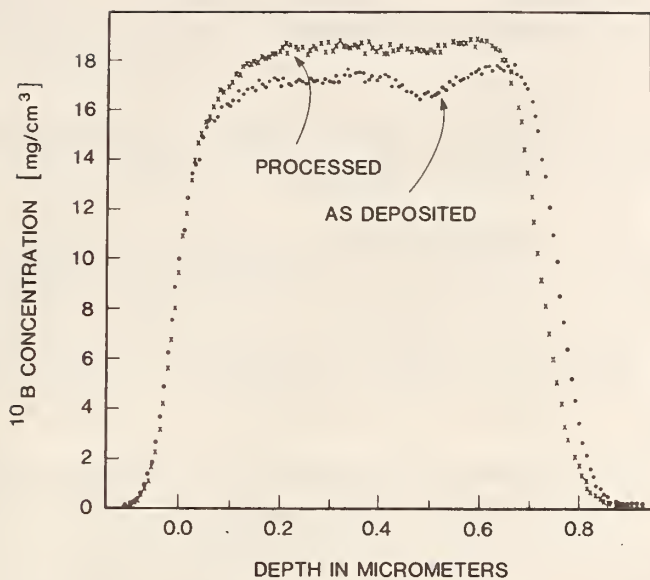


Figure 3. Boron concentration as a function of depth for a borophosphosilicate film on silicon as-deposited and after processing.

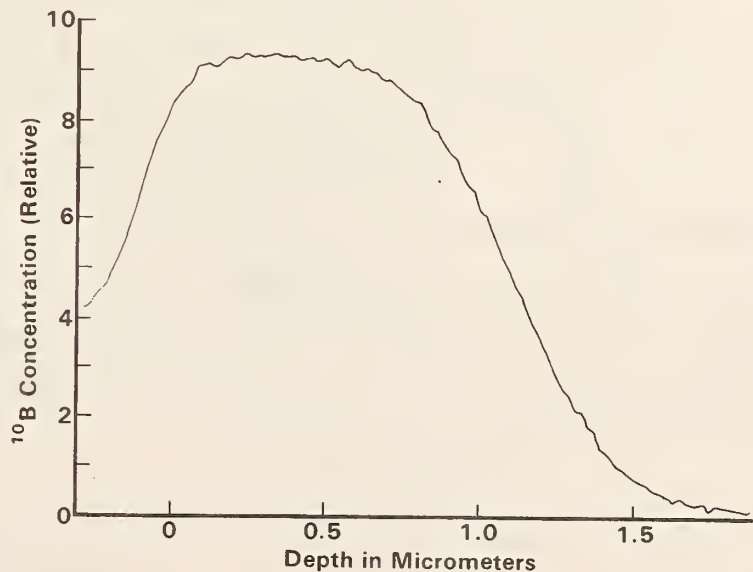


Figure 4. Boron concentration profile across a uniform $\text{Fe}_{0.8}\text{B}_{0.2}$ metglass, not corrected for detector resolution.

-
1. R. G. Downing, R. F. Fleming, J. K. Langland, and D. H. Vincent, "Neutron Depth Profiling at the National Bureau of Standards", Nuclear Inst. and Methods, (in press).
 2. J. F. Ziegler, G. W. Cole, and J. E. E. Baglin, "Technique for Determining Concentration Profiles of Boron Impurities in Substrates", J. Appl. Phys. 43, 3809 (1972).
 3. H. Ryssel, G. Prinke, K. Haberger, K. Hoffman, K. Müller, and R. Henkelmann, "Range Parameters of Boron Implanted into Silicon", Appl. Phys. 24, 39 (1981).
 4. D. L. Malm and J. E. Riley, Jr., "Characterization of Near Surface Composition of Borosilicate Glasses (BS6) by Secondary Ion Mass Spectrometry", J. Electrochem. Soc. 129, 1819 (1982).
 5. A. Savitzky and M. J. E. Golay, "Smoothing and Differentiation of Data by Simplified Least Squares Procedures", Anal. Chem. 36, 1627 (1964).
 6. W. Kern and G. L. Schnable, "Chemically Vapor-deposited Borophosphosilicate Glasses for Silicon Device Applications", RCA Review 43, 423 (1982).

3. Facilities for Activation Analysis

a. New MCA System

R. M. Lindstrom

As part of a continuing program of modernization of equipment, the PDP11/44 computer has been equipped with a multichannel analyzer to allow it to be used in data acquisition. In consultation with several domestic manufacturers, a modern data acquisition and processing system based on this computer has been defined which will make possible accurate measurements of elements which give activation products with half-lives as short as 1 sec. This application requires that the system be able to perform spectroscopy accurately at rapidly varying counting rates as high as 10^5 /sec, and to measure time intervals to better than 5 msec. A request for proposals based on these requirements stimulated three responses, involving substantial improvements in capabilities over the previous state of the art. The new-generation equipment is expected to be delivered before the end of the fiscal year, after which numerous new applications will become possible.

b. Pneumatic Transfer System and Sample Changer

J. K. Langland

The counting of short-lived nucleides requires a rapid transfer from the irradiation facility to the counting environment. Our highest quality counting systems are three floors above the irradiation facility. An existing small rabbit (bunny) flight tube has been fitted with a counting receiver and automatic controls. A magazine bunny loader allows the system to double as a sample changer. Figure 1 shows the arrangement of the system.

The existing 7/8 inch flight tube from C-001 to B-121 is used, the receiver in C-001 is retained, and in room B-121, the original receiver has been removed and replaced with a counting receiver mounted on a GeLi detector. Additional components in B-121 include a flight line switching valve, a soft landing air cushion, and a lead storage cave for holding previously counted samples.

The new counting receiver permits automatic operation of the system. It is made of lucite so that the sample and bunny remain in it for counting. A second flight tube goes from the receiver to a lead storage cave several meters away. At the completion of counting, compressed air sends the bunny out of the receiver via

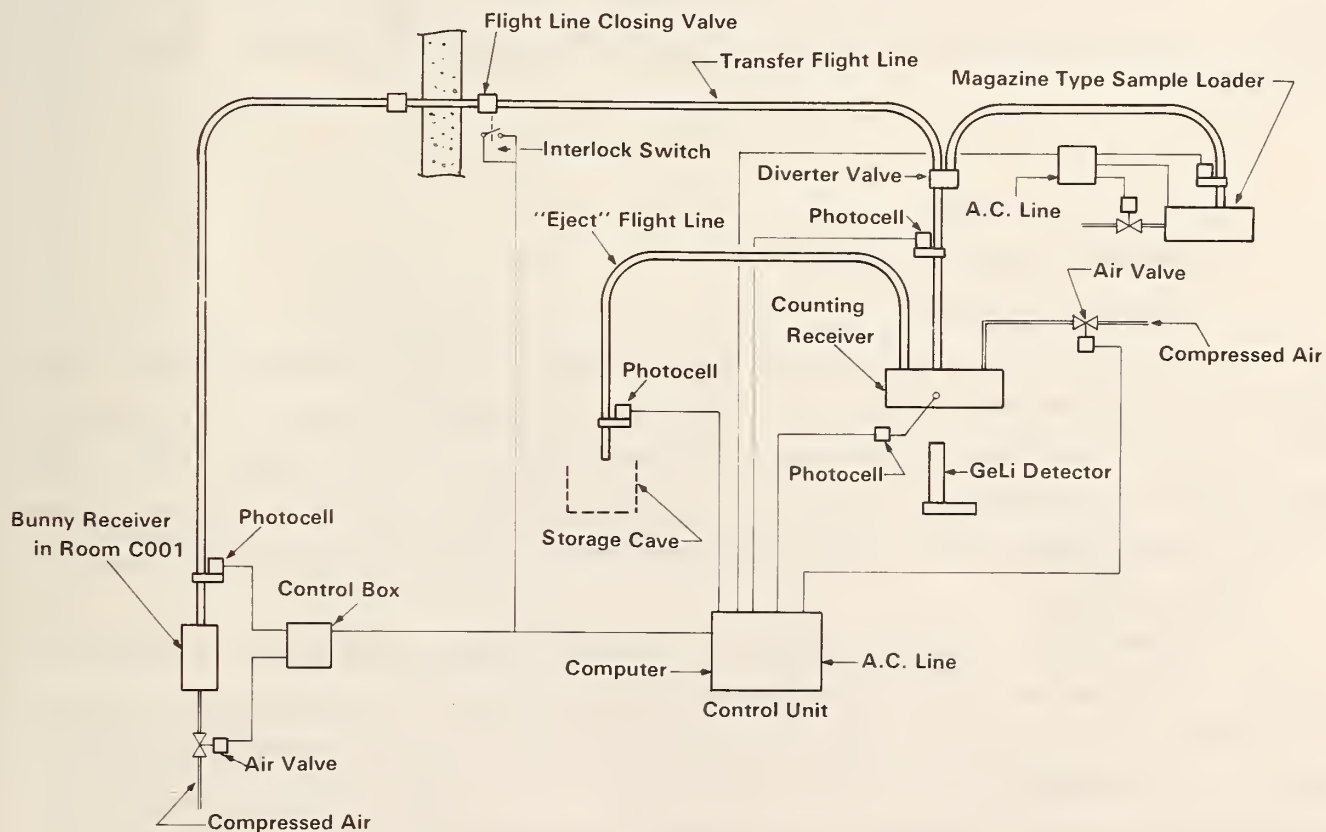


Figure 1. System Schematic

the second flight tube to the storage cave. The receiver is now ready to accept another sample. Counting geometry is manually adjustable from 0 to 65 cm.

A magazine type bunny loader is designed that will permit this system to be an automatic sample changer. A switching valve mounted in the flight line just before the air cushion allows selecting C-001 or the magazine loader as a sample source. As a sample changer, at the completion of a count, the bunny will be transferred to the storage cave and a new bunny transferred from the magazine loader to the counting receiver.

The controls consist of an electronic controller in B-121 and an auxiliary control panel in C-001. The system includes several photocell units, switches, indicator lights, and logic circuits to monitor bunny location, system status, fault conditions, and inform the operator of these conditions. Also included are interlock and shutdown circuits to prevent operation in the event of trouble (stuck bunny, valve malfunction, etc.). A computer interface is provided that allows our NO-6600, or D.E.C. computers, to control and monitor the system, both in shuttle and sample changer mode.

The automation of this system is providing safer sample handling, improved counting-timing accuracy, and uses less manpower. The sample changer allows fully automatic operation, permitting better use of the counting equipment during nights and weekends.

4. Collaborative Programs

a. Environmental Specimen Bank

S. F. Stone, R. Zeisler

In the past year, the Environmental Specimen Bank has continued banking and analyzing biological samples for trace elements and organic compounds. Instrumental Neutron Activation Analysis has been an integral part of the program. This year, a second sample type was added to the bank: Mytilus edulis, an aquatic accumulator. The first sample type, human livers, has continued to be collected and analyzed.

1. Human Livers

The banked livers were the subject of several areas of research. A homogeneity study was completed on an improved disk mill for cryogenic homogenization of samples up to 300 g. This study was used to confirm whether a one gram (fresh weight) test portion is representative of the whole liver. The data show no significant inhomogeneity at that sampling level, outside the errors due to counting statistics.

Table 1.

	Mytilus edulis - M2N005 ⁴	German Freshwater Mussel Homog.
Na	54200 ± 1000	nd
Mg	6430 ± 540	nd
Al	760 ± 70	nd
Cl	100000 ± 4900	nd
K	11700 ± 1500	nd
Sc	0.138 ± 0.007	0.699 ± 0.006
Cr	2.05 ± 0.20	14.8 ± 1.9
Mn	21.9 ± 1.2	nd
Fe	571 ± 27	978 ± 60
Co	0.538 ± 0.014	1.478 ± 0.013
Cu	≤ 70	nd
Zn	122 ± 5	154.7 ± 0.8
As	10.4 ± 1.0	6.90 ± 0.48
Se	2.47 ± 0.11	4.62 ± 0.15
Br	443 ± 40	38.6 ± 1.5
Rb	7.24 ± 0.56	0.251 ± 0.027
Mo	≤ 1.4	2.5 ± 0.3
Ag	0.104 ± 0.013	≤ 0.10
Cd	≤ 4	≤ 2.5
Sb	0.255 ± 0.007	0.033 ± 0.010
Cs	0.683 ± 0.003	0.165 ± 0.006
La	0.59 ± 0.09	0.472 ± 0.015
Ce	0.98 ± 0.10	0.79 ± 0.14
Sm	0.101 ± 0.014	0.130 ± 0.008
Eu	0.0193 ± 0.0004	0.557 ± 0.006
Hf	0.058 ± 0.011	59.0 ± 0.8
Hg	0.48 ± 0.24	≤ 0.2
Th	0.139 ± 0.006	nd

nd = not determined

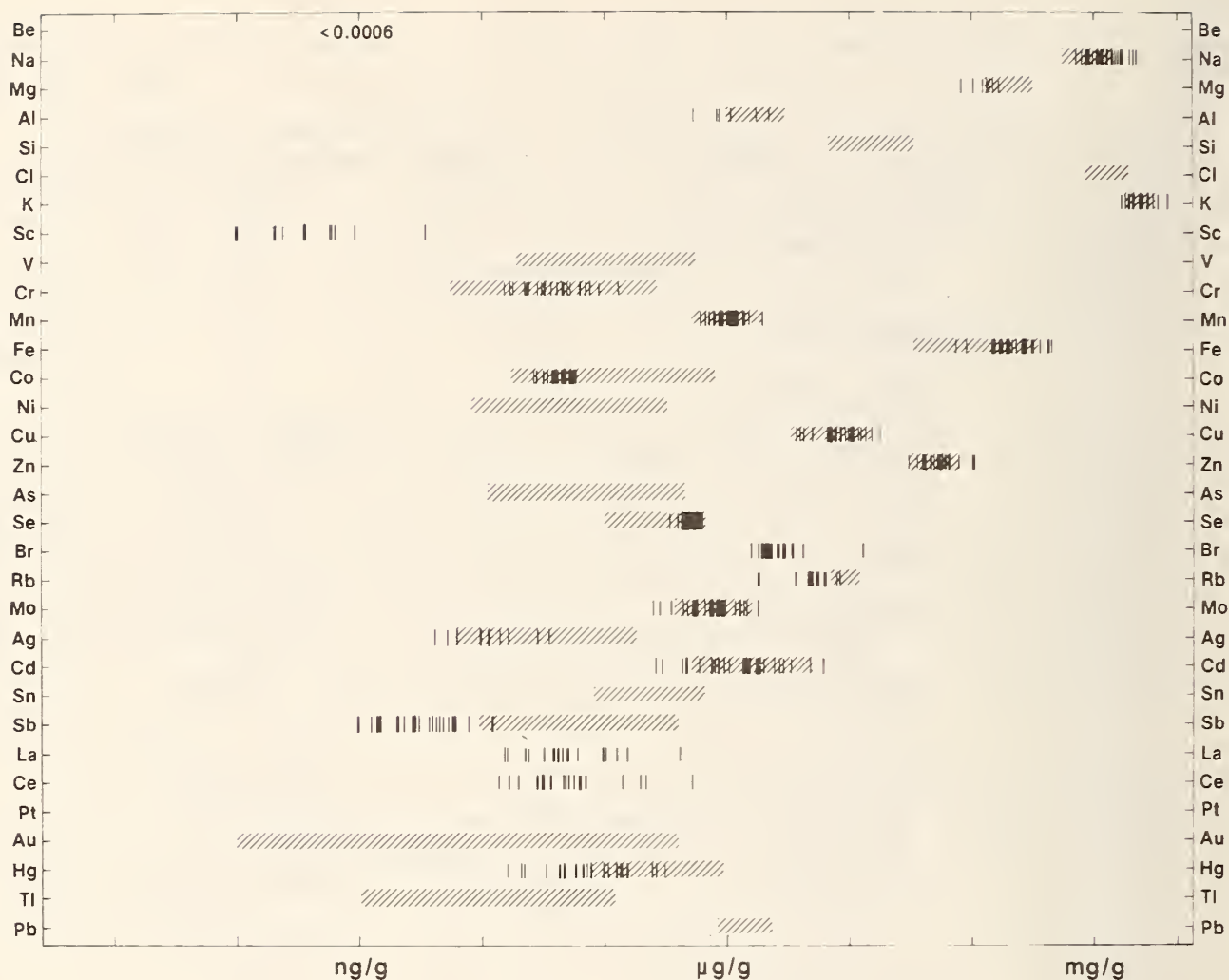


Figure 1. Human liver data.

Thus, the values depend more on the precision of the analytical technique rather than sampling uncertainty.

Liver collection has continued through our contractor in Seattle, Washington. As of June 1983, a total of 420 liver samples have been banked. Homogenization and analysis of the second year baseline samples were completed. This brings the total number of analyzed livers to 66. Figure 1 summarizes the distribution of elemental concentrations found during the second year of the study. The ranges are comparable to those found in the first year analyses.¹

A reanalysis of the first year samples has begun in order to evaluate the effects of the different storage conditions on elemental concentrations. In comparing data from samples stored at -25 °C, -80 °C, over liquid nitrogen vapor (-120 °C to -190 °C), and freeze-dried at room temperature, no significant changes have been found for trace elements.

2. Mussels

The marine mussels, Mytilus edulis, was added to the bank as the second environmental sample. Five-thousand mussels were collected from Narragansett Bay, Rhode Island, as part of a preliminary study to develop the sampling and analytical protocols. The mussels were separated into batches of seventy animals each and banked at four storage conditions: -25 °C, -80 °C, over liquid nitrogen vapor (-120 °C to -190 °C), and freeze-dried at room temperature. Two batches stored at liquid nitrogen temperatures have been homogenized and analyzed.

Concentrations for 28 trace elements were determined by neutron activation analysis. Table 1 shows the mean values and standard deviation for each of the elements. These values are compared to concentrations found in a mussel homogenate from the German Pilot Environmental Specimen Bank. The freshwater mussel homogenates were analyzed as part of an interlaboratory comparison of methods. Two major differences were noted in comparing the two sets of data. The hafnium level in the German homogenate was unusually high, almost 60 ppm. Also, the chromium levels in the same samples were more than ten times higher than in the marine mussels samples.

3. New Projects

A cooperative program is being developed with the Army Institute of Pathology. The goals are to look for possible relationships between elemental concentrations in different human organs and diseases, such as cancers. The study will begin with human liver tissue, but other organs will be studied as the program continues.

This cooperative effort is a positive indication that the technology developed for the Environmental Specimen Bank can be useful in many other areas. The research that has been involved in sample selection, transport, preparation, homogenization, storage, and analysis may be used throughout the scientific community.

-
1. R. Zeisler, "Results of the Inorganic Analysis of the First Year Human Liver Collection," The Pilot National Environmental Specimen Bank--Analysis of Human Liver Specimens, R. Zeisler, S. H. Harrison, and S. A. Wise, eds., National Bureau of Standards Spec. Publ. 656, 81-30 (1983).

ATMOSPHERIC AND ENVIRONMENTAL STUDIES BY INSTRUMENTAL NEUTRON ACTIVATION ANALYSIS

G. E. Gordon and W. H. Zoller
(University of Maryland, College Park, MD)

We continue to make extensive use of instrumental neutron activation analysis (INAA) to determine concentrations of about 35 elements in samples of atmospheric particulate matter collected from ambient air (now mostly at remote sites such as Hawaii and rural sites in the continental U.S.) and in particles released from major sources such as volcanoes. By measuring concentrations of such a large number of elements, we hope to be able to identify contributions from the sources to the atmospheric burden at ambient sampling sites. Examples of three studies are discussed briefly in the following sections.

1. Compositions of Atmospheric Particles at Mauna Loa Observatory, Hawaii

Until recently, there existed no long continuous record of concentrations of elements on particles at a site remote from local activities despite demonstration of the enormous value of the long-term CO₂ record (since 1957) at Mauna Loa Observatory (MLO) in Hawaii for observing CO₂ seasonal variations and long-term increase. Fortunately, since mid-1979, the National Oceanic and Atmospheric Agency (NOAA) has supported weekly collections of filters at MLO and analysis of them by our group using INAA. A distinct diurnal cycle exists at MLO at 3400 m alt, above the marine boundary layer: during the day, warming of the slopes of the mountain causes upslope winds whereas, during the night, cooling of air along the slopes causes downslope winds. Upslope conditions bring up air containing marine aerosol, crustal dust from the island and emissions from the small anthropogenic activity there. Downslope conditions bring down rather clean air from the upper troposphere. A control system alternately activates the pump on one of three filter systems depending on wind conditions and time-of-day to make separate collections of particles from upslope and downslope conditions. The third filter operates when neither condition is clearly established or when a condensation nuclei counter detects high counts due to contamination by motor vehicles, volcanic eruptions, etc.

Average elemental concentrations under various conditions are listed in Table 1. There are huge increases in crustal dust every spring, because of transport from arid regions of central and eastern Asia. Duce et al.¹ previously reported similar incursions of Asian dust at Eniwetok Atoll, with concentrations of airborne soil being 2.3 µg/m³ in mid-April, 1979. During non-dust conditions at MLO, average downslope Al concentrations are about 4.9 ng/m³, whereas weekly average

concentrations rise to $>250 \text{ ng/m}^3$ during the dust periods. Upslope samples are similarly affected, but the increases are not as dramatic because of higher normal concentrations.

The data are divided into dust and non-dust periods, as differences are so great that yearly averages are strongly influenced by the dust periods for most elements. Average concentrations of many elements are more than an order of magnitude higher during the dust periods, but there are some exceptions including Br and I, whose concentrations are scarcely affected by the dust, and Na and Se, which are only doubled.

During non-dust periods, downslope concentrations are among the lowest observed anywhere in the world, typically being about a factor of ten greater than at the South Pole for most elements. Thus, these samples represent upper tropospheric air of the North Pacific and, as such, will provide a valuable data set for global receptor modeling. As expected, upslope samples have higher concentrations for most elements, major exceptions being Br and I.

We have been interpreting this extensive data set by several techniques, including factor analysis and chemical element balances, with the intent of determining the sources of particles and elements and learning how they are transported to MLO. This work is described in detail in a series of papers that are published, submitted, or in preparation.²⁻⁷ Among other things, we see sharp spikes in the concentration plots for various elements superimposed on low backgrounds and smoothly varying concentrations from natural sources. Spikes often occur for characteristic groups of trace elements (including As, Se, V, Zn, In, W, etc.), often along with sulfate. Many of the spikes appear to result from anthropogenic activities in Asia or in North America. Occasionally, for example, we observed elemental concentration patterns similar to these of copper-smelter plumes in Arizona at the same time that back-trajectories calculated by NOAA indicate that air masses came to MLO from the southwest U.S.

2. Compositions of Emissions from Volcanoes

Airborne studies of the atmospheric emissions of four Central American volcanoes were conducted using a Lockheed Electra turbo-prop research aircraft modified for the collection of plume particles and gases. Two Costa Rican volcanoes, Poas and Arenal, and one Mexican volcano, Colima, were sampled in February, 1982. A subsequent mission in November was made to collect plume samples at El Chichon volcano, the violent eruptions of which earlier in the year produced the largest cloud of volcanic origin observed in the stratosphere this century.

Single high volume filter samples were collected using Teflon materials selected for their high flow rates and low INAA blank characteristics. A multiple filter package consisting of a Teflon pre-filter followed by four cellulose filters that had been treated with 1 M $^7\text{LiOH}$ in 30% glycerol was used to trap acid volatiles (e.g., SO_2 , HC1, HF, HBr). Cascade impactors were used to collect size-segregated samples of plume particles on polycarbonate films.

Although all plumes studied were quite diffuse and sampling volumes small (10-20 m^3), we were able to determine concentrations of up to 30 elements in the plume particulate samples because of the low blank contribution and the high sensitivity of INAA. Particulate concentrations were compared with those of total gaseous concentrations of S, Cl, and Br as determined by INAA of the base-treated filters. Less than 10% of total S and Cl, and less than 30% of total Br was found to be associated with the particulate phase.

Pronounced enrichments of volatile and chalcophilic elements relative to bulk pyroclastic material were observed in the pumice particles of all volcanoes studied. These observations are consistent with similar measurements made at other volcanic systems^{8,9} including Mount St. Helens.^{10,11} The highly enriched elements, As, Se, and Sb, were found by INAA of cascade impactor stages to be associated predominantly with fine particles (<1 μm diam) while non-enriched crustal elements such as Na and Ca were almost exclusively found on large (>3 μm) particles. Aluminum was found to be bimodally distributed with particle size suggesting that volcanoes may act as a high temperature source of fine Al-bearing particles. This observation was verified by analysis of samples collected on two ground missions into the crater of Poas volcano in February 1982, and to El Chichon in January 1983. Aluminum, most likely as volatile halide, was observed to be highly enriched in condensates of emissions from high temperature vents (> 300°C).

Estimates of the emission rates of enriched volatile elements have been calculated by normalization of plume concentrations to simultaneously determine S as determined by an onboard flame photometric detector. Shown in Table 2 are the emission rates so calculated for the four Central American volcanoes, as well as those determined for Mount St. Helens in an earlier study.

3. INAA Studies of Particles Collected in Rural Areas

One of the major environmental problems of our time is acid deposition. In order to control acid deposition in an optimal way, we must identify the sources of acid precursors, find out how they are transported and deposited, and how they are chemically converted to acids. In work supported by EPA, we are trying to identify

Table 1

Geometric Means of Concentrations of Elements Measured on Downslope and Upslope Particle Filters During Clean (July to mid-February) and Dust (mid-February to July) Seasons at Mauna Loa Observatory, Hawaii, from February 1979 to June 1982

Element (units)	Downslope		Upslope		Clean	Dust
	Clean	Dust	Clean	Dust		
Na (ng)	6.6 (2.7)	22 (2.0)	86 (2.2)	140 (1.9)		
Mg (ng)	2.6 (2.1)	26 (2.5)	14.2 (2.1)	45 (2.0)		
Al (ng)	4.9 (2.1)	56 (2.5)	16.0 (2.2)	73 (2.5)		
S (ng)	80 (2.0)	160 (1.7)	150 (1.8)	230 (1.7)		
Cl (ng)	2.4 (4.0)	3.4 (3.0)	19 (4.2)	30 (5.0)		
K (ng)	2.8 (1.8)	27 (2.3)	10 (1.9)	41 (1.9)		
Ca (ng)	3.7 (2.5)	64 (3.0)	13 (2.2)	83 (2.7)		
Sc (pg)	1.2 (2.2)	13 (2.6)	3.9 (2.1)	15 (2.1)		
Ti (ng)	0.53 (2.6)	4.3 (2.4)	2.4 (2.5)	7.3 (2.2)		
V (pg)	10 (2.5)	100 (2.4)	48 (2.2)	160 (2.2)		
Mn (pg)	62 (2.3)	810 (2.5)	280 (2.2)	1300 (2.4)		
Fe (ng)	4.0 (2.3)	42 (2.6)	15 (2.2)	52 (2.3)		
Co (pg)	3.2 (2.6)	20 (2.4)	9.0 (2.7)	30 (2.2)		
Cu (ng)	0.22 (5.0)	0.85 (3.0)	0.33 (4.0)	0.6 (3.0)		
Zn (pg)	90 (4.0)	320 (2.2)	250 (3.0)	700 (3.0)		
Ga (pg)	8.4 (4.0)	20 (2.5)	22 (2.7)	42 (2.0)		
As (pg)	13 (2.9)	70 (4.0)	39 (2.5)	110 (3.0)		
Se (pg)*	11 (2.0)	21 (1.7)	22 (1.7)	36 (1.7)		
Br (ng)*	1.45±0.60	1.60±0.45	1.63±0.50	1.92±0.90		
Rb (pg)	16 (.19)	130 (2.5)	21 (2.5)	150 (2.0)		
Sr (ng)	0.24 (3.0)	0.62 (2.6)	0.28 (1.8)	0.72 (2.1)		
Ag (pg)	1.4 (3.1)	1.8 (2.7)	2.8 (3.5)	2.8 (4.0)		
Sb (pg)*	1.8 (.26)	7.7 (2.4)	4.6 (2.4)	9.7 (1.9)		
I (ng)*	2.1±1.3	1.45±0.60	2.2±0.80	2.3±0.60		
Cs (pg)	0.95 (2.6)	9.9 (2.8)	1 (3.0)	11 (2.5)		
Ba (ng)	0.51 (4.0)	1.0 (2.1)	0.42 (2.7)	1.1 (3.0)		
La (pg)	3.0 (2.3)	53 (3.3)	12 (2.2)	66 (2.5)		
Ce (pg)	7.8 (2.3)	71 (2.5)	31 (2.5)	110 (2.6)		
Sm (pg)	0.52 (2.8)	7.0 (2.7)	2.0 (2.6)	10 (3.0)		
Eu (pg)	0.19 (2.5)	1.2 (2.4)	0.65 (2.2)	1.5 (2.4)		
Tb (pg)	0.20 (2.5)	0.96 (2.6)	0.41 (2.1)	1.1 (2.0)		
Yb (pg)	1.1 (2.1)	3.2 (2.2)	1.6 (2.0)	4.0 (2.0)		
Lu (pg)	0.36 (3.1)	0.51 (3.0)	0.48 (3.0)	0.85 (2.0)		
Hf (pg)	0.44 (2.1)	3.3 (2.5)	1.7 (2.5)	5.4 (2.2)		
Ta (pg)	0.23 (2.3)	0.86 (3.0)	0.58 (2.5)	1.5 (1.7)		
W (pg)	2.7 (3.3)	6.0 (4.0)	13 (4.0)	17 (1.7)		
Au (pg)	0.15 (3.0)	0.24 (4.5)	0.28 (3.5)	0.37 (2.5)		
Th (pg)	0.80 (2.6)	11 (3.0)	1.8 (2.8)	13 (2.6)		

*Normal means and standard deviations expressed for I and Br.

Table 2

Estimated Volcanic Emission Rates (tonnes/day) of Selected Volatile Elements

Species	Arenal 2/82	Poas 2/82	Colima 2/82	El Chichon ^a 11/82	Mt. St. Helens ^b 9/80
Ash	40	5	120	15	60
S (t)	100	400	160	400	450
S (p)	6.7	7.9	0.9	16	24
Cl (t)	30	16	20	53	-
Cl (p)	4	0.4	0.001	2	3
Br (t)	0.053	0.042	0.070	0.100	-
Br (p)	0.0054	0.0030	0.0068	0.030	0.020
As (p)	0.0052	0.0020	0.0011	0.200	0.800
Se (p)	0.0100	0.0043	0.0044	0.004	0.100
Sb (p)	0.00051	0.00019	-	0.020	0.030
Au (p)	0.00005	0.00004	0.00014	0.00070	0.0030

^aRef. 12.^bRef. 11.

(t) = total

(p) = particulate

Table 3

Concentration of Elements Borne by Fine Particles in the Shenandoah Valley,
July/Aug. 1980

Element	No. of Samples	Method	Concentration (ng/m ³) (avg±σ)
Na	33	INAA	46±24
Al	32	INAA	42±46
Si	30	XRF	140±160
S	32	XRF	4400±3300
Cl	33	XRF	19±20
K	32	INAA	67±31
Ca	32	INAA, XRF	41±29
Sc	10	INAA	0.014±0.015
Ti	10	INAA	11±5
V	32	INAA	1.1±0.8
Mn	31	INAA, XRF	2.5±1.8
Fe	32	INAA, XRF	57±47
Co	17	INAA, XRF	0.74±0.96
Cu	24	INAA, XRF	6.6±4.3
Zn	30	INAA, XRF	13±11
As	11	INAA	0.7±0.3
Se	23	INAA, XRF	1.5±0.9
Br	33	XRF	7.5±2.3
Sr	15	XRF	4±6
Sb	10	INAA	0.4±0.7
I	21	INAA	0.48±0.30
Cs	8	INAA	0.19±0.013
Ba	13	XRF	55±46
La	10	INAA	0.16±0.12
Ce	10	INAA	0.21±0.14
Sm	9	INAA	0.13±0.01
Pb	32	XRF	49±20

elements borne by atmospheric particles that can serve as characteristic signatures of certain types of sources or areas of the country. To do this, we are subjecting samples collected by EPA to analysis by INAA. They collected samples for 15 months at rural sites in Kentucky, Indiana, and Ohio and for one month in the Shenandoah Valley. They collected particles in two size fractions, greater and less than 2.5- μm diameter and analyzed them by x-ray fluorescence (XRF). The XRF method is a rapid, highly automated technique for analyzing large numbers of samples, but it mainly observes major elements. INAA is more expensive and time-consuming than XRF, but it yields data for many trace elements that are potentially useful tracers, e.g., Se, As, Sb, and In. The combined XRF and INAA results will yield data for about 40 elements. We are mainly analyzing fine particles, as they provide much more information about sources than large particles, which are dominated by local soil. Back-trajectories for air masses sampled during each period are being calculated using a model and meteorological data from NOAA so that we can identify the areas over which the air was transported in order see if the compositions of particles from different areas have characteristic signatures.

To date, complete INAA measurements have been done on ten Shenandoah samples and a total of 33 have been analyzed for short-lived species. The data obtained are listed in table 3.

1. R. A. Duce, C. K. Unni, B. J. Ray, J. M. Prospero, and J. T. Merrill, *Science* 209, 1522 (1980).
2. J. R. Parrington, W. H. Zoller, and N. K. Aras, *Asia Dust: Seasonal Transport to the Hawaiian Islands*, *Science* 220, 195 (1983).
3. J. R. Parrington and W. H. Zoller, Selective Sampling of Diurnal Changes in Aerosol Composition at Mauna Loa, Hawaii, *J. Geophys. Res.* (in press, 1983).
4. J. R. Parrington and W. H. Zoller, The Chemistry of Asian Dust, submitted to *J. Geophys. Res.* (1983).
5. J. R. Parrington, J. K. Whittaker, and W. H. Zoller, Instrumentation for and Results of Particulate Sampling of Diurnal Winds at Mauna Loa Observatory, Hawaii, submitted to *J. Appl. Meto.* (1983).
6. J. R. Parrington and W. H. Zoller, Sources and Seasonal Variations of Sulfur and Selenium at Mauna Loa Observatory, Hawaii, in preparation for submission to *Geophys. Res. Lett.* (1983).
7. J. R. Parrington, W. H. Zoller, and G. E. Gordon, Sources and Composition of Atmospheric Particles of the Free Troposphere over the North Pacific, in preparation for submission to *J. Geophys. Res.* (1983).

8. G. J. Mroz and W. H. Zoller, Composition of Atmospheric Particulates from the Eruption of Heimaey, Iceland, Science 190, 461-463 (1975).
9. E. A. Lepel, K. M. Stefansson, and W. H. Zoller, The Enrichment of Volatile Elements in the Atmosphere by Volcanoes: Mt. Augustine, 1976, J. Geophys. Res. 83, 6213-6220 (1978).
10. T. Vossler, D. L. Anderson, N. K. Aras, J. M. Phelan, and W. H. Zoller, Trace Element Composition of the Mt. St. Helens Plume: Stratospheric Samples from the May 18th Eruption, Science 208, 827-830 (1981).
11. J. M. Phelan, D. L. Finnegan, D. S. Ballantine, W. H. Zoller, M. A. Hart, and J. L. Moyers, Airborne Aerosol Measurements in the Quiescent Plume of Mount St. Helens: September 1980, Geophys. Res. Lett. 9, 1093-1096 (1982).
12. J. Phelan Kotra, W. H. Zoller, M. A. Hart, and J. L. Moyers, Elemental Characterization of Volcanic Plume Aerosols: Central America, February 1982, in press, J. Geophys. Res., (1983).

VALIDATION OF STABLE ISOTOPE TRACING FOR STUDY OF ZINC NUTRITION IN HUMAN SUBJECTS

G. E. Gordon, Inci Gokmen, N. K. Aras, and I. Olmez
 (University of Maryland, College Park, MD)

Under support of the U.S. Department of Agriculture, we have begun studies of trace element nutrition in human beings. The actual work with human subjects is being performed at Georgetown University Medical Center under the direction of Drs. Robert Henkin and K. Sivasubramanian and at NIH under Dr. Roger Aamodt. The following is the abstract of the Ph.D. Thesis of Dr. Inci Gokmen (July, 1983), who did the initial work on this project:

Stable isotopes are beginning to be used to study trace element nutrition in humans as they do not expose subjects to radiation as in the case of radioactive tracers. Stable isotopes will be very useful for population groups that cannot be studied with radioactive tracers (pregnant women and persons under age 18). A sample of the element in which the abundance of an isotope has been greatly enriched is administered to the subject. For Zn the stable tracer was Zn-70, whose abundance was increased from the normal 0.62% to 66%. Red blood cells (RBC), plasma, urine, and feces were collected at various times after administration of the tracer and the amount of tracer present determined from ratios of the abundance of the enriched isotope to those of one or more major isotopes (for Zn, the Zn-70/Zn-64 and Zn-70/Zn-68 ratios). Amounts of Zn isotopes in the samples were determined by neutron irradiation followed by observation of their radioactive products, Zn-65, -69m, and -71m. A pre- and post-irradiation separation scheme (based on Chelex resin

separations) was used to observe Zn isotopes free of interference from other irradiation products.

The stable isotope method was validated against the radioactive tracer method by simultaneous oral administration of stable Zn-70 and radioactive Zn-65 tracers. Samples of RBC, plasma, urine, and feces from four adult volunteers were collected and assayed for Zn-65, and whole-body and liver-thigh counts of Zn-65 were taken at various times after administration. Variations of Zn-70/Zn-68 and Zn-70/Zn-64 ratios in the samples were determined by neutron activation. The fraction of each type of tracer appearing in each of the four body pools versus time after irradiations was calculated from results of the two tracer measurements. The agreement between the stable and radioactive tracers was very good for urine and feces. The agreement was good, in general, for RBC and plasma, but there were occasional fluctuations of the stable isotope results. The latter problem appears to result from poor separations of RBC and plasma for some samples and large statistical errors in the determinations of chemical yields based on the *in vivo* Zn-65 tracer. Changes of the procedure are indicated for reducing these sources of error.

Methods for observing a stable isotope tracer of selenium were developed, but not tested in human subjects.

NEUTRON-CAPTURE PROMPT GAMMA-RAY ACTIVATION ANALYSIS

D. L. Anderson, G. E. Gordon, W. B. Walters, W. H. Zoller, and M. E. Kitto
(University of Maryland, College Park, MD)

and

R. M. Lindstrom
(Center for Analytical Chemistry)

A number of continued and new studies have been pursued using the vertical beam neutron-capture prompt- γ activation analysis (PGAA) facility at the NBSR. We have continued to study analytical procedures for the boron assay of lumped-burnable poisons, including sample pre-irradiation dilution (necessary due to boron's high cross section). We have continued our analysis of many types of NBS and other reference materials, studied an interesting matrix effect in PGAA due to the presence of significant amounts of H in some samples and analyzed a number of new types of samples. In addition, a concentrated effort has begun to measure the particulate and gas-phase boron concentration in air at various locations in order to determine if B can be used as a tracer element for coal burning. The following sections explain briefly some of these studies.

1. New Measurements of Beam Characteristics and System Improvements

The PGAA facility has been improved by the addition of three DEC RL02 and dual RX02 floppy disk drives. The operating system used for the PDP 11/34 minicomputer is now RSX 11M version 3.2, and two LA36 Decwriters are presently used for operation and I/O. A new, high resolution, hyperpure Ge detector was purchased for use in the anti-Compton and pair spectrometer. Its characteristics are: 27% efficient (relative to NaI) and FWHM = 1.76 keV at 1332 keV. For the routine analysis of the elements H, B, C, N, Na, Mg, Al, Si, P, S, Cl, K, Ca, Ti, V, Mn, Fe, Cd, Nd, Sm, and Gd, two Compton-suppressed γ -ray spectra with the energy ranges 0-4 and 3.5-11 MeV are collected and analyzed.

At the time the reactor shim rods were replaced, we observed a noticeable reduction in the thermal neutron beam flux while checking our elemental sensitivities (counts/s \cdot mg of material). As we use relative methods for standardization, absolute flux measurements were not necessary. However, in the past year we determined these characteristics, using Au and Au clad with Cd monitors. The new thermal flux determined by this method is $\phi_{th} = 1.37 \times 10^8 n/cm^2 s$ and a Cd(Au) ratio of 30/1, compared to the original $\phi_{th} = 1.7 \times 10^8 n/cm^2 s$ and Cd(Au) ratio of 55/1. Although the flux reduction is substantial, we have improved our background via better alignment and selection of materials for the sample holder. For these reasons and

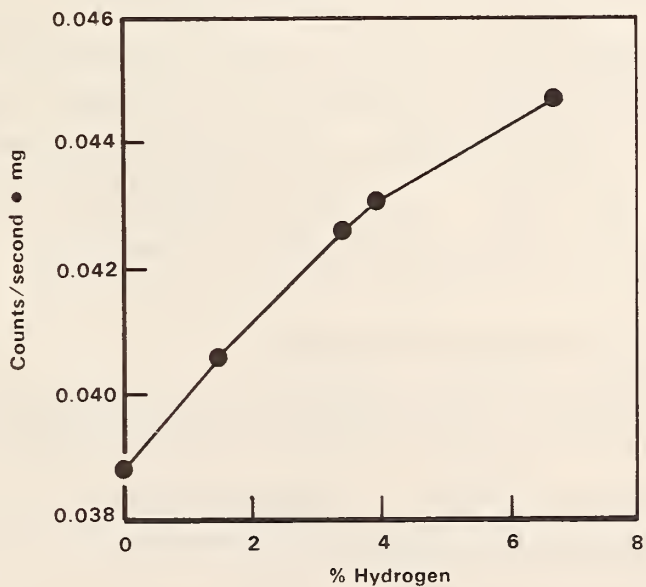


Figure 1. Sensitivity for sulfur (842 keV) vs. hydrogen content.

because of the other effective shielding techniques used, the U. Md-NBS PGAA facility remains equal to or (in the case of most elements) better than any other prompt- γ facility in terms of minimum detection limits. (Higher flux facilities, of course, have better sensitivities, but the larger backgrounds cancel out this feature when one considers detection limits.)

2. Hydrogen Matrix Effects

For some time, we have been aware of an important matrix effect observed in our analyses. Matrices containing percent levels of hydrogen can severely alter the mean neutron energy to which the sample is exposed. As this mean energy is shifted lower, for many elements, the effective cross section and, therefore, the count rates observed, increase. As a number of our pelletized standards (e.g., B, Cd, Sm, Gd) are dilute solutions pipetted onto filter paper, they would not yield correct answers if low-H samples (e.g., fly ash or rock material) were compared to them.

We have begun to study this effect by preparing pelletized standards of the element in a varying graphite-mannitol matrix (for the case of elements with large cross section) or of the element (or common compound of the element) in various proportions with mannitol. The result for S is presented in Figure 1. Table 1 lists the % difference in sensitivities ($c/s \cdot mg$) for several elements in a 0% H matrix compared to a matrix of ~ 6% H (preliminary results). A shift in the mean beam energy of ~ 0.03 eV (e.g., from 0.06 to 0.03 eV) would explain such behavior,¹ except for Sm, whose sensitivity behavior is hard to predict because of the large nearby resonance (0.04-0.11 eV).

As a result of these studies, we are updating our PGAA values for several elements in some important reference materials. As a number were run before the shim-rod replacement, a simple correction factor may not be valid [e.g., for SRM's 1632, 1632a, 1633, 1633a, and 1635²], and will be reanalyzed. Values given in last year's report³ for SRM 278 (obsidian) and SRM 688 (basalt) are revised as shown in Table 2.

3. Analysis of Geochemical Reference Standards

The PGAA study of twenty-two geochemical reference standards has been completed.⁴ Included are reference materials obtained from the U. S. Geological Survey, NBS, the International Atomic Energy Agency, and Pacific Northwest Laboratories. As the data tables are extensive, they are not presented here, but may be obtained by contacting D. L. Anderson.

4. Analysis of Construction Materials

Table 1. Percent increase in sensitivity (c/s mg of element) in a Whatman filter standard (~6% H) relative to a graphite matrix standard (0% H)

Element	E_{γ} (keV)	% Increase
B	477	11
Cl	517	10
Ca	1942	13
Cd	558	17
Sm	334	10
Gd	182	42

In collaboration with E. A. Lepel of Battelle Pacific Northwest Laboratories a number of cement, concrete aggregate, and steel samples from construction sites of the Washington Public Power Supply System (WPPSS) were analyzed. The results are presented in Tables 3 and 4. For a full discussion of these measurements, see reference (5).

5. Multitechnique Characterization of Boron in Glass

PGAA was used to measure boron in a series of borosilicate glasses, in collaboration with J. E. Riley, Jr., of Bell Laboratories and with the neutron depth profiling project described more fully elsewhere in this report. Large (25g) samples of bulk glass were ground to a powder (< 44 μm), blended with graphite, and pressed to a uniform shape and similar boron content for analysis in order to eliminate material inhomogeneity and self-shielding. The precision was excellent, the relative standard deviation of repeated analyses of individual glasses averaging better than 1%. Comparison with emission spectrographic analyses (ICP) showed good agreement. The measurements are more fully described in reference (6).

6. Measurement of B in the Atmosphere

We have begun to study the capabilities of PGAA as applied to atmospheric sampling. Results obtained from Mt. St. Helens plume samples⁷ encouraged us to attempt measurements of particles in the urban environment, as PGAA is sensitive

Table 2. Elemental concentrations in NBS geochemical standards ($\mu\text{g/g}$)

Element	SRM 278	SRM 688
B	27.9 ± 0.4	1.5 ± 0.2
Sm	6.08 ± 0.03	2.62 ± 0.02
Gd	5.95 ± 0.08	3.46 ± 0.10

Table 3. PGAA analyses of concretes and ingredients (one sample each).

Element	Concentrations (% unless noted)					
	WPPSS Samples				Rancho Seco	
	Sand	Cement	Aggregate	Concrete #1	Concrete #2	Concrete
H	0.28+0.01	0.088+0.014	0.15+0.01	0.61+0.01	0.61+0.01	0.60+0.01
B ($\mu\text{g/g}$)	8.0+0.4	66.1+0.3	5.7+0.2	15.4+0.3	15.1+0.1	25.9+0.1
Na	2.35+0.04	0.33+0.08	2.16+0.10	1.68+0.05	1.56+0.09	1.35+0.08
Mg	2.3+0.5	1.7+0.4	2.2+0.3	1.7+0.3	1.3+0.1	2.2+0.4
Al	7.43+0.13	2.00+0.01	6.71+0.08	5.25+0.10	5.18+0.05	5.85+0.19
Si	29.5+1.0	10.2+0.2	26.2+0.5	22.9+0.1	23.5+0.4	25.5+0.6
S	-	1.02+0.01	-	0.22+0.4	0.15+0.01	0.16+0.02
Cl ($\mu\text{g/g}$)	50+10	-	72+7	50+20	67+5	56+15
K	1.31+0.03	0.53+0.02	1.15+0.02	1.06+0.02	0.92+0.01	0.83+0.02
Ca	5.48+0.13	43.1+0.3	4.8+0.1	11.6+0.1	12.76+0.05	11.1+0.2
Ti	1.30+0.01	0.111+0.002	1.06+0.01	0.75+0.01	0.74+0.01	0.343+0.004
V ($\mu\text{g/g}$)	390+60	-	430+70	500+60	360+20	400+80
Mn ($\mu\text{g/g}$)	1210+60	1000+100	1160+40	1030+70	800+10	810+50
Fe	8.01+0.14	2.13+0.02	6.96+0.05	5.02+0.10	4.97+0.04	3.61+0.10
Cd ($\mu\text{g/g}$)	-	-	-	-	200+40	350+110
Nd ($\mu\text{g/g}$)	-	-	24+13	-	14+5	33+12
Sm ($\mu\text{g/g}$)	6.85+0.04	1.96+0.02	5.65+0.05	4.47+0.01	4.14+0.02	3.25+0.2
Gd ($\mu\text{g/g}$)	6.45+0.10	1.51+0.11	5.65+0.12	4.17+0.05	3.89+0.06	3.02+0.17
Total (as oxides)	109.6+2.3	96.9+0.9	96.7+1.2	96.1+0.8	97.8+0.9	99.4+1.5

NON-RRD PROGRAMS

Table 4. PGAA analyses of steel samples (one sample each).

Element	Concentration (% unless noted)				
	Low-Carbon		Stainless		NBS SRM 123C
	SA 302	SA 316	SA 304	This work (2 samples)	Certificate
B ($\mu\text{g/g}$)	1.0 \pm 0.3	5.0 \pm 0.4	3.2 \pm 0.2	2.35 \pm 0.05	-
Ti ($\mu\text{g/g}$)	160 \pm 60	-	-	60 \pm 10	-
V ($\mu\text{g/g}$)	110 \pm 50	740 \pm 150	670 \pm 100	350 \pm 20	-
Cr	\leq 0.12	17.3 \pm 0.2	19.2 \pm 0.2	17.7 \pm 0.3	17.4
Mn	1.4 \pm 0.2	1.3 \pm 0.2	1.76 \pm 0.10	1.69 \pm 0.03	1.7
Fe	96.6 \pm 1.1	65.5 \pm 0.6	69.3 \pm 1.2	67.2 \pm 0.1	67.2
Co	\leq 0.12	0.14 \pm 0.01	0.112 \pm 0.008	0.110 \pm 0.001	0.12
Ni	\leq 0.05	13.1 \pm 0.15	9.68 \pm 0.13	11.35 \pm 0.03	11.3
Mo	0.45 \pm 0.03	2.05 \pm 0.02	-	0.23 \pm 0.01	0.22
Total	98.6 \pm 1.2	99.2 \pm 0.7	100.1 \pm 1.2	98.3 \pm 0.3	97.9

Table 5. College Park sample period: June 8-12, 1983; 904 m^3 ; 1st stage untreated Whatman; stages 2-5 LiOH/glycerol treated; weather: clear, low AQI

but increasing

Species	Concentrations of Filter (ng/m^3)					total gas phase
	1	2	3	4	5	
B	4.7 \pm 0.2	13.8 \pm 0.3	2.0 \pm 0.2	1.7 \pm 0.2	0.8 \pm 0.3	18.3
NO ₃ (IC)	6340	3490	313	377	186	4366
Na	\sim 1100	-	-	-	-	-
Si	6040 \pm 600	-	-	-	-	-
S	3330 \pm 280	4980 \pm 150	2690 \pm 220	740 \pm 220	670 \pm 290	9080
SO ₄ \rightarrow S (IC)	3700	4840	2521	1160	289	8810
Cl	348 \pm 30	1060 \pm 30	58 \pm 27	49 \pm 27	<34	1201
Cl (IC)	323	1170	181	210	142	1703
Ti	140 \pm 25	-	-	-	-	-
Cd	0.52 \pm 0.06	-	-	-	-	-

Table 6a. Particle filter concentration ranges (ng/m^3) for B, Si, S, and Cl at various locations measured by PGAA.

Location	Range			
	B	Si	S	Cl
College Park	5-12	6000-14,000	3000-11,000	300-600
NBS	~3	<2000	~3000	~100
Mauna Loa Observatory, Hawaii	<0.3	<1500	<200	<50
Cape Kumakahi, Hawaii	<0.2	<1500	900-1200	10,000-13,000

Table 6b. Gas-phase concentration ranges measured by PGAA.

Location	Range		
	B	S	Cl
College Park	20-30	10,000-13,000	900-1200
NBS	~11	~5000	~350
Mauna Loa Observatory, Hawaii	<0.3	0-800	0-500
Cape Kumakahi, Hawaii	15-30	500-4000	200-9000

enough to measure, usually, B, Si, Cl, S, Ti, and Cd for air sample volumes of about 300 m^3 . Recent studies at the University of Rhode Island⁸ indicate there is much gas-phase B in the atmosphere (along with Cl and S). Therefore, preliminary measurements have been made at the University of Maryland, NBS, Hawaii, and Wallops Island, VA, in an attempt to establish the primary sources of B. We sample air through stacks consisting of a single untreated filter to collect particles followed by 4 LiOH-treated filters, which collect acidic gases. Our preliminary results are in general agreement with the University of Rhode Island work,⁸ showing that the ocean is a major source of gas-phase B in the form of H_3BO_3 , boric acid. There appears, however, to be more B in the atmosphere than can be attributed to the ocean and local dust. Another major source of B in the atmosphere is apparently coal-burning.⁹ The potential for using B as a tracer element for coal-plant emissions is now under study by our group.

The data for a stack of filters run at College Park are shown in Table 5. One half of each filter was analyzed by PGAA, the other by ion chromatography. As can be seen, the two techniques yield data that agree fairly well. The elemental concentrations ranges measured so far are presented in tables 6a and b.

1. D. J. Hughes and R. B. Schwartz, Neutron Cross Sections, Brookhaven National Laboratory Report BNL-325, July (1958).
2. M. P. Failey, D. L. Anderson, W. H. Zoller, G. E. Gordon, and R. M. Lindstrom, Anal. Chem. 51, 2209 (1979).
3. NBS Reactor: Summary of Activities July 1981-June 1982, NBS Technical Note 1178, F. Shorten, Ed.
4. D. L. Anderson, Y. Sun, M. P. Failey, and W. H. Zoller, in preparation, to be submitted to Geostandards Newsletter.
5. D. L. Anderson, G. E. Gordon, and E. A. Lepel, Canad. J. Chem. 61, 724 (1983).
6. J. E. Riley, Jr., R. G. Downing, R. F. Fleming, R. M. Lindstrom, and D. H. Vincent, to be published in J. Solid State Chem.
7. T. Vossler, D. L. Anderson, N. K. Aras, J. M. Phelan, and W. H. Zoller, Science 211, 827 (1981).
8. T. Fogg, Ph.D. Dissertation, University of Rhode Island (1983).
9. E. S. Gladney, L. E. Wangen, D. B. Curtis, and E. T. Jurney, Env. Sci. Technol. 12, 1084 (1978).

HIGH ACCURACY DETERMINATION OF U-235 BY GAMMA-RAY SPECTROSCOPY IN NONDESTRUCTIVE ASSAY STANDARDS

B. S. Carpenter
(National Measurement Laboratory)

and

R.R. Greenberg
(Inorganic Analytical Research Division)

A joint project is underway between the Central Bureau for Nuclear Measurements (CBNM) Geel, Belgium, and the National Bureau of Standards to produce a set of five uranium isotope abundance reference materials for nondestructive assay (NDA). This set is intended for worldwide safeguards use as primary reference materials for the determination of the U-235 abundance in homogeneous uranium bulk material by gamma-



Figure 1. A typical U-235 isotope abundance reference material for gamma spectrometry.

ray spectrometry. The reference material is in the form of uranium oxide (U_3O_8) and is placed in aluminum cans with nominal isotope abundance ($^{235}U/U$) of 0.003, 0.007, 0.019, 0.029, and 0.045. The material at each isotope abundance is characterized chemically by CBNM, NBS, and the DOE New Brunswick Laboratory for $^{235}U/U$ homogeneity and isotope abundance, uranium content, and material impurities.¹

Currently, high precision gamma-ray measurements are being made on 24 representative sample cans of the 140 total cans at each isotope abundance. The measurements, using a high purity germanium detector, are to determine the countrate uniformity of the U-235 185.7 keV gamma-ray as well as the U-235 isotope abundance for each sample. Since the samples are packaged such that the U_3O_8 is infinitely thick for the 185.7 keV gamma-ray, the measured countrate is not dependent on the material density. In addition the activity observed by the detector is collimated to simulate calibration conditions used to measure bulk material in the field (see Figure 1).

Preliminary gamma-ray results of the 1.9 percent material indicate that the $^{235}U/U$ isotope abundance is within 0.02 percent of the values determined by CBNM and NBS mass spectrometry measurements. The results of this material is based on counting statistics of 0.05 percent for each of the 24 samples analyzed. The observed standard deviation for the 24 samples was 0.05 percent (ls-relative) and the standard deviation of the mean was 0.01 percent.

-
1. P. DeBievre, H. Meyer, J. Van Audenhove, B. S. Carpenter, and J. W. Gramlich, "Progress Report on the Establishment of Uranium Isotope Abundance Reference Materials for NDA," Proceedings of 4th Annual Symposium - ESARDA on Specialist Meeting on Harmonization and Standardization in Nuclear Safeguards, Petten, The Netherlands, 27-29 April, 1982; Report ESARDA No. 15.

SUMMARY OF ACTIVITIES CARRIED OUT BY THE NEUTRON FIELD STANDARDS GROUP

R. Dallatore, C. Eisenhauer, D. Gilliam, J. Grundl, E. McGarry
(Center for Radiation Research)

The Neutron Field Standards Group, attached to the Center for Radiation Research (CRR), is engaged in the development and application of standard and reference neutron fields as permanent facilities for neutron detector calibrations, neutron dosimetry standardization, and reaction rate cross-section measurement.

A component of this group's activities makes use of the reactor thermal column and the tangential beam tubes where facilities, designed and built by the NFS Group, are in operation. Facility, development, and measurement projects which involve these facilities are as follows:

1. Cavity Fission Source Reworked

The cavity fission source was redesigned in order to allow irradiated neutron fluence standards to be removed separately from the highly radioactive fission source disks which now remain inside of the thermal column. The fission chamber monitor also was remounted on the insertion stem close to the source detector assembly. Two new shielding arrangements were designed and built to accommodate the new source. A 7" dia. lead cylinder on a rolling platform allows the fission source disks to come out of the thermal column into a shield that can be hand carried to a larger lead storage channel which is itself on a movable cart. A removable body shield with a lead glass aperture was attached to the side of the thermal column assembly table. Various operations and inspections can now be done with highly radioactive fission source disks. Personnel exposures involved with the handling of sources has been substantially reduced.

The cavity fission source, with these operational modifications and with final neutron scattering corrections, is now a convenient standard neutron field for routine use. The U-235 fission neutron flux at the midplane between the fission source disks is $1.8 \times 10^{10} \text{ n/cm}^2 \text{ s}$. For individual irradiated foils this flux is established to ± 2.6 percent based on neutron flux transfer from the NBS Cf-252 irradiated facility.

2. Neutron Scattering Corrections for Cavity Fission Source

The sack of nickel and indium activation foils in the NBS cavity fission source raises the question of perturbation of activation rate in one foil because of scattering of neutrons in the same foil or in nearby foils. Monte Carlo calculations were made for us by Los Alamos National Laboratory to determine this effect. It was found that flux gradient over the foil stack was small enough that the effect depended not on the absolute position of foil and scatterer but only on their separation distance. For foils of 1.27 cm diameter, the correction to the fluence per 0.0254 cm thickness of scatterer varies from 1.0 percent for self scattering (i.e., zero separation distance) to < 0.1 percent at 0.8 cm spacing. The Monte Carlo calculations from LANL now provide corrections for the entire cavity fission source detector assembly.

3. Production of Neutron Fluence Standards.

The cavity fission source for the first time produced a substantial number of neutron fluence standards for reactor dosimetry applications. In three primary irradiations, titanium, nickel, and iron foils were exposed to fission neutron fluences of between 4.5 and $7 \times 10^{15} \text{ n/cm}^2$. These fluence standards have been distributed to various dosimetry measurement laboratories in this country and abroad.

The test report for each fluence standard provides a free-field fission neutron fluence with an assigned error of ± 2.6 percent. The major components of this error are as follows:

- o Flux Transfer Measurements from the Cf-252 Standard Fission Neutron Field to the U-235 Cavity Fission Source:
 - (1) Absolute neutron source strength of the 252-Cf source $\pm 1.1\%$
 - (2) Distance measurement $\pm 0.3\%$
 - (3) Cf-252 to U-235 spectrum-averaged cross section ratio for In-115(n,n') monitor $\pm 1.6\%$
 - (4) Corrections for neutron scattering in Cf-252 irradiation $\pm 1.0\%$
 - (5) Reproducibility of flux transfer procedure (including counting statistics, and electronic system stability over period of measurement) $\pm 0.6\%$

o Preparation of Neutron Fluence Standards at the U-235 Cavity

Fission Source:

(1) Gradient corrections and positioning	$\pm 0.85\%$
(2) Corrections for neutron scattering in source detector capsule	$\pm 0.6\%$
(3) Reproducibility of fluence monitoring including random summing corrections and uncertainties in activation decay corrections	$\pm 0.45\%$

These threshold activation detectors are used to establish fast neutron exposure parameters (generally flux > 1 MeV, and "displacements per atom") for out-of-core components of power reactors. The fission neutron fluence standards provide a combined calibration of detection methods and data interpretation.

4. Test of B-10 and Li-6 Helium Production Cross Section

Experimental tests of the B-10 and Li-6 α production cross sections, relative to σ_f (U-235), were carried out in the Intermediate-Energy Standard Neutron Field (ISNF) facility. The B-10 and Li-6 reaction rates were measured using the Helium Accumulation Fluence Monitor (HAFM) method by B. Oliver and H. Farrar of Rockwell International. A variety of HAFM samples were included in the tests: nineteen welded capsules containing crystals of enriched Li-6F, B-10, and natural boron; ten empty capsules to check for any background of spurious helium generation; and six each of base crystals to enriched B-10 and Li-6F. The main irradiation was carried out in two segments to give a total fluence greater than $10^{14} n/cm^2$. A background run was also made with the fission drivers removed from the ISNF facility. Both gold and iridium foils were irradiated with the HAFM detectors to provide run-to-run monitoring which will correct the HAFM irradiations with a subsequent U-235 fission rate determination.

5. Fissionable Deposit Assay for Fission Cross Section Measurement

The Cf-252 fission-spectrum-averaged, U-235 fission cross section, $\sigma_f(\chi_{cf}, U-235)$, is the normalization parameter for all measurements of integral cross sections in NBS standard neutron fields. A new measurement of this quantity is nearing completion. The working fissionable deposits used for fission chamber measurements at the Cf-252 irradiation facility were mass assayed relative to the NBS U-235 archive deposit in a thermal beam. In this technique an effective mass or fragment emission efficiency for the heavy working deposit ($500 \mu g/cm^2$ with fission fragment

losses of 7 percent) is established relative to the light archive deposit (< 200 $\mu\text{g}/\text{cm}^2$) where the fragment loss correction is small and better understood.

In a separate investigation, fission fragment loss in a UF_4 deposit was compared with that in a U_3O_8 deposit. Both types of deposits are used in cross section measurements. The difference in fragment absorption between fluorine and oxygen comes from classic range-energy calculations for heavy ions. The comparison measurements carried out in a thermal beam indicated these calculations are satisfactory.

6. Fissionable Isotope Mass Standard Diagnostics

The neptunium-237 archive fissionable deposit (37S-2-2) was examined for small amounts of Pu-239 and other fissile contaminants. Thermal beam measurements were carried out with a thin Pu-239 deposit in back-to-back geometry. The amount of fissile contaminant found was 29 ± 5 nanograms (Pu-239 equivalent mass) 0.011 percent of the mass of the principal isotope.

A similar investigation was taken in support of fission chamber measurements performed in the Iron Shells Benchmark at SCK/CEN (Belgium). This specialized project was designed to test calculations of deep penetration of neutrons into steel. In addition to the conventional roster of fissionable detectors, the isotope U-236 was included for these measurements although it is not part of the NBS set of fissionable isotope mass standards. In the analysis, the U-236 fission rate was uniquely discrepant compared to the conventional set of fission detectors. The thermal beam examination indicated 110 nanograms of U-235 equivalent mass in the U-236 deposit as compared to ~ 2ng previously accepted from the isotopic assay of the base material. With 110ng of fissile isotope included in the analysis, the U-236 fission rate in the iron shells came into agreement.

7. Autoradiographic Study of Paintings

The thermal-neutron-radiography facility for diagnostic irradiations of paintings is described elsewhere in this report. In cooperation with the Reactor Division and the Smithsonian Institution, thermal column modifications were designed in order to achieve a high-intensity flux of thermal neutrons over a large area. The design also made possible rapid recovery of irradiated paintings so that short-lived activities could be included in the post-irradiation diagnostic procedures.

FISSION CROSS SECTION MEASUREMENTS IN REACTOR PHYSICS AND DOSIMETRY BENCHMARKS AT NBS

J. A. Grundl and D. M. Gilliam
(Nuclear Radiation Division)

Fission cross sections for eight fissionable isotopes of importance for nuclear technology have been measured in two fission neutron spectra and one fission-neutron-driven standard neutron field. New measurements for Pu-240, Pu-241, U-233, and Th-232 accompany revised values from earlier determinations for Pu-239, U-235, U-238, and Np-237.

The starting point for these measurements is an absolute cross-section measurement for Cf-252 fission spectrum neutrons. This absolute cross section is determined from a neutron source strength, a source-to-detector distance, and an absolute fission rate. Relative fission cross-section measurements for the Intermediate-energy Standard Neutron Field (ISNF) are put on an absolute scale by employing a flux transfer procedure from the Cf-252 source. For U-235 fission spectrum neutrons, cross-section ratios measured in a cavity fission source are normalized to the U-235 fission cross section measured in the Cf-252 fission neutron field.

Major components of these cross-section measurements are the same for all but one of the benchmark neutron fields and can be summarized individually. Errors are similar also and they will be assessed together for each measurement component.

1. Fission Rate Detection and Isotopic Masses

Double fission ionization chambers with detection efficiencies between 0.97 and 0.995 (depending on fissionable deposit thickness) were employed in these measurements. Uncertainties for fission fragment loss corrections were \pm 0.6 to 0.8% and counting imprecision was less than \pm 0.2% except for Cf-252 where counting imprecision for some isotopes was as high as \pm 0.6%.

Fissionable deposits in a thickness range of 8 to 600 $\mu\text{g}/\text{cm}^2$ were used in the fission chambers. Deposit masses were ascertained by a multiplicity of techniques:

1. low-geometry alpha counting
2. isotope dilution mass spectrometry (U-235, U-238, and Pu-239 only)
3. Maxwellian and monoenergetic thermal-neutron fission counting
4. selective intercomparisons with archive deposits from other laboratories.

Revised isotopic mass uncertainties for the National Bureau of Standards (NBS) set of fissionable isotope mass standards are now available and supercede all previously reported values. They are listed below at one standard deviation:

Table 1. Fission cross sections for reactor physics and dosimetry benchmarks.

Isotope	ISNF (mb)	Fission Spectra ^a	
		²⁵² Cf (mb)	²³⁵ U (mb)
²³² Th	38.4 \pm 1.2	89.4 \pm 2.7	-
²³³ U	2424 \pm 65	1893 \pm 48	-
²³⁵ U ^b	1606 \pm 35	1216 \pm 19	c
²³⁸ U ^b	149.0 \pm 3.6	326 \pm 6.5	309 \pm 8
²³⁷ Np ^b	829 \pm 22	1366 \pm 27	1344 \pm 54
²³⁹ Pu ^b	c	1824 \pm 35	1832 \pm 55
²⁴⁰ Pu	824 \pm 23	1337 \pm 32	-
²⁴¹ Pu	2152 \pm 108	1616 \pm 80	-
²³⁵ U/ ²³⁸ U	10.78 \pm 1.1%	3.73 \pm 1.2%	3.94 \pm 2.0%
²³⁵ U/ ²³⁹ Pu	0.866 \pm 1.0%	0.666 \pm 0.9%	0.664 \pm 2.5%
²³⁷ Np/ ²³⁸ U	5.56 \pm 1.7%	4.19 \pm 1.5%	4.35 \pm 3.0%
Revised Values		New Isotopes	
²³⁵ U:	\pm 0.5%	²³² Th:	\pm 2.0%
²³⁸ U:	\pm 0.7%	²³³ U:	\pm 1.5%
²³⁷ Np:	\pm 1.0%	²⁴⁰ Pu:	\pm 0.8%
²³⁹ Pu:	\pm 0.4%	²⁴¹ Pu:	\pm 4.0%

Corrections for fission in other than the principal isotope were between 0 and 1% for all but Pu-240 and Pu-241 where the corrections were 3.0 and 21%, respectively.

2. Neutron Flux and Scattering Corrections

The free-field neutron flux at 5 cm from the Cf-252 fission source can be established to $\pm 1.1\%$ on the basis of a measured detector separation distance and a neutron source strength determination performed at the NBS MnSO₄ Bath Facility. Neutron fluence transfer from the Cf-252 irradiation facility to the ISNF and to the U-235 fission spectrum irradiation facilities is carried out to be better than $\pm 1\%$ by means of the Pu-239 and U-235 fission reactions as indicated in Table 1.

Monte Carlo calculations have been performed for experimental arrangements at the Californium Irradiation Facility. Fission rates attributable to source neutrons scattered in the source capsule and in the fission chambers have been determined. Total corrections are 3.5% for fissile isotopes and 1 to 3% for the other isotopes; errors have been estimated at less than $\pm 0.7\%$. The correction for fission in fissile isotopes due to room return background at the californium facility is $\sim 0.5\%$ based on both measurement and calculation. At ISNF the only significant scattering element is the fission chamber, which is in a neutron flux that is nearly isotropic. Corrections are < 1.0%. Cavity fission source arrangements for the U-235 fission spectrum measurements (and Pu-239) are less ideal for scattering calculations and larger corrections and uncertainties are involved.

3. Results

Fission cross-section results are presented in Table 1, along with selected cross-section ratios for which errors are significantly less than for the individual cross sections. Errors are given at one standard deviation. These benchmark measurement results are intended to provide integral normalizations and a test of differential neutron cross-section data.

INTEGRAL CROSS SECTION MEASUREMENTS IN THE ^{235}U FISSION NEUTRON SPECTRUM

G. Lamaze, E. D. McGarry, and F. J. Schima
 (Center for Radiation Research)

An important method of fast neutron dosimetry is the use of radiometric monitors to measure neutron fluence and fluence rate. By selecting a set of reactions each of which is sensitive to a different neutron energy range, information on both the shape and magnitude of the fluence spectrum can be obtained.

To derive a neutron fluence from a measured reaction rate, the spectrum averaged cross section, $\bar{\sigma}$, must be known. By definition it is

$$\bar{\sigma} = \frac{\int \sigma(E) \phi(E) dE}{\int \phi(E) dE}$$

The differential cross section, $\sigma(E)$, is available as an evaluated nuclear data file, such as the Brookhaven ENDF/B file, which is based on both experimental data and calculations. In a complex environment, such as a reactor, the differential fluence rate $\phi(E)$ is usually obtained from a transport calculation of the energy and spatial distribution of the neutrons. However, if the neutron source and the radiometric monitors constitute a relatively well understood system, a measure of σ becomes a validation of the knowledge of $\sigma(E)$. Herein are reported measured values of $\bar{\sigma}$ for the $^{54}\text{Fe}(n,p)^{54}\text{Mn}$ and $^{58}\text{Ni}(n,p)^{58}\text{Co}$ reactions in a U-235 fission spectrum.

The U-235 fission irradiations were accomplished in the NBS Cavity Fission Source. This source operates at the center of a 30-cm diameter spherical cavity located at the center of the graphite thermal column at the NBS Research Reactor. The source-detector capsule (see Figure 1) consists of two coaxial source disks of U-235 metal (16 mm dia. x 0.13 mm thick) placed outside of a cadmium box which encloses the radiometric neutron detectors for exposure. The cavity and source-detector arrangement is shown in Figure 1.

The fluence rate gradient between the two fission disks has been measured by simultaneously irradiating 13 nickel foils, each 0.076 mm thick, which were uniformly placed within the Cavity Fission Source. The total mass of nickel approximates the total mass of a typical loading of four or five thicker foils. The results of the gradient measurement are given in Figure 2.

The fluence in the cavity is measured indirectly by using the $^{115}\text{In}(n,n')$ ^{115m}In reaction. The indium is first irradiated in a ^{252}Cf field from a point neutron source of known strength and the gamma count rate at the end of irradiation (counts

$\text{s}^{-1}\text{g}^{-1}$) is measured. The gamma detector used is then effectively calibrated in terms of the fluence rate to count rate ratio ($\text{n cm}^{-2}\text{s}^{-1}/\text{counts s}^{-1}\text{g}^{-1}$). Because the ratio of the spectrum averaged cross sections in the Cf-252 and U-235 is well known ($\pm 1.5\%$), indium foils are the irradiated in the U-235 fission field to measure the fluence rate. For each irradiation, the reactor power is monitored with a small fission chamber in the cavity to record any changes in the fluence rate during the irradiation.

$^{58}\text{Ni(n,p)}^{58}\text{Co}$ cross section:

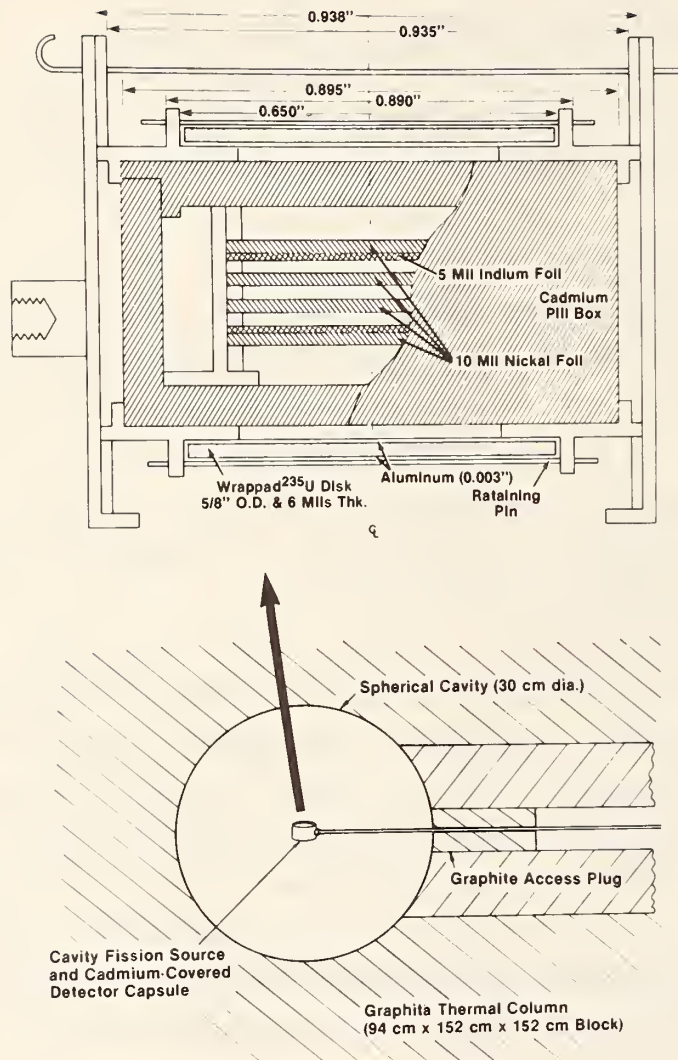
Two nickel irradiations have been accomplished. In the first, two 0.25 mm natural metal foils were irradiated for 30 hours in a total fluence of $2.11 \times 10^{15} \text{n/cm}^2$. In the second irradiation, two 0.09 mm natural metal foils were irradiated for 55 hours in a total fluence of $3.00 \times 10^{15} \text{n/cm}^2$. The results from these four foils give a value of 109 mb with a standard deviation of 0.9% indicating good reproducibility of the method. Combining all sources of uncertainty in quadrature (see Table 1) gives as a final value of the cross section 109 ± 3 mb.

$^{54}\text{Fe(n,p)}^{54}\text{Mn}$ cross section:

The value of the iron cross section is based on only one irradiation and, as such, must be considered preliminary. Two natural iron foils 0.13 mm thick were irradiated for 29 hours in a total fluence of $2.17 \times 10^{15} \text{n/cm}^2$. Taking the average value of two foils and combining all sources of uncertainty in quadrature (see Table 1) gives a value of 79 ± 3 mb for the $^{54}\text{Fe(n,p)}$ cross section. It should be noted that there is a 1.7% uncertainty assigned to the isotopic abundance of Fe-54 in natural iron. This uncertainty has not been included in the uncertainty of the measurement. If natural iron samples are used for neutron dosimetry, the abundance factor is eliminated in the application of the method.

Table 2 compares the present results as well as similiar results from Cf-252 spectrum measurements with calculated values from the NBS Compendium¹ and with an evaluation of measured values. The calculations are based upon the NBS evaluations of the U-235 and Cf-252 fission neutron spectra and on ENDF/B-V cross sections. All of the present results are in good agreement with previously measured values, as reported in the NBS compendium.

While the $^{54}\text{Fe(n,p)}$ results agree with the calculated values for both of the mentioned fission neutron spectra, the calculated results for $^{58}\text{Ni(n,p)}$ are low by 6-8% in both fields and the $^{115}\text{In(n,n')}$ results are low by 8% for the Cf-252 spectrum. These integral measurements do not indicate whether the problems are associated with ENDF/B-V cross sections or with the fission spectra evaluations, or with both.



U-235 Cavity Fission Source. Upper view: relative positions of neutron sensor foils, fission-disks and cadmium enclosure. Lower view: the upper assembly in the thermal column of the NBS reactor.

Figure 1. U-235 Cavity Fission Source. Upper view: relative positions of neutron sensor foils, fission-disks, and cadmium enclosure. Lower view: the upper assembly in the thermal column of the NBS reactor.

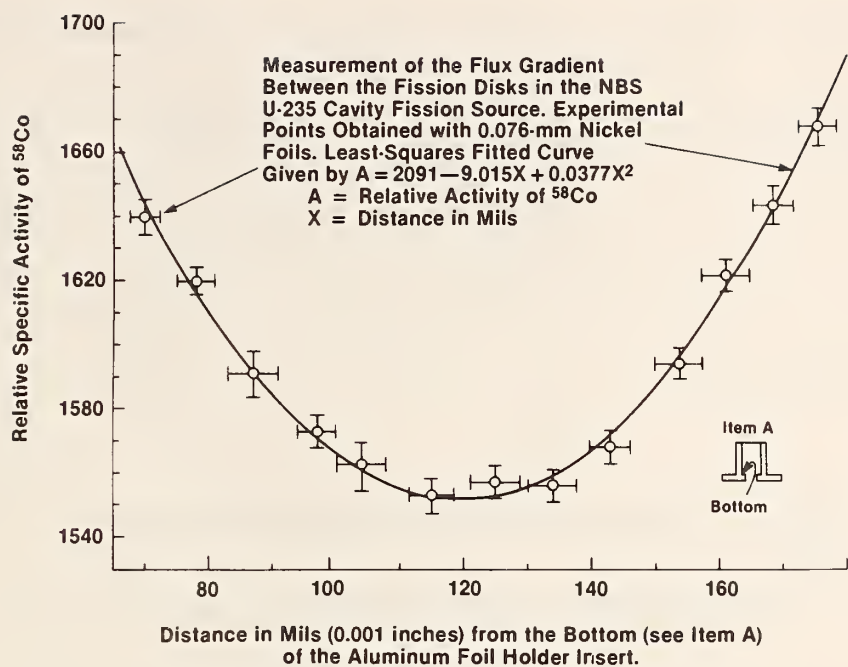


Figure 2. Flux gradients in the NBS cavity fission source.

Table 1. Summary of uncertainties for U-235 neutron field measurements.

Source	Contribution (%)
Source Strength of NBS-I	0.9
Ratio of Cf to NBS-I	0.6
Cf Source to In Foil Distance	0.4
Statistics of In Activity Counting	0.5
$\sigma_{\text{Cf}} / \sigma_{\text{U25}}$ of $\text{In}(n,n')$	1.6
Scattering Correction for In at Cf	1.0
Scattering Correction for In at Cavity	0.8
Total Uncertainty in Fluence	2.4
	^{54}Fe ^{58}Ni
Efficiency of γ Counting	0.75 0.75
Statistics of γ Counting	1.6 0.17
Flux Gradient in Cavity	0.4 0.4
Scattering Correction in Cavity	0.8 0.8
Total Uncertainty in σ	3.1% 2.7%

Table 2. Comparison of present results with previous results and calculations

Cf Fission Neutron Field	This Work	Calculated ^a	Previous Work ^b
$^{115}\text{In}(n,n')$ ^{115m}In	196 ± 4 mb	182 ± 1.5 mb	195 ± 5 mb
$^{54}\text{Fe}(n,p)$ ^{54}Mn	89 ± 2	88.3 ± 1.2	87 ± 2.4
$^{58}\text{Ni}(n,p)$ ^{58}Co	121 ± 2	114 ± 1.5	118 ± 3

U-235 Fission Neutron Field

$^{58}\text{Ni}(n,p)$ ^{58}Co	109 ± 3	101 ± 2.6	109 ± 8
$^{54}\text{Fe}(n,p)$ ^{54}Mn	79 ± 3	77.8 ± 2.2	83 ± 4

^a NBS evaluated fission spectra and ENDF/B-V cross sections; errors are for spectrum uncertainties only.

^b NBS evaluation of observed cross sections recorded in NBS compendium.

It should be noted that an erroneous, preliminary value of the $^{58}\text{Ni}(n,p)$ ^{58}Co cross section in the U-235 spectrum was reported as 101 mb in last year's annual report. The correct value (see Table 2) is 109 mb.

NEUTRON PERSONNEL DOSIMETER CALIBRATION AND TESTING

R. B. Schwartz
(Nuclear Radiation Division)

The reactor filtered beams, with energies of 2, 24, and 144 keV, together with the beam from the thermal column, were used for calibrating and testing existing types of dosimeters and remmeters and for testing new types currently under development.

In particular, personnel from the Naval Surface Weapons Center, in collaboration with CRR personnel, did extensive testing of the Navy's shipboard area monitoring system. The energy and angular response of the monitor system was determined using the four beams referred to above. In addition, the 144 keV beam was used for extensive testing of the different types of detector tubes which may be used in the monitor. The 144 keV beam is especially useful for these tubes since it is a very convenient, high-intensity source of neutrons with relatively little gamma contamination.

The energy response of a new type of dosimeter developed at Yale University was also measured using the filtered beams. This dosimeter essentially consists of superheated drops in a gel; the drops vaporize when they interact with neutrons. The dosimeter shows promise of having a nearly tissue response and of being inexpensive. The energy response measurements at the NBSR gave very promising results.

A new type of solid state track detector (CR-39) was tested in the 24 keV beam, and response measurements were made on a modified 9-inch remmeter, as well as on several types of commercial dosimeters.

RANGE OF INDIVIDUAL FISSION FRAGMENTS IN MATTER

I. Schroder and R. Fleming
(Nuclear Radiation Division)

A great deal of experimental information is available on the energy loss of charged particles in matter except for the case of individual fission fragments. There is even less information on the energy loss of individual fission fragments in heavy elements, especially in fissile materials. It is in this range where energy loss theories and phenomenological models tend to break down.

Accurate energy loss and range measurements for fission fragments (heavy ions) are of practical importance in the calculation of fragment losses in fissile targets for precise cross-section measurements as well as in direct energy conversion measurements and in magneto-hydrodynamics. These measurements would also make it possible to quantitatively assess the feasibility of depth profiling of fissile materials.

The purpose of the present experiment is to measure the range, in fissile materials, of individual fission fragments from the spontaneous fission of Cf-252 and the thermal neutron fission of U-235 and Pu-239. This is accomplished by making transmission measurements through a set of thin foils and using high resolution Ge(Li) γ -ray spectroscopy to identify the individual fission fragments transmitted.

A set of preliminary experiments have been made with Cf-252 to determine the detection efficiency for individual fission fragments and to calibrate the measurements using a series of thin aluminum foils. These measurements will be extended to cover the fission fragment from thermal neutron fission of U-235 and Pu-239. Once these calibrations have been completed, the aluminum foils will be replaced by U-238 foils and the measurements repeated.

C. REACTOR OPERATIONS AND SERVICES

The reactor was operated on a normal round-the-clock schedule for the entire year. Other than scheduled shutdowns for maintenance, refueling, testing, and for staff vacation, there were no interruptions in the operating schedule. The program of modernization of reactor components and instrumentation is continuing. Licensing activities to upgrade reactor power to 20 MW and renew the operating license are progressing. A final Environmental Impact Statement was issued by the Nuclear Regulatory Commission as required by regulations. The NRC is also preparing a safety evaluation report of the NBS submittals. In this connection NBS provided extensive additional information to NRC to assist in their review. A new license will be issued by the NRC, once the Safety Evaluation Report is published. The new license authorizing increased power and valid for a period of 20 years is expected in 1984.

Utilization of the reactor continued to be extensive and wide ranging. More than 125,000 instrument hours involving 25 simultaneously operable experimental facilities have been provided to more than 50 organizations from within and outside NBS.

1. Reactor Operations

Reactor operations continued at a high level with on-line time and fuel efficiency almost identical to that of the previous year which are among the best in the history of the facility. A summary of the overall operating statistics for the period July 1, 1982 to June 30, 1983 is presented in the following table.

NBSR Operating Summary July 82-June 83

No. of days at 10 MW	263
On-line time at 10 MW	72%
Average U-235 burnup	61%
No. of Irradiations	2820
Hours of Irradiations	1860
Hours per Irradiation	0.7

2. Irradiation Service

Heavy utilization of the reactor for major irradiation and activation analysis programs continued. Tens of thousands of specimens, involving foods, drugs, environmental monitoring, geological, and mineral examinations, forensic

investigation, and development of standard reference materials were irradiated at the NBS reactor.

3. Engineering Services

In addition to regular engineering and design services provided to reactor operations, experimenters, and users, the engineering staff was involved in a comprehensive program of reactor modernization. The new cooling tower is protected against fire by a new fire suppression system and turned over to the NBS fire department for maintenance and testing. The water treatment building and loading ramp for chemical treatment of the secondary water has been completed and is in use. A contract to fabricate new shim arm poison blades has been let. Tooling for this type of control rod was developed and used at Argonne National Laboratory and may be borrowed by the present vendor. Shim arm yokes, arbors, and bearings are in the process of fabrication. The regulating rod is being modified for 20 MW operation to operate more smoothly and reliably. A new fuel element contractor has been selected by the Department of Energy (DOE) and has made an NBSR prototype fuel assembly and a production prototype. Fabrication of fuel assemblies using fuel plates received from the previous contractor have been completed and accepted by NBS. Qualification plates are being fabricated and new plates will be in production by the end of 1983.

The program implementing the modernization of the reactor instrumentation is underway. For example, the medium sized recorders for the BTUR and main outlet flow have been replaced with modern and reliable units with a similar style of recorders recently installed for recording nuclear channels.

D. SERVICE PROGRAMS

NEUTRON ACTIVATION ANALYSIS AT THE FOOD AND DRUG ADMINISTRATION

W. B. Stroube, Jr. and W. C. Cunningham
(U. S. Food and Drug Administration, Washington, DC)

During the past year work was completed on a comprehensive set of food samples obtained through the FDA Total Diet Studies program. The Total Diet Studies is a continuing FDA program to examine chemical residue and trace nutrient content of foods purchased through retail markets and prepared as consumed. The foods were shipped to the FDA Total Diet Laboratory in Kansas City for preparation and analysis by standard procedures. They were prepared as if for consumption and then combined according to food type to make twelve composites. The 240 composites analyzed in this study represented 20 collections made between October 1979 and September 1980.

The samples were received by the FDA headquarters and freeze dried. Then approximately 300 mg of each sample was prepared and analyzed by INAA. Previously Ca, Cl, Mg, Mn, Na, and V were determined in these samples following short irradiations.¹

For the radioisotopes with longer half lives a 4-hour irradiation (at a neutron flux of $4.0 \times 10^{13} \text{ n/cm}^2\text{-sec}$) were used after a 5-day to 4-week decay. Spectra were acquired using an 80-cc Ge(Li) detector interfaced directly to a ND 6620 system. Spectra analysis and data reduction were accomplished using this system. The radioisotopes and γ -ray energies used are given in Table 1.

Results for four of the composites are given in Table 2. Elements included in this table are those for which concentrations were determined in most market baskets for at least one of the composites. When an element was found to be below detection for a specific composite, the observed detection limit is given. Analytical uncertainties (at the one sigma level) for Br, and Zn were <5% for nearly all samples. Depending on the food group, uncertainties for Fe and Rb ranged between a few percent and approximately 40% at the detection level. Elements which were near detection levels but observable in most samples include Co, Cs, Sc, Se, and V. Uncertainties for these elements were <15%.

Three elements were found to be observable in several samples but below detection for most. These include Ag, Cr, and Sb and are presented in Table 3. Also included in Table 3 are observed detection limits for As, Cd, and Eu. A qualitative search was made for several elements which were not in our standards. These include W, La, Sm, An, Lu, Ba, Th, Yb, Ce, Hf, Ta, Ti, Sr, In, S, and Mo, all of which were not observed.

Table 1. Radioisotopes, halflives, and γ -ray energies for elements determined in this work.

Radioisotope	Halflife (day)	γ -ray Energies (keV)	
Ag-110m	249.9	657.7,	884.7
As-76	1.10	559.1,	657.2, 1216.2
Au-198	2.696	411.8	
Ba-131	11.7	216.0,	496.2
Br-82	1.47	554.3,	619.1, 776.5
Cd-115	2.23	336.3,	527.9
Ce-141	32.53	145.4	
Co-60	46.214	1 173.2,	1 332.5
Cf-51	27.7	320.0	
Cs-134	18.058	795.8	
Eu-152	113.958	964.0,	1 408.0
Fe-59	44.6	1 099.2,	1 291.6
Hf-181	42.40	133.1,	482.2
La-140	1.676	208.4	
Lu-177	6.71	1 077.0	
Rb-86	18.65	1 691.0	
Sb-124	60.2	889.3,	1 120.5
Sc-46	83.8	136.0,	264.7
Se-75	120.0	103.2	
Sm-153	1.947	1 189.0,	1 221.5
Ta-182	115.0	311.9	
Th-233*	27.0	479.5,	685.7
W-187	1.00	177.2	
Yb-169	31.2	1 115.2	
Zn-65	243.8		
*Th-233 B-	233Pa		

Table 2. Average element concentrations and ranges in food ug/g (dry mass) except as noted.

	Dairy	Meat, Fish, Poultry	Grains Cereals	Potatoes
Br	14.1 6.4-25.5	6.35 4.0-9.7	14.5 9.6-34.3	4.71 1.1-14.4
Co ^a	81 49-124	44 21-76	35 15-60	92 44-245
Cs	0.110 ^b 0.084-0.157	0.058 ^b 0.041-0.069	0.047 ^b 0.046-0.047	0.050 ^b 0.048-0.053
Fe	49.6 ^c (<42)	46.1 32.8-70.6	49.3 24.6-98.0	35.2 18.6-63.6
K	9 550 7 450-11 200	6 270 3 870-7 970	1 600 859-2 300	14 900 9 870-19 500
Rb	10.14 5.81-18.5	6.66 4.96-10.5	2.50 1.29-5.84	6.36 2.20-9.46
Sc ^a	<9	<4	4.35 ^b 2.65-8.22	5.12 2.90-7.65
Se	1.35 1.30-1.40	0.73 0.46-1.42	0.58 0.28-0.85	<1.0
Zn	24.2 16.1-30.5	65.4 47.6-74.6	11.6 7.39-19.9	12.4 4.62-21.5

a. ng/g.

b. Most results below detection. This average may, therefore, be biased high.

c. Detected in only two samples.

SERVICE PROGRAMS

Table 3. Average element concentrations and regions in food ug/g (dry mass).

	Dairy	Meat, Fish, Poultry	Grains, Cereals	Potatoes
Ag	>0.60	0.23 ^c 0.16-0.37	0.18 ^c 0.15-0.23	<0.28
As	<10	<2	<0.4	<6
Cd	<2	<5	<5	<10
Cr	1.1 ^c 0.80-1.4	0.56 ^c	<1.4	<1.0
Eu	<0.050	<0.035	<0.045	<0.30
Sb	<0.15	<0.10	<0.13	<0.08

Although the procedure used did not maximize for any single element, careful treatment of the interferences enabled concentrations to be determined for 18 elements in the food samples. These data form a substantial base which covers a wide range of foods and samples from each of 20 food collections made in cities throughout the United States. The observed concentration ranges should, therefore, predict reasonably well what one will find in these types of foods. Consideration of these data, and for those elements near detection, the various factors controlling detection levels should enable one to predict the capabilities of INAA for further food analyses.

1. NBS Reactor: Summary of Activities July 1981 through June 1982, p. 199.

POSITRON ANNIHILATION IN CuGe AND CuZn ALLOYS

L. M. Pecora and A. C. Ehrlich
 (Naval Research Laboratory, Washington, DC)

We used data collected over the last several years to examine two features present in momentum densities of CuGe alloys. One is the enhancement of the measured momentum density $\rho(p)$ near the Fermi edge which results in a peak in $\rho(p)$ around 5.5 rad in these materials. It has been suggested^{1, 2} that this enhancement is well described by an empirical relation which we fit to our data.³ The other feature is the change in anisotropy of $\rho(p)$ at 7 mrad along the [100] direction. We have suggested that this is related to changes in s-d hybridization.⁴ Using a newly developed numerical technique⁵ we determine the population of s, p, and d states in this [100] region for Cu and Cu₉₂Ge₈ and compare the two populations to comment on hybridization.

1. Enhancement Formulas

Near the Fermi surface $\rho(p)$ is enhanced by a factor $\epsilon(p)$ so that if $\rho_m(p)$ is the measured momentum density we have

$$\rho_m(p) = \epsilon(p)\rho(p).$$

Several empirical forms for $\epsilon(p)$ have been suggested.^{1, 2} One by Kahana

$$\epsilon(p) = a + b(P/P_F)^2 + c(p/p_F)^4 \quad (1)$$

and the other by Mijnarends and Singru

$$\epsilon(p) = a + b(E/E_F) + c(E/E_F)^2. \quad (2)$$

In these formulas p_F = Fermi momentum E_F = Fermi energy, and E is measured from the bottom of the band. Note that in the free electron case (1) and (2) are the same. We used CuGe and CuZn data^{6, 7} to determine the empirical a, b, c's for (1) and (2). For energies in (2) we used the APW results of Papaconstantopoulos et al.⁸ Table 1 shows our results for (1), the momentum formula, and (2), the energy formula. Although there is scatter in the results from different alloys, the empirical constants for relations (1) and (2) are nearly equal in all cases. Further examination of the contribution of each band along a typical direction ([100]) to

$\rho(p)$ shows that the bands which are most nearly free-electron-like are precisely those bands which contribute most to $\rho(p)$ (see Figure 1). Since (1) and (2) are the same in the free electron case we can see that data from these alloys will not show preference for either (1) or (2) in describing enhancement, $\epsilon(p)$. This is probably true for all metals and metal alloys since, in the first zone, it is the free electron component of the wave function which contributes to $\rho(p)$ in all cases.

2. s-p-d Hybridization in CuGe Alloys

Quantum measurements which can be considered as independent particle measurements can be written as

$$\langle \theta \rangle = \text{tr } \underline{P}$$

where $\langle \theta \rangle$ is the expectation value (measurement in the experiment, \underline{P} is the population matrix, and θ is the operator representing the measurement. The diagonal elements of \underline{P} give the quantum mechanical population of the states in the basis.

In our case we chose s, p, and d tight binding wave functions for the basis. The expansion coefficients for Cu were provided by D. Papaconstantopoulos⁹ using a Slater-Koster fit to Cu APW results. The wave functions were atomic Herman-Skillman functions.

We then used a newly developed numerical technique⁵ to calculate \underline{P} for Cu₉₂Ge₈ in the region of 7 mrad along [100] where the momentum density is larger than for Cu (see Figure 2a and 2b). The results of the \underline{P} calculation are shown in figure 2c. It can be seen that the % d decreases and the % s increases as Ge is added to Cu. These quantitative results corroborate our original conclusion⁴ that the s-d hybridization changes along [100] as Ge is added to Cu.

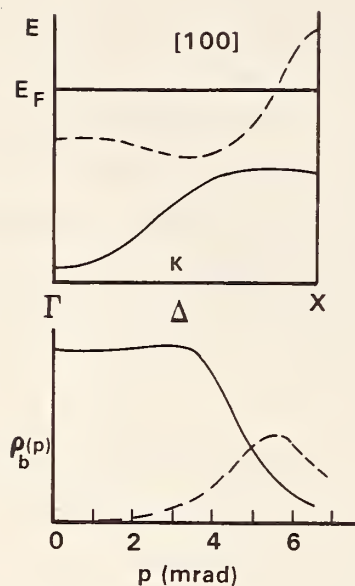


Figure 1. Top shows the band structure for Cu [100] for bands which contribute to $\rho(p)$. Bottom shows the relative contribute $\rho_b(p)$ of each band to $\rho(p)$.

Table 1. Parameters for enhancement formulas determined from momentum density data comparing our work to others for Cu and comparing momentum and energy formulations for various Cu alloys.*

<u>Alloy</u>	<u>Reference</u>	<u>Momentum Formula</u> Eqn. (1)		<u>Energy Formula</u> Eqn. (2)	
		<u>b/a</u>	<u>c/a</u>	<u>b/a</u>	<u>c/a</u>
Cu	Kahana	0.195	0.139		
	Sinclair, et al. (Proc. 6th Conf. Pos. Ann. 1982)	$0.131 \pm .02$	$0.110 \pm .036$		$0.12 \pm .15$
	Our Work	$0.27 \pm .1$	$0.03 \pm .15$	$0.26 \pm .1$	$0.12 \pm .15$
$\text{Cu}_{92}\text{Ge}_8$	Our Work	$1.13 \pm .2$	$-1.3 \pm .25$	$1.25 \pm .2$	$-1.5 \pm .3$
$\text{Cu}_{75}\text{Zn}_{25}$	Our Work	$0.3 \pm .2$	$0.62 \pm .25$	$0.195 \pm .2$	$1.0 \pm .3$

*Only the ratios b/a and c/a are given since absolute scale is not important.

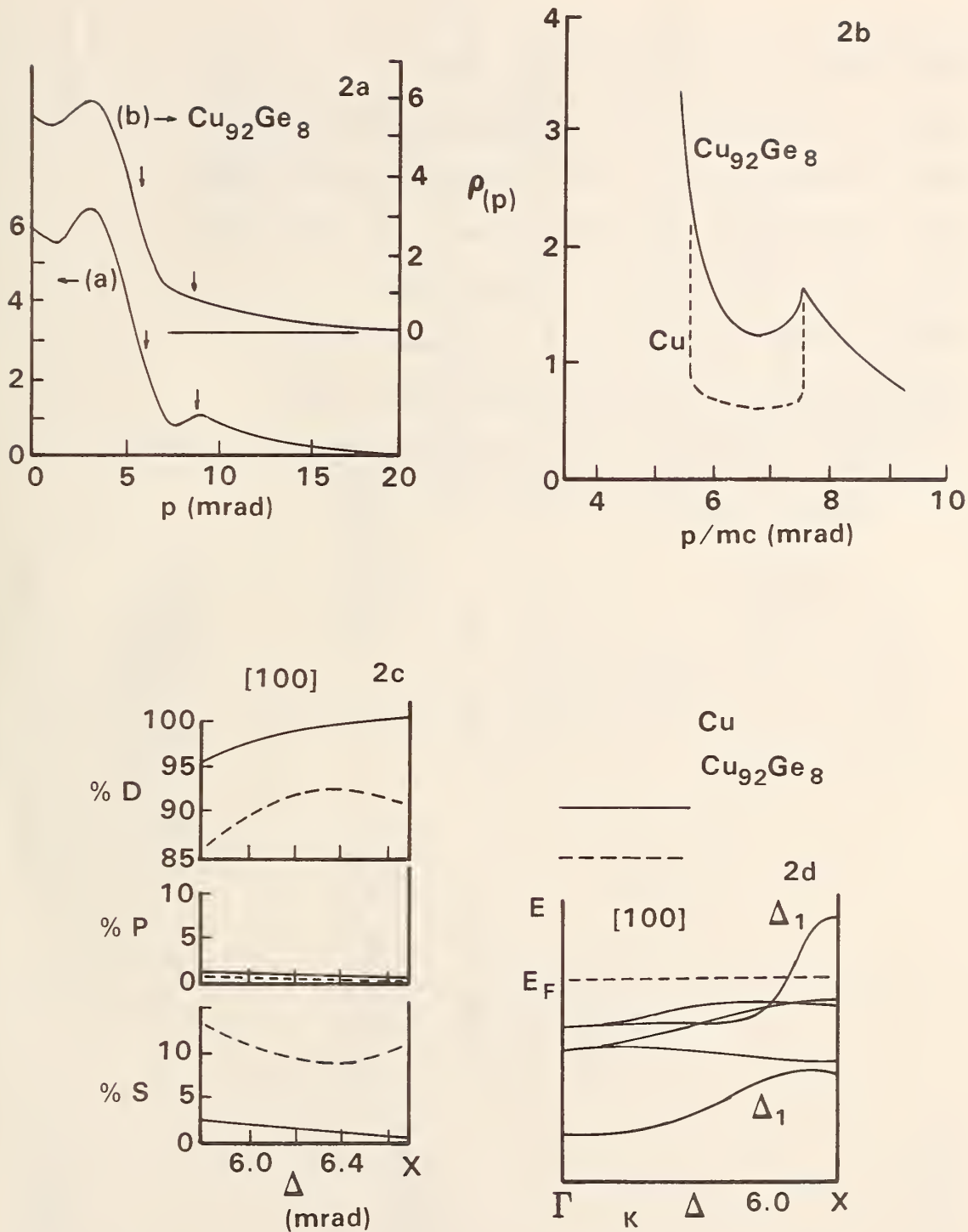


Figure 2. (a) $\rho(p)$ for Cu and $\text{Cu}_{92}\text{Ge}_8$ along [100]. Note changes between arrows. (b) Closeup between arrows of a. (c) Populations of Cu and $\text{Cu}_{92}\text{Ge}_8$ in the region of 2b for the lower Δ_1 band which contributes here. (d) Band structure of Cu [100] showing the 2 bands which contribute to $\rho(p)$ and the region of figure 2b (shaded).

-
1. Kahana, Physical Review 129, 1622 (1963).
 2. Mijnarends and Singru, Physical Review B19, 6938 (1979).
 3. Pecora and Ehrlich, Bull. Amer. Phys. Soc. 28, 307 (1983).
 4. Pecora and Ehrlich, Physical Review Lett. 46, 1476 (1981).
 5. Pecora, Bull. Amer. Phys. Soc. 28, 530 (1983).
 6. Pecora and Ehrlich, NBS Reactors Users Report (1981).
 7. Pecora and Ehrlich, NBS Reactors Users Report (1982).
 8. D. A. Papaconstantopoulos, et al., Phys. Rev. B15, 4221 (1977).
 9. D. A. Papaconstantopoulos, private comm.

E. PERSONNEL ROSTER

REACTOR RADIATION DIVISION

566

Reactor Operations	T. M. Raby, Chief J. J. F. Torrence, Deputy Chief C. Harrison, Secretary	Engineering Services	J. H. Nicklas, Chief C. Harrison, Secretary	Neutron S-S P J. J. Rush, Ch P. Andrew, Sec
--------------------	--	----------------------	--	---

Reactor Operators

R. Beasley	E. Guglielmo	#C. Choi	#H. Alperin	M. Ganoczy
J. Bell	J. Sturrock	D. Fravel (1/2)	#N. Koon	#T. Cheng
N. Bickford	N. Browning	J. LaRock (1/2)	+J. Lynn	
J. Chapman	A. Chapman	E. Prince	J. Rhyne	
H. Dilks	H. Hayes	W. Rymes (1/2)	#R. Williams	
L. Lindstrom	L. Shuman	A. Santoro		<u>Biological Materials</u>
K. Mueller		+V. Himes		
T. Myers		A. Michell		
J. Ring		J. Stalick	#H. Savage	
R. Stiber		+D. Stakes	A. Wlodawer	
A. Toth				
D. Wilkison				
<u>Metal Hydrides and Molecular Materials</u>				
D. Fravel (1/2)	N. Berk			
#H. Prask	C. Glinka			
J. Rowe (1/2)	J. LaRock (1/2)			
W. Rymes (1/2)	J. Rowe (1/2)			
#S. Trevino	S. Singhhal, IPA			
	S. Werner, IPA			
<u>Advanced Neutron Methods</u>				
D. Fravel (1/2)	N. Berk			
#H. Prask	C. Glinka			
J. Rowe (1/2)	J. LaRock (1/2)			
W. Rymes (1/2)	J. Rowe (1/2)			
#S. Trevino	S. Singhhal, IPA			
	S. Werner, IPA			
<u>*Part-time</u>				
<u>*WAE, Coop, Stay-in-school</u>				
<u>#Guest Worker, research assoc.</u>				

*Part-time
+WAE, Coop, Stay-in-school
#Guest Worker, research assoc.

PERSONNEL ROSTER

NON-RRD NBS STAFF LOCATED AT REACTOR

Division 354

J. Arras
I. Bartky
D. Hoaney
I. Jensen
F. Moore
J. Shubiak

Division 532

R. A. Dallatore
C. Eisenhauer
D. Gilliam
J. A. Grundl
G. Lamaze
L. Li
E. McGarry
I. Schröder
R. Schwartz

Division 500

B. Carpenter
Division 551
G. Downing
R. Fleming
K. Fitzpatrick
S. Harrison
J. Langland
R. Lindstrom
G. Lutz
S. Stone
M. Vinocur
J. Vogt
R. Zeisler

GUEST WORKERS AND COLLABORATORS

Division 501

H. T. Yolken

Division 506

D. Becker

Division 520

E. Kessler

Division 522

R. Dove

Division 532

A. Wasson

Division 533

R. Placious

Division 541

J. Kelly
T. Udovic

Division 544

D. Tsai

Division 545

R. Cavanagh

Division 552

S. Wise
L. Sander

Division 553

H. Rook

PERSONNEL ROSTER

Division 561

F. Brinckman
E. Fuller
K. Hardman-Rhyne
G. Olsen
C. Robbins
R. Roth

Division 562

R. Fields

Division 563

B. Bauer
C. Han
M. Mathew
S. Takagi
R. Waterstrat
W. Wu

Division 564

F. Biancanello
J. Early
R. Reno
R. Shull
H. Wadley

Aberdeen Proving Ground

C. Heimbach

Army Armament Research and Development Command

C. Choi
H. Prask
S. Trevino

Federal Bureau of Investigation

R. Asbery
R. Bilko
J. Haverkost
J. Kilty
P. Kostella

Federal Bureau of Investigation
(Continued)

C. Peters
J. Riley
P. Tangren
P. Thompson

Food and Drug Administration

W. Cunningham
W. Stroube, Jr.
J. Tanner

National Gallery of Art

B. Miller
C. Parkhurst

National Institutes of Health

D. Davies
R. Frank
G. Gilliland
D. Jackson
S. Szu

Naval Research Laboratory

P. D'Antonio
A. Ehrlich
M. Fatemi
N. Koon
L. Pecora

Naval Surface Weapons Center

H. Alperin
M. Lia
G. Riel

Smithsonian Institution

M. Blackman
T. Chase
Y. Cheng
J. Mishara
J. Olin
L. Zacherman

PERSONNEL ROSTER

U. S. Geological Survey

P. Baedecker
H. Evans
J. Morgan
G. Wandless

Argonne National Laboratory

H. Flotow
J. Jorgenson
S. Susman

Battelle, N. W.

L. Brackenbush
G. Endres
W. Nicholson

Brookhaven National Laboratory

J. Johnson

C.R.N.S. Grenoble, France

P. Bordet
J. Hodeau
M. Marezio

Institute Laue-Langevin
Grenoble, France

A. Magerl
R. Pynn

KFA Jülich, Germany

P. Hempleman
D. Richter

Nuclear Energy Center, Mol, Belgium

A. Fabry

Oak Ridge National Laboratory

F. Kam

University of Alabama

J. Segrest

Howard University

D. Chung

Iowa State University

R. Shelton

Kyoto University (Japan)

H. Hasegawa
T. Hashimoto
H. Kawai

M.I.T.

B. Averbach
L. Schioler
C. Skarda
B. Wuenscher

Northwestern University

S. Kim
J. Weertman

Pennsylvania State University

L. Pilione

State University of New York

H. Herman

Technical University of Munich
Germany

H. Wipf

University of Antwerp (Belgium)

K. Michel

PERSONNEL ROSTER

University of Connecticut

J. Budnick

University of California (Berkley)

R. Bragg
E. Case

University of Ife (Nigeria)

L. Kehinde
A. Oluwole

University of Illinois

H. Birnbaum
R. Chasnov
D. Neumann
H. Zabel

University of Maryland

D. Anderson
F. Baca
A. Bagheri
D. Ballantine
D. DeMers
D. Delozier
R. Erwin
D. Finnegan
F. Geunther
J. Gotaas
D. Herman
M. Kitto
W. Linthicum
I. Olmez
J. Parrington
J. Phelan
J. Robertson
S. Stone
P. Sheridan
C. Thompson
G. Tuncel
W. Walters
W. Zoller

University of Michigan

D. Vincent

University of Milan (Italy)

M. Zocchi

University of Minnesota

T. Lodge

University of Missouri (Columbia)

D. Alger

University of Missouri (Rolla)

W. James

University of New Hampshire

R. Blackmore

University of Pittsburgh

R. Buttera
S. Malik
H. Smith
W. Wallace

University of Rhode Island

S. Pickart

University of Wisconsin

E. Amis
T. Kitano
M. Landry
J. Miller
H. Shepard
D. Urso

Allied Corporation

G. Fish

PERSONNEL ROSTER

Allied Corporation (Continued)

R. Hasegawa
A. Maeland

Bell Laboratories

R. Cava
C. Chen
J. Mitchell
D. Murphy
J. Riley

B-K Dynamics

N. Chesser

E.I. DuPont de Nemours Co.

J. Parise

Exxon

J. Gethner
D. Lohse

3M Research Laboratory

A. Siedle

Sandia Corporation

J. Harris

Union Carbide Corporation

E. Goddard
P. Leung

Westinghouse-Hanford Corp.

W. McElroy
J. Rawlins

PUBLICATIONS

F. PUBLICATIONS

COLLABORATIVE PROGRAMS

AMMON, H. L., MURPHY, K. C., SJOLIN, L. WLODAWER, A., HOLCENBERG, J. S., and ROBERTS, J., "The Molecular Symmetry of Glutaminase-Asparaginases Rotation Function Studies of the Pseudomonas 7A and Acinetobacter Enzymes," *Acta Cryst. Sect. B* 39, 250-257 (1983).

BERK, N. F., ROSENTHAL, J., and YARMUS, L., "Spin Relaxation of Triplet Excitons in Molecular Crystals," *Phys. Rev. B* (in press).

CASE, E. and GLINKA, C. J., "Small Angle Neutron Scattering Study of Microcracks in Yttrium Chromate," *J. Matls. Sci.* (in press).

CASELLA, R. C., "Generalized Theory of Neutron Scattering from Hydrogen in Metals," *Phys. Rev. B* (in press).

CASELLA, R. C., "Theory of Excitation Bands of Hydrogen in bcc Metals and of their Observation by Neutron Scattering," *Phys. Rev. B* 27, 5943-5954 (1983).

CAVA, R. J., SANTORO, A., MURPHY, D. F., ZAHURAK, S., and ROTH, R. S., "The Structures of the Lithium Inserted Metal Oxides $\text{Li}_{0.2}\text{ReO}_3$ and $\text{Li}_{0.36}\text{WO}_3$," *J. Solid State Chem.* (in press).

CAVA, R. J., SANTORO, A., MURPHY, D. F., ZAHURAK, S., and ROTH, R. S., "The Structure of Lithium Inserted Metal Oxides: $\text{Li}_2\text{FeV}_3\text{O}_8$," *J. Solid State Chem.* (in press).

CAVANAGH, R., KELLEY, R. D., and RUSH, J. J., "Neutron Vibrational Spectroscopy of Hydrogen and Deuterium on Raney Nickel," *J. Chem. Phys.* 77, 1540 (1982).

CHOI, C. S. and PRASK, H. J., "The Crystal Structure of ND_4NO_3 Phase V by Neutron Powder Diffraction," *Acta Cryst.* B38, 2874-2876 (1982).

CHOI, C. S. and MIGHELL, A. D., "Neutron Diffraction Study of Sodium Sesquicarbonate Dihydrate," *Acta Cryst.* B38, 2324-2328 (1982).

CHOI, C. S. and PRASK, H. J., "Single-Crystal Neutron Diffraction Study of Ammonium Nitrate Phase III," *Acta Cryst.* B38, 2324-2328 (1982).

COHEN, J. S. and WLODAWER, A., "Diffraction and NMR Studies of Proteins: An Uneasy Alliance," *Trans. Biochem. Sci.* 7, 389-391 (1982).

D'ANTONIO, P., KONNERT, J. H., RHYNE, J. J., and HUBBARD, C. R., "Structural Ordering in Amorphous TbFe_2 and YFe_2 ," *J. Appl. Cryst.* 15, 452-460 (1982).

DEYOREO, J. J., MEISSNER, M., POHL, R. O., ROWE, J. M., RUSH, J. J., and SUSMAN, S., "Low Energy Excitations in $(\text{KBr})_{1-x}(\text{KCN})_x$ in the Orientational Glass State," *Phys. Rev. Lett.* (in press).

EVANS, H. T., Jr. and PRINCE, E., "Location of Internal Hydrogen Atoms in the Paradodecatungstate Polyanion by Neutron Diffraction," *J. Am. Chem. Soc.* (in press).

FARNOUX, B. and MOZER, B., "Neutron Intensity Distribution at the End of the Neutron Guides at the Reactor Orphee." *Report of Leon Brillouin Laboratory LLB13* (1982).

PUBLICATIONS

- FARNOUX, B. and MOZER, B., "Preliminary Measurements of the Gain from the Cold Sources at the Reactor Orphee," Report of Leon Brillouin Laboratory LLB14 (1982).
- GLINKA, C. J. and BERK, N. F., "The Two-Dimensional PSD at the National Bureau of Standards Small-Angle Neutron Scattering Facility," Forsythe, B., ed. Proceedings of the Workshop on Position-Sensitive Detection of Thermal Neutrons, Grenoble, France (in press).
- GLINKA, C. J., FIELDS, R., HAN, C., RHYNE, K., ROTH, R., ROWE, J., RUSH, J., SHULL, R., and STEINER, B., "Neutron Scattering, Present and Future Activities in the Center for Materials Science" (1983).
- GLINKA, C. J., "The National Bureau of Standards Small-Angle Neutron Scattering Spectrometer," Faber, J., ed American Institute of Physics Conference Proceedings No. 89, (1982).
- GUNNING, J., BEDARKER, S., TAYLOR, G. L., GOODFELLOW, J. M., BLUNDELL, T. L., WLODAWER, A., HODGSON, K. O., SHOOTER, E. M., FOURME, R., GABER, B., and WILLIAMS, R., "Conformational Studies of Polypeptide Growth Factors: IGF and NGF in Cell Function and Differentiation," Part A, Alan R. Liss Inc. (1982).
- HARDMAN-RHYNE, K. and RHYNE, J. J., "Short and Long-Range Magnetic Ordering of $Y_6(Fe_{1-x}Mn_x)_{23}$ and Related Compounds Using Neutron Scattering Techniques," *J. Less-Common Met.*, 94, 23-36 (1983).
- HARDMAN-RHYNE, K., RHYNE, J. J., PRINCE, E., CROWDER, C., and JAMES, W. J., "Magnetic and Crystallographic Structure of $Y_6Mn_{23}D_{23}$," *Phys. Rev. B* (in press).
- HIMES, V. L. and MIGHELL, A. D., "A Matrix Method for Lattice Symmetry Determination," *Acta Cryst. Sect. A*38, 748-749 (1982).
- HODEAU, J. L., MAREZIO, M., SANTORO, A., and ROTH, R. S., "Neutron Diffraction Structure Determination of the High-Temperature Form of Lithium Tritantalate, H-LiTa₃O₈," *J. Solid State Chem.* (in press).
- HODEAU, J. L., MAREZIO, M. SANTORO, A., and ROTH, R. S., "Neutron Profile Refinement of the Structures of Li₂SnO₃ and Li₂ZrO₃," *J. Solid State Chem.* 45, 170-179 (1982).
- KELLEY, R. D., CAVANAGH, R. R., and RUSH, J. J., "Co-Adsorption and Reaction of H₂ and CO on Raney Nickel: Neutron Vibrational Spectroscopy," *J. Catalysis* (in press).
- KOKOSKA, G. F., BARANOWSKI, J., GOLDSTEIN, C., ORSINI, J., MIGHELL, A. D., HIMES, V. L., SIEDLE, A. R., "Two-Dimensional Dynamical Jahn-Teller Effects in a Mixed-Valance Benzotriazolato Copper Cluster, Cu₅(BTA)₆(RNC)₄," *J. Am. Chem. Soc.* (in press).
- LYNN, J. W., "Neutron Scattering Studies of Magnetic Phase Transitions in Superconductors," *J. Less-Common Met.* (in press).
- LYNN, J. W., SHELTON, R. N., HORNG, H. E., and GLINKA, C. J., "Investigation of the Magnetic and Superconducting Properties of (Er_{1-x}Ho_x)Rh₄B₄," *Physica*, 120B, 224-226 (1983).

PUBLICATIONS

- LYNN, J. W., ERWIN, R. W., RHYNE, J. J., and CHEN, H. S., "Ferromagnetic and Spin Glass Behavior Near the Critical Concentration in Amorphous $(Fe_xNi_{1-x})^{75}G_{125}$ ", *J. Mag. Matls.* 31-34, 1397-1398 (1983).
- LYNN, J. W., ERWIN, R. W., CHEN, H. S., and RHYNE, J. J., "Evolution from Ferromagnetism to Spin-Glass Behavior," *Sol. St. Comm.* 46, 317-320 (1983).
- LYNN, J. W., RHYNE, J. J., and BUDNICK, J. I., "Observation of Spin Waves in Pd (1.5% Fe)," *J. Appl. Phys.* 53 (1982).
- LEUNG, P. S., GODDARD, E. D., HAN, C. C., and GLINKA, C. J., "Small Angle Neutron Scattering Study of Polycation and Anionic Surfactant Complexes," *J. Colloid Sci.* (in press).
- LUDEMAN, S. M., SHAO, K. L., ZON, G., HIMES, V. L., MIGHELL, A. D., TAKAGI, S., and MIZUTA, K., "O-iminyl Esters of N,N-bis(2-chloroethyl)phosphorodiamidic Acid. Synthesis, X-ray Structure Determination, and Anticancer Evaluation," *J. Medicinal Chem.* (in press).
- MAGERL, A., ZABEL, H., RUSH, J. J., and DIANOUX, A. J., "Dynamical Properties of Alkali Intercalates in Graphite," *Synthetic Metals* (in press).
- MAGERL, A., ZABEL, H., and RUSH, J. J., "Phonons in LiC₆ and in Heavy Alkali Metal Graphite Intercalation Compounds," *Synthetic Metals* (in press).
- MAGERL, A., ROWE, J. M., RUSH, J. J., WIPF, H., and RICHTER, D., "Influence of Impurities on Local Hydrogen Vibrations in a Niobium Host Lattice," *Jana, P., Satterthwaite, K., ed., Proceedings of the International Symposium on the Electronic Structure and Properties of Hydrogen in Metals* (in press).
- MAGERL, A., RUSH, J. J., ROWE, J. M., RICHTER, D., and WIPF, H., "Local Hydrogen Vibrations in Nb in the Presence of Interstitial (N, O) and Substitutional (V) Impurities," *Phys. Rev. B27*, 927-934 (1983).
- MCCARTHY, G. J., SILBER, H., and RHYNE, J. J., ed., "The Rare Earths in Modern Science and Technology," Vol. 3 (1982).
- MIGHELL, A. D., HIMES, V. L., and RODGERS, J. R., "Space Group Frequencies for Organic Compounds," *Acta Cryst. Sect. A* (in press).
- MILLER, M., WEINSTEIN, J. N. and WLODAWER, A., "Preliminary X-Ray Analysis of Single Crystals of Ovalbumin and Plakalbumin," *J. Biol. Chem.* 258, 5864-5866 (1983).
- MOOK, H. A. and LYNN, J. W., "Magnetic Excitations in Amorphous Isotropic Ferromagnets," *Phys. Rev.* (in press).
- MOSS, S., RUSH, J. J., SCHWARTZ, L., and ULLMAN, R., "Report to the National Science Foundation on the Center for Small Angle Scattering Research," (1983).
- MOZER, B., SINGHAL, S. P., and SHULL, R. D., "Phase Decomposition in Cu-Ti Metallic Glass," *Proceedings of the Summer Meeting of the American Crystallographic Association* (in press).

PUBLICATIONS

MOZER, B., SINGHAL, S. P., and SHULL, R. D., "Phase Decomposition in Cu-Ti Metallic Glass," Proceedings of the Fall Meeting of the Metallurgical Society of AIME (in press).

NICHOLSON, W. L., PRINCE, E., BUCHANAN, J., and TUCKER, P. A., "Robust/Resistant Technique for Crystal Structure Refinement in Progress and Problems in Crystallographic Statistics," S. Ramaseshan, M. F. Richardson, A. J. C. Wilson, ed. Madras, India: Indian Academy of Sciences (1982).

PARISE, J. B., PRINCE, E., and COX, D., "The Crystal Structure of the Synthetic Zeolites (Cs, K)-ZK5 and (Cs, D)-ZK5 Determined from Neutron Powder Diffraction Data," Z. Kristallogr. (in press).

PARISE, J. B., BRIXNER, L. H., and PRINCE, E., "Refinement of the Structure of $\text{La}_3\text{WO}_6\text{Cl}_3$ from Neutron Powder Diffraction Data," Acta Cryst. Sect. C (in press).

PARISE, J. B., JORGENSEN, J. D., and PRINCE, E., "Concerning the Flexibility of the Framework of Zeolite RHO: Structural Variation from 11 K to 573 K," J. Phys. Chem. (in press).

PARISE, J. B. and PRINCE, E., "The Structure of Cs-RHO at 295 K and 493 K Determined from High Resolution Neutron Powder Data," J. Zeolites (in press).

PICKART, S., ALPERIN, H., MENZINGER, F., MAZZONE, G., and SACCHETTI, F., "Neutron Depolarization by Amorphous Magnets in the Critical Region," Phys. Lett. 95A, 397 (1983).

PRINCE, E. and NICHOLSON, W. L., "A Test of a Robust/Resistant Refinement Procedure on Synthetic Data Sets," Acta Cryst. Sect. A39, 407 (1983).

RHYNE, J. J. and KOON, N. C., "Effects of Crystal Field and Exchange Interactions on the Spin Excitations in Rare Earth Laves-phase Compounds," Proceedings of the International Conference on Magnetism of Rare-Earths and Actinides, eds., E. Burzo and M. Rogalski, Abstracts and Proceedings Series CIP-AP, Cent. Inst. of Physics, Bucharest, Romania, 4, 9-17 (1983).

RHYNE, J. J., HARDMAN-RHYNE, K., SMITH, H. K., and WALLACE, W. E., "Deuterium Site Occupation and Magnetism in $\text{Ho}_6\text{Fe}_{23}\text{D}_x$ Compounds," J. Less-Common Met., 94, 95-105 (1983).

RHYNE, J. J., "Magnetic Phase Transition Temperatures of the Elements," Bull. Alloy Phase Diag., 3, 401-402 (1982).

RHYNE, J. J. and KOON, N. C., "Spin Dynamics of HoAl_2 ," J. Mag. Matls., 31-34, 608-610 (1983).

RHYNE, J. J., "Magnetic Materials in Concise Encyclopedia of Solid State Physics," R. G. Lerner and G. L. Trigg, ed. (1983).

RHYNE, J. J. and KOON, N. C., "Ground State Spin Excitations in HoAl_2 ," J. Appl. Phys. 53, 8354-8356 (1982).

RICHTER, D., RUSH, J. J., and ROWE, J. M., "Localized Modes and Hydrogen Trapping in Niobium with Substitutional Impurities," Phys. Rev. B27, 6227-6233 (1983).

PUBLICATIONS

- ROWE, J. M., RUSH, J. J., and SUSMAN, S., "Neutron Powder Diffraction Study of Phase Transitions and Structures of $(\text{KCN})_x(\text{KBr})_{1-x}$ Mixed Crystal," Phys. Rev. (in press).
- ROWE, J. M., RUSH, J. J., and LUTY, F., "The Crystal Structure of Rubidium Cyanide at 4 K Determined by Neutron Powder Diffraction," Phys. Rev. Brief Comm. (in press).
- ROWE, J. M., BIRGENEAU, R. J., BRUGGER, R. M., CARPENTER, J. M., and PYNN, R., "Report to the Director of Physics," Los Alamos National Laboratory (1983).
- RUSH, J. J. CAVANAGH, R. R., and KELLEY, R. D., "Neutron Scattering from Adsorbates on Platinum Black," J. Vac. Sci. Technol. A1, 1245-1246 (1983).
- SANTORO, A., D'ANTONIO, P., and CAULDER, S. M., "A Neutron Powder Diffraction Study of - and -PbO_2 in the Positive Electrode Material of Lead-Acid Batteries," J. Electrochem. Soc. (in press).
- SANTORO, A., "The Role of Modern Neutron Powder Diffraction Techniques in the Study of Solid State Ionics," Proceedings of the 4th International Conference on Solid State Ionics: Grenoble, France (in press).
- SANTORO, A., "New Developments in Neutron Powder Profile Analysis," Proceedings of the Third Italian-Yugoslavian Crystallographic Conference: Bled, Yugoslavia (in press).
- SANTORO, A., CAVA, R. J., MURPHY, D. W., and ROTH, R. S., "Use of the Pearson Type VII Distribution in the Neutron Profile Refinement of the Structures of LiReO_3 and Li_2ReO_3 in Neutron Scattering," Farber, J., ed., American Institute of Physics Conference Proceedings No. 89 (1982).
- SHORTEN, F. J., ed. "NBS Reactor: Summary of Activities July 1981 through June 1982," Nat. Bur. Stand. Tech. Note 1178 (1983).
- STALICK, J. K., HUBBARD, C. R., MIGHELL, A. D., RODGERS, J. R., and HORN, A. S., "2-Amino-6,7-dihydroxytetralin hydrobromide, $\text{C}_{10}\text{H}_9(\text{OH})_2\text{NH}_3^+\text{Br}^-$," Acta Cryst. Sect. C (in press).
- SUSMAN, S., DELBECQ, C. J., BRUN, T. O., and PRINCE, E., "Structure and Conductivity of the NASICON Analog $\text{Na}_3\text{Sc}_2(\text{PO}_4)_3$," Electrochim. Soc. Ext. Abst. (1982).
- THOMLINSON, W., SHIRANE, G., LYNN, J. W., and MONCTON, D. E., "Neutron Scattering Studies of Magnetic Ordering in Ternary Superconductors," Chapter 8 in Superconductivity in Ternary Compounds, Topics in Current Physics Series, Vol. 34, M. B. Maple; O Fischer, ed., New York, NY, Springer-Verlag (1982).
- TREVINO, S. F. and TSAI, D. H., "Model Simulation of Chemical Reaction in a Diatomic Crystal, Part I: Energy Exchange in Rapid Exothermic Dissociation," Proceedings of the American Physical Society Conference on Shock Waves in Condensed Matter (in press).
- TREVINO, S. F. and TSAI, D. H., "Model Simulation of Chemical Reaction in a Diatomic Crystal, Part II: Kinetics of Equilibrium Chemistry," Proceedings of the American Physical Society Conference on Shock Waves in Condensed Matter (in press).

PUBLICATIONS

- TSAI, D. H. and TREVINO, S. F., "Molecular Dynamical Studies of the Dissociation of a Diatomic Molecular Crystal, Part I: Energy Exchange in Rapid Exothermic Reactions," *J. Chem. Phys.* (in press).
- WADLEY, H., FANCONI, B., FORTUNKO, E., FULLER, E., HUNSTON, E., LINZER, M., SINGHAL, S., and STEINER, B., "Nondestructive Evaluation, Present and Future Activities," *Center for Materials Science* (1983).
- WLODAWER, A., "A Facility for Data Collection and Processing at the National Bureau of Standards Reactor," *Methods in Enzymology*. H. W. Wyckoff, C. H. W. Hirs, and S. N. Timasheff, ed. Academic Press (in press).
- WLODAWER, A. and SJOLIN, L., "Application of Joint Neutron and X-ray Refinement to the Investigation of the Structure of Ribonuclease A at 2.0 Å Resolution," *Brookhaven Symposia in Biology* (in press).
- WLODAWER, A., "Structure of Bovine Pancreatic Ribonuclease" in "Structural Biology," Vol. II: Nucleic Acid Binding Proteins," A. McPherson, F. Jurnak, ed. (in press).
- WLODAWER, A., and SJOLIN, L., "Structure of Ribonuclease A: Results of Joint Neutron and X-Ray Refinement at 2.0 Å Resolution," *Biochem.* 22, 2720-2728 (1983).
- WLODAWER, A., MILLER, M., and SJOLIN, L., "Active Site of RNase: Neutron Diffraction Study of a Complex with a Transition State Analog," *Proc. Natl. Acad. Sci. USA* 80, 3628-3631 (1983).
- WLODAWER, A., "Neutron Diffraction of Crystalline Proteins in Progress in Biophysics and Molecular Biology," Vol. 40. T. Blundell, ed. Oxford, England, Pergamon Press, Ltd. (1982).
- WLODAWER, A. and SJOLIN, L., "Improvement of the Quality of the Data Collected Using a Position-Sensitive Detector," *Nucl. Instrum. Methods* 201, 117-122 (1982).
- ZABEL, H., RUSH, J. J., and MAGERL, A., "Elastic Neutron Scattering Results on $C_{24}Rb(D)_{2}X$ in the Dilute Concentration Regime," *Synthetic Metals* (in press).
- ZABEL, H., MAGERL, A., DIANOIX, A. J., and RUSH, J. J., "Planar Diffusive Motion of Alkali Intercalant Atoms in Graphite," *Phys. Rev. Lett.* 50, 2094 (1983).
- ZABEL, H., MAGERL, A., and RUSH, J. J., "Phonons in LiC_6 ," *Phys. Rev.* B27, 3930-3933 (1983).
- ZOCCHI, M., GATTI, M., SANTORO, A., and ROTH, R. S., "Neutron and X-Ray Diffraction Study on Polymorphism in Lithium Orthotantalate, Li_3TaO_4 ," *J. Solid State Chem.* (in press).

PUBLICATIONS

INDEPENDENT PROGRAMS

DOWNING, R. G., FLEMING, R. F., LANGLAND, J. K., and VINCENT, D. H., "Neutron Depth Profiling at the National Bureau of Standards," Proceedings of the Sixth International Conference on Ion Beam Analysis, Tempe, AZ, May 23-27, 1983, Nucl. Instr. and Method (in press).

DOWNING, R. G., FLEMING, R. F., SIMONS, D. S., and NEWBURY, D. E., "Neutron-Induced Reactions and Secondary Ion Mass Spectrometry: Complementary Tools for Depth Profiling," Microbeam Analysis-1982, K. F. J. Heinrich, ed., San Francisco, 219 (1982).

EPSTEIN, M. S., GEARY, T. D., GOWER, G., TAVSCH, W., MILLS, K. J., and POLT, D., "Provisional Guidelines for Listing Specifications of Atomic Absorption Spectrometers," Clin. Chim. Acta, 122, 117F (1982).

FLEMING, R. F., PEI, P., and HSU, S. M., "Test Methods for Total Chlorine in Lubricating Base Oils," (in press).

FLEMING, R. F., "Neutron Self-Shielding Factors for Simple Geometries," Int. J. of Applied Radiation and Isotopes, 33, 1263 (1982).

GREENBERG, R. R., FLEMING, R. F., and ZEISLER, R., "High-Sensitivity Neutron Activation Analysis of Environmental and Biological Standard Reference Materials," (submitted for publication).

GREENBERG, R. R., "Radiochemical Procedures Used at NBS for High-Sensitivity Certification Analysis of Standard Reference Materials," Trans. Am. Nucl. Soc., 43, 269 (1982).

GREENBERG, R. R., "Neutron Activation Analysis Techniques Used For Ultra-trace Level Elemental Characterization of New NBS Milk Powder Standard Reference Material," Trans. Am. Nucl. Soc., 44, 28 (1983).

GREENBERG, R. R., and KINGSTON, H. M., "Trace Element Analysis of Natural Water Samples by Neutron Activation Analysis with Chelating Resin," Anal. Chem. 55, 1160 (1983).

KINGSTON, H. M. and GREENBERG, R. R., "An Elemental Ratioing Technique for Assessing Concentration Data From a Complex Water System," (submitted for publication).

KINGSTON, H. M., GREENBERG, R. R., BEARY, E. S., HARDAS, B. R., MOODY, J. R., RAINS, T. C., and LIGGETT, W. S., "The Characterization of the Chesapeake Bay: A Systematic Analysis of Toxic Trace Elements," National Technical Information Service, Order No. PB82-265-265 (1982).

KINGSTON, H. M. and LUTZ, G. J., "Adsorption and Stability Prior to Analysis of Simulated Nuclear Waste Leachate," Nuclear and Chemical Waste Management, 3, 245 (1982).

KOCH, W. F., STOLZ, J. W., KELLY, W. R., PAULSEN, P. J., LINDSTROM, R. M., FLEMING, R. F., and GREENBERG, R. R., "Methods and Procedures Used at the National Bureau of Standards to Certify NBS Sulfur in Coal SRM's for Sulfur Content, Calorific Value, Ash Content," T. E. Gills, ed., Nat. Bur. Standards (U.S.) Spec. Publ. 260 (1983).

PUBLICATIONS

LUTZ, G. J., ROOK, H. L., and LINDSTROM, R. M., "Determination of I-129 at Natural Levels by Thermal Neutron Activation Analysis," (submitted for publication).

WISE, S. A., FITZPATRICK, K. A., HARRISON, S. H., ZEISLER, R., LANGLAND, J. K., KRATOCHVIL, B., RAINS, T. C., RUSH, T. A., BUTLER, T. A., GRAMLICH, J. W., POWELL, L. J., BRLETIC, K. A., MURPHY, T. J., BAILEY, J., MAIENTHAL, E. J., KOCH, W. F., KLINE, W. F., ALLEN, C. F., CHESLER, S. N., HILPERT, L. R., GREENBERG, R. R., MACCREHAN, W. A., and ANDERSON, D. F., "The Pilot National Environmental Specimen Bank--Analysis of Human Liver Specimens," Zeisler, R., Harrison, S.H., and Wise, S. A., eds., Nat. Bur. Standards (U.S.) Spec. Publ. 656, 127 (1983).

ZEISLER, R., HARRISON, S. H., and WISE, S. A., "Trace Elements in Human Livers Using Quality Control in the Complete Analytical Process," Biol. Trace Element Res. (in press).

ZEISLER, R., LANGLAND, J. K., and HARRISON, S. H., "Cryogenic Homogenization Procedure for Biological Tissues," Anal. Chem. (in press).

U.S. DEPT. OF COMM.

**BIBLIOGRAPHIC DATA
SHEET** (See instructions)1. PUBLICATION OR
REPORT NO.

NBS TN 1190

2. Performing Organ. Report No.

3. Publication Date

April 1984

4. TITLE AND SUBTITLE

NBS Reactor: Summary of Activities July 1982 to June 1983

5. AUTHOR(S)

F. J. Shorten, Ed.

6. PERFORMING ORGANIZATION (If joint or other than NBS, see instructions)

NATIONAL BUREAU OF STANDARDS
DEPARTMENT OF COMMERCE
WASHINGTON, D.C. 20234

7. Contract/Grant No.

8. Type of Report & Period Covered

July 1982 to June 1983

9. SPONSORING ORGANIZATION NAME AND COMPLETE ADDRESS (Street, City, State, ZIP)

Same as item 6.

10. SUPPLEMENTARY NOTES

 Document describes a computer program; SF-185, FIPS Software Summary, is attached.

11. ABSTRACT (A 200-word or less factual summary of most significant information. If document includes a significant bibliography or literature survey, mention it here)

This report summarizes all those programs which depend on the NBS reactor. It covers the period from July 1982 through June 1983. The programs range from the use of neutron beams to study the structure and dynamics of materials through nuclear physics and neutron standards to sample irradiations for activation analysis, isotope production, radiation effects studies, neutron radiography, and nondestructive evaluation.

12. KEY WORDS (Six to twelve entries; alphabetical order; capitalize only proper names; and separate key words by semicolons)

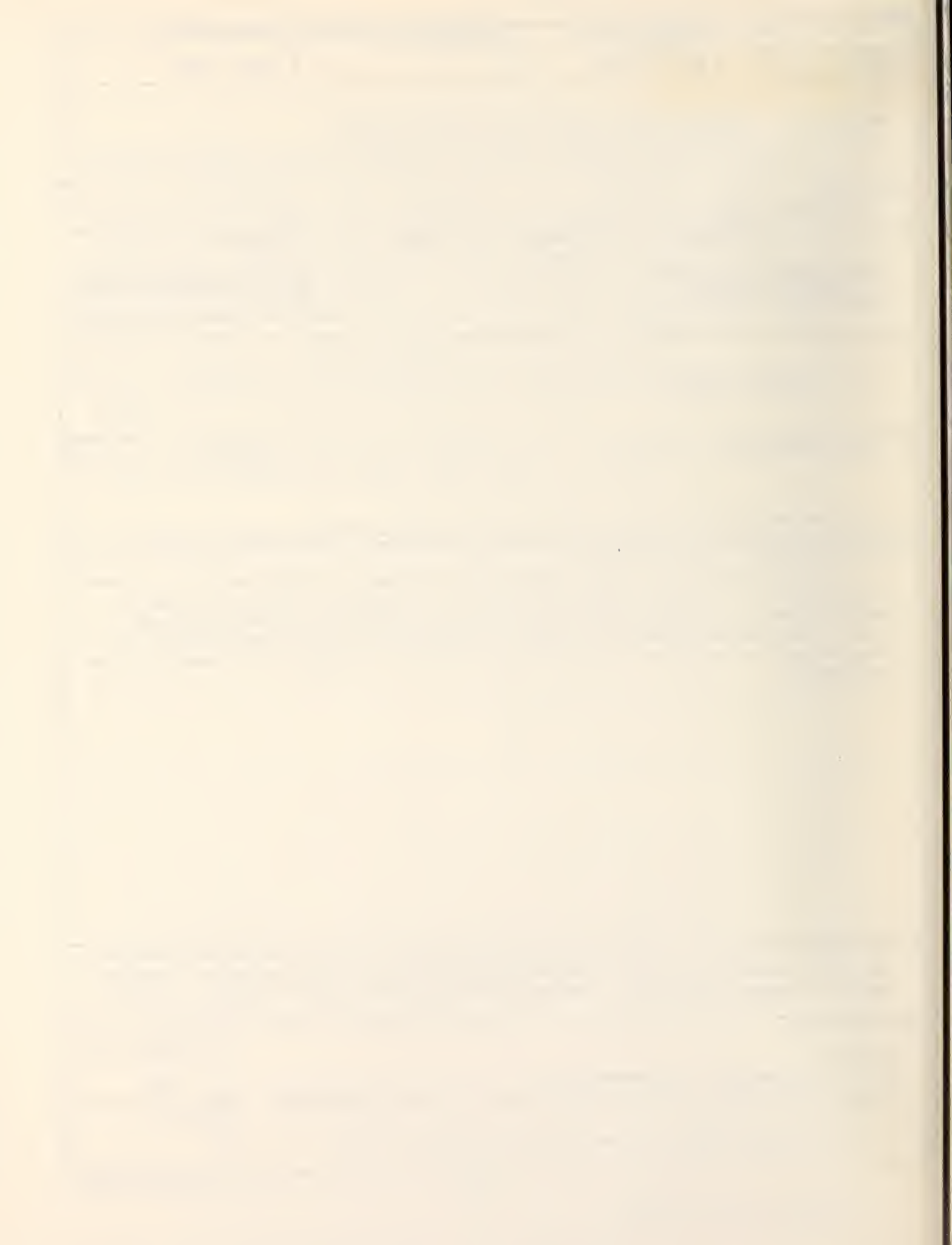
Activation analysis; crystal structure; diffraction; isotopes; molecular dynamics; neutron; neutron radiography; nondestructive evaluation; nuclear reactor; radiation.

13. AVAILABILITY

 Unlimited For Official Distribution. Do Not Release to NTIS Order From Superintendent of Documents, U.S. Government Printing Office, Washington, D.C. 20402. Order From National Technical Information Service (NTIS), Springfield, VA. 2216114. NO. OF
PRINTED PAGES

202

15. Price



NBS TECHNICAL PUBLICATIONS

PERIODICALS

JOURNAL OF RESEARCH—The Journal of Research of the National Bureau of Standards reports NBS research and development in those disciplines of the physical and engineering sciences in which the Bureau is active. These include physics, chemistry, engineering, mathematics, and computer sciences. Papers cover a broad range of subjects, with major emphasis on measurement methodology and the basic technology underlying standardization. Also included from time to time are survey articles on topics closely related to the Bureau's technical and scientific programs. As a special service to subscribers each issue contains complete citations to all recent Bureau publications in both NBS and non-NBS media. Issued six times a year. Annual subscription: domestic \$18; foreign \$22.50. Single copy, \$5.50 domestic; \$6.90 foreign.

NONPERIODICALS

Monographs—Major contributions to the technical literature on various subjects related to the Bureau's scientific and technical activities.

Handbooks—Recommended codes of engineering and industrial practice (including safety codes) developed in cooperation with interested industries, professional organizations, and regulatory bodies.

Special Publications—Include proceedings of conferences sponsored by NBS, NBS annual reports, and other special publications appropriate to this grouping such as wall charts, pocket cards, and bibliographies.

Applied Mathematics Series—Mathematical tables, manuals, and studies of special interest to physicists, engineers, chemists, biologists, mathematicians, computer programmers, and others engaged in scientific and technical work.

National Standard Reference Data Series—Provides quantitative data on the physical and chemical properties of materials, compiled from the world's literature and critically evaluated. Developed under a worldwide program coordinated by NBS under the authority of the National Standard Data Act (Public Law 90-396).

NOTE: The principal publication outlet for the foregoing data is the *Journal of Physical and Chemical Reference Data (JPCRD)* published quarterly for NBS by the American Chemical Society (ACS) and the American Institute of Physics (AIP). Subscriptions, reprints, and supplements available from ACS, 1155 Sixteenth St., NW, Washington, DC 20056.

Building Science Series—Disseminates technical information developed at the Bureau on building materials, components, systems, and whole structures. The series presents research results, test methods, and performance criteria related to the structural and environmental functions and the durability and safety characteristics of building elements and systems.

Technical Notes—Studies or reports which are complete in themselves but restrictive in their treatment of a subject. Analogous to monographs but not so comprehensive in scope or definitive in treatment of the subject area. Often serve as a vehicle for final reports of work performed at NBS under the sponsorship of other government agencies.

Voluntary Product Standards—Developed under procedures published by the Department of Commerce in Part 10, Title 15, of the Code of Federal Regulations. The standards establish nationally recognized requirements for products, and provide all concerned interests with a basis for common understanding of the characteristics of the products. NBS administers this program as a supplement to the activities of the private sector standardizing organizations.

Consumer Information Series—Practical information, based on NBS research and experience, covering areas of interest to the consumer. Easily understandable language and illustrations provide useful background knowledge for shopping in today's technological marketplace.

Order the above NBS publications from: Superintendent of Documents, Government Printing Office, Washington, DC 20402.

Order the following NBS publications—FIPS and NBSIR's—from the National Technical Information Service, Springfield, VA 22161.

Federal Information Processing Standards Publications (FIPS PUB)—Publications in this series collectively constitute the Federal Information Processing Standards Register. The Register serves as the official source of information in the Federal Government regarding standards issued by NBS pursuant to the Federal Property and Administrative Services Act of 1949 as amended, Public Law 89-306 (79 Stat. 1127), and as implemented by Executive Order 11717 (38 FR 12315, dated May 11, 1973) and Part 6 of Title 15 CFR (Code of Federal Regulations).

NBS Interagency Reports (NBSIR)—A special series of interim or final reports on work performed by NBS for outside sponsors (both government and non-government). In general, initial distribution is handled by the sponsor; public distribution is by the National Technical Information Service, Springfield, VA 22161, in paper copy or microfiche form.

U.S. Department of Commerce
National Bureau of Standards

Washington, D.C. 20234

Official Business

Penalty for Private Use \$300